

**Avalanche dynamics of structural phase
transitions in shape memory alloys by
acoustic emission spectroscopy**

Von der Fakultät für Mathematik, Informatik und
Naturwissenschaften der RWTH Aachen University
zur Erlangung des akademischen Grades eines
Doktors der Naturwissenschaften
genehmigte Dissertation
vorgelegt von

Diplom-Physiker Benno Ludwig
aus Bremen

Berichter: Universitätsprofessor Dr. Uwe Klemradt
Universitätsprofessor Dr. Antoni Planes

Tag der mündlichen Prüfung: 24. September 2009

Diese Dissertation ist auf den Internetseiten der
Hochschulbibliothek online verfügbar

**Avalanche dynamics of structural phase
transitions in shape memory alloys by
acoustic emission spectroscopy**

Von der Fakultät für Mathematik, Informatik und
Naturwissenschaften der RWTH Aachen University
zur Erlangung des akademischen Grades eines
Doktors der Naturwissenschaften
genehmigte Dissertation
vorgelegt von

Diplom-Physiker Benno Ludwig
aus Bremen

Berichter: Universitätsprofessor Dr. Uwe Klemradt
Universitätsprofessor Dr. Antoni Planes

Tag der mündlichen Prüfung: 24. September 2009
Diese Dissertation ist auf den Internetseiten der
Hochschulbibliothek online verfügbar

Abstract

In this work the avalanche dynamics of five shape memory samples has been analyzed by acoustic emission spectroscopy. The acoustic emission spectroscopy is particularly suitable for this analysis as it couples with high sensitivity to small structural changes caused by nucleation processes, interface movements, or variant rearrangements [91]. Owing to its high time resolution it provides a statistical approach to describe the jerky and intermittent character of the avalanche dynamics [20].

Rate-dependent cooling and heating runs have been conducted in order to study time-dependent aspects of the transition dynamics of the single crystals $\text{Ni}_{63}\text{Al}_{37}$, $\text{Au}_{50.5}\text{Cd}_{49.5}$, and $\text{Fe}_{68.8}\text{Pd}_{31.2}^{\text{single}}$, and the polycrystalline sample $\text{Fe}_{68.8}\text{Pd}_{31.2}^{\text{poly}}$. Moreover, a ferromagnetic $\text{Ni}_{52}\text{Mn}_{23}\text{Ga}_{25}$ single crystal has been studied by temperature cycles under an applied magnetic field and additionally by magnetic-field cycles at a constant temperature in the martensitic phase. All samples analyzed in this work show power law behavior in the acoustic emission features amplitude, energy, and duration, which indicates scale-free behavior. The access to these power law spectra allows an investigation of energy barriers separating the metastable states, which give rise to avalanche transition dynamics.

By performing rate-dependent experiments the importance of thermal fluctuations and the impact of martensite respectively twin stabilization processes have been examined. In the case of the $\text{Ni}_{52}\text{Mn}_{23}\text{Ga}_{25}$ sample, the magnetic-field-induced variant rearrangement at slow field cycles leads to stronger signals than the rearrangement at quick cycles. This behavior can be explained by twin stabilization processes, which are accompanied by a reduction of the twin boundary mobility. For $\text{Ni}_{63}\text{Al}_{37}$, the combination of relevant thermal fluctuations, different involved time scales, and a high degree of intrinsic disorder leads to a lower acoustic activity and weaker signals under decreasing cooling rates. In the case of $\text{Au}_{50.5}\text{Cd}_{49.5}$, by contrast, the low rates allow aging to become significant. This leads to higher energy barriers and, as a consequence, to stronger acoustic emission signals. The excellent agreement of this result with a model introduced by Otsuka *et al.* [127], suggests that aging should be included into the framework of driving rate effects in avalanche-mediated phase transitions [135].

In contrast to what has been stated earlier [20, 172], the author concludes that only the detection of rate-dependent acoustic activity or the detection of incubation times are necessary and sufficient conditions for time-dependent

dynamics. Rate-dependent exponents are a sufficient but not necessary condition for time-dependent behavior.

The determination of power law exponents has been proven to be a reliable tool for the characterization of the transition dynamics and associated energy barriers, because the exponents are robust and do not depend on experimental details. This observation reveals a close relation to the concept of self organized criticality [9].

In this work it has been shown for the first time by the evaluation of power law exponents how an applied magnetic field alters energy barriers during structural transitions of magnetic shape memory alloys. Depending on the symmetry of the product phase opposing results can be found: The symmetry-breaking process of a martensitic transition under an applied magnetic field leads to an increase of the activity due to a twofold process, including phase and twin boundary motion. Furthermore, the application of a magnetic field breaks the degeneracy, which leads to larger constraints reflected in stronger signals due to the satisfaction of the invariant habit plane condition. By contrast, less acoustic activity and weaker signals appear in association with the symmetry-conserving premartensitic transition under an applied field. The application of a field leads to an alignment of the magnetic moments. The lowered disorder reduces the energy barriers, which leads to less acoustic activity and weaker signals. At fields higher than 2.5 kOe the acoustic activity is completely suppressed, which suggests an overall weakening of the first order character of the premartensitic transition.

The amplitude and energy exponents of the material systems NiAl, FePd, and Ni₂MnGa (field-dependent) have been for the first time experimentally determined in this work. The amplitude exponents of NiAl and CuZnAl (3.1 ± 0.2) and of Ni₂MnGa and FePd (2.4 ± 0.2), determined in this work and reported in literature (see [22, 94, 139]), can be grouped into different classes. This reinforces the universality hypothesis [52] and the assumption that the symmetry of the product phase determines the universality class of the exponents [22]. Moreover, the results of this work suggest that further criteria, such as the degree of disorder or rate-dependent aging effects, should be taken into consideration as well.

Kurzfassung

Die Lawindynamik von fünf Formgedächtnislegierungen wurde im Rahmen dieser Arbeit mittels akustischer Emissionsspektroskopie untersucht. Die akustische Emissionsspektroskopie ermöglicht die Detektierung kleiner struktureller Änderungen, hervorgerufen durch Nukleationsprozesse, Grenzflächenbewegungen oder Variantenreorientierungen [91]. Aufgrund der hohen Zeitaufösung eröffnet diese Methode einen statistischen Zugang für die Beschreibung des sprunghaften Charakters der Lawinenprozesse [20].

Zur Untersuchung der zeitabhängigen Aspekte der Umwandlungsdynamik wurden ratenabhängige Kühl- und Heizzyklen mit den Einkristallen $\text{Ni}_{63}\text{Al}_{37}$, $\text{Au}_{50,5}\text{Cd}_{49,5}$ sowie $\text{Fe}_{68,8}\text{Pd}_{31,2}^{\text{single}}$ und dem Polykristall $\text{Fe}_{68,8}\text{Pd}_{31,2}^{\text{poly}}$ durchgeführt. Darüber hinaus wurde ein ferromagnetischer $\text{Ni}_{52}\text{Mn}_{23}\text{Ga}_{25}$ Einkristall einerseits mittels Temperaturzyklen unter Einfluss eines Magnetfelds und andererseits mittels Magnetfeldzyklen bei konstanter Temperatur innerhalb der martensitischen Phase untersucht. Alle in dieser Arbeit untersuchten Proben zeigen Potenzgesetzverhalten in der Signalamplitude, -energie und -dauer, was auf skalenfreies Verhalten hinweist. Die Messung der Potenzgesetzepektren ermöglicht die Untersuchung von Nukleationsbarrieren, welche die metastabilen Zustände trennen und zum Lawinenverhalten führen.

Die Bedeutung von thermischen Fluktuationen und von Martensit- respektive Zwillingsstabilisierung wurde mittels ratenabhängiger Messungen untersucht. Im Fall von Magnetfeld induzierter Reorientierung von Varianten in $\text{Ni}_{52}\text{Mn}_{23}\text{Ga}_{25}$ führen langsame Zyklen zu stärkeren akustischen Signalen als schnelle Zyklen. Dieses Verhalten kann mittels Zwillingsstabilisierung erklärt werden, die zu einer geringeren Beweglichkeit der Grenzfläche führt. Im Fall von $\text{Ni}_{63}\text{Al}_{37}$ führen kleinere Raten zu weniger akustischer Aktivität und zu schwächeren Signalen. Die Erklärung liegt in dem Zusammenspiel thermischer Fluktuationen, verschiedener relevanter Zeitskalen und dem hohen Maß an intrinsischer Unordnung. Im Gegensatz dazu führen bei $\text{Au}_{50,5}\text{Cd}_{49,5}$ kleinere Raten zu Stabilisierungseffekten, die höhere Nukleationsbarrieren und damit stärkere akustische Signale zur Folge haben. Diese Ergebnisse legen nahe, dass Stabilisierungsphänomene mit in die Gruppe ratenabhängiger Effekte in lawinengetriebenen Umwandlungen [135] einbezogen werden sollten.

Im Gegensatz zu früheren Veröffentlichungen [20, 172] wird in dieser Arbeit gezeigt, dass ausschließlich der Nachweis von ratenabhängiger akustischer Aktivi-

tät oder von Inkubationszeiten ein notwendiges und hinreichendes Kriterium für eine explizit zeitabhängige Dynamik ist. Ratenabhängiges Verhalten der Exponenten ist zwar hinreichend jedoch nicht notwendig für eine explizit zeitabhängige Dynamik.

Im Rahmen der Arbeit wurde gezeigt, dass die Untersuchung von Übergangsdynamiken und Energiebarrieren über Potenzgesetz-Exponenten eine robuste Methode darstellt, da die Exponenten nicht von experimentellen Details abhängen. Diese Beobachtung stellt einen engen Zusammenhang zum Konzept der selbstorganisierten Kritikalität her.

In dieser Arbeit wurde zum ersten Mal mittels Potenzgesetzespektren analysiert, wie sich Nukleationsbarrieren struktureller Phasenübergänge durch magnetische Felder ändern. In Abhängigkeit der Symmetrie der Produktphase ergeben sich gegenläufige Ergebnisse: Der symmetriebrechende Charakter der martensitischen Umwandlung führt bei angelegtem Feld zu einem Anstieg der akustischen Aktivität aufgrund von Bewegung der Phasen- und der Zwillingsgrenzflächen. Des Weiteren führt das angelegte Magnetfeld zur teilweisen Aufhebung der Entartung unter gleichzeitiger Erfüllung der Invariantenbedingung, was stärkere akustische Signale zu Folge hat. Im Gegensatz dazu führt ein angelegtes Feld in der symmetrieerhaltenden premartensitischen Umwandlung zu einer geringeren akustischen Aktivität und zu schwächeren Signalen. Das angelegte Feld richtet die magnetischen Momente aus und verringert damit die Unordnung des Systems. Dies führt zu einer Reduktion der Nukleationsbarrieren und damit zu einer geringeren akustischen Aktivität und zu schwächeren Signalen. Bei Feldern größer als 2,5 kOe ist die akustische Aktivität komplett unterdrückt, was auf eine Schwächung des diskontinuierlichen Charakters der Umwandlung hinweist.

In dieser Arbeit wurden erstmals die Exponenten der Amplitude und Energie für die Materialsysteme NiAl, FePd und Ni₂MnGa (feldabhängig) untersucht. Die Exponenten der Amplitude von NiAl und CuZnAl ($3,1 \pm 0,2$) sowie von Ni₂MnGa und FePd ($2,4 \pm 0,2$), die in dieser Arbeit bestimmt wurden (siehe auch [22, 94, 139]), können in unterschiedliche Klassen eingeteilt werden. Diese Ergebnisse bestätigen die Universalitätshypothese [52] und bekräftigen die Schlussfolgerung, dass die Universalitätsklassen der Exponenten durch die Symmetrie der Produktphase bestimmt werden [22]. Darüber hinaus legen die Ergebnisse dieser Arbeit nahe, dass weitere Kriterien, wie der Grad der Unordnung oder Alterungseffekte, für die Klassifizierung in Betracht gezogen werden sollten.

Contents

1. Introduction	1
2. Phase transitions	5
2.1. Landau theory	6
2.2. Power laws in phase transitions	11
2.3. Universality and self-organized criticality	16
3. Martensitic transitions in shape memory alloys	21
3.1. Classification of phase transitions	21
3.2. Characterization of martensitic phase transitions	25
3.2.1. Transition dynamics, hysteresis, and disorder	29
3.2.2. Precursor effects and premartensitic transitions	37
3.2.3. Magnetic shape memory alloys	43
3.3. Effects in (magnetic) shape memory alloys	48
3.3.1. Shape memory effect	49
3.3.2. Superelasticity	51
3.3.3. Magnetic-field-induced strain	53
3.4. Acoustic emission	56
3.4.1. Origin of acoustic emission in martensitic phase transitions	56
3.4.2. Propagation of ultrasonics in solids	58
3.5. Analyzed material systems	62
3.5.1. Ni-Al	63
3.5.2. Au-Cd	65
3.5.3. Fe-Pd	65
3.5.4. Ni-Mn-Ga	68
4. Experimental Details	75
4.1. Acoustic emission setup	75
4.2. Sample environment	80
4.2.1. Vacuum setup	80
4.2.2. Magnetic field setup	82
4.2.3. Differential scanning calorimeter	85

5. Tests, calibrations, and simulations	87
5.1. Test of the acoustic emission system	87
5.2. Temperature calibration	88
5.2.1. Setup and measurement procedure	89
5.2.2. Analysis and results	91
5.3. Temperature simulation and evaluation	93
5.3.1. Static simulation	93
5.3.2. Dynamic simulation	97
6. Measurement procedures	105
7. Results	109
7.1. Data processing and evaluation procedures	109
7.2. Sample characterization	114
7.2.1. Ni ₆₃ Al ₃₇	116
7.2.2. Au _{50.5} Cd _{49.5}	123
7.2.3. Fe _{68.8} Pd _{31.2} ^{single} and Fe _{68.8} Pd _{31.2} ^{poly}	128
7.2.4. Ni ₅₂ Mn ₂₃ Ga ₂₅	136
8. Discussion	153
8.1. Ni ₆₃ Al ₃₇	165
8.2. Au _{50.5} Cd _{49.5}	173
8.3. Fe _{68.8} Pd _{31.2} ^{single} and Fe _{68.8} Pd _{31.2} ^{poly}	184
8.4. Ni ₅₂ Mn ₂₃ Ga ₂₅	187
8.4.1. Premartensitic transition	188
8.4.2. Martensitic transition	191
8.4.3. Rearrangement of variants under magnetic field	194
8.5. Comparison of results	201
9. Conclusions and summary	207
10. Outlook	211
A. Appendix	213
A.1. Results of temperature calibration	213
List of Figures	215
List of Tables	239
Bibliography	243

1 Introduction

For over 3000 years the martensitic transition has played an essential role in steel processing for the development of tools and weapons [93]. The quenching of iron carbon alloys, after hot forging, leads to improved material properties, such as an enhanced hardness. In 1878 Martens for the first time found an explanation for the new material characteristics by analyzing its microstructure: In contrast to the high temperature phase, the low temperature phase shows a highly oriented microstructure after quenching [102–104]. In order to acknowledge Martens' pioneering work, Osmond proposed to call these materials *martensites*. About 50 years later in 1932 Ölander discovered in Au-Cd remarkable elastic properties associated with the martensitic transition. The so-called pseudoelasticity describes a fully reversible elastic response to an applied stress. Strains of the order of 10% that originate from the stress-induced martensitic transition can be achieved. Twenty years later two research groups around Kurdjumov and Khandros [153] and Chang and Read [26] found out that the temperature-induced martensitic transition can lead to a complex behavior which is called shape memory effect. The shape memory effect enables a sample to recover its shape after being deformed in the low temperature phase by applying heat and thereby inducing the martensitic reverse transition. The microscopic origin of this effect lies in the symmetry-breaking character of the diffusionless forward transition under cooling. Due to the lower symmetry, structural domains are formed that retain an orientational relationship with the cubic structure of the high temperature phase. The newest development in the field of shape memory alloys, introduced by Ullakko *et al.* in 1996 [183], are magnetic shape memory alloys which allow a magnetic control of the shape change.

Both, the shape memory alloys and the magnetic shape memory alloys broaden the class of smart materials,¹ which are characterized by a non-linear response to the change of an external parameter. They inherently combine characteristics of a sensor and a self-adapting actuator. These functionalities in combination with a high ratio of possible strains (or force excitation) to weight make (magnetic) shape memory alloys the material class of choice for several high-tech applications:²

¹To the class of smart materials additionally belong piezoelectric materials, non-Newtonian fluids, and ferrofluids beside others.

²(Magnetic) shape memory alloys can either reach large strains (up to 10%) or exert high forces (up to 700 MPa). Both extremes lead to a reduction of the achievable cycle numbers from about 10^6 to 10^3 [107].

In medical engineering shape memory alloys find application in self-expanding stents and in miniaturized self-expanding blood pumps. In the aerospace industry they are, beside many other applications, used for self-unfolding solar-panels of satellites and in self-adapting winglets [81]. Magnetic shape memory alloys are very promising for the design of new actuators because their magnetic-field-induced strains can be controlled at rates in the kHz range [101, 182, 195, 196].

Martensitic transitions can be analyzed by several experimental techniques, such as differential scanning calorimetry, X-ray diffraction, X-ray photo correlation spectroscopy, resistivity methods, or vibrational techniques. In this work, the technique of acoustic emission spectroscopy³ has been chosen in order to analyze avalanche dynamics and acoustic signal strength of martensitic transitions. It is one of the most suitable techniques as it monitors changes in the strain field of the sample, which are inherently associated with the martensitic transition.⁴ It is very sensitive towards small structural changes and has a high time resolution in the submicrosecond range. This enables the analysis of the jerky and intermittent transition dynamics that results from an avalanche-like propagation of the phase boundary through a sequence of metastable states arising in the high dimensional energy landscape. This measurement technique opens two distinct experimental approaches: Structural changes arising in the samples can be analyzed either by the acoustic activity, which is the number of acoustic emission events per time respectively temperature interval, or by the distribution of the signal strength. The first mentioned approach allows to classify the transition dynamics i. e. time-dependent aspects by rate-dependent measurements. The second approach focuses on the signal strength that can be accessed by the observables amplitude, energy, and duration and is related to the height of the energy barriers separating the metastable states.

Power law behavior can be found in all signal parameters (amplitude, energy, and duration) analyzed in this work. The concept of power laws is closely related to the occurrence of scale-free behavior. In solid-state physics scale-free behavior is primarily known from continuous phase transitions. It can be observed at the critical point where the absence of interfacial energies promotes the occurrence of fluctuations at all length scales. However, many other systems in science and socio-economics show power law behavior as well and can be characterized by power law exponents. A prominent example is the Gutenberg-Richter law which relates the strength of earthquakes with their frequency of occurrence. Additionally, power laws can, for example, also be found in the distribution of forest fires, income, or the distribution of words in novels. The observation that processes of such diverse nature all can be described by power laws gave

³The acoustic emission technique is well established in the field of non-destructive testing.

⁴The selection of *strain* as the order parameter of the martensitic transition underlines the fundamental relation between the transition mechanism and the released acoustic emission.

rise to the formulation of two hypotheses: The hypothesis of *universality* [52], widely discussed in experimental and theoretical work (e. g. [19, 22, 164, 189]), claims that systems can be grouped into the same universality class based on fundamental system properties such as dimension and interaction range, which do not depend on the details of the system. The hypothesis of *self-organized criticality* by Bak, Tang, and Wiesenfeld arose from the observation that a large group of systems shows power law behavior without being actively tuned or driven into this state and assumes that the critical state is an attractor for the dynamics of many systems [9, 10].

This work sheds light on both the avalanche dynamics and the power law exponents of the shape memory materials Ni-Al, Au-Cd, Fe-Pd, and Ni-Mn-Ga analyzed by rate- and magnetic-field-dependent experiments by acoustic emission spectroscopy. This work confirms universality classes proposed in the literature and analyzes for the first time the martensitic transition in Fe-Pd by acoustic emission spectroscopy in a single and a polycrystalline sample. It studies the effect of an applied magnetic field on the intermediate and martensitic transition in Ni-Mn-Ga and analyzes for the first time the magnetic-field-induced rearrangement of structural domains by acoustic emission spectroscopy. Furthermore it proposes an explanation of observed driving rate effects within the framework of martensite aging.

2 Phase transitions

A phase is a region of space in a thermodynamical system, which is equilibrated with its surroundings and all its physical properties are uniform on a macroscopic scale [175]. Phase transitions are well known phenomena. Commonly known examples are the transitions of water between the solid, the liquid and the gas state (figure 2.1). Phase transitions can be triggered by the external change of a thermodynamical parameter like temperature, pressure or a (generalized) field. In the vicinity of a phase transition the energies of the involved phases compete. In many cases two phases compete, but there are as well occasions where more than two phases are involved. A prominent example is the triple point of water where all three phases coexist under thermodynamic equilibrium conditions (see figure 2.1). Already in 1878, Gibbs found a general relationship between the number of coexisting phases P , the number of thermodynamical degrees of freedom F , and the number of components C the thermodynamical system consists of. The so-called Gibbs-phase rule is formulated as

$$P + F = C + 2. \quad (2.1)$$

In case of the triple point of water, which is a one-component substance ($C=1$), there are three coexisting phases ($P=3$) and no degrees of freedom ($F=0$) because the phases meet at a (zero-dimensional) point. A phase transition is not necessarily

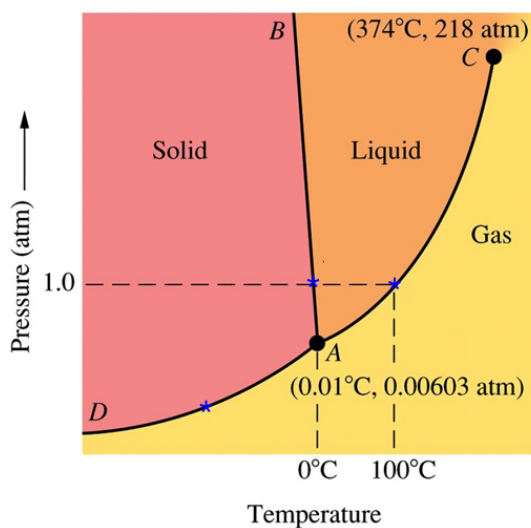


Figure 2.1: Phase diagram of water with the triple point (A), the critical point (C), the sublimation line (D), the vaporization line between (A) and (C), and the melting line (B).

associated with a change of the state of matter, although the contrary is widely assumed. In fact, several transitions exist within the solid state, for example the martensitic transition, which will be analyzed in the present work.

For an exact microscopic description of phase transitions it would be necessary to consider all degrees of freedom of the physical system. Within the framework of statistical mechanics this can be realized by evaluating the canonical distribution $\exp(-\mathcal{H}/k_B T)$, where k_B is the Boltzmann constant and \mathcal{H} the Hamiltonian of the system [39]. Microscopic degrees of freedom and macroscopic thermodynamic quantities are connected by a sum over all microscopic states, which is called the partition function

$$Z = \text{tr}(e^{-\mathcal{H}/k_B T}). \quad (2.2)$$

The free energy can be obtained from the partition function by $F = -k_B T \ln Z$ [39]. However, from an experimental point of view it is impossible to measure all degrees of freedom of a thermodynamical system; the involved degrees of freedom need to be reduced. A very successful approach related to this issue was introduced by Landau in 1937 (detailed description in section 2.1). He described phase transitions using a macroscopic observable, which represents the *order parameter*. In equilibrium conditions (thereby ignoring for a moment surface energies, which are discussed below in see section 2.2) the phase of the system is determined by the minimization of the free energy (figure 2.2), which can be expressed as a Taylor series of the order parameter. The order parameter is defined as having a zero value in one phase and a non-zero value in the other phase. The behavior of the order parameter at the phase transition determines whether the transition is called continuous or discontinuous. Examples of the order parameter are the density difference $\rho - \rho_{gas}$ at the solid-gas transition and the magnetization M at the ferromagnetic transition. For other transitions, such as the martensitic ferroelastic phase transition, the identification of an order parameter turns out to be more complicated. In case of a magnetic shape memory alloy the order parameter is the strain, which is coupled to the magnetic order parameter [171].

2.1 Landau theory

In the description of thermodynamical systems and, in particular phase transitions, the Gibbs free energy G (respectively the free energy F) is a central physical quantity. The status of the system is defined by its attempt to minimize the free energy.

In the year 1937 Lev Davidovich Landau introduced the concept of a macroscopic order parameter η to describe phase transitions. The so-called *Landau theory* uses a mean field approach by condensing all microscopic degrees of

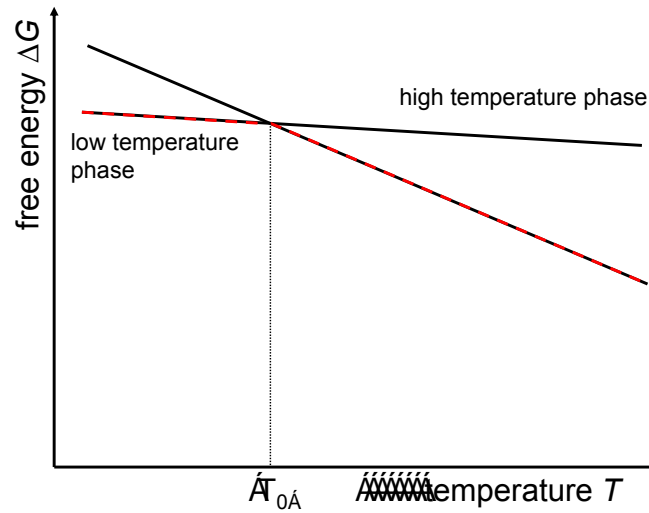


Figure 2.2: Representation of the free energies of two phases in the vicinity of the phase transition. At the thermodynamic equilibrium temperature T_0 both phases have the same free energy. At a lower temperature, the low temperature phase is energetically favored whereas at a higher temperature the high temperature phase is favored. The temperature is only one example of a possible control parameter.

freedom of a thermodynamical system into the macroscopic observable η . The order parameter is defined in a way that its mean value

$$\overline{\eta(T \geq T_c)} = 0 \quad (2.3)$$

vanishes at the transition temperature T_c and above. The experimental observation that the order parameter continuously tends towards zero while approaching the transition temperature ($T < T_c$), leads to the idea of expanding the free energy G as a function of the order parameter in the vicinity of the phase transition.¹ For the expansion of G two conditions have to be assumed: First, the free energy needs to be analytic and second, the symmetry of the expanded energy and its Hamiltonian needs to be identical. The expanded energy is

$$G(T, h, \eta) = G_0(T) + a(T - T_c)\eta^2 + b\eta^4 - h\eta \quad a, b \geq 0, \quad (2.4)$$

where T is the temperature, T_c the transition temperature, a and b positive constants, and h an external parameter. The order parameter η directly couples to the parameter h . In case of ferromagnetic materials the order parameter η represents the magnetization ($\eta = M$) and the parameter h represents the magnetic

¹According to the continuous behavior of the free energy as a function of the order parameter, the transition is called continuous phase transition.

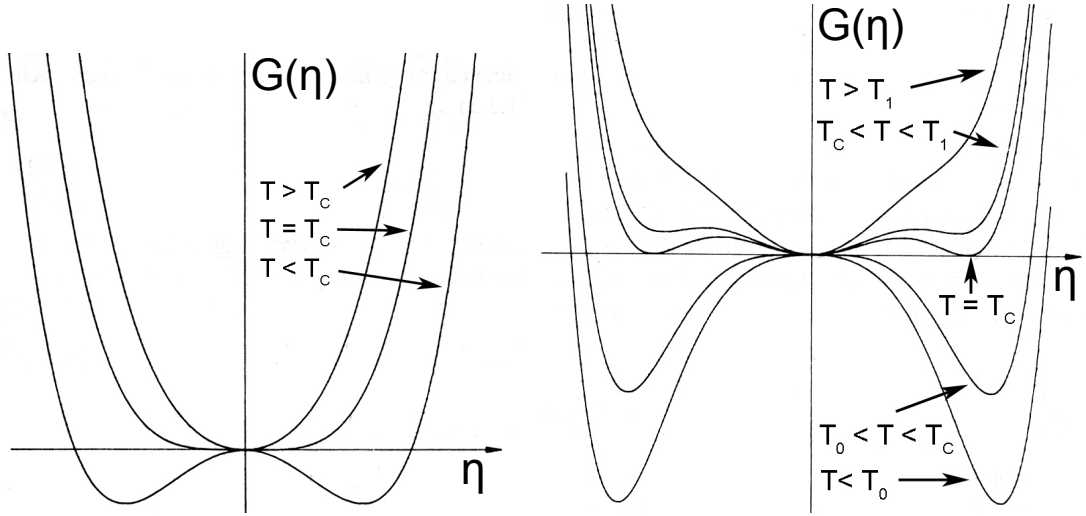


Figure 2.3: Representation of the free energy G calculated within a Landau theory as a function of the order parameter η at selected temperatures. (Left for a continuous, right for a discontinuous phase transition.) Note the different local and global energy minima for both transitions at the relevant temperatures, which reveal the continuous respectively the discontinuous character of the transitions (adapted from [78] and [172]).

field ($h = H$). Under thermodynamic equilibrium conditions with $h = 0$, only the second term can change its sign as a function of the temperature. In figure 2.3 (left) it can be seen that the low temperature phase ($T < T_c$) reveals energetic minima at $\pm\eta \neq 0$ and a maximum at $\eta = 0$, whereas the high temperature phase ($T > T_c$) has no maximum but a global minimum at $\eta = 0$. For a quantitative evaluation of the energy minima the expanded energy is derived with respect to the order parameter

$$\begin{aligned} \frac{\partial G}{\partial \eta} &\stackrel{!}{=} 0 \\ \Leftrightarrow 2a(T - T_c)\eta + 4u\eta^3 &= 0. \end{aligned} \quad (2.5)$$

Solutions are

$$\eta = \begin{cases} 0 & \forall T \quad \text{max. for } T < T_c, \text{ min. for } T \geq T_c \\ \pm\sqrt{\frac{a}{2b} \cdot (T_c - T)} & T \leq T_c \quad \text{min. for } T < T_c. \end{cases} \quad (2.6)$$

For temperatures lower than the transition temperature T_c the minimization is achieved with a non-vanishing order parameter. The relation between η and T

shows power law behavior $\eta(T) \propto (T - T_c)^\beta$ with $\beta = 1/2$ (further details on power laws can be found in section 2.2). At the transition temperature and above, the order parameter vanishes and remains zero. The change of the order parameter from zero to a finite value is described as a spontaneously broken symmetry. In case of the ferromagnetic transition, the symmetry-breaking character can be noticed directly by the experimental observation. In the absence of an external field the paramagnetic field ($T > T_c$) has no magnetization ($\eta = M = 0$). During the transition a spontaneous magnetization M occurs, which is not related to any externally applied magnetic field. The paramagnetic state turns into an anisotropic ferromagnetic phase [39]. In the vicinity of continuous phase transitions several observables can be described by power laws such as the specific heat or the susceptibility. The exponents are called critical exponents according to the critical phenomena at the critical point.

Landau's approach holds as well for the description of discontinuous phase transitions. In contrast to the expansion of continuous transitions a sixth order term is included in case of a symmetric free energy.

$$G(T, h, \eta) = G_0(T) + a(T - T_0)\eta^2 - b\eta^4 + c\eta^6 - h\eta \quad a, b, c \geq 0, \quad (2.7)$$

where T is the temperature, T_0 a formal temperature related to the transition temperature, a , b , and c are positive constants, and h is an external parameter which couples to η . In case of a martensitic transition, the order parameter η represents the internal strain, h can be for example external stress. Because of the alternating signs of the involved terms, the shape of the free energy is more complex, and more cases have to be distinguished than for continuous transitions (see figure 2.3 left and right). At high temperatures above $T_0 + \frac{u^2}{3ac} =: T_1$, the energy has a global minimum at $\eta = 0$. For lower temperatures $T_0 + \frac{u^2}{4ac} =: T_c < T < T_1$, the global minimum remains at $\eta = 0$, but two symmetric local minima appear at $\eta = \pm\eta_0(T) \neq 0$. While temperature further decreases, three energetic equivalent minima form at $\eta = 0$ (as before) and $\eta = \pm\eta_0(T) \neq 0$, both depending on the temperature. At the critical temperature $T = T_c$ three equivalent minima exist at $\eta = 0$ and $\eta = \pm\eta_0(T) \neq 0$. Passing the critical temperature $T < T_c$, the extremum at $\eta = 0$ becomes a local minimum and two energetic equivalent global minima develop at $\eta = \pm\eta_0(T) \neq 0$. For temperatures below T_c the minimum at $\eta = 0$ converts into a local maximum and the two minima at $\eta = \pm\eta_0(T) \neq 0$ remain. In summary, for temperatures $T \geq T_c$ the free energy $G(\eta, T)$ is minimized by a vanishing order parameter $\eta = 0$. In case of lower temperatures, $G(\eta, T)$ has its lowest value at $\eta = \pm\eta_0(T) \neq 0$. The (discontinuous) jump of the order parameter from $\eta = 0$ to $\eta_0 \neq 0$ is a crucial phenomenon of discontinuous phase transitions, which is contrasted by the continuous variation in the continuous transition. Both characteristic features are consistently shown by the Landau theory. In case of the martensitic transition the symmetry-breaking character is directly

visible in the formation of martensitic variants of lower symmetry, which as a consequence lowers the lattice symmetry. Furthermore, the Landau theory correctly describes qualitative aspects of the behavior of the order parameter in martensitic transitions: Internal strains can be measured at low temperatures in the martensitic phase which disappear at the phase transition. The resulting high temperature austenitic phase is strain-free.

The Landau theory provides both a qualitatively good understanding of phase transitions and mathematical relations, such as the power law behavior of order parameters as a function of the temperature with an exponent of $\beta = 1/2$. However, the numerical values of the Landau exponents do usually not agree with experimental results.²

A limitation of the Landau theory is the absence of (thermal) fluctuations of the order parameter, which are of particular importance for continuous phase transitions. At the critical point, fluctuations of all length scales occur. A well known example is the *critical opalescence*. At its critical point water is not transparent for visible light. The light is scattered by the steam bubbles of all length scales. The unlimited growth (and collapse) of structures at the critical point is a consequence of the equality of all characteristics of both phases. In other words, there is no difference between both phases; they have become one. In the case of critical opalescence it is visible to the naked eye that no stable interfaces exist between water and steam. Both, the interfacial energy and the volume energy exactly compensate each other. In the absence of all restoring forces the only active driving forces are thermal fluctuations. Very small energy fluctuations can either lead to an infinite growth or to a collapse of developed mixed-state structures.

Large values or even singularities of the order parameter are not included in the Landau approach, which assumes small order parameters for an analytic expansion. Another succeeding approach of interest in this context is the Ginzburg-Landau theory, including spatial variations. The *Renormalization Group Theory*, which was introduced by K. Wilson in the 1970's and rewarded the Nobel prize in 1982, provides better numerical values of the critical exponents [202–204]. The core idea of the renormalization group is to analyze the behavior of evolution laws of a system under rescaling to longer scales. In this approach, all system spaces for possible evolution laws undergo a mapping during coarse-graining. A fixed point in the system that remains stable under rescaling is mapped into itself and reveals self-similarity. All systems attracted under coarse-graining by the fixed point share the same universality class [164]. The concept of scale-invariance

²Systems with long-range interactions show Landau-like behavior, because the Landau theory is based on integrated degrees of freedom. Examples are ferroelastic and ferroelectric transitions. The ferromagnetic transition is a counterexample.

(see section 2.2), which is closely connected to the idea of self-similarity, plays an important role in this approach.

2.2 Power laws in phase transitions

Discontinuous phase transitions occur with an exchange of latent heat. Examples among many others are the solid-liquid transition of water and the martensitic phase transition. The involved latent heat and the entropy of the system ΔS (first derivative of the Gibbs free energy G) show a discontinuity at the phase transition - the reason why the transition is called discontinuous. Both quantities are related via $L = T\Delta S$ with T being the temperature. The combination of the discontinuous state function (here enthalpy) with an as well discontinuous order parameter (here volume) leads to the Clausius-Clapeyron-law describing the coexistence lines in phase diagrams

$$\frac{dp}{dT} = \frac{S_B - S_A}{V_B - V_A} = \frac{L}{T\Delta V}. \quad (2.8)$$

In the nucleation process of discontinuous transitions surface effects play an important role. Two energy terms have to be compared: the surface energy needed and the volume energy gained by the difference between the energies of the old and the new phase (see figure 2.2 and 2.4). Because of the different exponents involved, it is obvious that the critical nucleus radius r_c has to be overcome in order to convert the nucleation into growth of the new phase. The nucleation process can proceed in two ways: homogeneously or heterogeneously. In the homogeneous conditions the whole surface energy has to be gained from the volume term. This leads to a high energy barrier and to the formation of metastable states. For a successful nucleation a large undercooling or long waiting times are necessary. In case of heterogeneous nucleations the energy barriers are reduced by the existence of small particles working as crystallization nuclei. The particles provide surfaces which are used as a starting interface for the new phase. Heterogeneous nucleation reduces the required undercooling (see figure 2.4).

In contrast to discontinuous transitions continuous phase transitions occur without latent heat. The first derivative does not show any discontinuity whereas the second derivative shows a singularity. In figure 2.5, both transition types are schematically compared. Continuous phase transitions occur for example between the liquid and the gas state (see figure 2.1), between the ferromagnetic phase and the paramagnetic phase, and between the ordered and the disordered phase in alloys. In the vicinity of the critical point the involved phases differ only infinitesimally; their physical properties are basically the same. The vanishing difference between the phases can be seen in figure 2.6, where the normalized density difference of several substances are displayed against the normalized temperature. Because of the almost absent interfacial energies, both phases

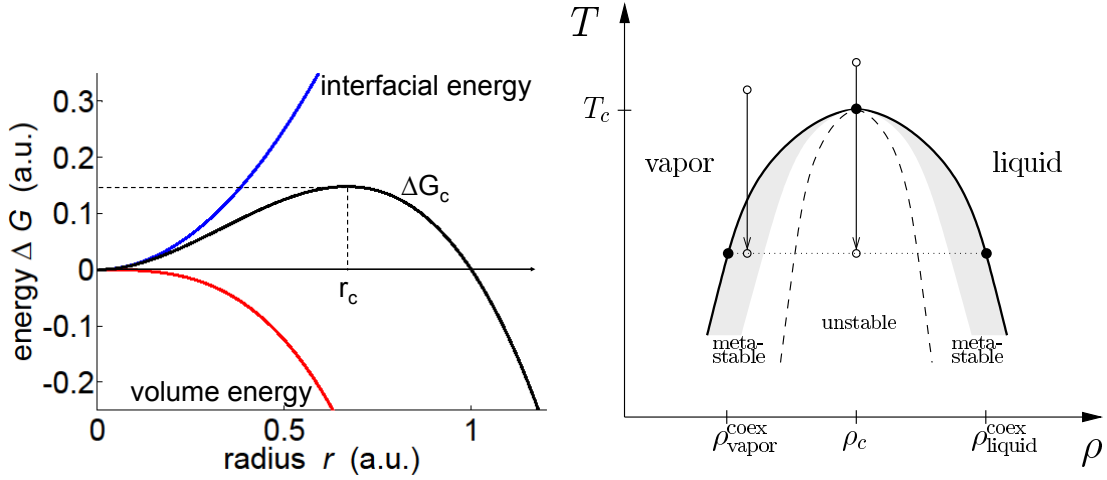


Figure 2.4: Nucleation energy barrier as a result of competing interfacial and volume energies (left). A generic radius dependence is supposed, $G \propto r^2$ for the interfacial term (blue line) and $G \propto r^3$ for the volume term (red line). The resulting nucleation barrier (black line) has its maximum at the critical radius r_c , which has to be overcome for a successful nucleation. On the right hand side is shown the non-equilibrium temperature-density phase diagram of a fluid. The area of coexistence is divided into an unstable and a metastable region between the phase boundary curve and the (dotted) spinodal curve. By quenching outside the critical point the system crosses a metastable state of undercooling and reaches the (unstable) area of spinodal decomposition, which is the separation of two macroscopic phases inside the coexisting region.

can fluctuate and form nuclei in the other phase. The fluctuation size can be characterized by the correlation length ξ . Exactly at the critical point all differences vanish completely; the former differing phases can no longer be differentiated and the correlation length reaches all scales which are in agreement with the boundary conditions of the system.³ This phenomenon is called critical behavior and the involved fluctuating quantities can be described by power laws. In their asymptotic form power laws can be written as $f(x) = c \cdot x^\alpha$, where c is a constant (see as well equations 2.18 and 2.19).

Power laws are scale invariant. This mathematical feature characterizes a function whose shape remains unchanged under a rescaling (x is projected on $n \cdot x$). The mathematical relation showing the scale-free behavior of power laws

$$f(x) = c \cdot x^\alpha \rightarrow f(n \cdot x) = c \cdot (n \cdot x)^\alpha = \underbrace{c \cdot n^\alpha}_{c'} \cdot x^\alpha = c' \cdot f(x) \quad (2.9)$$

³At the critical point the differentiation between homo- and heterogenous nucleations becomes meaningless and undercooling is impossible (see figure 2.4).

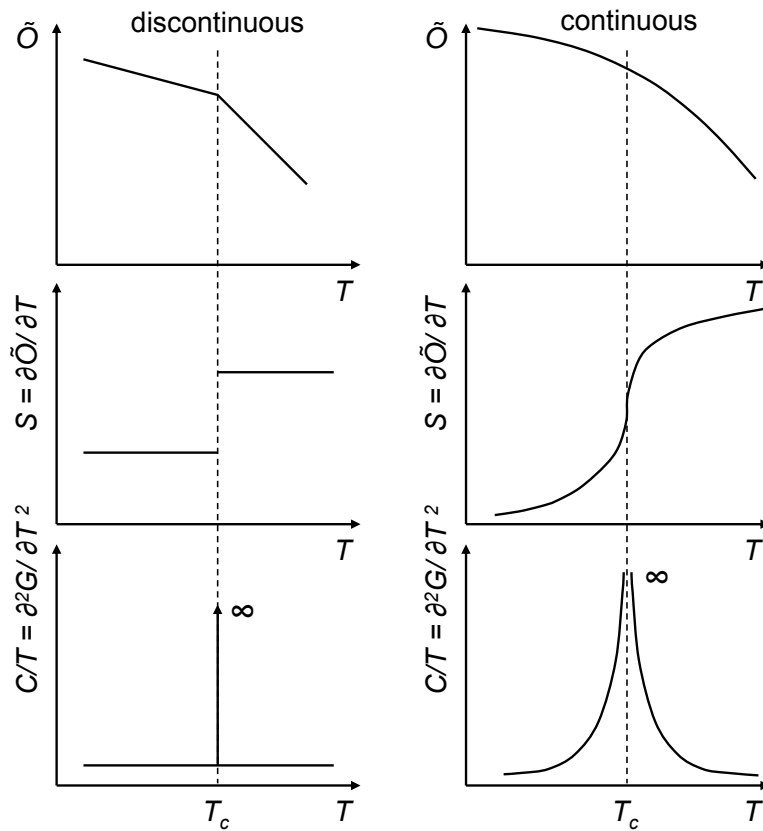


Figure 2.5: Comparison of the discontinuous (left) and the continuous (right) phase transition. The figure shows the behavior of the free energy and its first and second derivative as a function of the temperature.

is illustrated by figure 2.7, where exponential functions are added to illustrate the unique feature of power laws. The inset shows a power law on a log-log scale. On a log-log scale all power laws have a linear shape and the numerical value of its slope is equivalent to the critical exponent

$$f(x) = c \cdot x^\alpha \rightarrow \log f(x) = \underbrace{\log c + \alpha \cdot \log x}_{\text{linear equation}}. \quad (2.10)$$

Scale invariance is closely related to the concept of self-similarity, a typical property of fractals. In self-similar objects no length scales exist which can be used to identify the scale of the object.

For the derivation of power laws in physical systems their thermodynamical potentials are an appropriate starting point. The Gibbs free Energy G of a

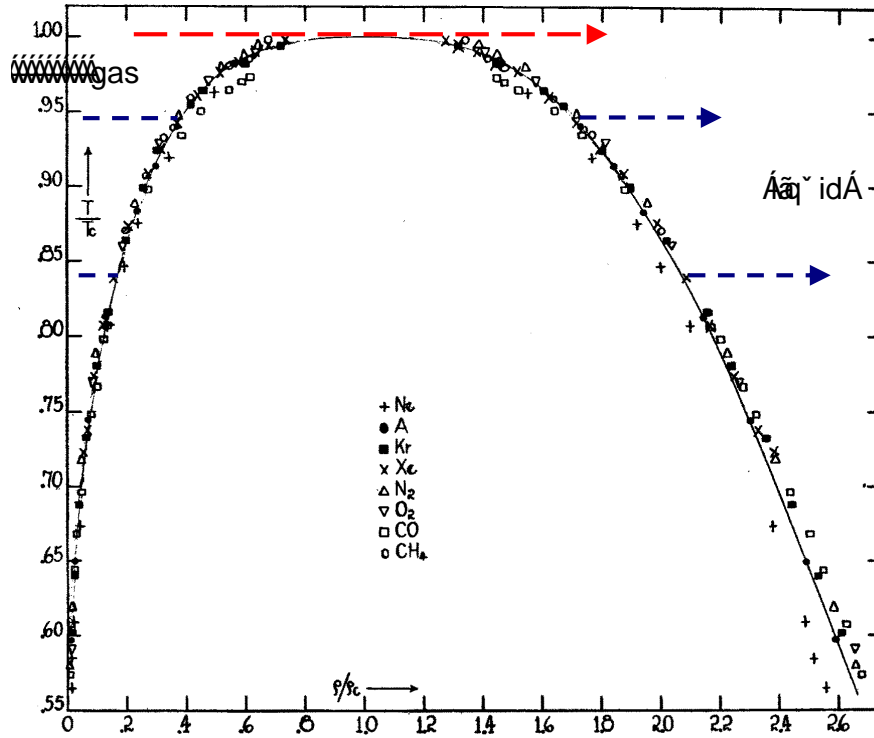


Figure 2.6: Temperature-density phase diagram of several fluids including a discontinuous (blue isotherms with short bars) and a continuous phase transition (red isotherm with long bars) at and below the critical point. After normalizing the data of all substances to their critical values all curves collapse on an universal curve. The fitted line represents a power law $(\rho - \rho_c) \propto (T - T_c)^\beta$ with $T \leq T_c$ and a critical exponent $\beta = 1/3$ (adapted from [53]).

magnetic system can be expressed by

$$G = U - MH - TS \tag{2.11}$$

where U is the internal energy, M the magnetization, H the magnetic field, T the temperature and S the entropy [87]. The total derivative of the Gibbs free energy G is

$$dG = dU - HdM - MdH - SdT - TdS. \tag{2.12}$$

With the internal energy

$$dU = TdS + HdM \tag{2.13}$$

one gets

$$dG = -MdH - SdT. \tag{2.14}$$

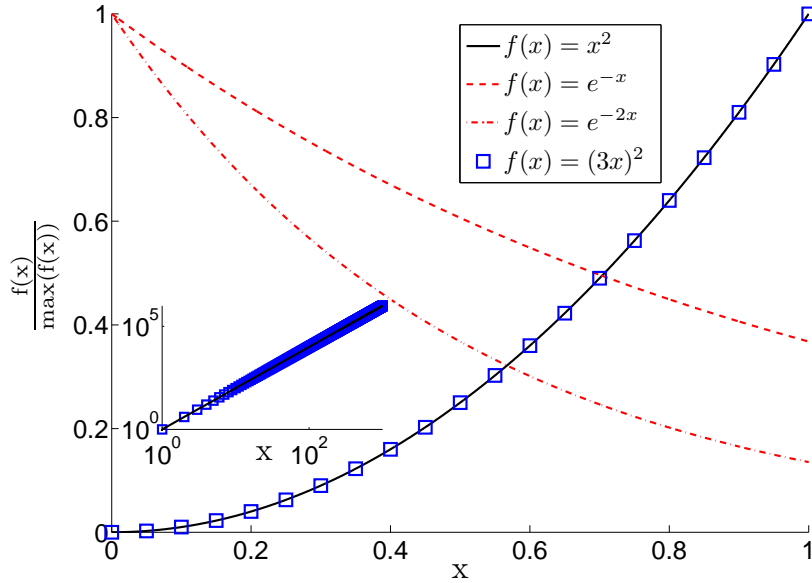


Figure 2.7: A power law $f(x) = x^\alpha$ is form-invariant under a linear rescaling of x . Graphically, this can be understood by comparing the two scaled functions $f(x) = x^\alpha$ and $f(n \cdot x) = (n \cdot x)^\alpha$ normalized by their maxima $\max(f(x))$ and $\max(f(n \cdot x))$, respectively. By contrast, exponential functions cannot be normalized in a way that they scale after a rescaling of x .

In the vicinity of the Curie temperature (ferromagnetic \rightarrow paramagnetic phase transition) the quantities magnetization M and susceptibility χ show among others power law behavior. By a partial derivative of the Gibbs energy with respect to the field H one gets the magnetization M

$$-\frac{\partial G}{\partial H} = M \propto (T_c - T)^\beta \Big|_{B=0, T \leq T_c}. \quad (2.15)$$

The susceptibility can be derived by

$$\frac{\partial M}{\partial H} = \chi \propto |(T - T_c)|^{-\gamma} \Big|_{H=0}. \quad (2.16)$$

The occurring exponents β and γ are called critical exponents as they can only be observed in the vicinity of the critical temperature T_c where continuous transitions take place. To discuss critical exponents it is useful to define the reduced temperature as

$$t = \frac{T - T_c}{T_c}. \quad (2.17)$$

The critical exponent λ is defined as

$$\lambda = \lim_{t \rightarrow 0} \frac{\ln|f(t)|}{\ln|t|} \quad (2.18)$$

where $f(t)$ is a general thermodynamical function which can be described in terms of the reduced temperature

$$f(t) = a|t|^\lambda (1 + bt^\nu + \dots). \quad (2.19)$$

For small t (in the vicinity of the critical point) the equation simplifies to

$$f(t) = a|t|^\lambda. \quad (2.20)$$

Critical exponents are very powerful in describing physical systems because they condense approximately 10^{23} degrees of freedom and describe the behavior of physical response functions (e.g. specific heat and susceptibility) or the distribution of characteristic features (e.g. correlation length) by only one numerical value.

2.3 Universality and self-organized criticality

The critical exponent is an observable, which can experimentally be derived. The comparison of critical exponents of different response functions reveals a surprising result. Even for systems that are in many aspects quite different, the numerical values of the critical exponents can be identical. This observation led to the *universality hypothesis* which was published in 1970 by R. B. Griffiths [52]. In his approach many critical exponents are universal, i. e. many thermodynamical systems can be described by the same exponent. Instead of showing a dependence on microscopic details, the only three relevant factors are:

1. the dimension d of the system,
2. the particle interaction range L ,
3. the spin dimension n .

In this approach the interaction range can be described by

$$L(d, x) = r^{-(d+2+x)}, \quad (2.21)$$

where x is a parameter which distinguishes between short-, middle-, and long-range interactions. A positive x leads to a short-range interaction. In this case of diverging correlation lengths ξ , details of the interaction are irrelevant and critical behavior is realized. The occurring exponents are universal. For a $x < d/2 - 2 < 0$, the interaction is classified to be long-range and the Landau theory can be applied (see section 2.1). The case of $d/2 - 2 < x < 0$ is more complicated because the exponents can depend on x . Here universality is not guaranteed [116].

The spin dimension n numbers the relevant components of the spin vector S_i . In case of the Ising model of magnetization the Hamiltonian has the following form

$$\mathcal{H} = - \sum_{i,j} J_{i,j} S_i S_j, \quad (2.22)$$

where $J_{i,j}$ is the strength of the interaction between the spins S_i and S_j . The interaction is called ferromagnetic for a positive interaction ($J_{i,j} > 0$) and antiferromagnetic for a negative interaction ($J_{i,j} < 0$). In the case of ($J_{i,j} = 0$) the spins do not interact. Depending on the used model, the spin dimension can have different values. In the Ising model the spin has only one component ($n = 1$). The XY model has a two-dimensional spin vector ($n = 2$) and the Heisenberg model has a three-dimensional spin vector ($n = 3$). It is worth mentioning that the measured critical exponents of real systems can deviate from calculated exponents and that, depending on the model, the calculated exponents can vary for the same analyzed system. The universality hypothesis has been proven several times by experimentalists and theorists (e. g. [19, 32, 58, 164, 189]) and, after the introduction of the renormalization group theory in the 1970's by K. Wilson, it is commonly accepted [202–204] (see section 2.1).

To reach critical behavior all parameters of a system must be located in the vicinity of the critical point. Because of a high dimensional parameter space and several decades of possible values, meeting the critical point is quite a rare situation. Nevertheless, it can be accomplished in two ways: either the system is tuned actively to the critical point (such as in the experiment of the critical opalescence) or the system tunes itself to the critical point. The latter case is described by the concept of self-organized criticality (SOC), which was for the first time coherently introduced by Bak, Wang, and Wiesenfeld in 1987 [9, 10]. In the SOC concept a system tunes itself into a non-equilibrium state which is inherently critical. The critical state is an attractor for the dynamics of the system. Besides some boundary conditions (see below), the system does not need any external fine tuning, which supports the idea of self organization. The aspect of criticality refers to the dynamics of self-organized systems, which show a close connection to critical phenomena, such as avalanche dynamics (see section 3.2.1), fractal behavior, and power laws (see section 2.2).

The systems exhibiting SOC behavior only need to meet a few requirements: slowly driven dynamics and large dimensions, with a high number of degrees of freedom, which are highly coupled and cannot be reduced or decoupled. Due to the strong coupling, perturbations can propagate through the system, which is another parallel to critical phenomena where fluctuations can spread throughout the whole system. The system dynamics has no smooth character while responding to the continuous driving force in a series of discrete avalanches spanning over a broad range of scales, which again is as well characteristic for

critical phenomena (see section 3.2.1). In both cases the distributions of the individual events can be described by power laws, which imply the existence of self-similarity. Power laws are found in different observables such as the energy or the duration of the events, the waiting time between the events, or the space involved in the avalanche events.

A visualization of the concept of SOC is given by the sandpile model, which has been introduced by Bak, Wang, and Wiesenfeld [9]. In the described gedankenexperiment single sand grains are dropped at different positions on a horizontal area. After dropping a certain amount of sand grains a sandpile builds up. The grains accumulate as long as the local slope is lower than the critical slope and the system has not reached its stability limit yet. By adding additional grains critical areas of the system become supercritical (i. e. unstable) and avalanches are released. After the propagation of an avalanche the system locally falls below the critical limit and the process starts again. This simple procedure creates a system that tunes itself constantly towards criticality.

Mathematically this system is realized via cellular automata, consisting of a grid of n cells. Each cell has a finite number of states m . The time evolves by discrete (dimensionless) steps $\delta t:=1$. The state of one cell is coupled to a finite number of other cells at the time $t - 1$ (in many cases it is a nearest-neighbor-interaction). Bak *et al.* have performed numerical simulations with one, two, and three-dimensional grids. A two-dimensional grid is exemplarily presented in the following. Every cell (i, j) has a value $z(i, j)$, which can be e. g. the number of sand grains in this cell. In every time step a grain is added to a specific randomly chosen cell (i, j) . Until a critical number of grains z_c is reached the variable z increases one by one $z(i, j) \rightarrow z(i, j)+1$. At the moment the lattice site becomes overcritical four grains are passed to other cells, one to each nearest neighbor

$$\begin{aligned} z(i, j) &\rightarrow z(i, j) - 4 \\ z(i \pm 1, j) &\rightarrow z(i \pm 1, j) + 1 \\ z(i, j \pm 1) &\rightarrow z(i, j \pm 1) + 1. \end{aligned} \tag{2.23}$$

If at least one of the nearest neighbors itself is at the stability limit z_c the process continues. If the total number of activated cells per time step is greater than or equal to one, a chain-reaction starts. This simple model is a prototypical example of the occurrence of avalanche dynamics. In the majority of cases the dropped grains lead to a linear increase of the cell variable z . The response of the system changes dramatically when at one grid the critical value is reached and the cascaded hopping from one cell to the other results in avalanche propagation through the system. It is worth mentioning that the size of each avalanche, which is defined as the number of coherently involved cells, is variable and that small avalanches are more probable to develop than large ones. The occurring

avalanche cluster-size distributions follow a power law whose critical exponent solely depends on the dimension of the grid.

The question whether such a concept can be applied to the physics of real systems leads to the question in what way the numerical system responds to a change of its boundary conditions and to perturbations. Two different boundary conditions have been tested: first, that grains can leave the system (open boundaries) and second, that grains cannot leave the system (closed boundaries). Furthermore, disorder has been introduced into the system by excluding randomly chosen cells from the dynamics (for further remarks on the role of disorder see section 2.23). In all three cases the dynamics seems to be robust and the exponent remains identical.

The estimation of the exponents r that characterize the cluster-size distributions $D(s) \propto s^{-r}$ revealed the following results: in case of two dimensions $r_{2D}=1.0$ and in case of three dimensions $r_{3D}=1.37$ [10]. The power laws span over three decades ($10^0 - 10^3$), which coincides with the number of cells used in the simulation ($50 \times 50 = 2500$ in two and $20 \times 20 \times 20 = 8000$ in three dimensions). Inspired by the predictions of the simulation of Bak *et al.* several groups conducted real experiments with sand grains [62] and different types of rice [45]. In general, the experiments have shown ambiguous results. However, in the case of the rice experiment a power law over 1.5 decades in energy has been found [45].

3 Martensitic transitions in shape memory alloys

The following chapter introduces the martensitic transition, discusses several associated phenomena and effects, and presents the material classes analyzed in this work. Section 3.1 starts with the classification of (martensitic) phase transitions regarding symmetry aspects, growth characteristics, and energetic considerations. The subsequent section 3.2 characterizes the martensitic transition first addressing its most fundamental features and afterwards addressing its dynamics, pretransitional phenomena, and the interplay of magnetic and structural degrees of freedom. Section 3.3 introduces effects associated with the martensitic transition such as the shape memory effect, superelasticity, and (giant) magnetic-field-induced strain. Section 3.4 sheds light on the origin of acoustic emission (AE) during the martensitic transition and proceeds with the propagation of ultrasonics in solids. In section 3.5 this chapter closes with an overview of the material classes analyzed in this work.

3.1 Classification of phase transitions

The samples analyzed in this work belong to the group of (multi-) ferroics. Aizu defines a ferroic crystal by the existence of two or more orientation states in the absence of an external field which can be shifted from one state to another by the application of one or more fields [3]. The four different types of ferroic order are: 1. ferromagnetism with a spontaneous magnetization; 2. ferroelectricity with a spontaneous polarization; 3. ferroelasticity with a spontaneous strain and 4. ferrotoroidicity with an ordered arrangement of magnetic vortices [185].¹ The common prefix *ferro* is borrowed from the word ferromagnetism, whose domain structure was proposed for the first time by Weiss in 1907 [200]. Ferroics can be distinguished by their symmetry characteristics under space and time inversion ($(x, y, z) \rightarrow (-x, -y, -z)$, respectively $t \rightarrow -t$), as visualized in figure 3.1. It is worth mentioning that each ferroic order belongs to one of the four parity groups (e. g. ferroelasticity is invariant under space and time inversion). Materials combining

¹Ferrotoroidicity is added subsequently to the group of multiferroic phases and was first observed by Van Aken *et al.* in 2007 [185]. It is under current debate if it should be added to the group of multiferroics (e. g. [185]).

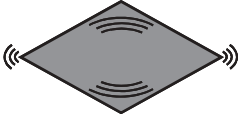
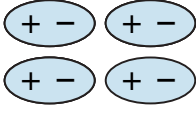
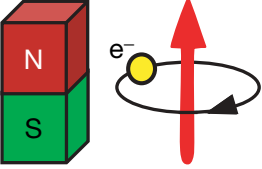
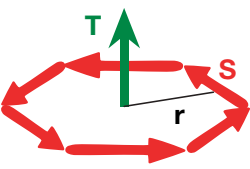
Time \ Space	Invariant	Change
Invariant	<p>Ferroelastic</p> 	<p>Ferroelectric</p> 
Change	<p>Ferromagnetic</p> 	<p>Ferrotoroidic</p> 

Figure 3.1: All forms of ferroic order and their characterization under parity operations of space and time (adapted from [185]).

two ferroic properties are called multiferroics. Because of the coexistence of two order parameters multiferroics are both time- and space-asymmetric. As a consequence, one order parameter violates time or space symmetry.

A large amount of different phase transitions can be observed in solid-state physics. They can be classified in several ways according to different criteria, which usually depend on the emphasis of the analysis. In this work the focus lies on ferroelastic transitions, and in the case of Ni_2MnGa , on a combination of ferroelastic and ferromagnetic transitions. As both transitions fit into the framework of ferroics (see figure 3.1), a classification regarding their point group symmetry is useful (see figure 3.2). The analysis of the transformation kinetics via rate-dependent experiments is a main component of this work. The classification given in figure 3.3 points at kinetics aspects of the transition by distinguishing between thermally activated and athermal nucleation and grows. The evaluation of associated energies and driving forces is particularly helpful in the analysis of phase transitions (see figure 3.4). These classifications lead to the differentiation between martensitic transitions of strong and weakly discontinuous character. For particular alloys this classification is still under debate (e. g. [65–67, 112, 138, 143]). The introduced classifications can partly overlap but do not compete, because they describe the same subject from different perspectives.

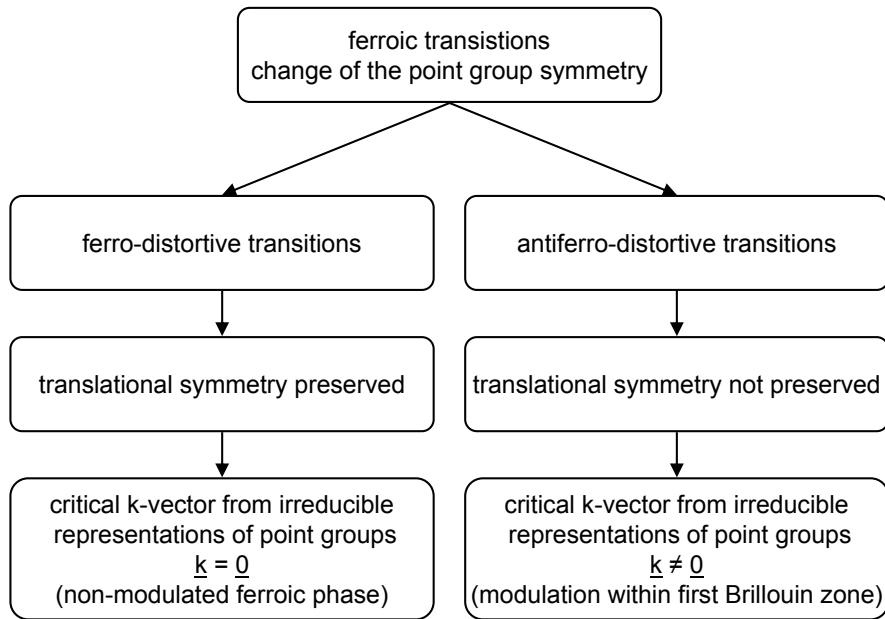


Figure 3.2: Classification of solid-solid phase transitions by their symmetry characteristics [80, 178] (and adapted from [75]).

All ferroic transitions occur in association with a change of the point group symmetry. They can be classified in ferro-distortive and antiferro-distortive transitions (see figure 3.2). In the case of ferro-distortive transitions the translational symmetry of the high symmetry phase (commonly the high temperature phase) is preserved, whereas this is not the case for antiferro-distortive transitions. The modulation of the broken symmetry can be described by a critical vector \vec{k} from the irreducible representations of point groups. A non-modulated phase with a homogenous deformation of the unit cell can be described by $\vec{k} = \vec{0}$. By contrast, the modulated phase is described by $\vec{k} \neq \vec{0}$ with a modulation length of $\lambda = 2\pi/|\vec{k}|$. Normally, this leads to a considerable increase of the unit cell length $L_{\text{modulated}}$ because of $\lambda \gg L_{\text{non-modulated}}$. The martensitic transition can either occur with (e. g. Ni-Al) or without modulation (e. g. Au-Cd, Fe-Pd).

The classification of phase transitions with respect to their dynamics in terms of nucleation and growth starts with the differentiation between homogeneous and heterogeneous nucleation, as described in section 2.2. Martensitic transitions exhibit heterogeneous nucleations, which represent the initial point of the classification in figure 3.3. The phase transitions can either occur athermally or thermally activated (isothermal) (see as well [153, 176] and section 3.2.1). Usually, martensitic transitions in shape memory alloys are classified as athermal; however, recent experiments have shown (partly) isothermal dynamics in some

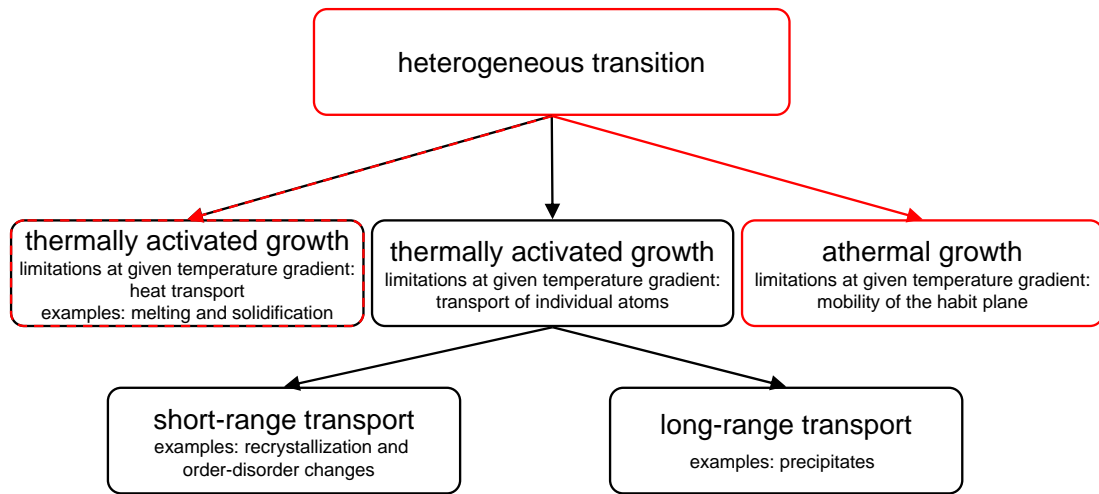


Figure 3.3: Classification of heterogeneous solid-solid phase transitions with regard to their predominant growth processes. The characteristics marked in red are typical for martensitic transitions (adapted from [27] and [75]). Some numerical values of characteristic properties of typical classical martensitic transitions and of shape memory alloys can be found in table 3.1.

cases (see section 3.5 for sample description and section 7.2 for results of this work). In the classical athermal case the growth process is limited by the mobility of the habit plane (see section 3.4.1), which separates the parent and the product phase and, under ideal circumstances, can be as fast as the speed of sound. In case of thermally activated growth the heat transport is the limiting factor. The martensitic transition occurs diffusionless as it is manifested by the definition of the martensitic transition and as indicated in the figure. The diffusionless character enables the orientation relationship between the parent and the product phase and is therefore vital for the shape memory effect.

Another reasonable classification scheme has been introduced by Cohen, Olson, and Clapp in 1979, which is based on the involved energies. It is depicted in a simplified form in figure 3.4 [30]. The amount of strain energy determines whether the diffusionless transition has a shuffle or a lattice-distortive character. The following division is based on the ratio between the dilatational and the deviatoric component. In case of the martensitic transitions of shape memory alloys the volume is quasi preserved [18] and deviatoric components are essential. (Quasi-) martensitic transitions² of shape memory alloys are characterized by a

²In the following, the martensitic transition of shape memory alloys will be discussed primarily. The classical and the (quasi-) martensitic transition will be referred to as martensitic transition, which is in line with the majority of solid state physics publications.

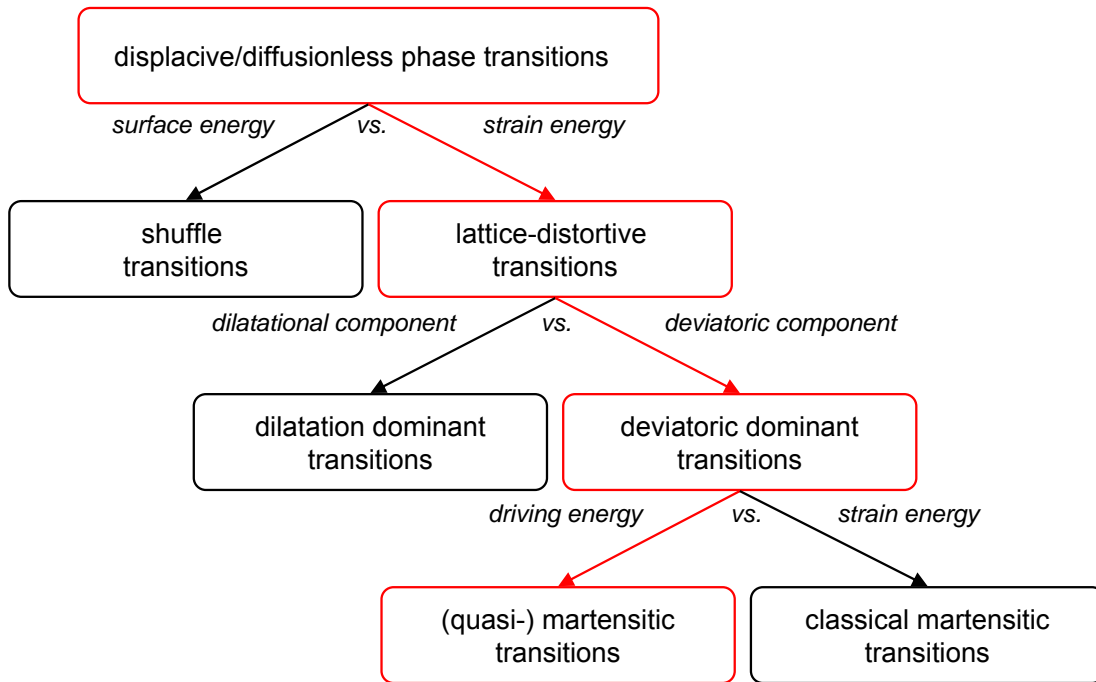


Figure 3.4: Classification of diffusionless phase transitions in solids by energetic considerations. The path marked in red is characteristic for shape memory alloys (adapted from [30] and [75]).

small amount of strain energy of the total driving force ΔG . This is in contrast to classical martensitic transitions of steel, which show large hystereses [30]. It is worth mentioning that the classifications of figure 3.4 and in parts of figure 3.3 as well do not represent a binary decision process. By contrast, real transitions are characterized at each step of the diagram by a mixture of the depicted extremes and the quotient of the involved energy terms can serve as a classification criterion.

3.2 Characterization of martensitic phase transitions

In the following section the martensitic transitions of classical ferrous alloys and in particular of shape memory alloys will be characterized. Some of the characteristics were already referred to in section 3.1 in association with the classification of phase transitions, others will be introduced here. Clapp gave a striking definition of the martensitic transition in a keynote lecture at ICOMAT 1995 [29]: *A martensitic transition involves a cooperative motion of a set of atoms*

3. Martensitic transitions in shape memory alloys

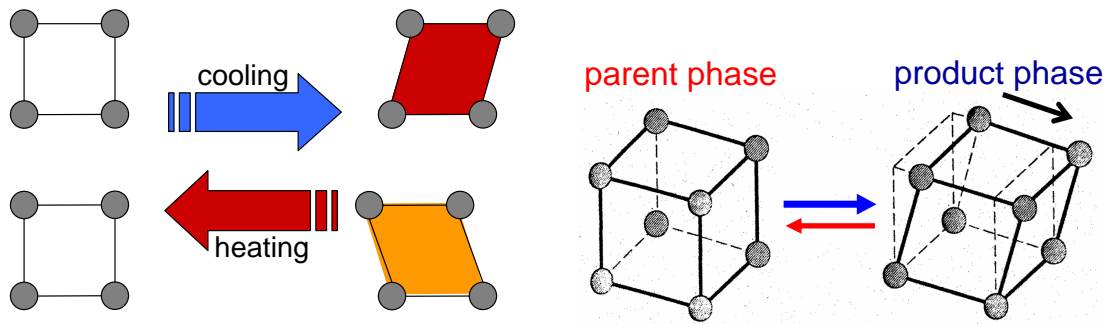


Figure 3.5: Formation of martensitic variants under cooling in two dimensions (left) and three dimensions (right). The transition leaves the orientation relationship and nearest neighbors unchanged. Nevertheless, the distortion results in a reduction of the symmetry of the unit cell. On the left hand side is shown the distortion of the square two-dimensional elementary cell into the two possible variants. Note that the two occurring variants cannot be converted into each other by a rotation. On the right hand side can be seen a three-dimensional cubic unit cell in the parent phase and one possible variant in the product phase. In higher dimensions more variants are available to be formed.

across an interface causing a change of shape and sound. The vivid definition contains several characteristics regarding all involved length scales (micro-, meso-, and macroscopic)³, including optical and acoustical experimental observations.

In contrast to critical phenomena the martensitic transition is a multi-scale phenomenon, which involves intrinsic discrete length scales [79]. The microscopic scales are associated with the cooperative shear- and shuffle-movement of a group of atoms. This so-called military movement leaves nearest neighbors unchanged and guarantees a lattice correspondence with an orientation relationship between the high symmetric high temperature phase and the low-symmetric low temperature phase (figure 3.5).

The high and the low temperature phases coexist during the forward transition in the temperature interval between M_s and M_f (for martensitic start respectively finish temperature) and during the reverse transition in the interval between A_s and A_f (for austenitic start respectively finish temperature) (see figure 3.6). In the case of weakly discontinuous transitions of shape memory alloys both

³The scales associated with the martensitic transition are used in the following manner: microscopic length scales cover the dimensions of single atoms and of atom configurations such as unit cells (range of nm). Macroscopic length scales include structures of (sub-) millimeters and larger, which are typically visible to the naked eye. The mesoscopic length scale lies in between the macro- and micro-scale with structures in the range of μm such as domains or grains.

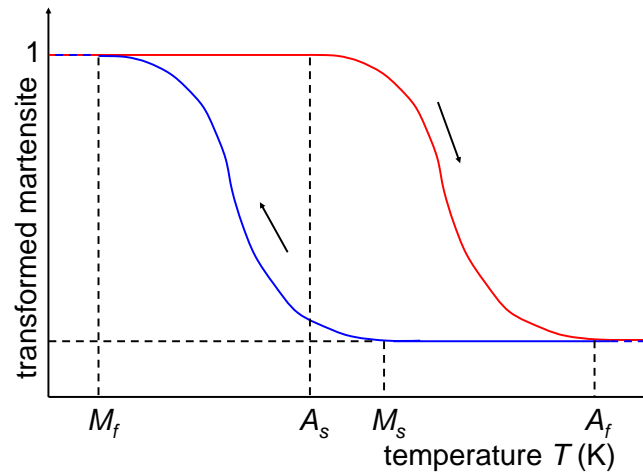


Figure 3.6: Hysteretic dependence of the amount of transformed martensite as a function of the temperature. The blue line represents the cooling and the red line the heating process. The hysteresis widths vary between 100 K in case of classical ferrous alloys and 10 K in case of shape memory alloys (see as well table 3.1).

temperature intervals can have a width of some Kelvin and they are not centered at the same temperature (see table 3.1). This hysteretic character can be explained by the fact that internal strains occur during the transition. In order to minimize the strain energy the involved mesoscopic variants display a self-accommodation into elastic domains (with some analogies to ferromagnetic and ferroelectric domains)[115]. The detailed self-accommodation strongly depends on the disorder which is related to the defect structure of the alloy. By manipulating the defect concentration of the crystal one can stabilize or even control the transition temperatures. This can be realized either by repeated thermal cycles through the forward and reverse transition or by plastic deformations or by thermal treatments such as annealing or quenching. The former leads to an optimization of the transition path in the complex energy landscape and is called *training*. The accommodation process equally involves all available variants [125] and proceeds in order to avoid mechanical work without changes of the sample volume [18]. Although the general shape of the sample remains unchanged, the surface of the martensitic phase shows a characteristic relief, which represents a manifestation of the variant accommodation in the volume. The surface relief is characterized by highly oriented wedges on mesoscopic or macroscopic scales [75]. Figure 3.7 shows a micrograph of the martensitic surface relief of a $\text{Ni}_{63}\text{Al}_{37}$ sample which has been analyzed in this work.

During the transition a habit plane separates the coexisting phases of high and lower symmetries. During the growth process appropriate amounts of

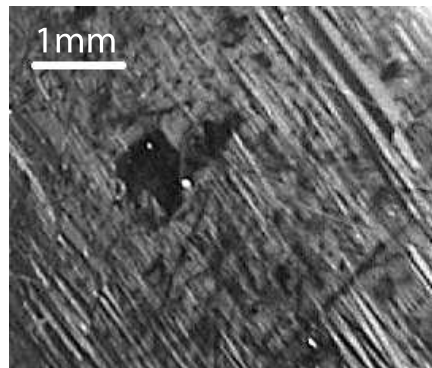


Figure 3.7: The minimization process of strain energies during the martensitic transformation leads to a spontaneous self-arrangement of strain domains resulting in a highly oriented surface relief.

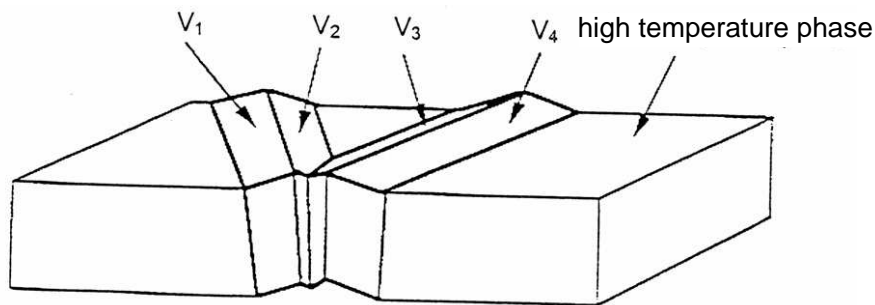


Figure 3.8: Schematic representation of self-accommodated variants during the martensitic transition separated by the habit plane from the high temperature phase. The variant pairs V_1 and V_2 , and V_3 and V_4 each share a twin boundary [54].

each variant are formed in order to satisfy the invariant plane condition, which presupposes that the habit plane remains unchanged during the transition [73]. The high mobility of the habit plane is responsible for several characteristics of weakly discontinuous martensites such as the shape memory effect (see section 3.3.1). The intermittent kinetics of the transformation can be understood as jumps from one marginally stable state to another metastable state because of a self-limitation by induced stresses and pinning processes at defects (see section 3.2.1). Figure 3.8 depicts the self-arranged variants of the product phase, the habit plane, and the flat parent phase. The high and the low temperature phases (after self-accommodation the of distorted variants) are mainly stress-free because each atom is located on its energetically favored lattice site. The atoms situated at the

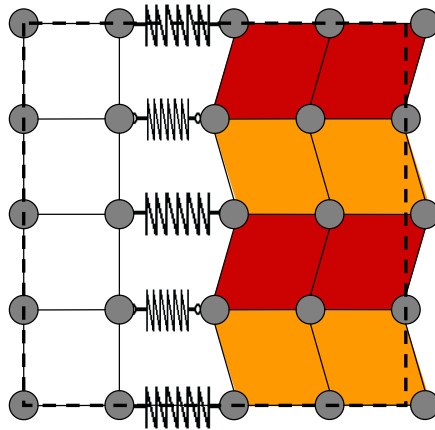


Figure 3.9: Microscopic delineation of a half-transformed crystal with the martensitic variant structure on the right (twin boundaries) and the parent phase on the left. The atoms situated along the interfacial boundary store elastic energy due to the crystal lattice misfit, which is indicated by small springs.

habit plane (during the transformation) show a different pattern: The interfacial atoms belong to both crystal structures and elastic energies occur (figure 3.9). As the habit plane moves on, changes arise in the local strain field and acoustic emission waves are released, carrying the dissipated energy [21].

Both observation methods - the optical and the acoustical - mentioned by Clapp can be used for sensitive non-destructive testing techniques, which are schematically depicted in figure 3.10. The acoustic emission spectroscopy is the principal experimental technique of this work, which will be described in detail in section 4.1 and chapter 6.

This section closes with another definition of the martensitic transition given by Christian, Olsen and Cohen, which is based on microscopic arguments and includes the discontinuous character of the transition (see figure 3.11). They characterize a martensitic transition as *a shear-dominant, lattice-distortive, diffusionless transformation occurring by nucleation and growth* [28].

3.2.1 Transition dynamics, hysteresis, and disorder

Martensitic transitions can be characterized with regard to their nucleation and growth dynamics. The majority of martensitic transitions is classified as athermal, although isothermal transition kinetics can be observed, too, such as in Fe-Mn-Ga alloys [49, 148]. Additionally, some measurements characterize alloys that have been formerly classified as athermal, to have partly isothermal characteristics. This seeming contradiction is well-known and Kurdjumov already stated in

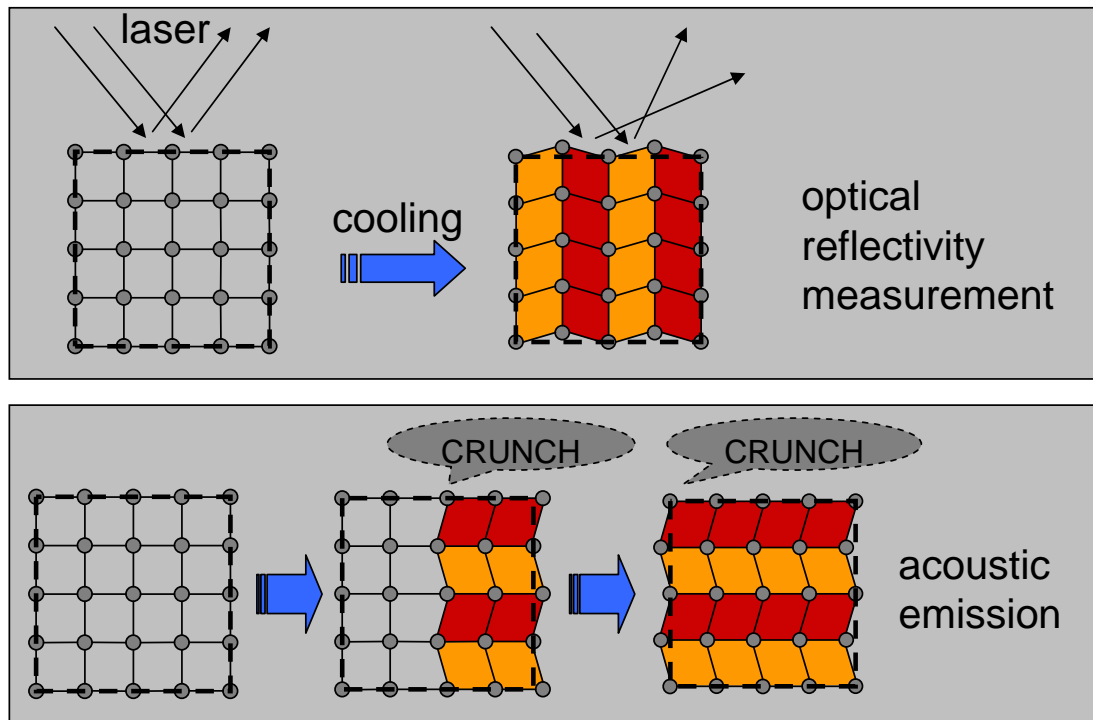


Figure 3.10: The martensitic transition implies a change of shape and sound (see definition of Clapp [29]), which allows for both optical and acoustical experimental methods. Several experimental methods (x-ray techniques, neutron scattering, AE-techniques and optical reflection methods) are possible, from which two suitable techniques are schematically depicted. The optical method (top) works with the reflection of a laser beam which is scattered in a characteristic pattern by the martensitic surface relief (e. g. [77, 90, 111]). The acoustic emission (AE) technique (bottom) used in this work is a volume-sensitive method measuring the acoustic emission generated during the martensitic transition (for details see section 4.1 and 6).

the late 1940's a close relation between both kinds of dynamics, the isothermal transition however representing the general case [153]. In more recent times, the interest in this topic has been renewed and particularly Kakeshita *et al.* worked on this issue. The group around Kakeshita stated the possibility of switching between both transition kinetics by applying external pressure or magnetic fields [65, 66, 68, 69]. In addition, they proposed a model explaining both the athermal and the isothermal nature of the transition [67]. In the following there will be first given a short overview of the classical understanding. Second, some approaches of the last approximately 15 years will be presented explaining the new results.

3.2. Characterization of martensitic phase transitions

Table 3.1: Characteristics of strongly and weakly discontinuous martensitic phase transitions. The given quantities are typical examples of each group [38, 75, 141, 198].

	strongly discontinuous transition	weakly discontinuous transition
prime example	classical ferrous alloys	shape memory alloys
hysteresis	large: $\mathcal{O}(100 \text{ K})$	small: $\mathcal{O}(10 \text{ K})$
lattice dilatation	large: $\mathcal{O}(0.1)$	small: $\mathcal{O}(0.01)$
transition entropy	large: $\mathcal{O}(1 \text{ J/K}\cdot\text{mol})$	small: $\mathcal{O}(0.1 \text{ J/K}\cdot\text{mol})$
ΔG for nucleation	large: $\mathcal{O}(1000 \text{ J/mol})$	small: $\mathcal{O}(10 \text{ J/mol})$
growth process	self-accommodation unclear	self-accommodation in variants
transition front	no transition with a single front known	transition occurs with one habit plane
phase boundary	low mobility and irreversible character	high mobility, almost fully reversible
kinetics	athermal or isothermal, autocatalytic transition	athermal, thermoelastic equilibrium

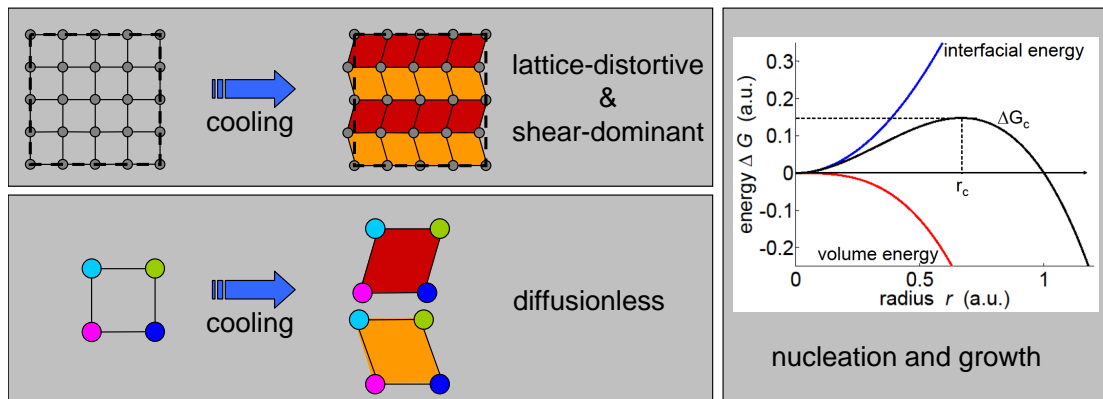


Figure 3.11: Depiction of the concise definition of a martensitic transition given by Christian, Olsen, and Cohen [28], which serves as a summary of the main characteristics of martensitic transitions described in this section.

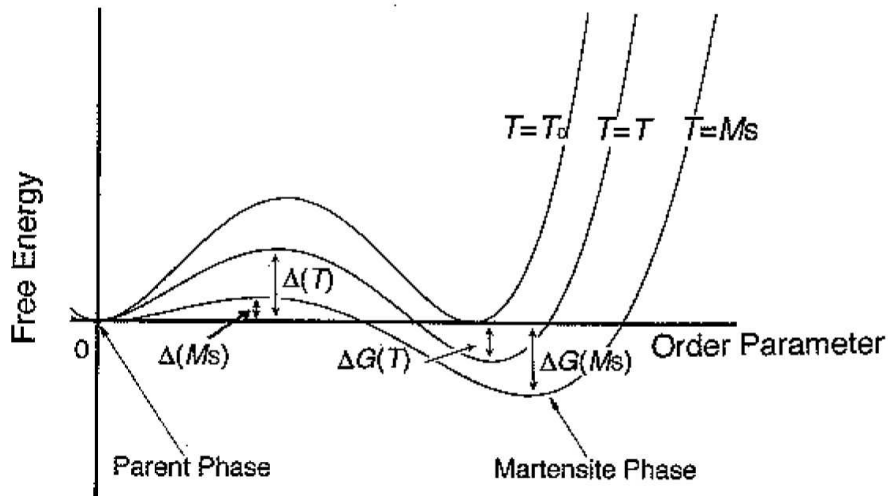


Figure 3.12: Depiction of nucleation thermodynamics for both isothermal and athermal transitions [68]. The nucleation barrier and driving force ΔG are displayed at the thermodynamical equilibrium temperature T_0 , at the martensitic transition temperature M_s , and at a temperature T in between [68].

Concerning their general nucleation processes, both transitions do not show fundamental differences. Both have to reach an supercritical nucleus where the gained volume energy exceeds the required surface energy (see section 2.2). An illustration of the nucleation thermodynamics is depicted in figure 3.12. The differences between both transitions arise from the mechanism that determines how the nucleation barrier can be overcome and the growth process starts. Whereas isothermal transitions are thermally activated and can occur with an explicit time-dependence at different temperatures, athermal transitions need to be triggered by the change of an external parameter at a fixed temperature and thereupon evolve with speed of sound.

The explicit time-dependence in the isothermal case results from the interplay of two opposing temperature effects. On the one hand, higher temperatures lead to an enhanced thermal activation, which promotes the transition due to increased local diffusion⁴, for example. On the other hand, lower temperatures give rise to a higher driving force due to a larger energy difference ΔG between the parent and the product phase. The superposition of both effects forms a maximum at a certain temperature and the transition shows a characteristic C-shape in a time-temperature-transformation diagram (TTT-diagram). The maximum of the

⁴Local diffusion enables the system to anticipate the structure of the new phase before transforming by testing different nuclei structures. Local diffusion plays an essential role in effects such as rubber-like behavior or martensite stabilization (see e. g. section 8.2)

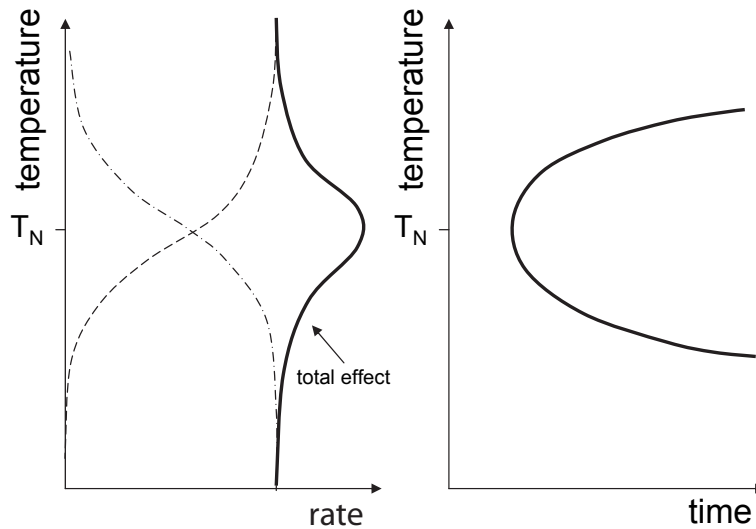


Figure 3.13: Thermodynamics of isothermal transitions. On the left is shown a schematic depiction of two opposing effects leading to a maximum of the transition rate. High temperatures enable thermal activation but reduce the driving force of the transition. Low temperatures lead to a high driving force, but result in a low thermal activation. On the right hand side is depicted a TTT-diagram of a generic isothermal transition with the characteristic nose-temperature T_N where the waiting time shows a minimum until a certain amount has transformed.

superposition and the nose-temperature T_N of the C-shaped curve correspond with each other (see figure 3.13). Isothermal martensitic transitions can be characterized by time constants τ of several hours.

The athermal transition occurs with speed of sound at a fixed temperature and the growth proceeds with speed of sound. The corresponding time constant τ can be estimated by $\tau = \text{sample diameter} / \text{speed of sound}$. Because of high energy barriers thermal fluctuations do not play a relevant role. The system remains in its metastable state until the barriers disappear due to an external change of the driving force [190]. Both growth dynamics are compared with each other in figure 3.14.

The classical interpretation, which is characterized by a rigid distinction between both dynamics, is contrasted by recent experimental results which show that it is not useful to draw a strict line between athermal and isothermal behavior. The experimental results concerning athermal and isothermal transitions can be explained by

3. Martensitic transitions in shape memory alloys

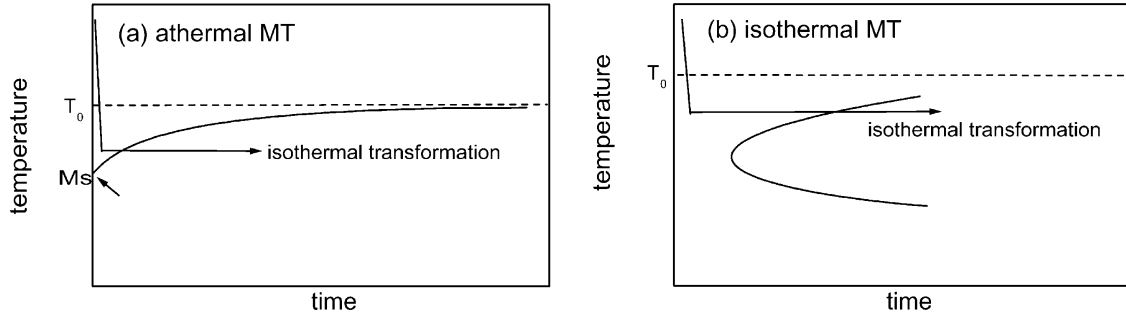


Figure 3.14: TTT-diagrams of an athermal (a) and an isothermal transition (b) in the Kakeshita model. The arrows indicate the holding temperatures [128].

$$\frac{d\eta(T(t), t)}{dt} = \frac{\partial\eta(T(t), t)}{\partial T} \underbrace{\frac{\partial T(t)}{\partial t}}_{\text{rate}} + \frac{\partial\eta(T(t), t)}{\partial t}, \quad (3.1)$$

where η is an order parameter (or an observable coupled to the order parameter) characterizing the transformed amount of the new phase, T is the temperature, and t is the time. The observable used in this work are the acoustic emission in case of acoustic measurements and the enthalpy in calorimetric measurements. Equation 3.1 reveals two experimental ways of deriving the transition kinetics. One is the execution of incubation time measurements. An incubation time is the waiting time prior to the spontaneous martensitic transition under isothermal conditions (and at fixed external parameters) at a temperature above the classical martensitic start temperature M_s and below the thermodynamic equilibrium temperature T_0 . If no transition can be detected after a long waiting time $\frac{d(T(t), t)}{dt} = 0$ at constant (external) parameters ($T = \text{const.}$) an explicit time-dependence can be excluded $\frac{\partial(T(t), t)}{\partial t} = 0$. An experimental obstacle in incubation time measurements is the sensitivity to small temperature variations; thus a very precise temperature control is crucial for incubation time experiments [90]. A second way is the analysis of transitions at different rates $r_i = \Delta T/\Delta t$ and the comparison of the results. If $\frac{d\eta(T(t), t_1=T/r_1)}{dt} = \frac{d\eta(T(t), t_2=T/r_1)}{dt} = f(T)$ is true for all r 's the transition has no explicit time-dependence and the curves of all rates scale. If the curves do not scale, the dependence $\frac{d\eta(T(t), t=T/r)}{dt} = f(T, r)$ reflects an explicit time dependence of the transition.

After observing isothermal dynamics that does not fit into the classical framework some researchers proposed phenomenological models with different approaches. A graphical overview of the classical understanding and the models of Kakeshita *et al.* [67], Otsuka *et al.* [128], and Planes *et al.* [143] can be found in figure 3.15. In the classical theory, athermal transitions do not show any

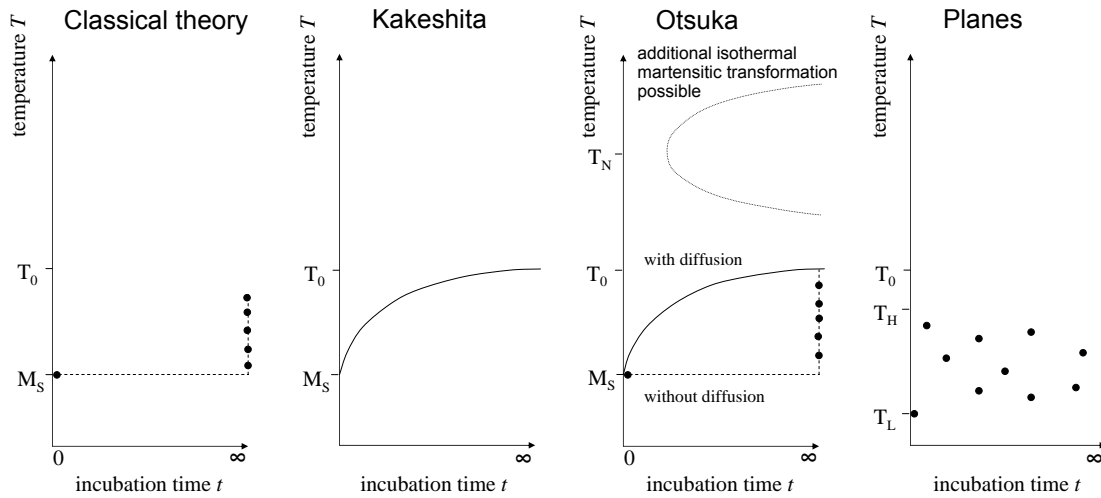


Figure 3.15: Comparison of the classical picture of athermal transition kinetics with the models proposed by Kakeshita *et al.* [67], Otsuka *et al.* [128], and Planes *et al.* [143]. The authors follow different approaches which are contradictory with respect to the role of diffusion, the statistical nature of M_s , and the coexistence of isothermal and athermal transitions [90, 112].

incubation time. The transition only occurs at M_s ; at higher temperatures the transition probability is zero and at M_s it is 100%. Kakeshita *et al.* proposed finite incubation times between T_0 and M_s , which decrease the closer the holding temperature gets to M_s . In the Otsuka model the occurrence of incubation time is coupled to the existence of diffusion. Additionally, an isothermal transition is possible at higher temperatures T with $T \gg T_0$. In the model of Planes *et al.*, the concept of a constant transition temperature M_s is substituted by a stochastically distributed M_s in the temperature interval (T_L, T_H) below T_0 , where an isothermal character is observable.

Measurements of athermal martensitic transitions with a high time resolution reveal interesting transition dynamics. Despite a continuous change of the driving force, the transition proceeds intermittently in jumps (see figure 3.16). An analysis of the kinetics shows that the jerky evolution is caused by the relaxation from one metastable state to another marginally stable state [191]. The dissipated energy associated with the transition is responsible for the hysteresis, and the pinning-depinning characteristic leads to the sharp, rectangle-type hysteresis. The released energy propagates through the crystal in form of acoustic waves, which can be analyzed (see section 3.4.1). The avalanches can be caused either by a simultaneous motion of different interfaces spatially distributed in the crystal or by the discontinuous motion of a single habit plane [192].

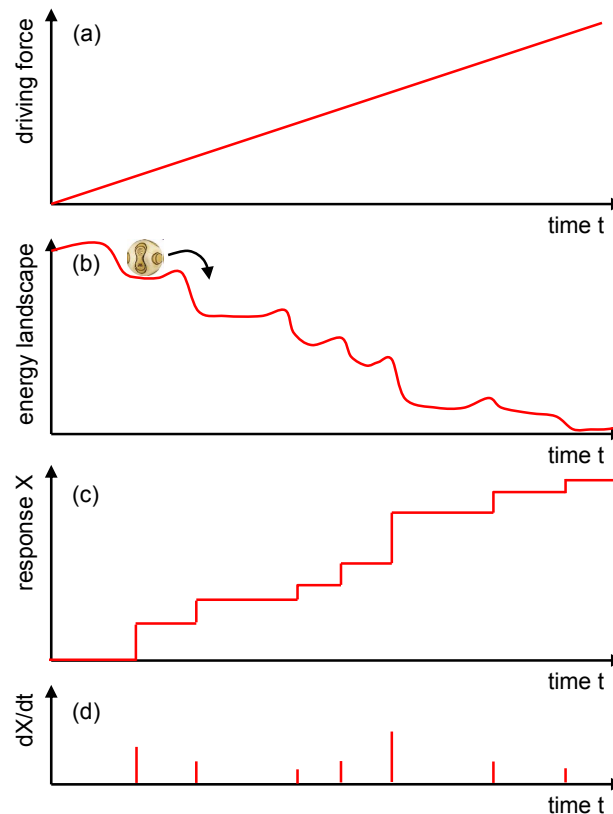


Figure 3.16: Schema of the development of avalanche dynamics in athermal martensites. A continuous driving force is applied to a system, for example by changing the temperature at a fixed rate (a). The way through the complex energy landscape consisting of several metastable states (here represented by the football *Teamgeist*) (b) leads in spite of the continuous excitation to a discontinuous response (c). The sudden changes of the response function (d) indicate the avalanche behavior of the transition dynamics.

The occurring avalanches reflect critical behavior and can be described by power laws (see the detailed discussion in section 2.2) [192]. According to Sethna *et al.* criticality has its origin in the intrinsic disorder of the system [163]. The above mentioned group proposed a random-field Ising model at 0 Kelvin with an applied field as the driving force for the description of fluctuationless first-order phase transitions. With a low degree of disorder, the system transforms in a single infinite avalanche, whereas with a high amount of disorder the transition proceeds in many (small) avalanches leading to a broad transition range. It is worth mentioning that pure power laws only occur at a critical amount of disorder. A deviation from power law behavior can be corrected by an exponential

correction factor:

$$p(A) = \frac{1}{Z(\alpha, \lambda_A)} A^{-\alpha} e^{-\lambda_A A}, \quad (3.2)$$

where A is the quantity that shows the power law behavior (e.g. energy or amplitude of an acoustic event), α is the corresponding exponent, and λ an exponential correction [190]. A negative value of λ indicates that the distribution is *supercritical* and leads (in case of a large A) to a positive deviation of the power law where large values of A are overrepresented. A supercritical distribution is associated with a small degree of disorder. A positive value of λ indicates a *subcritical* distribution with an exponential decay at the correction value $1/\lambda$. In the subcritical case, large values of A are underrepresented and a large degree of disorder is supposed. At $\lambda = 0$ the distribution is called critical and can be described by a pure power law (see figure 3.17)⁵. In short, the parameter λ measures the distance to criticality.

The disorder in martensitic alloys can either arise from static or dynamic origins. Static disorder is caused by quenched-in defects such as vacancies, impurities, interstitials, dislocations and chemical disorder in case of off-stoichiometry alloys. Dynamic disorder has its origin in the competing long-range interactions depending on the variant arrangement, which keep on changing during the transition process [192].

Some features of a martensitic transition indicate its non-equilibrium character [208]. Perhaps one of the experimentally most obvious phenomena is the occurrence of hystereses, which can widths of some Kelvin in the case of shape memory alloys or some hundred Kelvin in the case of classical ferrous alloys (see table 3.1). An interesting explanation approach for hystereses in martensites is the occurrence of two competing time scales. On the one hand, there is the characteristic time scale of the driving rate and on the other hand the scale of the relaxation time of the system towards thermodynamical equilibrium [190]. A mis-match of the time scales does not only arise at high driving rates but as well in systems that are characterized by a logarithmically slow response, such as disorder systems [190].

3.2.2 Precursor effects and premartensitic transitions

Shape memory alloys show a wide range of martensitic precursor effects. This is surprising to a certain extent, because precursor effects are especially known as an inherent characteristic of continuous transitions where the absence of interfacial energies enables the facile growth of the new phase consuming the old phase. By contrast, strongly discontinuous phase transitions cannot show precursor effects,

⁵The study of zero temperature properties of hystereses was realized with a site-diluted Ising model [190].

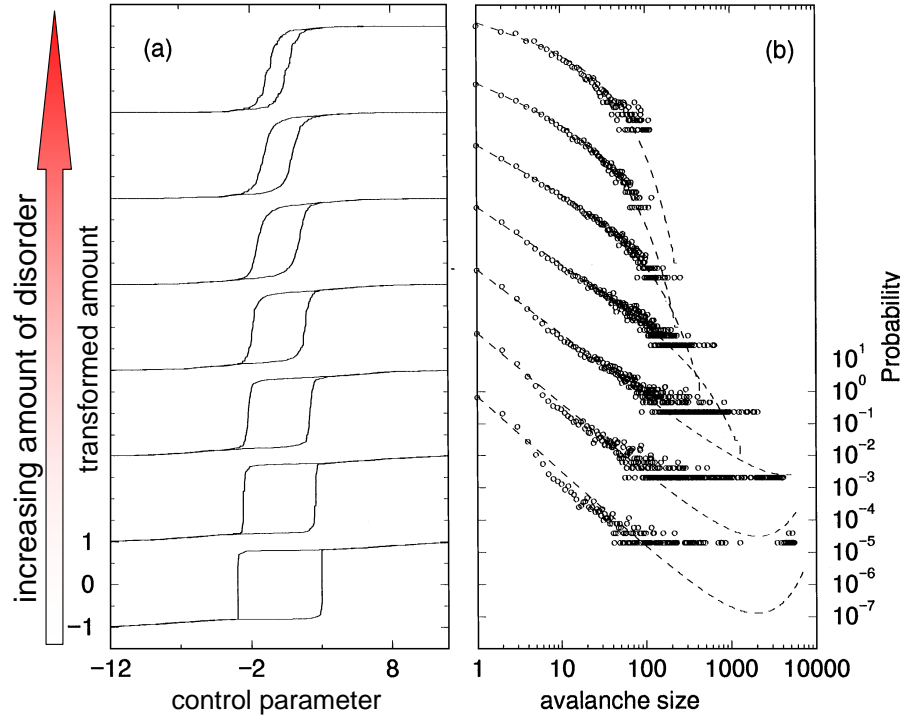


Figure 3.17: Simulation of a fluctuationless first-order phase transition of Cu-Al-Mn as a function of disorder. Hysteresis cycles at different degrees of disorder on the left. Little disorder leads to a few (large) avalanches and a sharp hysteresis (bottom), whereas large disorder results in many (tiny) avalanches with a smooth hysteresis (top). The corresponding avalanche distributions on the right are shown as a function of disorder, too. The dotted curves are fits of equations 3.2. The first four histograms show subcritical behavior ($\lambda > 0$). The fifth histogram almost displays critical behavior without exponential correction ($\lambda \approx 0$) and the last two histograms show supercritical behavior ($\lambda < 0$) (adapted from [190]).

because a large amount of energy is needed to form a supercritical nucleus (see section 2.2).

Phonon softening is a very prominent precursor effect describing the dramatic frequency decrease of distinguished phonon modes. The entire frequency decrease towards zero is a complete phonon softening and leads to a static modulation of the crystal structure. Such a frozen phonon prior to the upcoming transitions can be observed in SrTiO_3 , Nb_3Sn , and K_2SeO_4 . The (incomplete) freezing can be described by

$$E^2 = (\hbar\omega)^2 \propto T - T_c, \quad (3.3)$$

where T_c is the transition temperature and ω the phonon frequency. The observed power law behavior of the energy is correctly described by the Landau theory (see section 2.1). Figure 3.18 shows an example of a dispersion curve with a pronounced but incomplete softening (a), the corresponding central peak (b), and the power law decay of the squared energy (c) (TA_2 mode of $\text{Ni}_{62.5}\text{Al}_{37.5}$ at $[\zeta\zeta 0]$ $\zeta = 0.16$). The occurrence of a central peak in inelastic neutron scattering is a phenomenon closely related to phonon softening. The central peak is a new diffraction pattern, which arises as a consequence of the strongly modulated parent phase (see e. g. [166]). The appearance of a central peak as a function of the temperature in a Ni-Al alloy can be seen in figure 3.18 (b).

Soft mode analyses by means of inelastic neutron scattering experiments are widely used for they reveal interesting insights into the transition dynamics of structural phase transitions. A soft mode can be understood as a preparation process for the upcoming new phase. In many cases, the structure of the product phase is already anticipated or even realized by the soft mode, which reduces the energy barrier for the upcoming phase. The degree of softening can be associated with the degree of discontinuity of the transition: the more complete the soft mode, the lower the arising restoring forces and the resulting energy barrier for a fixed modulation. An almost complete softening leads to a weakly discontinuous character, whereas a by far incomplete softening would promote the discontinuous character of the upcoming transition due to the high restoring forces. The degree of softening can be identified by the dependence of the squared phonon energy and the temperature, as shown in equation 3.3 and in figure 3.18 (c). The closer the energy minimum approaches zero, the more complete the soft mode.

It is worth mentioning that almost all soft modes in shape memory alloys occur in the same phonon mode TA_2 , in the same direction $[\zeta\zeta 0]$, and at selected positions inside the Brillouin zone (e. g. at $\zeta = 0.16$ as in the case of Ni-Al). All these features can be explained by the fact that the structure of the high temperature phase of shape memory alloys are usually derivatives of the body-centered cubic crystal structure, that is if all atoms were the same, the crystals had an ordinary body-centered cubic structure. Due to the different atoms the real unit cell gets larger leading to a smaller unit cell in reciprocal space. The absolute position of the soft mode is invariant. But, its value, expressed in units of the lattice parameter, deviates from its position $\zeta = 0.16$ in pure body-centered cubic structures (e. g. $\zeta_{\text{Ni-Al}} = 0.16 \pi/a_{bcc} = \zeta_{\text{Ni}_2\text{MnGa}} = 2 \cdot 0.16 \pi/2a_{bcc}$). Already in 1947 Zener showed that lattices with a body-centered cubic structure have an inherent instability against shearing at $q \rightarrow 0$ [206], which corresponds to vanishing restoring forces.

Another research analyzing Ni_2MnGa by means of grazing incident diffraction reveals interesting results. At low penetration depths, the phonon softening of the surface phonon is more pronounced than the phonon softening in the

3. Martensitic transitions in shape memory alloys

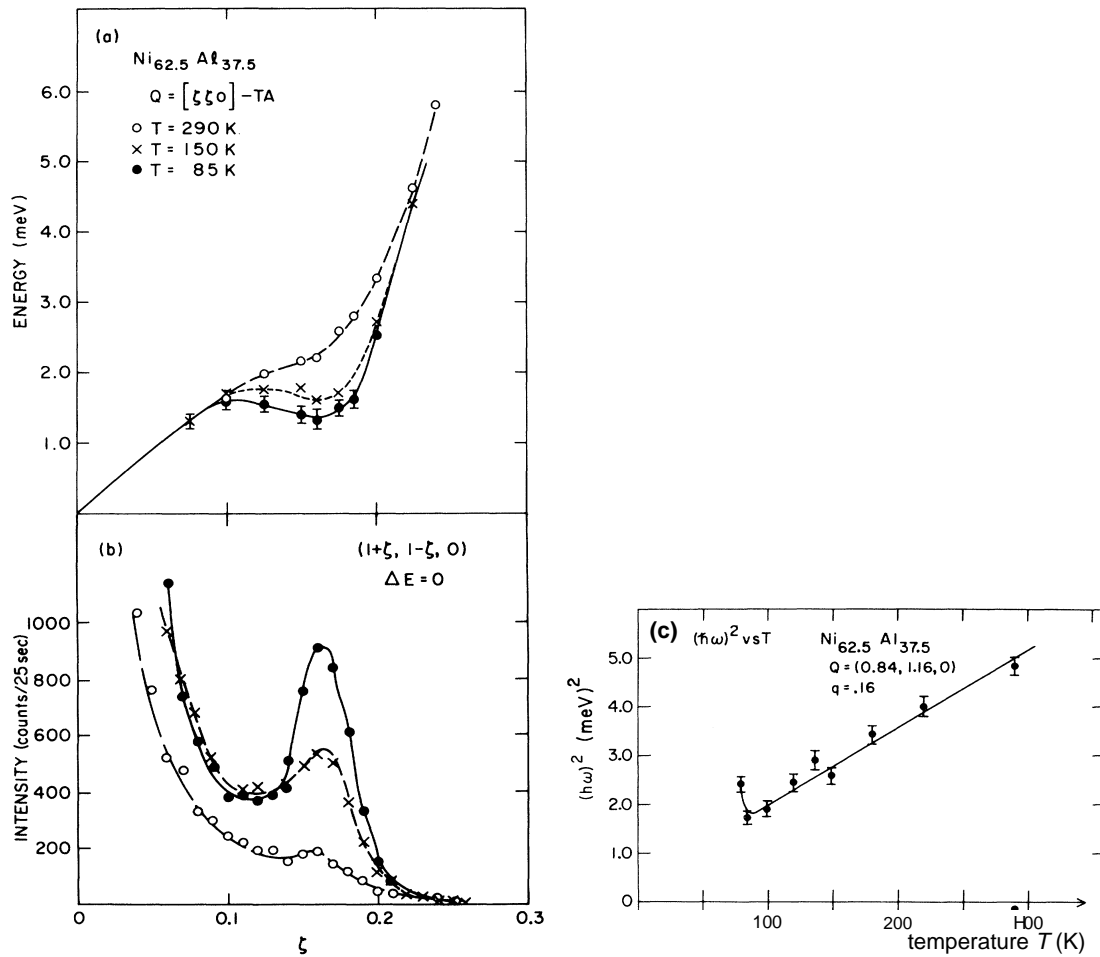


Figure 3.18: Incomplete phonon softening of the $[\zeta\zeta 0] TA_2$ mode in $\text{Ni}_{62.5}\text{Al}_{37.5}$, analyzed by neutron scattering. (a) Dispersion curves of the TA_2 mode at different temperatures with a minimum at $\zeta = 0.16$. (b) Temperature-dependence of elastic neutron scattering in the same direction leading to the central peak. (c) Temperature-dependence of the squared energy of the same mode at its minimum (adapted from [166]).

volume of the crystal [85]. Subsequently, the energy barrier is reduced for surface nucleation. Here, in contrast to what is widely believed, the transformation starts at the sample surface and grows afterwards into the volume. Normally, surface effects (e. g. a surface relief e. g. [6, 77]) are interpreted as a manifestation of a volume transformation.

In the case of the magnetic Heusler alloy Ni_2MnGa an almost complete phonon softening occurs [209], which is the consequence of magnetoelastic coupling [142], gives rise to a premartensitic transition with a micromodulated cubic $3M$ structure. This premartensitic transition is proposed to be a magnetically driven locking of the tweed structure, which is a pretransitional phenomenon (see below) [23]. The instability of the high temperature phase against the modulated $3M$ structure is assumed to be related to a Fermi surface nesting effect [92], which applies for all soft modes. The premartensitic transition has been evidenced by several measurement techniques such as neutron scattering [209], x-ray experiments [46], electron microscopy [24], ultrasonic measurements [96], and calorimetric measurements [142]. Calorimetric measurements revealed a small latent heat and verified the weakly discontinuous character of the transition. More recently, the premartensitic transition has been analyzed by first-principle calculations [181] and a Landau approach [142]. In analogy to figure 3.18, figure 3.19 shows the dispersion relation and the temperature-dependence of the squared energy of Ni_2MnGa . By comparing both figures it becomes apparent that the softening in the case of Ni_2MnGa is almost complete.

The coupling of the structural and magnetic degrees of freedom (see section 3.2.3) leads to a dependence of the premartensitic transition on the applied magnetic field. Several authors stated a field-dependent change of the transition temperature (see [16, 34, 92, 117, 197, 211]). Other authors report a decreasing energy of the $[\zeta\zeta 0] TA_1$ phonon branch, which corresponds to the elastic constant $(C_{11}-C_{12})/2$ around the Γ point as the magnetization increases [156]. Additionally, the influence of stresses applied along different directions (e. g. [95]) and the dependence on the stoichiometry (e. g. [95]) have been analyzed. In this work, the field-dependence of the premartensitic transition will be analyzed via AE measurements.

Tweed is a precursor effect of the sample showing a mesoscopic cross-hatched morphology. The diagonal striations with a scale of some tens of atomic spacings are characteristic for tweed patterns (see figure 3.20) [72]. The tweed pattern arises due to a modulation between the untransformed parent phase and a state similar to the martensitic deformed phase. In a two dimensional model of Kartha *et al.* its occurrence is related to an elastic anisotropy between the diagonal, vertical, and horizontal elasticity [71]. Tweed can be observed some ten or even a hundred Kelvin prior to the transition. Figure 3.20 compares two tweed patterns; one experimentally observed and the other one gained by simulations.

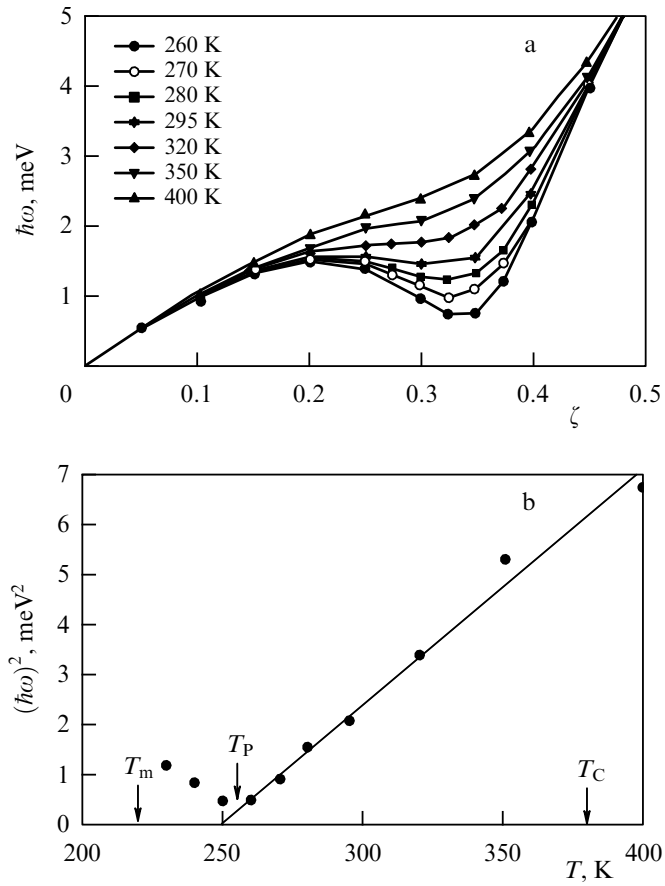


Figure 3.19: Incomplete phonon softening of the $[\zeta\zeta 0]$ TA_2 mode in Ni_2MnGa , analyzed by neutron scattering. (a) Dispersion curves at different temperatures with a minimum at $\zeta = 0.33$. (b) Temperature-dependence of the squared energy of the same mode at its minimum. T_p indicates the premartensitic transition, T_m the martensitic transition and T_c the Curie temperature [209].

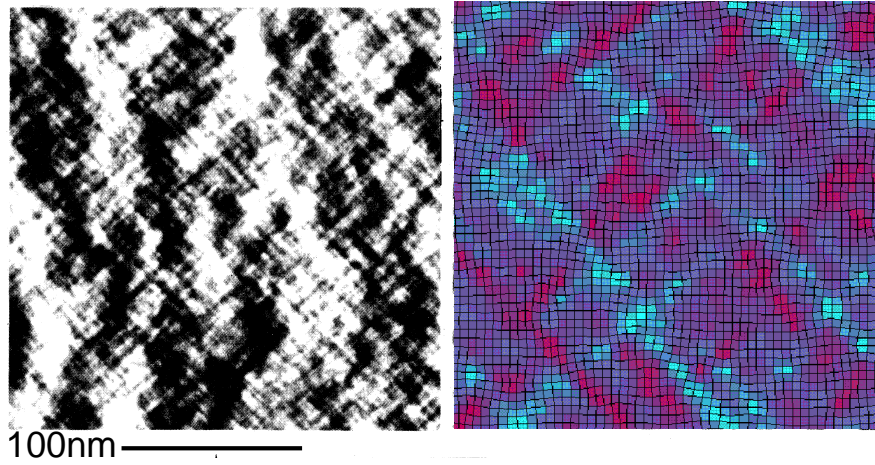


Figure 3.20: Pretransitional tweed pattern experimentally observed (left) and simulated (right). Micrograph of the mesoscopic tweed structure of a Ni-Al sample observed via transmission electron microscopy [72] (left). Visualization of calculations based on a two dimensional model for tweed pattern [71] (right) (for more details about the simulation process and for some visualizations of the simulation results see [162]).

3.2.3 Magnetic shape memory alloys

Magnetic shape memory alloys exhibit both a ferromagnetic and a martensitic phase transition. At temperatures below both the Curie temperature (T_C) and the martensitic start temperature M_s (normally $T_C \gg M_s$, see section 3.5.4), the structural and magnetic degrees of freedom are coupled to each other and give rise to effects such as the magnetic-field-induced strain (see section 3.3.3) and the magnetic-field-controlled shape memory effect, which is based on the field-dependent shift of M_s (see section 3.3.1) [118]. Several magnetic shape memory alloys exist, including Fe-Pd (see section 3.5.3), Fe-Mn-Si, Co-Mn, Fe-Co-Ni-Ti, and the Heusler alloy Ni_2MnGa (see section 3.5.4), the latter being perhaps the most prominent example [118].

The magnetic field-dependence of the equilibrium temperature T_0 of a discontinuous phase transition can be described by the Clausius-Clapeyron-law, which has been already used in equation 2.8:

$$\frac{dT_0}{dH} = -\frac{\Delta M}{\Delta S}. \quad (3.4)$$

T_0 (in the case of martensitic alloys) can be experimentally (roughly) estimated by $T_0 = 1/2(M_s + A_f)$ [179], $\Delta M = M^m - M^h$ is the magnetization difference between the martensitic phase (M^m) and the austenitic phase (M^a), and ΔS is the

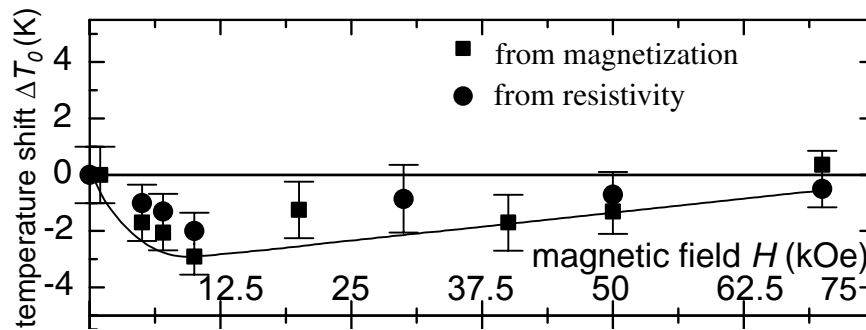


Figure 3.21: Magnetic-field-dependent shift of the martensitic equilibrium temperature T_0 for a Ni_2MnGa alloy. The solid curve represents the calculated result using the integrated Clausius-Clapeyron equation 3.4 (adapted from [74]).

entropy difference between both phases.⁶ Figure 3.21 compares experimental field-dependent temperature shifts⁷ of a Ni_2MnGa alloy and calculations using the Clausius-Clapeyron equation 3.4 [74].

In the following, a phenomenological model of the magneto-mechanical phenomenon of field-induced strain by twin-boundary and phase-boundary motion will be presented. The model was introduced by O’Handley in 1997. His publication [118] also includes quantitative considerations, which will not be part of this summary.

The model takes the elastic energy into account, as well as the magnetocrystalline anisotropy⁸ of a material comprising two twin variants. It includes twin-boundary motion, i. e. the switching respectively rotation of variants by their magnetic moments, the rotation of magnetic moments inside of fixed variants, and phase-boundary motion.⁹

In the model, the twin-boundary motion and the phase-boundary motion are driven by the energy difference between both sides of the corresponding interface. The energies involved are the Zeeman energy ($M_s H$) of a (not aligned) magnetic moment in an applied field and the magnetic anisotropy energy (K_u), which

⁶The Clausius-Clapeyron equation 3.4 applies as well for the transition temperature of the premartensitic transition.

⁷The magnetic field was applied in the [001] crystallographic direction [74].

⁸Magnetocrystalline anisotropy is the energy cost per atom to align its magnetic moment with the direction of the applied field. The effect of a high magnetocrystalline anisotropy is that the magnetic moment is fixed in a variant. With a strong anisotropy the energetic cost of rotating a magnetic moment inside a variant is higher than rotating the whole variant. The expressions *magnetocrystalline anisotropy*, *magnetic anisotropy*, and *anisotropy* will be used synonymously in this section.

⁹In case of tetragonal variant shapes, as realized in Ni_2MnGa , all variants can be reached by rotation.

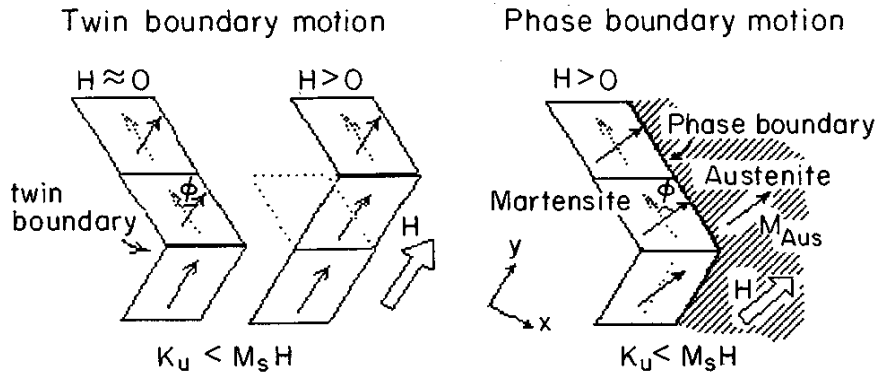


Figure 3.22: Mechanism of the magnetic-field-induced twin boundary motion (left) and phase boundary motion (right) in case of the weak anisotropy limit with a relatively large Zeeman energy [118].

is an indicator of the required amount of energy in order to rotate a magnetic moment inside a variant. The model suggests three regimes expressed by the dimensionless parameter $h_a = M_s H / K_u$:

1. $h_a \gg 1$: weak anisotropy,
2. $h_a \ll 1$: strong anisotropy,
3. $h_a \approx 1$: intermediate anisotropy.

The case of a weak anisotropy and a comparable large driving force (case 1) is depicted in figure 3.22. The conditions relevant for twin boundary motion are shown on the left and the conditions relevant for a phase boundary motion are shown on the right side of the figure. In the weak anisotropy regime a magnetic field rotates the magnetic moments inside those variants whose magnetic easy axis is not aligned with the external magnetic field. After the field application the Zeeman energy levels of both variants become equal in size because of a parallel magnetization. As there is no driving pressure on the twin-boundary arising from the Zeeman term, the only driving force emanates from the difference in the anisotropy energy. The anisotropy energy can be calculated by $P = K_u \sin^2 \sigma$ with σ being the angle between the field and the magnetization. Due to the fact that the anisotropy is weak by definition in this regime, the magnetic saturation can be easily achieved. In this (ideal) case, no strains arise because of the absence of structural changes.

The austenitic parent phase is considered to have a weak magnetocrystalline anisotropy (see section 3.5.4) and an applied field leads to the rotation of the magnetization. In this situation, both phases are characterized by a weak anisotropy.

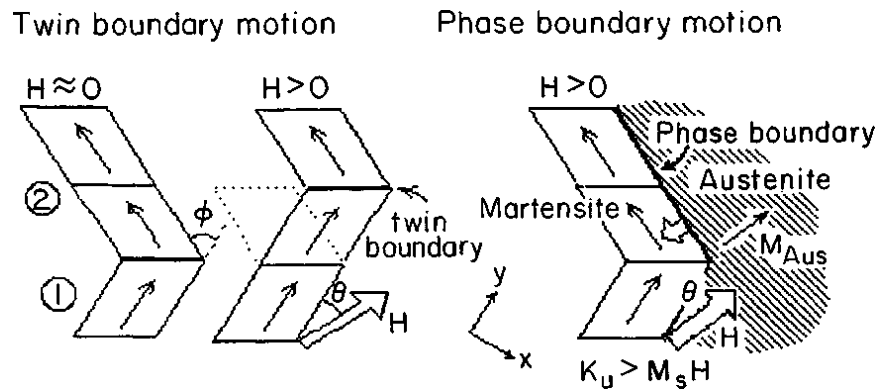


Figure 3.23: Mechanism of the magnetic-field-induced twin boundary motion (left) and phase boundary motion (right) in case of the strong anisotropy limit with a relatively low Zeeman energy [118].

Because of the absent Zeeman energy, the only energy difference between the martensitic and austenitic phase arises in association with the (slightly) varying magnetocrystalline anisotropy. As a consequence a magnetic-field-induced twin- or phase-boundary motion is very unlikely. Within the weak anisotropy limit the quantitative model (see [118]) correctly describes the nonlinearity in the achieved magnetization and strain as a function of the applied magnetic field.

Figure 3.23 depicts the case of a strong magnetocrystalline anisotropy (case 2) with the conditions of the twin boundary motion on the left and the phase boundary motion on the right. Here, the anisotropy is that strong that the energy cost, associated with the rotation of the magnetization within a variant, is higher than the energy needed for the rotation of the whole variant. Thus, the effect of an applied field (due to the difference in Zeeman energy $-(M_1 - M_2) \cdot H$) results in rotating the variants which are not aligned with the field. This process of twin boundary motion leaves the magnetization easy axis within the variant unchanged. As a consequence the anisotropy energy remains the same. The calculation of the optimal field orientation for achieving maximal strains in the strong anisotropic limit reveals a surprising result: Counterintuitively, the magnetic force on a twin boundary is not maximized by applying the field along the direction of the easy axis of one variant. In fact, the magnetic force due to Zeeman energy differences is maximized by an applied field parallel to the twin boundary (see figure 3.24).

Considering the phase boundary motion it is worth noting that, in the presence of an arbitrarily oriented magnetic field, the magnetization is on average better aligned with the field for the austenite phase, as compared to the martensitic phase. The reason is that the martensite phase always has to satisfy the two variants [118]. Therefore, an energy minimization becomes possible by consuming martensitic

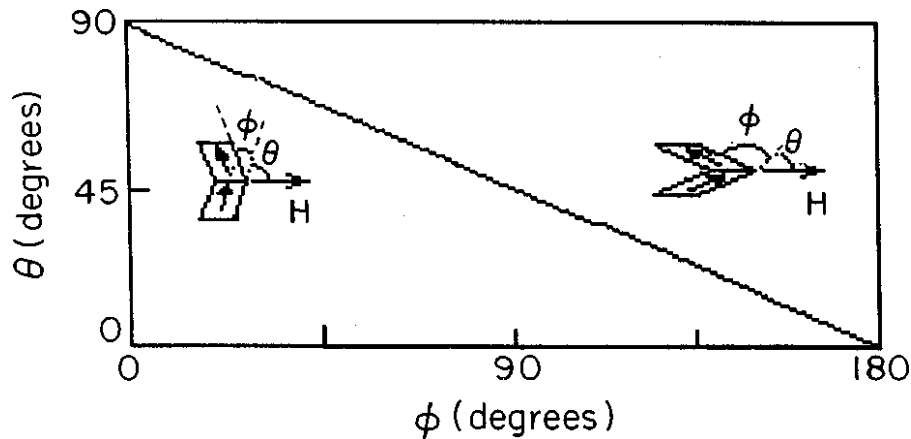


Figure 3.24: Depiction of the optimal field orientation for achieving large strains regarding the twin boundary Θ as a function of the angle ϕ , describing the orientation relation between both twin variants [118].

variants that are not favored by the field, i. e. by moving the phase boundary into the martensitic phase. Martensitic variants consumed by the austenitic phase can no longer take part in the field-induced strain, even if the field is increased afterwards. In order to achieve large strains in the strong anisotropy limit, it is important to finish the forward transition and to eliminate all residual austenite.

If the Zeeman term is comparable to the anisotropy term (case 3), the occurring phenomena are mixtures of the two situations described above. A change of the magnetization is possible as a result of both the magnetization rotation inside unfavorably oriented twins and twin boundary motion. When a field is applied and the magnetization has not yet been rotated, the Zeeman energy exerts a pressure on the twin boundary. Increasing the field leads to a rotation of the magnetic moments inside the variants (because of a relatively low anisotropy by definition) and the variants are less likely to switch. Under some experimental conditions regarding the strength of the magnetic field, the field direction, the orientation of the variants, and the anisotropy strength, it is even possible that a further increase of the field leads to flip-back of some variants to their zero field positions. The quantitative model reveals that the magnetization and the strain only show a linear response to small fields. Under higher fields, saturation is reached more slowly.

Limitations of the model arise from the fact that only two variants are involved. In addition, the role of the Curie and the martensitic start temperature is not considered. Furthermore, microstructural aspects relevant for the martensitic transition, such as defects that pin twin boundaries, have not been taken into

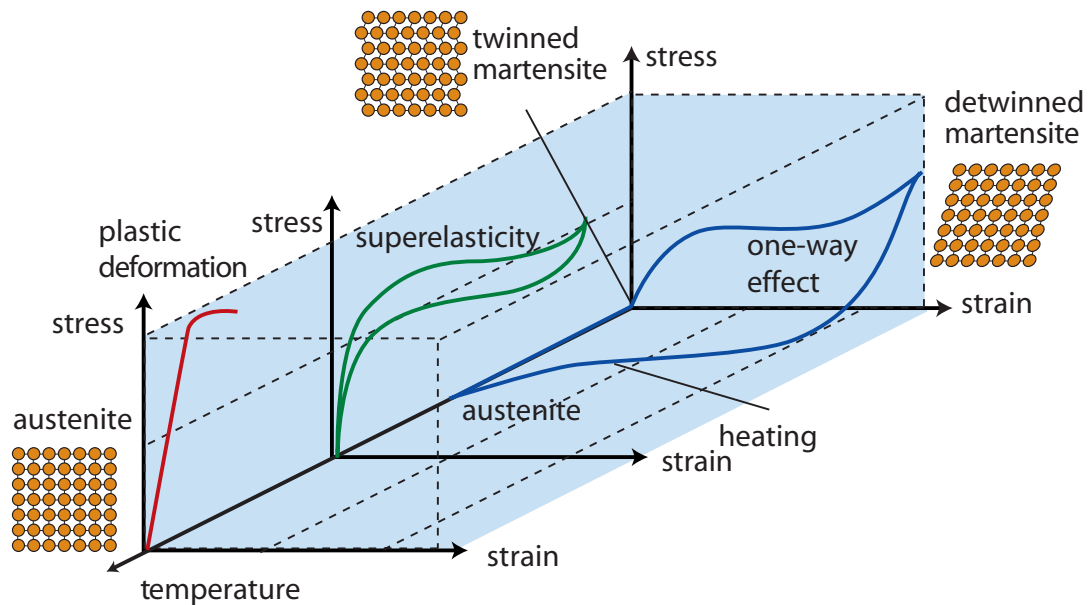


Figure 3.25: Summary of the stress-strain behavior of a generic shape memory alloy at different temperatures. The first coordinate system in the front shows the usual stress-strain behavior of solids with the linear elastic strain and a plastic deformation at high stresses. The second coordinate system shows superelasticity at a constant temperature. In the back of the coordinate system the shape memory effect is shown (adapted from [11]).

account. Nevertheless, the model correctly describes the main characteristics of twin and phase boundary motion under an applied magnetic field.

3.3 Effects in (magnetic) shape memory alloys

The martensitic transition of shape memory alloys leads to three remarkable phenomena that are interesting both from a scientific point of view as well as for applications. The temperature-induced martensitic transition gives rise to the shape memory effect, whereas the stress-induced martensitic transition results in the phenomenon of superelasticity. Both effects are summarized in a stress-strain-temperature diagram in figure 3.25. The effect of a (giant) magnetic-field-induced strain leads to the field-induced reorientation of martensitic variants, which results in a macroscopic shape change of the sample.



Figure 3.26: Two applications of the shape memory effect: A stent used in medical engineering (left) and an adaptive winglet as part of an aircraft (right).

3.3.1 Shape memory effect

The shape memory effect enables a sample exhibiting a martensitic transition to recover its shape after being deformed in the low temperature phase by applying heat and thereby inducing the martensitic reverse transition. During the transition process, the alloys can exhibit large forces, which make them interesting for technical applications such as general-purpose actuators (a wire of $300\ \mu\text{m}$ diameter generates a load force of $20\ \text{N}$ [63]), adaptive winglets, or stents (see figure 3.26). The most important ingredients of the shape memory effect are the diffusionless formation of different variants, which are characterized by a lower symmetry, the cooperative movement of a set of atoms, and the high mobility of the interfaces between the involved variants.

The mechanism behind the shape memory effect is illustrated in the figures 3.27 and 3.28. The former depicts the microscopic mechanism and the latter shows the macroscopic shape change of a paper clip together with the associated domain structure. In both figures, the description of the shape memory effects starts with the high temperature phase, where the materials have characteristics typical for their material class (mostly metals). In this phase the material receives its high temperature shape, which will be recovered by the shape memory effect. During cooling, the martensitic transition changes the crystal structure from a high (cubic) symmetry of the parent phase to a low-symmetry of the martensitic phase. The occurrence of the cooperative atom movement, where nearest neighbors remain the same, leads to a lattice relationship (more details can be found in section 3.2). During the transition, the shape and the volume of the sample remain (almost) unchanged. On a micro- and mesoscopic scale however the situation is different (see footnote 3): The deformed microstructure of the martensitic

3. Martensitic transitions in shape memory alloys

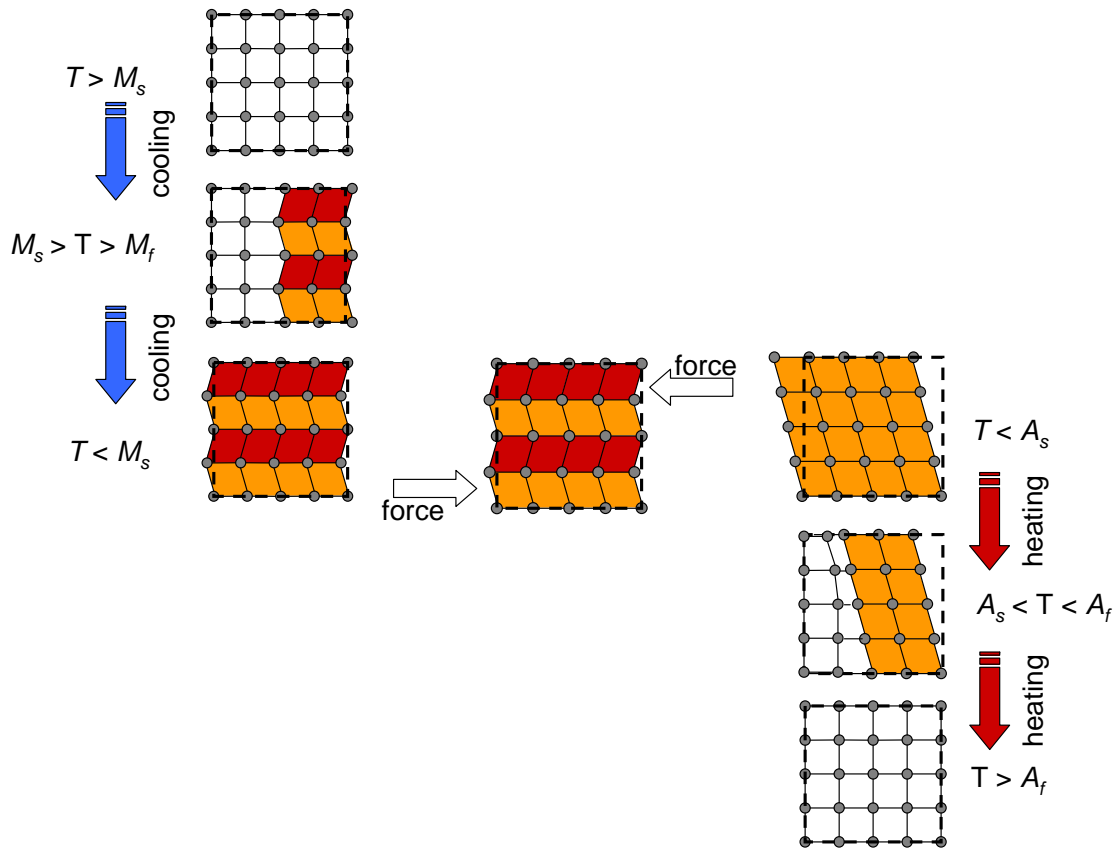


Figure 3.27: Schematic representation of the microscopic mechanism responsible for the shape memory effect. One cycle consists of three steps: 1) cooling into the martensitic phase, 2) deformation by an external force, and 3) heating into the high temperature phase.

phase consists of self-accommodated variants due to the shear-dominant character of the forward transition. The process of self-accommodation minimizes the elastic energy at the domain boundaries. All involved variants are energetically equivalent and can easily be switched from one to another by external forces. The stress-induced variant rearrangement leads to a macroscopical change of the sample shape, the lattice correspondence however remains the same. The maximum of the non-plastic deformation is reached when only one variant type remains, giving rise to a single-variant state. The reverse transition during heating reverses the forward transition and all variants jump back to their cubic parent structure of the high temperature phase. On a macroscopic scale, the sample returns to its original (high temperature) shape without any applied external forces.

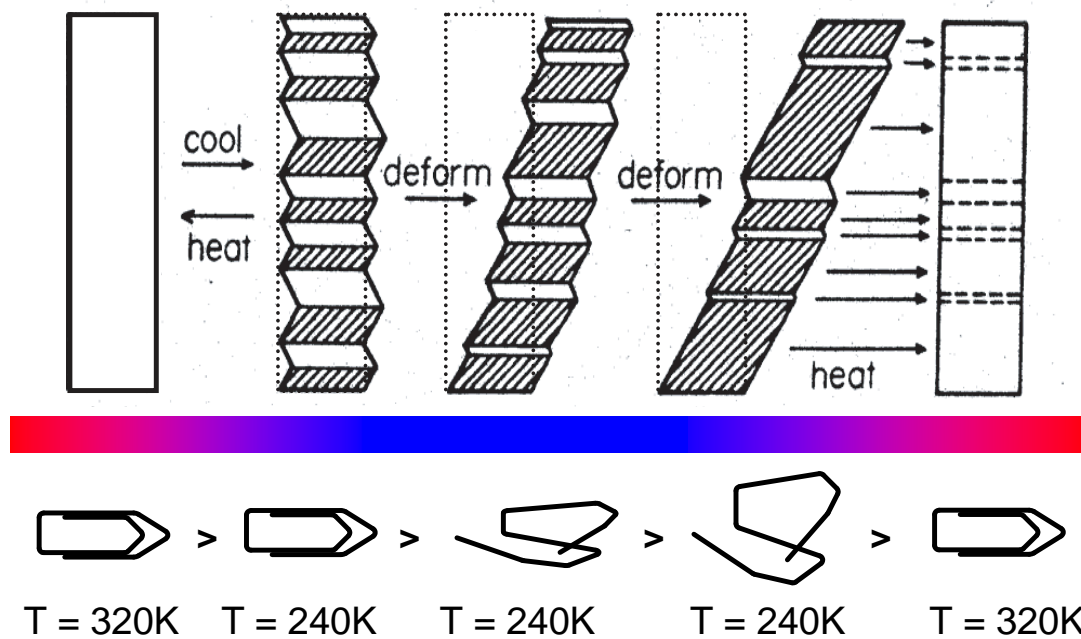


Figure 3.28: Illustration of the shape memory effect. The temperatures of the paper clip example at the bottom have been chosen according to the transition temperatures of the $\text{Ni}_{63}\text{Al}_{37}$ sample analyzed in this work ($M_s = 298 \text{ K}$, $A_s = 264 \text{ K}$; see table 7.1 in section 3.5.1) (adapted from [129] and [56]).

In perfect crystals, this cycling could be repeated infinite times. However, this does not apply to real crystals, where, due to a change of the defect structure of the crystal, the cycling process leads to fatigue effects. Fatigue starts with the accumulation of defects and leads to the formation of cracks; later crack propagation gives rise to rupture. The number of transition cycles before rupture is a function of the tensile stress applied to the sample respectively the resulting strain. In case of a $\text{Ni}_{0.508}\text{Ti}_{0.492}$ alloy the number of cycles ranges between 10^3 in case of high stress (several hundred MPa) and 10^6 in case of low stress (a few hundred MPa) [60].

3.3.2 Superelasticity

Superelasticity is based on the stressed-induced martensitic transition and describes the elastic response to an externally induced stress. Alloys exhibiting superelasticity belong to the larger family of shape memory alloys. It is evident that superelasticity can only occur in the austenitic high temperature phase [76]. The most important ingredients of superelasticity are the volume change

3. Martensitic transitions in shape memory alloys

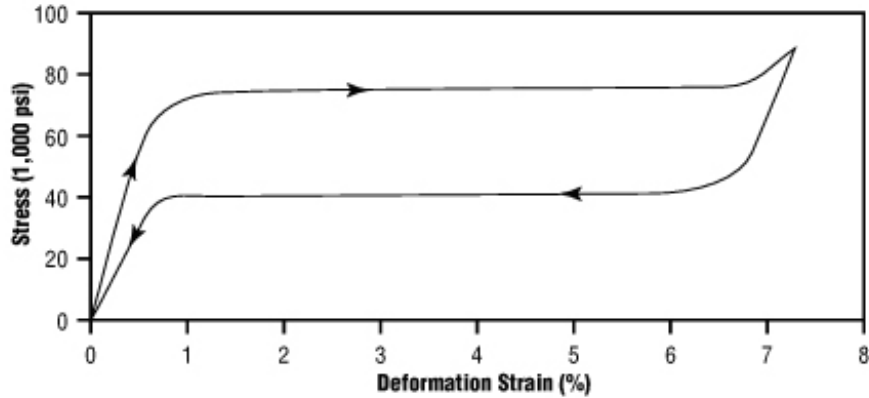


Figure 3.29: Typical stress-strain diagram of a NiTi shape memory alloy exhibiting superelasticity [105].

associated with the martensitic transition, the fully reversible transition character, and the high mobility of the habit plane.

The application of an external stress provides an additional contribution to the thermodynamic driving force of the system, resulting in transition temperature changes. In case of the superelasticity, an external stress leads to an increase of the martensitic equilibrium temperature T_0 . At a certain amount of stress, the martensitic transition temperature exceeds the sample temperature and the martensitic forward transition starts. The stress-induced shift of the transition temperature can be described by the generalized Clausius-Clapeyron-law, which was already introduced in equation 2.8

$$\frac{dT_0}{d\sigma_{ij}} = \frac{\epsilon}{\Delta S}, \quad (3.5)$$

where ϵ is the strain, σ_{ij} are the external stresses corresponding to ϵ , and ΔS is the entropy change associated with the transition [186].

The fully reversible strain of more than 10 % and the fact that the stress is constant over a broad strain range (see figure 3.29) make superelastic materials interesting for technical applications such as dental braces, implants, splints, and spectacle frames in medical engineering [76]. The high damping characteristics of superelastic materials due to internal friction (which results in the hysteretic response) makes them an interesting material class for the construction of earthquake-proof buildings.

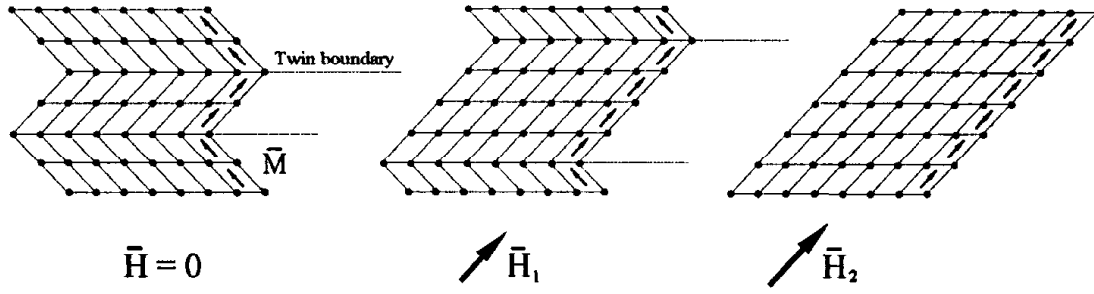


Figure 3.30: Magnetic-field-induced growth of twin-variants with a favorable orientation consuming the unfavorably oriented variants with respect to the externally applied field. At zero field (left) the martensitic structure consists of self-accommodated variants. At small fields H_1 (middle), when the pressure caused by the differences in anisotropy energy exceeds the effective elastic modulus, some variants rotate and align with the field. Fields H_2 larger than the critical field H_c give rise to a single-variant state (right). An important factor in this process is the mobility of the martensitic domain walls [184].

3.3.3 Magnetic-field-induced strain

The possibility of controlling the shape and size of objects from certain substances by applying electric or magnetic fields leads to their specification as functional materials. Representatives of this group are magnetostrictive alloys (MS), piezoelectric alloys (PE), and magnetic shape memory alloys (SM). These alloys can be grouped according to the order of magnitude of their recoverable strains, as can be seen from this hierarchy [186]:

$$\begin{aligned} \frac{\Delta L_{\text{MS}}}{L} &\approx 10^{-3}, \\ \frac{\Delta L_{\text{PE}}}{L} &\approx 10^{-2}, \\ \frac{\Delta L_{\text{SM}}}{L} &\approx 10^{-1}. \end{aligned} \quad (3.6)$$

The large magnetic-field-induced strains of more than 10 % make magnetic shape memory alloys particularly interesting for science and technical applications.

The mechanism of field-induced rearrangement of magnetic variants was proposed [182] and experimentally observed [183] for the first time by Ullakko *et al.* in 1996. Figure 3.30 schematically illustrates the underlying process of a variant rearrangement. A summary of a model explaining this effect by considering the Zeeman and magnetocrystalline anisotropy energy differences between the involved variants can be found in section 3.2.3.

The maximum value of recoverable strain is determined by the tetragonality of the martensitic variants and can be expressed by $1-c/a$. In the martensitic phase stoichiometric Ni_2MnGa has a short c -axis parallel to the easy axis of the magnetization. This distortion leads to the maximal possible strain of $1-c/a = 1 - 0.94 = 6\%$.¹⁰ The realization of these giant strains requires that the crystal is biased by stress or a magnetic field in order to guarantee that the whole crystal consists of variants of only one type. Experimental results [113] as well as a calculation based on an energy density comparison between the stress- and magnetic-field-induced rearrangement of variants [118] revealed that a field of approximately 10 kOe is sufficient to reach a single-variant state.

In a bias-free alloy all existing variants (in case of Ni_2MnGa three¹¹.) [89] are equally likely to be nucleated. In this case the recoverable strains are smaller, because a certain number of variants is already aligned with the field. The fraction of a selected variant orientation f_c as a function of the strain can be calculated by

$$f_c = \frac{(a_A \cdot (1 + \Delta/l) - a_M)}{c_M - a_M}, \quad (3.7)$$

where a_A, a_M, c_M are lattice parameters of the austenite (A) respectively martensite phase (M) and Δ/l is the strain in the corresponding direction [125]. In the case of an absent field and absent strains ($\Delta/l = 0$) the fraction of one of the three variants of stoichiometric Ni_2MnGa can be calculated as follows: $f_c = a_A - a_M / c_M - a_M \approx 0.3$ (lattice parameters are given in table 3.2). This result is in agreement with three equally distributed variant orientations.

In Ni_2MnGa crystals with an electron per atom concentration of approximately 7.6 and larger, magnetic-field-induced strains exceeding 6% are possible due to a tetragonality of approximately $c/a = 1.2$ (see figure 3.41). Sozinov *et al.* reported a giant magnetic-field-induced strain of about 9.5% in a $\text{Ni}_{0.488}\text{Mn}_{0.297}\text{Ga}_{0.215}$ alloy with $e/a = 7.6$ at magnetic fields less than 10 kOe [170].

By the application of an external uniaxial load the maximal recoverable strain can be drastically reduced as can be seen in figure 3.31. When the applied field is reduced under the condition of small or absent loads the acquired strain remains. Under field-cycling conditions at higher loads the strain exhibits hysteretic behavior.

Because of their unique characteristics magnetic shape memory alloys exhibiting (giant) magnetic-field-induced strains have great potential for mechanical engineering. Magnetostructural actuators can act as feasible alternatives to hydraulic, pneumatic, and electromagnetic drives [182], or they can potentially be

¹⁰The corresponding lattice parameters can be found in table 3.2.

¹¹The three types of martensitic variants belong to six twin systems (twin planes parallel to (110) and $(\bar{1}\bar{1}0)$, (101) and $(10\bar{1})$, (011) and $(01\bar{1})$). Each twin system can form four different habit planes with the cubic austenite. This results in 24 possible martensite microstructures (austenite-martensite interfaces) [89, 130]

Table 3.2: Lattice parameters of cubic and tetragonal crystal structures of the austenite respectively martensite phase in a stoichiometric Ni_2MnGa crystal [125]. Note the little volume difference between the martensitic and austenitic elementary cell $V_A/V_M = 0.992$ which gives rise to the stress-dependent transition temperature (see section 7.2.4) and the phenomenon of superelasticity (see section 3.3.2).

lattice parameters	austenite	martensite
a (nm)	0.582	0.5925
b (nm)	0.582	0.5925
c (nm)	0.582	0.557
volume $V(\text{nm}^3)$	0.197	0.1955
c/a	1	0.94

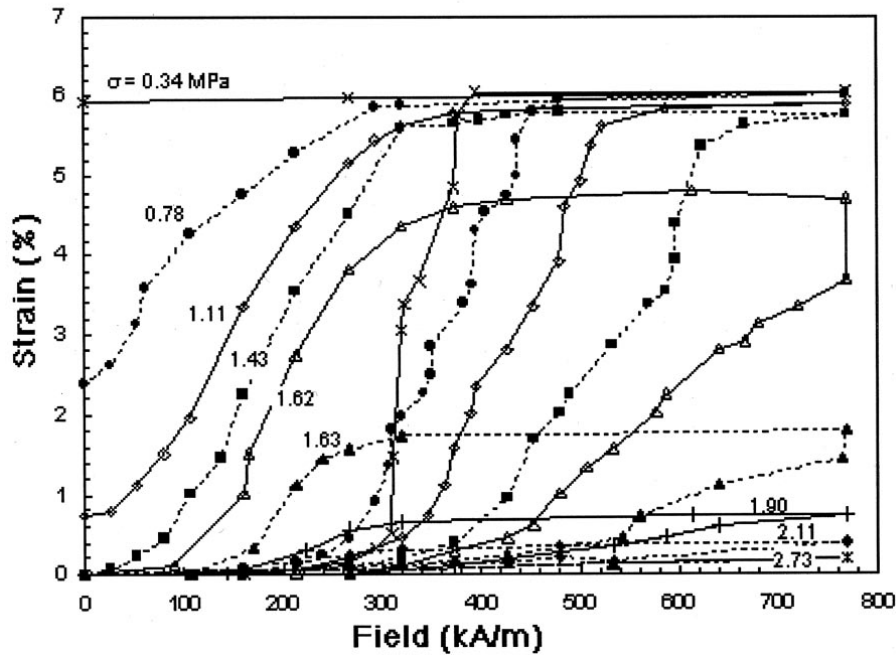


Figure 3.31: Magnetic-field-induced strains in a $\text{Ni}_{0.498}\text{Mn}_{0.285}\text{Ga}_{0.217}$ single crystal at selected stresses externally applied opposing the strain (with 795.77 kA/m being equivalent to 10 kOe being equivalent to 1 T) [113].

used in high-force positioning systems such as in robotics [195]. However, even today technical problems arising from the temperature-dependence, the high control power, and the relatively poor position control of such actuators are still not completely resolved [195].

3.4 Acoustic emission

In the following section a brief discussion on the origin of acoustic emission during the martensitic transition in shape memory alloys is given. Subsequently, an introduction to the propagation of ultrasonics in solids is presented. The description of the stress, strain, and stiffness tensor in form of Hooke's law proceeds to the formulation of the equation of motion and ends with a specific solution in the isotropic case.

3.4.1 Origin of acoustic emission in martensitic phase transitions

Many externally driven processes in solids which are intrinsically associated with a generalized friction emit acoustic signals. Such phenomena, occurring at length scales from nanometer to micrometer [91], are dislocation dynamics, microcrack propagation, and discontinuous phase transitions of multiferroic materials [191]. A shared characteristic of these quite different processes is the discontinuous response to a continuous driving force (see section 3.2.1), resulting in the emission of intermittent acoustic waves that carry information on the source mechanism [91].

The martensitic transition is accompanied by acoustic emission (AE) in the frequency range of kHz to MHz. Assuming a speed of sound in metals of approximately 5000 m/s, the corresponding wavelength ranges between mm and m.

Shape memory alloys are prototypical systems for the interplay of localized, short-range interactions (interfacial energies) and long-range interactions (strain fields) [194, 207], leading to a self-accommodated domain structure. Generally, the movement of the habit plane proceeds in discontinuous jumps under any driving force. This happens primarily because of two reasons that stop the transformation process until a further undercooling takes place. The first reason is a self-limiting effect arising from the strain fields that accumulate during the transition at the habit plane where the atoms belong, by definition, to both phases. The second hindering reason are pinning processes of the habit plane at defects such as dislocations. Both processes lead to the formation of metastable states, which are separated by energy barriers. In the course of an athermal transition, increasingly large driving forces are needed to overcome these barriers and to

continue the transition (details of the transition dynamics can be found in section 3.2.1). In both cases, the depinning processes of the habit plane release a certain amount of energy in form of phonons. The phonons propagating throughout the crystal can be detected via acoustical transducers coupled to the sample surface (see section 4.1). Anharmonic effects and damping lead to dispersion and a finite phonon lifetime [108]. After a certain propagation time (including reflections at grain and sample boundaries), the phonon (ordered lattice movement) transforms into a disordered lattice movement, i. e. heat.

A very recent publication of Bonnot *et al.* [21] provides further insights into the origin of the acoustic emission during the martensitic phase transition of a Cu-Zn-Al single crystal. Bonnot *et al.* analyzed a stress-driven martensitic transition at a constant temperature slightly above the martensitic transition temperature M_s . Because of a constraint-free sample mounting and the athermal transition character, the transition, i. e. the habit plane, can freely propagate throughout the crystal. By the combination of optical, strain, and AE measurements the propagation speed of the habit plane has been measured and correlated with the acoustic activity.

After a first (stress-induced) heterogenous nucleation in the center of the rectangular sample, two habit planes propagate in opposite directions to the sample edges by building needle domains with an estimated thickness of $10\ \mu\text{m}$. The front propagation, which was derived from the associated strain change, shows an intermittent character and occurs at high speed.¹² The stepwise propagation of the variants is assumed to be caused by the interaction with defects (dislocations), which hinder a smooth propagation and lead to a pinning-depinning process (see above and section 3.2.1). The volume that is spanned from one habit position to the next is known to be proportional to the dissipated energy in this step [152]. Bonnot *et al.* additionally have shown that the acoustic activity is proportional to the advance of the habit plane (which can be estimated by means of a strain gauge correlated with AE measurements). The combination of both findings show that the amount of dissipated energy in the growth process of martensitic variants is proportional to its released acoustic activity, which in addition has been confirmed by a phenomenological model. Figure 3.32 shows a plot of the in-situ measured propagation speed and the acoustic activity against the time. A clear correlation can be found between both features. This correlation, which becomes especially evident because of the intermittent character of the transition, has been validated by the computation of a correlation function (see inset of figure 3.32 b).

¹²In spite of the athermal transition character of Cu-Zn-Al the habit plane movement does not reach the speed of sound [188].

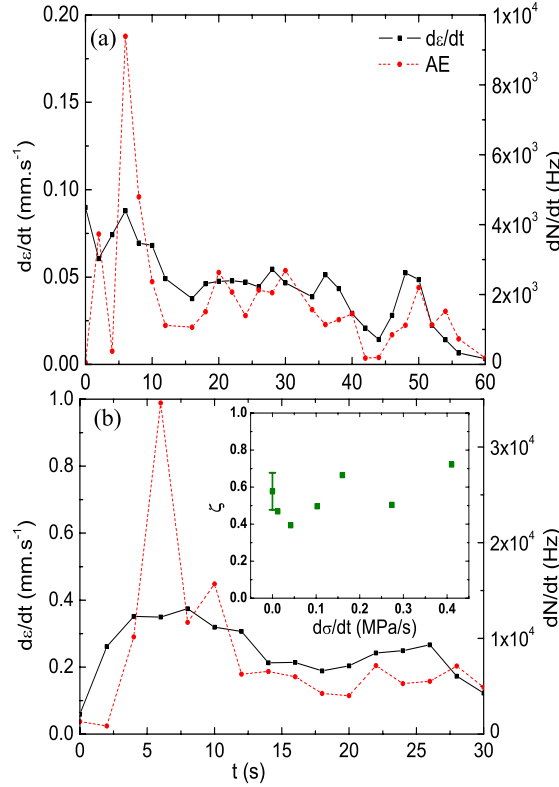


Figure 3.32: Acoustic activity of a stress-driven martensitic transition. The red dashed line shows the acoustic activity \dot{N} and the black continuous line represents the time derivative of the strain $\dot{\epsilon}$, both as a function of time. The correlation indicates a proportionality relation between the transformed fraction of martensite and the corresponding acoustic activity \dot{N} . The curves in (a) correspond to a constant stress and the curves in (b) to increasing stress at a fixed rate ($\dot{\sigma} = 0.28$ Mpa/s). The inset shows the correlation function between the acoustic and the strain data [21].

3.4.2 Propagation of ultrasonics in solids

In the following section, a compact introduction into the propagation of ultrasonics is given. A more comprehensive overview can be found in the standard reference of Landau and Lifshitz [83] and the book of Sutilov [173].

Within the theory of elasticity the propagation of sound waves can be described as a periodic particle displacement from equilibrium position by an elastic force. The particle medium is assumed to be continuous and the elongation is assumed to be infinitesimal, which applies for acoustic waves [173]. The displacement of a particle P from its arbitrary equilibrium position \vec{x} is given by $\vec{u}(\vec{x}, t)$ (in case of equilibrium conditions $\vec{u}(\vec{x}, t) = 0$). All displacements $\vec{u}(\vec{x}, t)$ form a displacement

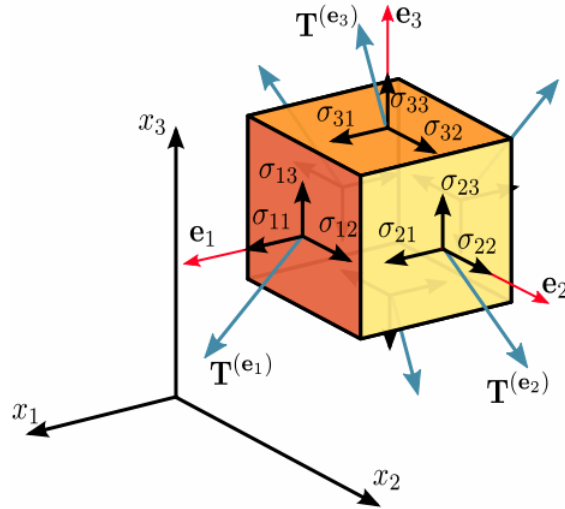


Figure 3.33: Illustration of possible components of a strain tensor $\sigma_{ij}(t, \vec{x})$ in Cartesian coordinates [155].

field. The origin of the particle displacement, i. e. the origin of the deformation of the small volume, lies in the exertion of surface forces.¹³ The force on a unit area is called mechanical stress¹⁴ and can be described by a stress tensor $\bar{\sigma}(t, \vec{x})$. One component of the stress tensor $\sigma_{ij}(t, \vec{x})$ describes a stress that acts on a plane normal to the x_i axis, with the force being directed parallel to x_j (see figure 3.33). The stress tensor is symmetric ($\sigma_{ij} = \sigma_{ji}$), i. e. it has in three dimensions six independent components in its general form (derivation see e. g. [83]). If $i = j$, σ_{ij} describes normal stresses and if $i \neq j$, it describes shear stresses.¹⁵

In case of a non-compensated stress, a surface force is exerted on a given volume element, which can be described in Cartesian coordinates by dx , dy , and dz . The cuboid is assumed to have a volume of $dV = dx dy dz$, a mass of dm , and a density of $\rho = dm/dV$. In order to formulate the equation of motion, a force F_1 is applied parallel to \vec{e}_1 on the described cuboid

$$\begin{aligned}
 F_1 = & (\sigma_{11}(x_1 + dx_1) - \sigma_{11}(x_1)) dx_2 dx_3 \\
 & + (\sigma_{21}(x_2 + dx_2) - \sigma_{21}(x_2)) dx_1 dx_3 \\
 & + (\sigma_{31}(x_3 + dx_3) - \sigma_{31}(x_3)) dx_1 dx_2.
 \end{aligned} \tag{3.8}$$

With small displacements that are realized by definition and small cuboid dimensions the stress change can be assumed to be linear. The stress components

¹³Volume forces such as gravity will not be considered in this case [173].

¹⁴The expressions *mechanical stress* and *stress* will be used synonymously in this section.

¹⁵In ideal fluids (liquids and gases) no shear stresses occur due to the absence of shear-restoring forces.

parallel to \vec{e}_1 applied on the three areas of the cuboid can be described by

$$\begin{aligned}\sigma_{11}(x_1 + dx_1) &= \sigma_{11}(x_1) + \frac{\partial\sigma_{11}}{\partial x_1} dx_1 \\ \sigma_{21}(x_2 + dx_2) &= \sigma_{21}(x_2) + \frac{\partial\sigma_{21}}{\partial x_2} dx_2 \\ \sigma_{31}(x_3 + dx_3) &= \sigma_{31}(x_3) + \frac{\partial\sigma_{31}}{\partial x_3} dx_3.\end{aligned}\tag{3.9}$$

The corresponding force components are

$$\begin{aligned}F_{11} &= \frac{\partial\sigma_{11}}{\partial x_1} dx_1 dx_2 dx_3 = \frac{\partial\sigma_{11}}{\partial x_1} dV \\ F_{21} &= \frac{\partial\sigma_{21}}{\partial x_2} dx_1 dx_2 dx_3 = \frac{\partial\sigma_{21}}{\partial x_2} dV \\ F_{31} &= \frac{\partial\sigma_{31}}{\partial x_3} dx_1 dx_2 dx_3 = \frac{\partial\sigma_{31}}{\partial x_3} dV.\end{aligned}\tag{3.10}$$

The whole force applied parallel to \vec{e}_1 on the three areas, i. e. on the volume element dV , is the sum

$$F_1 = F_{11} + F_{21} + F_{31} = \left(\frac{\partial\sigma_{11}}{\partial x_1} + \frac{\partial\sigma_{21}}{\partial x_2} + \frac{\partial\sigma_{31}}{\partial x_3} \right) dV.\tag{3.11}$$

The displacement of a particle parallel to \vec{e}_1 can be described by the equation of motion which can be formulated with Newton's second law of motion and the equation 3.11:

$$F_1 = m \cdot a_1 = \rho dV \frac{\partial u_1(t)}{\partial t^2} = F_1 = \left(\frac{\partial\sigma_{11}}{\partial x_1} + \frac{\partial\sigma_{21}}{\partial x_2} + \frac{\partial\sigma_{31}}{\partial x_3} \right) dV.\tag{3.12}$$

After dividing equation 3.12 by the volume and writing it as a sum, the equation of motion in its general form can be expressed by

$$\rho \frac{\partial u_j(t)}{\partial t^2} = \sum_i \frac{\partial\sigma_{ij}}{\partial x_i}.\tag{3.13}$$

Equation 3.13 can be solved using Hooke's law, which can be written as

$$\sigma_{ij} = \sum_{kl} c_{ijkl} \epsilon_{kl},\tag{3.14}$$

where c_{ijkl} is the fourth order stiffness tensor and ϵ_{kl} the strain tensor with $\epsilon_{kl} = \partial u_k / \partial x_l$. Because of the symmetries of the stress and the strain tensor (which

is called minor symmetry) the stiffness tensor can be written in its general form in three dimensions as

$$\begin{pmatrix} c_{1111} & c_{1122} & c_{1133} & c_{1123} & c_{1131} & c_{1112} \\ c_{2211} & c_{2222} & c_{2233} & c_{2223} & c_{2231} & c_{2212} \\ c_{3311} & c_{3322} & c_{3333} & c_{3323} & c_{3331} & c_{3312} \\ c_{2311} & c_{2322} & c_{2333} & c_{2323} & c_{2331} & c_{2312} \\ c_{3111} & c_{3122} & c_{3133} & c_{3123} & c_{3131} & c_{3112} \\ c_{1211} & c_{1222} & c_{1233} & c_{1223} & c_{1231} & c_{1212} \end{pmatrix} \equiv \begin{pmatrix} c_{11} & c_{12} & c_{13} & c_{14} & c_{15} & c_{16} \\ c_{21} & c_{22} & c_{23} & c_{24} & c_{25} & c_{26} \\ c_{31} & c_{32} & c_{33} & c_{34} & c_{35} & c_{36} \\ c_{41} & c_{42} & c_{43} & c_{44} & c_{45} & c_{46} \\ c_{51} & c_{52} & c_{53} & c_{54} & c_{55} & c_{56} \\ c_{61} & c_{62} & c_{63} & c_{64} & c_{65} & c_{66} \end{pmatrix}, \quad (3.15)$$

where the right hand matrix is given in the Voigt notation. The symmetry of the stiffness tensor ($c_{ij} = c_{ji}$) is called major symmetry and leads to 21 independent components for a system without any symmetry element (e. g. triclinic crystal system) [173]. With Hooke's law (equation 3.14) the equation of motion 3.13 transforms to

$$\rho \frac{\partial u_j(t)}{\partial t^2} - \sum_{ikl} c_{ijkl} \frac{\partial u_k}{\partial x_i \partial x_l} = 0. \quad (3.16)$$

A plane wave approach with $u_i = a_i e^{i(\vec{k}\vec{r} - \omega t)}$ leads to the equation

$$\left(\sum_k (\rho \omega^2 \delta_{ik} - \sum_{jl} c_{ijkl} k_l k_j) \right) a_k = 0, \quad (3.17)$$

where δ_{ik} is the Kronecker delta. With the substitution of $\alpha_{ik} = \sum_{jl} c_{ijkl} k_l k_j$ equation 3.17 can be written in matrix form

$$\begin{pmatrix} \rho \omega^2 - a_{11} & -a_{12} & -a_{13} \\ -a_{21} & \rho \omega^2 - a_{22} & -a_{23} \\ -a_{31} & -a_{32} & \rho \omega^2 - a_{33} \end{pmatrix} \begin{pmatrix} a_1 \\ a_2 \\ a_3 \end{pmatrix} = 0. \quad (3.18)$$

This system of equations can be solved when the determinant becomes zero:

$$|(\rho \omega^2 \delta_{ij} - \alpha_{ik})| \stackrel{!}{=} 0. \quad (3.19)$$

The solutions of the defining equation 3.19 are cubic polynomials in ω^2 as a function of \vec{k} , with up to three real roots in ω^2 . If equation 3.19 is satisfied, equation 3.18 returns a displacement vector (a_1, a_2, a_3) for every ω^2 . In general, there are one longitudinal and two transversal solutions (for the high symmetry directions).

Only in materials without any symmetry element the stiffness tensor has 21 independent components. In materials with a higher symmetry their number is reduced. In a cubic geometry only three independent components remain (c_{11} , c_{12} , and c_{44}). In isotropic materials the elastic behavior can be described by two parameters

$$\sigma_{ik} = \lambda\Theta\delta_{ik} + 2\mu\epsilon_{ik}, \quad (3.20)$$

where Θ is the volume change ($\Theta = \epsilon_{11} + \epsilon_{22} + \epsilon_{33} = \partial u_1/\partial x_1 + \partial u_2/\partial x_2 + \partial u_3/\partial x_3 = \text{div } \vec{u}$), δ_{ik} is the Kronecker delta, and λ and μ are the Lamé parameters for volume change respectively the occurring shear ($\mu = E/2(1+\hat{\mu})$, where E is Young's modul and $\hat{\mu}$ is Poisson's ratio). The solutions of the equations of motion

$$\frac{\rho}{\lambda + 2\mu} \frac{\partial^2 \vec{u}}{\partial t^2} - \Delta \vec{u} = 0 \quad \text{with} \quad \text{rot } \vec{u} = 0 \quad \text{i.e.} \quad \vec{u} \parallel \vec{k} \quad (3.21)$$

$$\frac{\rho}{\mu} \frac{\partial^2 \vec{u}}{\partial t^2} - \Delta \vec{u} = 0 \quad \text{with} \quad \text{div } \vec{u} = 0 \quad \text{i.e.} \quad \vec{u} \perp \vec{k} \quad (3.22)$$

are either perfectly longitudinal waves (equation 3.21) or transversal waves (equation 3.22).¹⁶ The speed of sound of longitudinal waves can be determined to be $c_l = \sqrt{\frac{\lambda+2\mu}{\rho}}$ and the speed of transversal waves can be calculated to be $c_t = \sqrt{\frac{\mu}{\rho}}$.

3.5 Analyzed material systems

Shape memory alloys show a wide range of phenomena and effects. Only the most fundamental characteristics can be found in all shape memory alloys such as the lattice distortion, the occurrence of shear forces, the diffusionless first-order character¹⁷, and a highly mobile habit plane. This diversity makes it impossible to define a prototypical shape memory alloy. However, it is possible to identify material systems which serve as prime examples for some of the occurring phenomena because they display the corresponding feature in an explicit and rather pure manner. The heterogeneity of the effects is reflected in a lively controversy on shape memory alloys in the literature (e. g. in the fields of precursor effects, transition dynamics, or the degree of discontinuity; see e. g. [7, 67, 112, 210]). It is worth mentioning that there is no unifying model approach including all phenomena and characteristics of the broad spectrum of experimental observations.

In this work, three two-component material systems, Ni-Al, Au-Cd, and Fe-Pd, as well as one three-component system, Ni-Mn-Ga, have been analyzed. These materials have been chosen because they all show a martensitic phase

¹⁶In ideal fluids (liquids and gases) with zero viscosity only longitudinal waves occur.

¹⁷A definition of the martensitic transition consists of these characteristics.

transition within a temperature range accessible by a precise Peltier cooling device (see section 4.1). Additionally, they are well known for showing precursor effects, which imply a deviation from the classical athermal behavior (see e. g. [5–7, 20, 47, 77]).¹⁸ The material Ni-Mn-Ga is prototypical for the combination of a ferromagnetic and a ferroelastic transition. The occurring magneto-structural interplay is strongly related to the (discontinuous) intermediate phase transition.¹⁹ In addition, the alloy is a prototype for the effect of (giant) magnetic-field-induced strain of 6% and more, depending on the tetragonal distortion associated with the transition.

3.5.1 Ni-Al

In the compositional range of $0.60 \leq x \leq 0.68$ $\text{Ni}_x\text{Al}_{1-x}$ shape memory alloys show an athermal martensitic transition occurring exclusively from a quenched metastable high-temperature β -phase [8, 25, 166, 168]. It is worth mentioning that in the given stoichiometric range these alloys are not in thermodynamic equilibrium but in a metastable state resulting from quenching from high temperatures close to the melting point. Therefore, the preparation process of the metastable alloys is quite delicate. The as-cast ingot needs to be quenched at high rates in order to prevent a decomposition of the alloy (see phase diagram in figure 3.34). The high quenching rates lead to a freezing of a high vacancy density. Because of the non-equilibrium situation thermal treatments of the sample, as e. g. defect annealing, is either difficult to realize or not possible at all. Due to their statistical filling of the lattice sites non-stoichiometric alloys have a high intrinsic disorder. By definition phase diagrams are equilibrium diagrams, which cannot be applied to non-equilibrium alloys. However, the martensitic phase transition temperatures of Ni-Al are added afterwards to the equilibrium phase diagrams as can be found in figure 3.34.

The parent (high temperature) phase is cubic with a B2-structure (caesium chloride structure) and is called the β -phase [25, 42, 51, 57]. The product (low temperature) phase is reported to be face-centered tetragonal ($L1_0$) [42, 51, 57]. Different layer sequences are reported according to stoichiometry: For $\text{Ni}_x\text{Al}_{1-x}$ with $60 \leq x \leq 63$ a 7M ($5, \bar{2}$) or 7R sequence and for $63 \leq x \leq 68$ a 3R sequence [37, 159, 166]. A noteworthy feature of the model alloy is the strong dependence of the transition temperature on the stoichiometry, which is reported to be between 100 K/at. % and 160 K/at. % [25, 166].

Usually, the transition is classified as athermal. However, recent incubation time measurements via optical [7, 90] and acoustic experiments [31, 172] (see section

¹⁸Fe-Pd combines the ferromagnetic and ferroelastic phase transition which leads to an interplay of structural and magnetic degrees of freedom, which has received a lot of modeling [61].

¹⁹Field-dependent experiments with Fe-Pd will not be in the focus of this work.

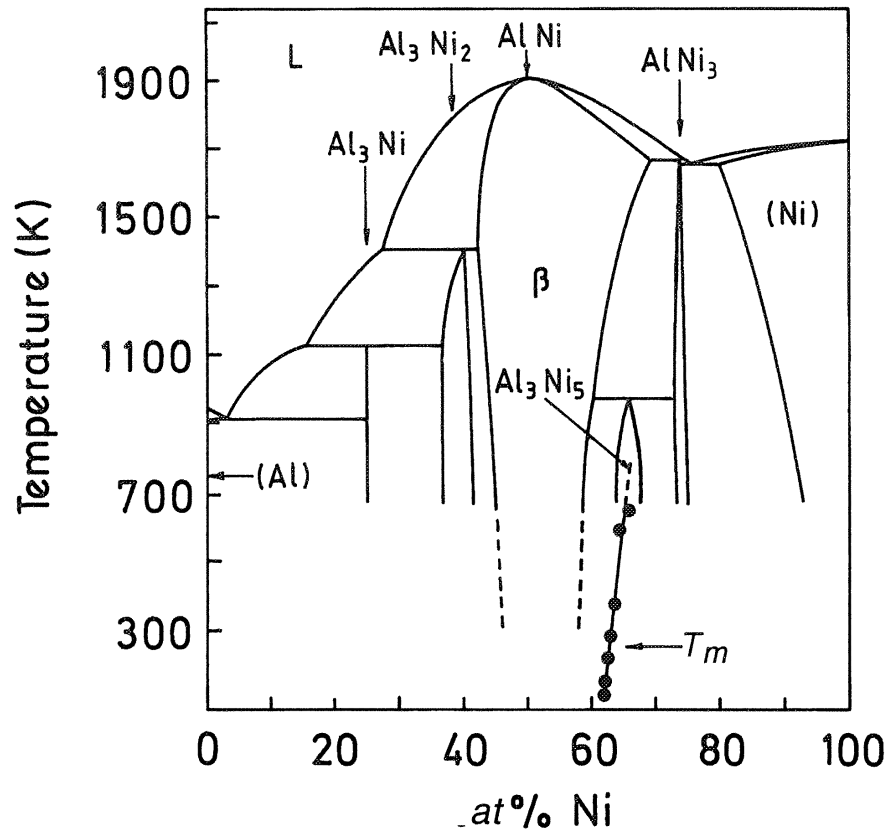


Figure 3.34: Equilibrium phase diagram of Ni-Al [145] which has been extended to the martensitic transitions. Martensitic transitions are observed only in a narrow composition range of $0.60 \leq x \leq 0.68$ $\text{Ni}_x\text{Al}_{1-x}$. The represented martensitic transition temperatures have been extracted from [154]. The combined phase diagram can be found in [141].

3.2.1) as well as rate-dependent AE measurements presented in this work have shown that the transformation also reveals isothermal characteristics. Different precursors of the martensitic phase have been reported which provide evidence for the weak first-order character of the transition. Two phonon anomalies are reported in the material system: the incomplete softening of the $[\xi\xi 0]$ - TA_2 -mode with $\xi = 0.16$ (see figure 3.18), and an anomalous minimum of the longitudinal acoustic branch $[\xi\xi\xi]$ -LA-mode at $\xi = 0.66$ [165, 166]. The phonon softening provides a displacement pattern that can be related to the static modulation of the martensitic phase. During neutron experiments strong elastic diffraction patterns can be observed which are related to the phonon softening and lead to the so-called *central peak* [166]. Additionally, Ni-Al displays a *tweed* pattern characteristic [159, 166].

3.5.2 Au-Cd

$\text{Au}_x\text{Cd}_{1-x}$ is a metallic alloy which shows a martensitic transition with shape memory character in a small compositional range of approximately $0.50 \leq x \leq 0.53$. The parent phase has a cubic B2 structure with a statistical distribution of the gold atoms in case of $x \neq 0.50$. The structure of the low temperature phase varies depending on the composition. A phase named ζ'_2 is realized for $x = 0.505$ [122, 187], which is reported to have a hexagonal, trigonal ($P\bar{3}1$) [187], or trigonal (P3) structure without symmetry center [114, 120]. For crystals with $x = 0.525$ an orthorhombic symmetry has been found, which is classified as γ'_2 (B19-structure) [84, 119]. In contrast to the Ni-Al shape memory alloy, here both the low and the high temperature phase are in thermodynamic equilibrium and can be found in the phase diagram of figure 3.35. The transition dynamics of Au-Cd is traditionally classified as athermal, which excludes the thermal activation of the nucleation and growth processes. This classification is contrasted by recent optical incubation time measurements (see 3.2.1), which show also isothermal aspects of the transition [111, 158]. AE measurements presented in this work reveal as well a rate-dependent, behavior which implies (partly) isothermal dynamics. Additionally, the time-dependent training effect, aging, and rubber-like behavior is observed in Au-Cd [84, 111, 121, 149, 151]. Phonon softening of the $[\xi\xi 0] - \text{TA}_2$ -mode is reported to occur at $\xi = 0.35$ [123] and at $\xi = 0.5$ [122] depending on the composition of the sample. In elastic neutron scattering experiments a central peak is observed [122, 167]. The occurrence of tweed has been stated by different authors (e. g. [124]).

3.5.3 Fe-Pd

$\text{Fe}_{itx}\text{Pd}_{1-x}$ is a ferromagnetic alloy which shows in the compositional range of $0.344 \leq x \leq 0.395$ a martensitic phase transition, shape memory effect, and superelasticity [146]. The combination of both ferroelastic and ferromagnetic properties allows to trigger the phase transition not only by temperature or pressure changes, but by applying magnetic fields as well. Two phase diagrams of Fe-Pd are given in figure 3.36: the equilibrium phase diagram on the left and the non-equilibrium diagram with the martensitic transition on the right. In thermodynamic equilibrium at high temperatures, there is a $\gamma(\text{Fe}, \text{Pd})$ phase with a face-centered cubic elementary cell. Under cooling it separates into two equilibrium phases: the intermetallic phase with a tetragonal unit cell and the $\alpha(\text{Fe})$ phase with a body-centered cubic structure.

The martensitic transition is depicted in the phase diagram on the right. In the high temperature phase the alloy (with an appropriate stoichiometry) has a face-centered cubic structure (fcc) [20]. Under cooling, as indicated by the arrow, the martensitic transition occurs and the material transforms into a face-centered

3. Martensitic transitions in shape memory alloys

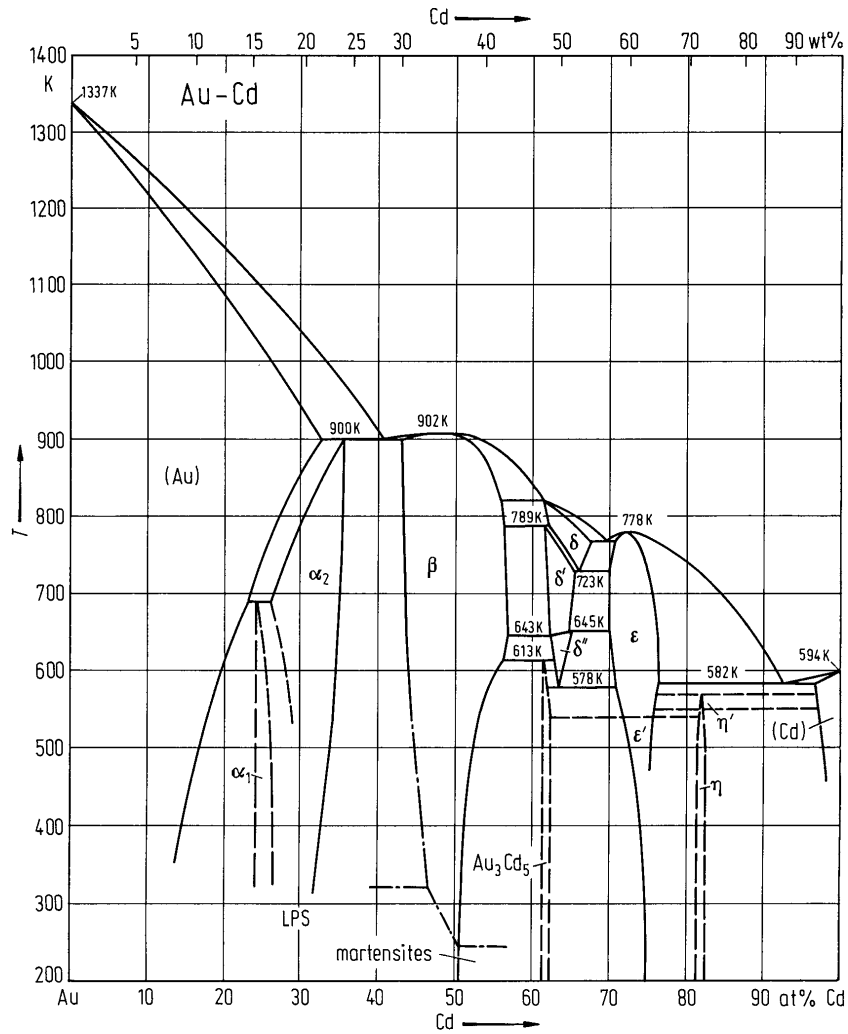


Figure 3.35: Equilibrium phase diagram of Au-Cd with indicated martensitic phase [145]. Close to its stoichiometric composition Au-Cd shows a martensitic transition and the shape memory effect.

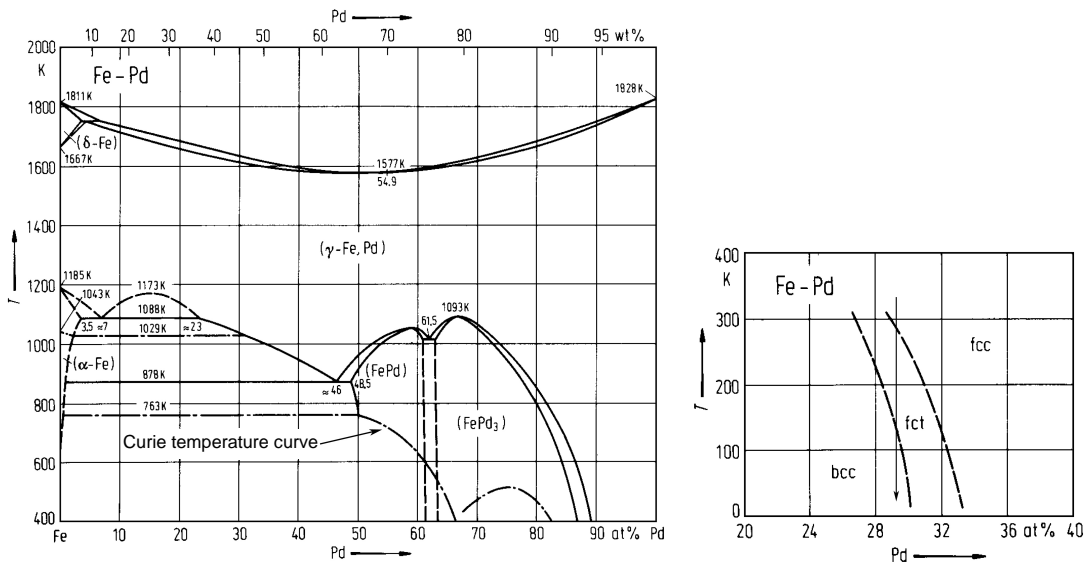


Figure 3.36: Equilibrium phase diagram of Fe-Pd (left). Martensitic phase diagram with a composition of approximately 30 % Palladium (right). The black arrow indicates a possible path through the martensitic transition. The shape memory effect occurs in the ferromagnetic phase which enables a magnetoelastic coupling (adapted from [146]).

tetragonal structure (fct) [20]. Further cooling leads to a second transition and a body-centered structure (bcc) can be observed. As can be seen in figure 3.36 (right), the martensitic transition temperature is highly sensitive to the composition and varies with 50 K/at. % [126]. In addition figure 3.37 shows the lattice parameters a and c as a function of temperature. Strong deviations from 1 can be seen in the c/a -ratio at low temperatures, as shown in figure 3.37. The coupling of ferromagnetic moments to ferroelastic variants leads to interesting applications such as magnetic-field-induced transitions or magnetic-field-induced strains (see section 3.3.3).

Fe-Pd shows rich precursor phenomena [20]. Inelastic neutron diffraction reveals phonon softening of the $[\xi\xi0]TA_2$ mode around the Γ point as the magnetization increases [156]. The occurring soft mode can be understood as a dynamic feature of the premartensitic transition. Tweed is reported to appear as a static pre-translational feature prior to the transformation [110]. Some authors reported premartensitic phenomena more than 100 K above the transition temperature (e. g. [20]). Because of the occurring latent heat the transition was commonly classified as discontinuous. However, in more recent studies it is classified as nearly continuous due to the marked precursor effects [33].

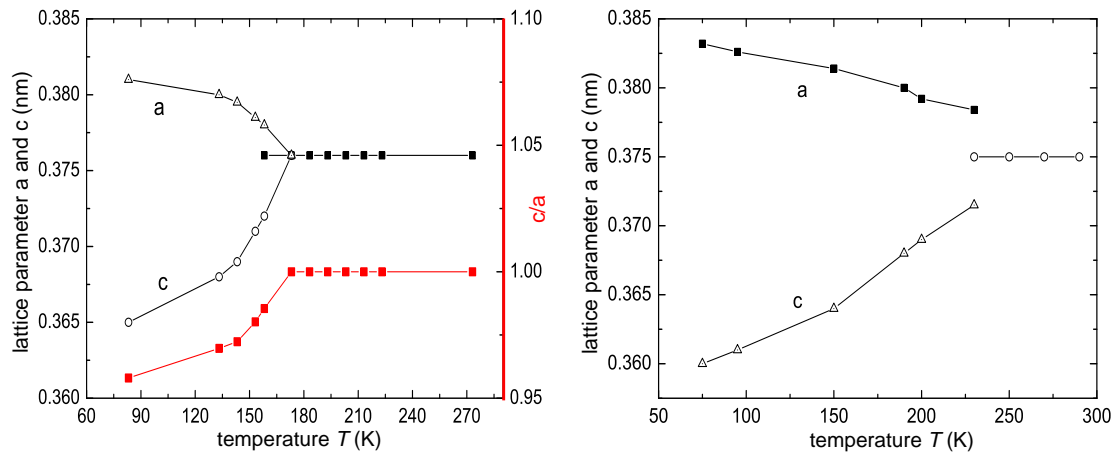


Figure 3.37: Lattice parameters *a* and *c* of the cubic high temperature phase and the tetragonal low temperature phase of a $\text{Fe}_{0.312}\text{Pd}_{0.688}$ polycrystal on cooling (left) (adapted from [169]). Lattice parameter *a* and *c* of a $\text{Fe}_{0.312}\text{Pd}_{0.688}$ single crystal as function of temperature under cooling (right) (adapted from [64]). Both samples have the same nominal composition as the samples analyzed in this work.

3.5.4 Ni-Mn-Ga

The coupling of structural and magnetic degrees of freedom, which is analyzed in this work, leads to a broad range of characteristics of Ni-Mn-Ga. The following description starts with the elastic subsystem and the crystal structure of the stoichiometric alloy Ni_2MnGa . The subsequent paragraph describes the magnetic subsystem, followed by a brief discussion on the dependence of the magnetic and martensitic transition temperatures on the stoichiometry.

Ni-Mn-Ga alloys are ternary intermetallic compounds, which can be described by the general formula of Heusler alloys X_2YZ (in the stoichiometric case). At room temperature, Ni_2MnGa and slightly deviating off-stoichiometric alloys have an L_{21} structure, as depicted in figure 3.38. This structure is related to a body-centered cubic unit cell in the sense that an L_{21} structure can be obtained from a body-centered cubic unit cell if the position in the center is occupied by Ni (blue) and if the positions at the corners are occupied by either Mn or Ga (red, respectively green), corresponding to the exact composition. At temperatures of 1380 K and above, Ni_2MnGa has a liquid phase. As the temperature decreases, Ni_2MnGa transforms into the partially ordered $\text{B}2'$ phase. In the course of further cooling a continuous phase transition of the disorder-order type from $\text{B}2'$ to L_{21} occurs at about 1070 K [186]. The martensitic transition is preceded by an intermediate (or premartensitic) transition to a 3M modulated phase with a

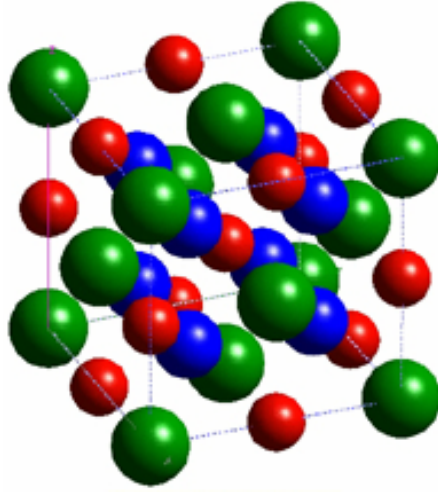


Figure 3.38: Unit cell of the austenitic phase of Ni_2MnGa in the $L2_1$ structure. Ni atoms are represented in blue, Mn and Ga in red and green, respectively.

Table 3.3: Electronic and magnetic characteristics of Ni_2MnGa .

element	magnetic moment (μ_B)	electron configuration	c/a
Ni	≤ 0.3	$[\text{Ar}] 3d^8 4s^2$	10
Mn	≈ 4.17	$[\text{Ar}] 3d^5 4s^2$	7
Ga	0	$[\text{Ar}] 3d^{10} 4s^2 4p^1$	3

preserved cubic structure [40, 209, 210]. This weakly discontinuous transition²⁰ is heralded by strong but incomplete softening of the $[\chi\chi 0]$ TA_2 phonon at $\chi \approx 0.33$ [85, 98]. Magnetoelastic coupling has been proposed to play an essential role for this transition to occur [142]. Discontinuous martensitic transitions take place at about 200 K and lead to a tetragonal structure with $c/a < 1$. At room temperature the lattice constant a is reported to be 5.82 Å. At a lower temperature in the martensitic phase the lattice constants are $a = 5.925$ Å and $c = 5.57$ Å, which leads to a small reduction of the volume of the unit cell from $V_{\text{austenite}} = 197$ Å³ to $V_{\text{martensite}} = 195.5$ Å³ (details on the stoichiometric dependence of c/a can be found in the section below and in the figures 3.40 and 3.41) [125].

In Ni_2MnGa the magnetic moment is distributed quite heterogeneously. It is primarily localized at the Mn atoms $\mu_{\text{Mn}} \approx 4.17\mu_B$, whereas Ni atoms only contribute $\mu_{\text{Ni}} \leq 0.3\mu_B$ and Ga atoms do not have a magnetic moment (see table 3.3) [199]. At 376 K Ni_2MnGa transforms to the ferromagnetic phase. At the

²⁰The latent heat involved in the transition is about ten times less than the latent heat corresponding to the martensitic transition (see table 7.4).

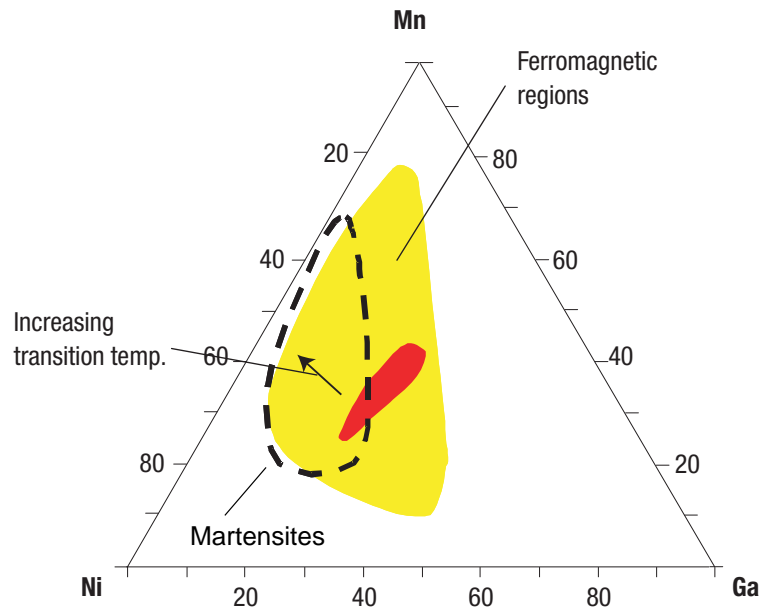


Figure 3.39: Functional phase diagram of the ternary alloy Ni-Mn-Ga. In the ferromagnetic region (yellow), the red area has the highest magnetization. The dotted line surrounds the region of reversible martensites. In the overlapping areas a magnetostructural interplay is possible (adapted from [174]).

martensitic transition the susceptibility to weak fields ($H \lesssim 10 \text{ kOe}$) shows a sharp decline, which corresponds to an increase of the magnetocrystalline anisotropy. At magnetic fields larger than approximately 10 kOe the susceptibility shows a moderate increase of the (saturation) magnetization. In the premartensitic phase the (statically) modulated structure leads to an increase of the magnetostructural anisotropy, which can be observed by a small decrease of the magnetization.

In the high temperature phase the easy magnetization axis is oriented along the crystallographic [100] direction and 180-degree domains are formed [186]. When a martensitic structure of lower symmetry is formed, the magnetic structure changes dramatically. In the martensitic phase several magnetic 180-degree domains with a diameter between $5 \mu\text{m}$ and $40 \mu\text{m}$ are formed within a single structural domain, which is called a variant. The coupling of the magnetic moments to the variants opens the possibility of magnetic-field-induced strain (see section 3.2.3 and section 3.3.3).

The compositional regions where the ferromagnetic and the ferroelastic transitions occur are displayed in a functional phase diagram, figure 3.39 [174]. The dependence of the magnetic and the elastic transition temperatures on the Mn concentration is illustrated in figure 3.40. The Curie temperature decreases with

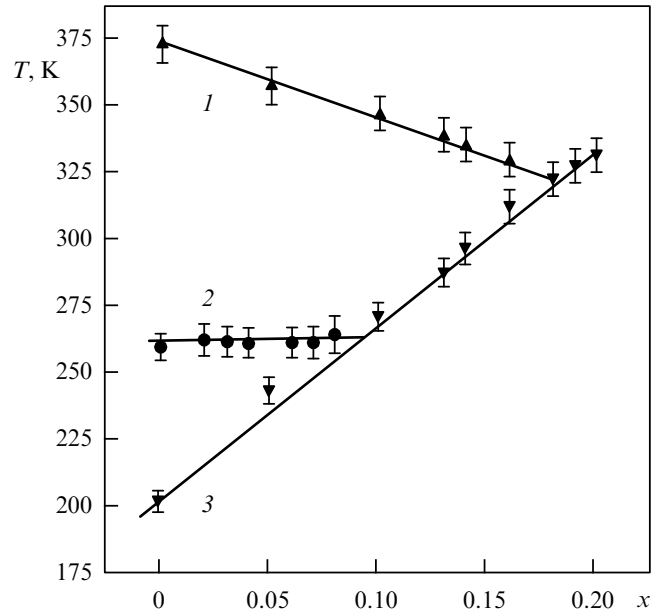


Figure 3.40: Transition temperatures of $\text{Ni}_{2+x}\text{Mn}_{1-x}\text{Ga}$ as a function of the composition parameter x . The number 1 labels the ferromagnetic-paramagnetic coexistence line. Line 2 represents the temperature of the premartensitic transition. Line 3 represents the martensitic transition. Note that there is a composition where the premartensitic transition temperature meets the martensitic transition temperature and the martensitic transition temperature is equal to the Curie temperature (adapted from [174]).

decreasing amount of Mn with about $25 \text{ K}/x$ where x is the off-stoichiometric Ni concentration in $\text{Ni}_{2+x}\text{Mn}_{1-x}\text{Ga}$. The premartensitic transition temperature remains basically constant with increasing Mn until it disappears at a composition where the extrapolated premartensitic transition temperature and the interpolated martensitic transition temperature meet. The martensitic transition temperature increases with increasing Ni with a slope of about $62.5 \text{ K}/x$.

The transition temperature-dependence on the electron concentration is depicted in figure 3.41 (a). The cross-like formation includes the martensitic transition as well as the Curie temperature. Both temperature curves show a roughly linear dependence on the electron concentration and cross each other at an electron concentration of about $e/a = 7.7$ and a temperature of $T = 360 \text{ K}$. It is worth mentioning that the martensitic transition temperature changes its slope after crossing the Curie temperature. In the range of $M_s > T_c$ ($e/a \geq 7.7$) the martensitic transition temperature follows roughly $500 \text{ K}/e/a$, whereas for $M_s < T_c$ ($e/a \leq 7.7$) the slope can be estimated as approximately $900 \text{ K}/e/a$. The occurrence

3. Martensitic transitions in shape memory alloys

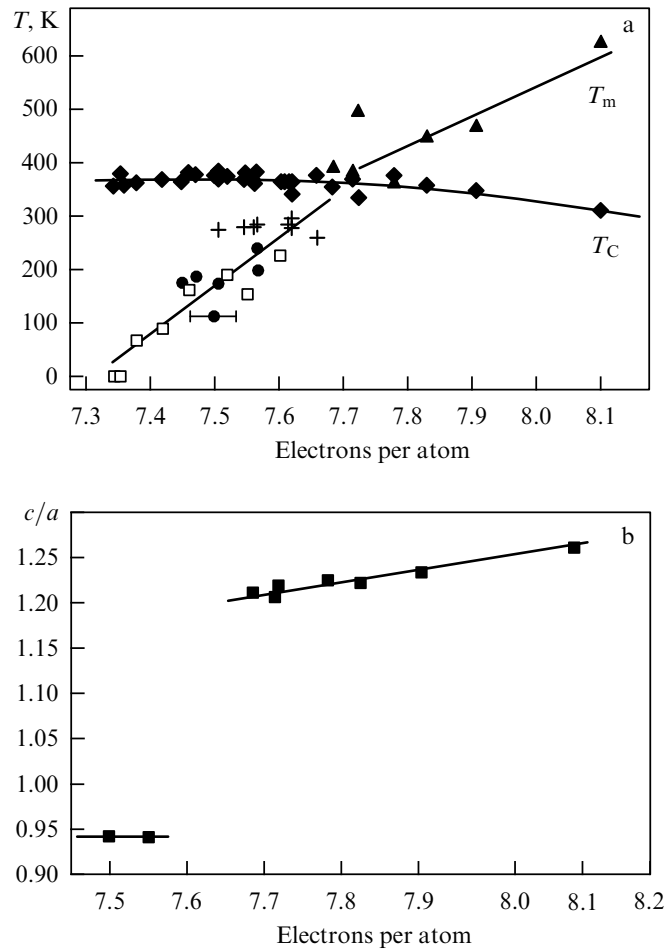


Figure 3.41: The magnetic and martensitic transition temperatures (a) and the tetragonal distortion of the martensitic unit cell via the c/a -ratio (b) as a function of the electron concentration. The relation between the stoichiometry and the electron concentration can be found in table 3.3 (adapted from [186] and [174]).

of the martensitic transition in both the paramagnetic and the ferromagnetic phase changes the realized c/a ratio from a value greater than one to a value smaller than one, as can be seen in figure 3.40 (b). With an electron concentration of $e/a \approx 7.4 - 7.6$ the Curie temperature is lower than the martensitic transition temperature and the c -axis diminishes to a value of $c/a \approx 0.94$ ($e/a(\text{Ni}_2\text{MnGa})=7.5$). At a concentration of $e/a \geq 7.7$ the martensitic transition takes place within the paramagnetic phase and the c -axis grows to $c/a \approx 1.25$. Tsuchiya *et al.* estimated the electron concentration to be $e/a = 7.62$ for the case that both transitions occur at the same temperature $T_c \approx M_s$ [180].

The martensitic transition of Ni_2MnGa is associated with latent heat and therefore discontinuous. Before the existence of a small latent heat had been reported for the first time, the order of the premartensitic transition was discussed controversially (see footnote 20) [142]. Results presented in this work provide some evidence that the discontinuous character of the premartensitic transition is lowered by the application of a magnetic field (see section 8.4.1).

Several precursor effects have been reported such as phonon softening at $\zeta = 0.33$ [$\zeta\zeta 0$] TA_2 mode [85, 98], where the minimum temperature of the linearly decreasing squared phonon energy marks the premartensitic transition temperature. A further phonon anomaly is the substantial softening of the shear moduli C_{44} and C' . In addition to that, tweed is reported to occur [144].

Besides magnetostriction and the magneto-caloric effect, the shape memory effect (see section 3.3.1), superelasticity (see section 3.3.2), (giant) magnetic-field-induced strain (see section 3.3.3), and aging effects such as martensite stabilization and rubber-like behavior [36, 88, 161, 205] occur.

4 Experimental Details

The acoustic emission results presented in this work were measured at two different laboratories - one at the *II. Physikalisches Institut* of *RWTH Aachen University* and the other one at the *Departament d'Estructura i Constituents de la Matèria* of the *University of Barcelona* - using two very similar acoustic emission setups. Both setups are identical models from the same manufacturer *Physical Acoustics* and each one consists of an acoustic transducer, a preamplifier, and a data acquisition computer card (section 4.1). The only difference between these setups is a slightly varying configuration concerning a frequency hardware bandpass. The following experimental description applies to both setups. Apart from the acoustic emission system the experimental setups consist of a temperature-controlled sample environment. The Barcelona setup additionally comprises an electromagnet (section 4.2.2). The temperature stage of the Aachen setup is located inside a vacuum chamber whereas the experiments in Barcelona are conducted under ambient conditions (section 4.2.1). In the following the setup at RWTH Aachen University will be called *vacuum setup* and the setup at the University of Barcelona will be named *field setup*.

4.1 Acoustic emission setup

The acoustic emission setup enables the user to detect acoustic events, which are released during structural changes inside the sample, e. g. during a martensitic phase transition or the reorientation of martensitic variants. The measurement chain, beginning with the detection of acoustic signals leading to their digitalization, processing, and finally storage on a personal computer, is shown in figure 4.1.

The ultrasonic signals emitted from the sample during a structural change at micro- and mesoscopic length scales are in the range of hundreds of kHz to some MHz and are detected by a commercial piezoelectric transducer from *Physical Acoustics*. Some characteristics of the used transducers (figure 4.2), which are based on the piezoelectric effect, are summarized in table 4.1. A deformation of the transducer produces a voltage signal $U_0(t)$, which is preamplified by 60 dB (equal to a factor of 1000), using a *2/4/6 amplifier* from the same manufacturer. The preamplified signal is transmitted to the *Physical Acoustics pci-2* data acquisition card. In order to process the incoming analog voltage signal it is digitized and

4. Experimental Details

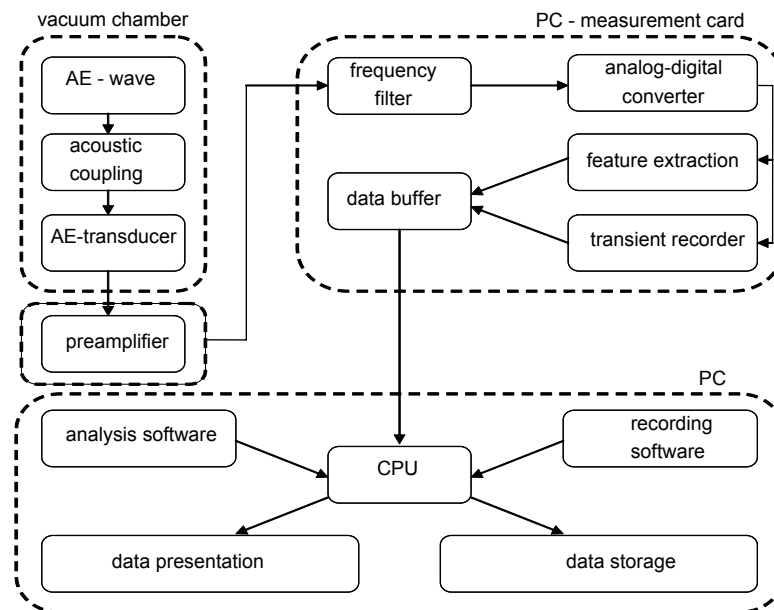


Figure 4.1: Flow process chart of the acoustic emission measurement chain (adapted from [50]).

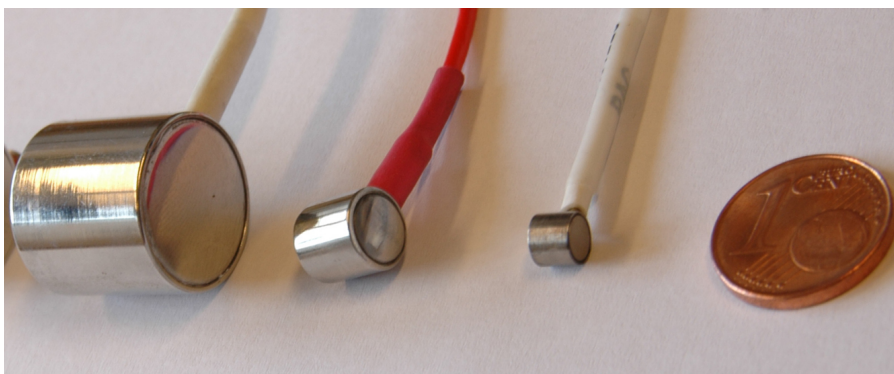


Figure 4.2: Photograph of the acoustic emission transducers used in this work. From left to right: R15-LT, NANO30, PICO, and as a reference a 1-cent coin (adapted from [172]).

Table 4.1: Characteristics of the piezoelectric acoustic emission transducers used in this work [1], which are depicted in figure 4.2.

name	dimensions dia (mm) x height (mm)	operating temperature (K)	case material	face material	peak sensitivity in dB	operating frequency (kHz)	resonant frequency (kHz)
PICO	5 x 4	208 - 450	steel	ceramic	54	200 - 750	450
NANO 30	8 x 8	208 - 450	steel	ceramic	62	125 - 750	300
R15-LT	18 x 17	77 - 473	Inconel 600	Inconel 600	69	100 - 700	150

converted into decibel according to the following relation:

$$20 \text{ dB} \log_{10} \left(\frac{U_{\text{amplified}}}{1 \mu\text{V}} \right) = 20 \text{ dB} \log_{10} \left(\frac{U_0}{1 \mu\text{V}} \right) + \underbrace{60 \text{ dB}}_{\text{preamplification}}. \quad (4.1)$$

For a transducer output voltage of e. g. $U_0 = 10 \mu\text{V}$ and with an amplification factor of 60 dB the signal would be amplified to $U_{\text{amplified}} = 10 \text{ mV}$ and then stored as 20 dB.

To separate environmental noise from the signals associated with the transition (transition signal) a threshold can be set. A lower noise level allows a lower threshold level. The vacuum setup allows a lower detection limit of 22 dB, for the field setup it is 25 dB. The corresponding transducer voltages are $12.6 \mu\text{V}$ and $17.8 \mu\text{V}$, respectively. As shown in equation 4.1 a voltage increase of 20 dB equals an order of magnitude. In the case of very high voltage signals the preamplification can be reduced to a value of 40 dB or 20 dB. In the presented experiments only the highest preamplification of 60 dB has been used. Besides the pure amplification there is a bandpass filter included in the preamplifier. The vacuum setup has a bandpass of 100 kHz to 1 MHz whereas the field setup has a broader bandpass of 20 kHz to 2 MHz. By using a bandpass, low and high frequency noise can be filtered. Low frequency noise can be caused e. g. by

constant pressure on the transducer, noise from other instruments running in the background, vibrations from moving objects, or persons and so on. High frequency noise is emitted e. g. by switching power supplies and other sources of electrical noise. Comparing both filter sets it is worth mentioning that there is no significant difference in the analyzed data between both configurations.

The *pci-2 data acquisition card* has four channels: two acoustic emission channels and two parametric channels for other transducers or other voltage inputs in general. The AE-measurement card has an internal amplification of 6 dB and an additional onboard bandpass. It is reasonable to tune the onboard bandpass to the same values as the hardware bandpass in order to filter the electrical noise, which is coupled into the circuit on the way from the preamplifier to the measurement card, and to guarantee a sharp cutoff frequency.¹ The filtered signal is digitized at a rate f_{ad} of 40 Msample/s and with an 18 bit conversion scheme for an input voltage of ± 10 V. The other two existing channels are used to record external parameters, which must be available as a voltage signal in the range of ± 10 V. The converter works at a rate of 10 kHz and with 16 bit. The external parameters can be selected according to experimental demand. In the presented measurements the sample temperature is recorded. In addition to that the field setup allows for the application and recording of a magnetic field H .

The computer card provides two different analysis methods for the digitized acoustic emission data. On the one hand, a transient signal of infinite length can be recorded with a real time storage on the hard disc.² A part of a typical transient signal, which was detected during a martensitic transition, is shown in figure 4.3. On the other hand, several waveform features can be extracted from every single detected wave packet in the so-called "parameter-based analysis". In the following, a wave packet will be named a *hit*, which is in line with industry standards for non-destructive testing methods. A big advantage of the parameter-based analysis is the enormous data reduction. Instead of dealing with the whole waveform only characteristic hit parameters are saved, which provides a more abstract characterization of the acoustic signals - a kind of an acoustic fingerprint.

For the parameter-based analysis the data-acquisition card uses an implemented algorithm, which consists of a three-step process: 1. differentiation between noise and transition signals. 2. identification and separation of hits. 3. feature extraction from detected hits. A hit starts with the first crossing of a tunable threshold at the time t_0 . The time t_0 is the starting time of the hit and initiates a time measurement. If the acoustic signal crosses the threshold within an adjustable time interval *hit definition time* (HDT) a second time, the procedure is reactivated. In this case, a hit consists of at least two counts, which is the number

¹The high-pass onboard filter is a 4th order Butterworth filter and the low-pass filter is a 6th order Butterworth filter. A n^{th} order low-pass filter (high-pass filter) reduces the amplification above (below) the critical frequency f_c about $n \cdot 20$ dB per decade of $|f - f_c|/f_c$.

²The length of the recorded stream is only limited by the available disk space.

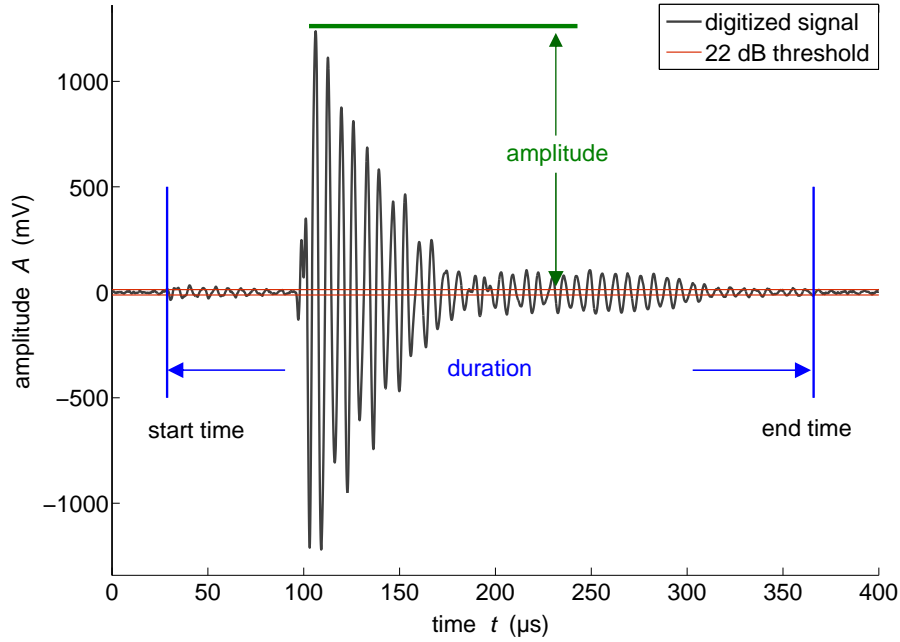


Figure 4.3: A wave packet recorded during a martensitic transition. Two extracted acoustic emission features, amplitude, and duration of a hit are illustrated (adapted from [172]).

of threshold oversteps. If there is finally no anew crossing of the threshold, the hit ends and the last starting time of the HDT measurement is determined as the end time of the hit. The *hit lockout time* (HLT) defines a time interval in which the system does not detect a new hit ($HLT_{\min} = 2 \mu\text{s}$). Figure 4.3 shows an example of a typical hit, which was recorded by the described setup during a martensitic transition and indicates the most relevant features. The red line represents the threshold, the first blue vertical line marks the start time t_0 , and the second vertical blue line shows the end time t_{end} . The green horizontal line indicates the amplitude which is the maximum intensity of a hit (positive or negative). The hit energy is an integrated quantity calculated from the power of the signal. An AE signal produces a voltage and a resulting current in the transducer with a power of $P(t) = U(t)I(t) = U^2/R$. R is an internal reference resistance of $10 \text{ k}\Omega$. The energy is the time integral of the power

$$E = \int_{t_0}^{t_{\text{end}}} P(t) dt = \frac{1}{R} \int_{t_0}^{t_{\text{end}}} U(t)^2 dt \approx \frac{1}{Rf_{\text{ad}}} \sum_i^k U_i^2, \quad (4.2)$$

replacing an integral by a sum owing to discrete data. For every detected hit a real time *discrete fourier transform* (DFT) is computed. The DFT is a reasonable

approximation of the frequency spectrum of the transient signal of a hit.³ By means of the computed spectrum, the center of mass of the frequency spectrum and the frequency with the highest amplitude can be calculated (which is named *peak frequency* in the following). The peak frequency e. g. is used in the data processing as a filter criterion.

Other AE features are e. g. the duration of the rise of a hit from the first threshold crossing until the amplitude maximum is reached (*rise time*) or the total number of threshold crossings in a hit (*counts*). In sum, ten independent AE features can be derived from a hit. Although another 7 features are calculated as well in real time, they only include redundant information, e. g. the *average frequency*, which is the number of counts per hit divided by the hit duration.

4.2 Sample environment

The description of the sample environment is divided into two subsections. In the first subsection there will be a description of the vacuum setup, consisting of a small and well adapted vacuum chamber with a very accurate temperature control. The second subsection deals with the field setup, which combines a temperature-controlled sample holder with an electromagnet for the application of fields H of $H_{max} = 13 \text{ kOe}$.⁴

4.2.1 Vacuum setup

The tested sample and the acoustic transducer are situated inside a vacuum chamber, which operates at medium vacuum with a pressure of approximately $p = 0.3 \text{ mbar}$. The conduction of experiments under vacuum conditions has several advantages over measurements at ambient conditions. The most important advantage is to prevent water from condensing and, in case of negative Celsius temperatures, from freezing on the sample, which causes a large amount of noise. Another positive result of the vacuum is the acoustic decoupling of the AE setup from the laboratory environment. It is worth mentioning that in spite of the vacuum conditions convection still plays a role for the thermal properties of the setup. The central physical quantity for the estimation of pressure-dependent convection is not the number of molecules per cm^3 but their mean free path. To hinder convection, the mean free path of the molecules should be much larger than the characteristic system dimensions. In the case of the present

³The DFT is calculated by means of a fast fourier transform (FFT). For this reason, the DFT needs a fixed number of input values m , which is a power of 2 with an integer as the exponent n : $m = 2^n$. If the number of hit values k is smaller than m , the empty entries are filled with the value 0. Otherwise ($k > m$), the supernumerary values are not taken into account.

⁴A magnetic field of $H = 10 \text{ kOe}$ is equivalent to $B = 1 \text{ T}$ ($B = \mu_0 H$)

vacuum chamber with a diameter d_c in the order of 10 cm, the mean free path of the medium vacuum l_{mfp} of some 10 mm is not sufficiently long. To suppress convection as far as possible and to ensure $l_{mfp} \gg d_c$ high or ultra high vacuum with a mean free path of some meters to ten thousands of km is necessary. Because of a non-suppressed convection a "microclimate" establishes itself inside the vacuum chamber. This microclimate is dominated by the temperature of the heat reservoir of approximately 245 K (for a further analysis see section 5.3.1).

The heat transfer due to the released or absorbed enthalpy during the discontinuous phase transition can temporarily lead to an offset between the real and the measured sample temperature. This gives rise to a deviation from the temperature set point.

Inside the vacuum chamber a sample holder is situated on a three-stage thermopile. The thermopile heats or cools the sample against a reference temperature when a voltage is applied (figure 4.4). A thermopile is a thermoelectrical device which works with the *Peltier effect*. An applied voltage leads to a heat flow: depending on the polarity there is a negative or positive temperature difference between the top and the bottom of the element. Combined with a thermal reservoir a thermopile can thus be used for cooling or heating processes. A thermopile can work as well the other way round measuring heat flux (see section 4.2.3). The commercial temperature controller *LakeShore 340* realizes the temperature control with a PID feedback loop.⁵ The temperature input signal T_A to the feedback loop is generated by a Pt-100 temperature sensor⁶, which is embedded in the sample holder. The temperature controller is capable of controlling two temperature loops simultaneously - loop A for temperature T_A and loop B for an additional temperature T_B . For an easy to handle temperature-time-profile programming a custom-made control program is developed on the basis of *Lab View*. This program allows to schedule a user-defined temperature profile consisting of plateaus and ramps. Because of a quite different control responses between ramps and plateaus,⁷ two sets of PID values can be defined for ten different temperature

⁵A proportional-integral-derivative controller (PID controller) is a generic control loop feedback mechanism widely used in research and industrial control systems. A PID controller tries to correct the difference between a measured process variable and a requested set point by calculating and then outputting a corrective action that can adjust the process according to the equation: $U_{out} = P(T_s(t)) - T_A(t) + I \int (T_s(t) - T_A(t)) dt + D \frac{d(T_s(t) - T_A(t))}{dt}$, with U_{out} the output voltage, T_s the temperature set point and T_A the temperature of the sample holder.

⁶A Pt-100 is a platin temperature sensor with an electrical resistance of 100 Ω at $T = 273.15$ K. In general Pt-100 temperature sensors have their operating temperature in the range where a linear relation between the temperature and the resistance holds: $\rho(T) = \rho(T_0) \cdot (1 + \alpha \cdot (T - T_0))$, with α being a material specific temperature coefficient and T_0 an arbitrary temperature with a known resistance $\rho(T_0)$.

⁷A quickly changing process variable can be controlled better by relatively large D values, whereas a large P value supports a constant set point.

zones. For a realtime check of the temperature stability during the measurements several histograms are plotted in real time.

The thermopile is placed upon a heat reservoir. An oil, which is temperature-controlled by a liquid circulator from the manufacturer *Julabo*, streams through the heat reservoir. A vacuum- and low temperature resistant thermal conductivity grease⁸ is applied in order to minimize thermal resistivity at various interfaces: sample/sample holder, sample holder /embedded temperature sensor, sample holder/thermopile, and thermopile/heat reservoir. In combination with a custom-made low-noise high-power linear amplifier ($U_{max\pm} = 15\text{ V}$ and $I_{max} = 10\text{ A}$), a temperature range of 200 K to 340 K is accessible, with rates spanning over two decades from 0.1 K/min to 10 K/min. Owing to a very precise gain, a very good temperature stability of $\pm 3\text{ mK}$ over several days can be achieved. To guarantee an optimal acoustic contact between the sample and the transducer an acoustical coupling⁹ is applied. The transducer is pressed on top of the sample by an applied force via a disc made out of PVC or plexiglass. This sandwich construction permits the application of a well defined pressure and gives stability to the fragile system.

Because of five vacuum windows located in the upper part of the vacuum chamber, the experiments can be controlled visually during their execution. For upcoming experiments the construction of the chamber allows for an in-situ combination of AE measurements and optical measurements using a laser reflection (e. g. [90]), x-rays (e. g. [112]), or resistivity measurements (e. g. [74]).

The vacuum chamber contains several lead-throughs for voltage signals, Peltier element currents, cooling liquid, and air (figure 4.5). To uncouple the experimental setup acoustically and electrically from the laboratory environment, the vacuum chamber itself and the table which holds the setup are placed on rubber mats. All leads are shielded and two 50 kHz low pass filters are connected in series with the power supplies and the thermopile in order to suppress the coupling of electrical noise emitted by the power supplies at some 100 kHz. As a result of all filters and insulations the noise level is reduced to a minimum of 22 dB, which is, according to the manufacturer, close to the inherent noise level of the transducers. In section 5.2 the temperature calibration of the setup is described and in section 5.3.1 and 5.3.2 a static and a dynamic simulation of the temperature behavior can be found.

4.2.2 Magnetic field setup

A temperature-controlled sample holder and an electromagnet are the core of the field setup. The sample holder is a copper tube which is cooled by a cycling liquid. The temperature of the liquid is controlled by a *Lauda proline cooling system*,

⁸ 70-AM heat conductivity grease from *GLT* with a specific thermal conductivity of 0.7 W/mK .

⁹ *High vacuum grease* from *Dow Corning* with a specific thermal conductivity of 0.2 W/mK .

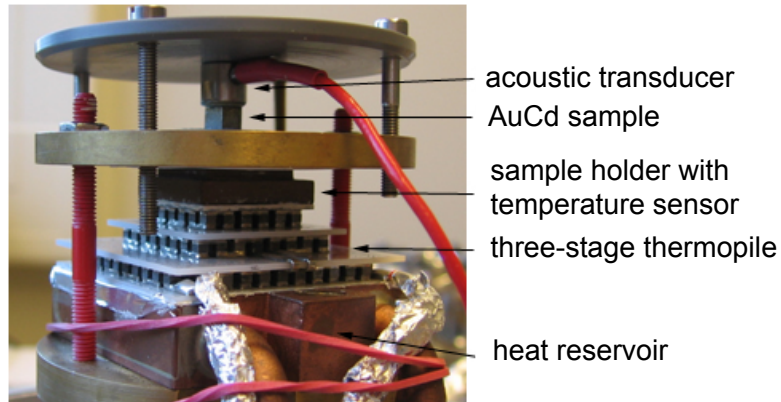


Figure 4.4: Interior view of the vacuum chamber. The compound of the heat reservoir, the thermopile, and the sample holder with an embedded temperature sensor are mounted on an isolated column (adapted from [172]).

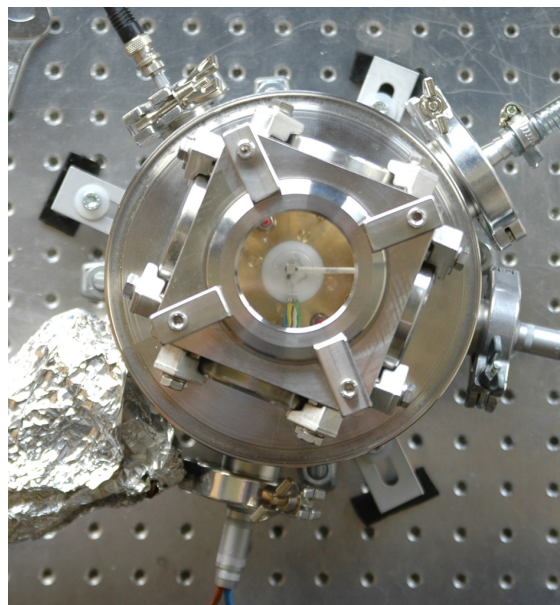


Figure 4.5: Top view of the vacuum chamber and its lead-throughs. Starting at the bottom, the following lead-throughs can be seen in a clockwise order: power supply for the thermopile, tubes for the cooling liquid, measuring leads for the AE signals, vacuum tube, and measuring leads for the temperature sensor [172]).

which works with an integrated PID controller (see footnote 5). A temperature-time-profile can be programmed consisting of temperature plateaus and ramps in the temperature range of 195 K to 300 K. Due to the large thermal mass of the circulating liquid only low rates of a few K/min are accessible. The sample temperature is measured by a Pt-100 temperature sensor (see footnote 6), which is embedded in the copper sample holder. To guarantee a good thermal contact between the sample and the sample holder, a thermal conductivity grease is used.

An AE transducer is placed on top of the sample. A good acoustical impedance matching is achieved by the application of a gel. The sample is situated on top of the sample holder between the poles of an electromagnet. The gap d_p of the poles can be varied between a few and several ten millimeters. In the presented experiments two different pole distances d_p are used ($d_p = 28$ mm and $d_p = 34$ mm). With a gap of 28 mm (34 mm), a maximal magnetic field of 13 kOe (10 kOe) can be applied. The magnetic field can be applied in one direction only; a switching of the field direction is not possible. The magnetic field H is measured by means of a Hall probe, which is situated between the coils and next to the sample. The applied field strength is converted into a voltage signal and recorded by the pci-2 data acquisition card. A current I with $I_{max} = 66$ A feeds the electromagnet. Because of a power of several hundred watts, the electromagnet is water cooled to prevent a heating-up of the coils. Despite proper cooling, a warming of the coils is noticeable at constant operation with high fields. To avoid heat transfer from the poles to the sample holder and subsequently to the sample, the whole sample holder is insulated with thermally insulating foam material. Only a small hole is left open for the placement of the sample (figure 4.6).

Magnetic-field-dependent measurements are conducted with Ni_2MnGa , which is ferromagnetic below the Curie temperature of $T_c = 359.5$ K. A magnetic dipole responds to a homogenous field with a torque. In an inhomogeneous field there is also a net force on the dipole. The field of real magnets is always a superposition of an inhomogeneous and a homogeneous part, which makes a proper mounting necessary. The sample is fixed by a robust polystyrene frame to prevent any translation or rotation. The frame is placed between the magnet coils and additionally locked by an elastic tape. In some experiments the sample is additionally fixed by a weight, which applies a small pressure on top of the sample. This pressure adds up to the pressure of the tape, the corresponding force is oriented perpendicular to the applied field. The force of the elastic tape is approximately 5 N and that of the weight approximately 10 N. Both values sum up to a pressure of approximately 0.15 MPa, which is enough to guarantee a stable sample position but still has no detrimental effect on the martensitic transition.

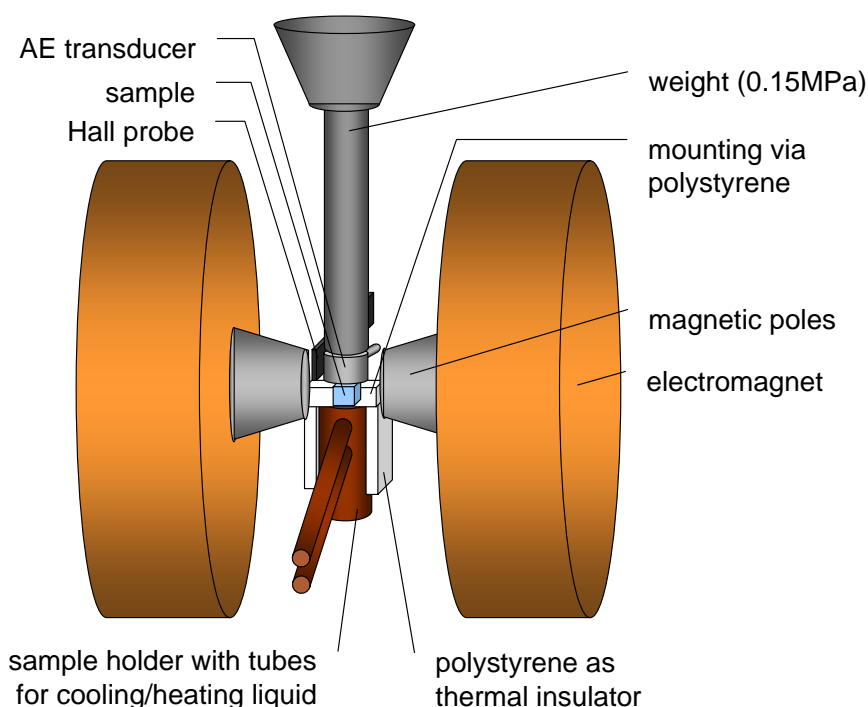


Figure 4.6: Schematic representation of the acoustic emission setup consisting of a temperature-controlled sample holder and an electromagnet.

4.2.3 Differential scanning calorimeter

For reference measurements a differential scanning calorimeter (DSC) is available at the University of Barcelona. It is a custom-made copper setup working with two calibrated thermopiles (figure 4.7). The calorimeter has the shape of a cylinder with a diameter of 4.8 cm and a height of 6.7 cm. Inside the copper housing two thermopiles are located, which hold the sample to be analyzed and a reference sample. A copper block of the same mass and of similar size as the sample serves as reference sample. The measurement of two samples, one with a discontinuous phase transition and the reference sample without, permits the subtraction of the normal thermal flux due to the specific heat and permits the determination of the latent heat associated with the phase transition. Both samples are fixed by a copper disk. In contrast to standard commercial systems, the calorimeter allows measurements with large samples of several mm edge length and a weight of some ten grams. Owing to the large possible sample volumes and high precision thermopiles, the calorimeter is able to detect very small latent heats.

The calorimeter has a large heat capacity to guarantee a homogenous temperature and a smooth temperature change. For temperature changes the copper

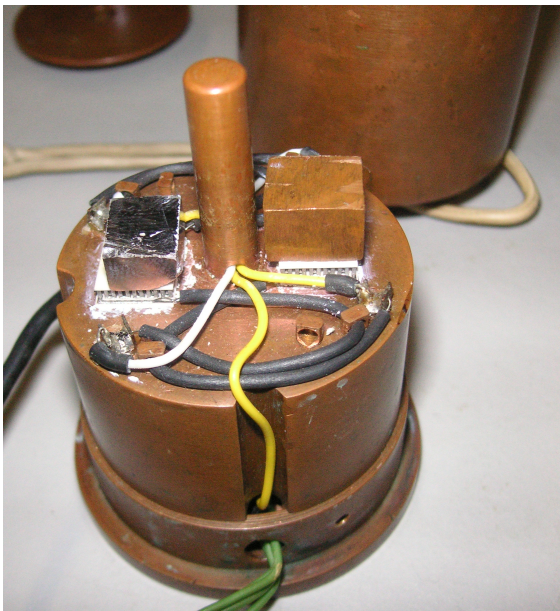


Figure 4.7: The figure shows a photograph of the disassembled custom-made differential scanning calorimeter. On the left thermopile the $\text{Ni}_{52}\text{Mn}_{23}\text{Ga}_{25}$ sample (analyzed in this work) is placed, and on the other thermopile is situated a copper reference sample. In the background can be seen the copper housing of the apparatus on the right and the disk for sample fixing on the left.

cylinder, which has no integrated heating or cooling system, is placed into a prepared dewar. For cooling purposes, the bottom of the dewar is filled with liquid nitrogen and the setup is cooled in its gas atmosphere. For heating purposes, a thermal resistor inside the dewar heats the air. A temperature interval from 100 K to 350 K with rates of some K/min is thus reachable.

5 Tests, calibrations, and simulations

To ensure high quality measurements the AE system and especially the transducers, which are exposed to large changes in temperature and pressure, should be tested in planned intervals. A quick evaluation procedure is the so-called *lead breaking test* (section 5.1).

For measurements with temperature as the control variable a very accurate temperature control is vital for experimental success. A calibration of the sample temperature is necessary to correct the temperature offset between the measured sample holder temperature T_A and the real sample temperature T_B . The calibration measurements, which are executed with the vacuum setup, show a linear dependence between both temperatures (section 5.2).

For a better understanding of the quite complex temperature distribution and the resulting heat flux between the setup components inside the vacuum chamber two kinds of simulations are performed. One simulation is performed for equilibrium conditions (section 5.3.1) and the other one for different cooling and heating rates (section 5.3.2).

5.1 Test of the acoustic emission system

A quick and easy to handle performance test of the AE-system can be done with the lead breaking test [44]. In this test procedure a lead is broken on a metal block under well defined conditions and the acoustic emission thus generated is measured. A breaking lead is used because of its broad and flat frequency spectrum. To guarantee well defined testing conditions the following procedure should be followed. The acoustic transducer is acoustically coupled to a metal block with a grease (see footnote 9) and fixed with a rubber strap. Eight points separated by an angle of 45° are marked on a circle with the transducer at its center. The radius of the circle depends on the transducer size; there should be a distance of 2.2 cm to the housing of the transducer. The points mark the positions where the lead fractures occur (figure 5.1).

Following the *DGfzP* standards (German society for non-destructive testing), the lead with a hardness of 2H protrudes 3 mm from the pencil case. The breaking angle to the metal block surface is 45° . The breaking proceeds in

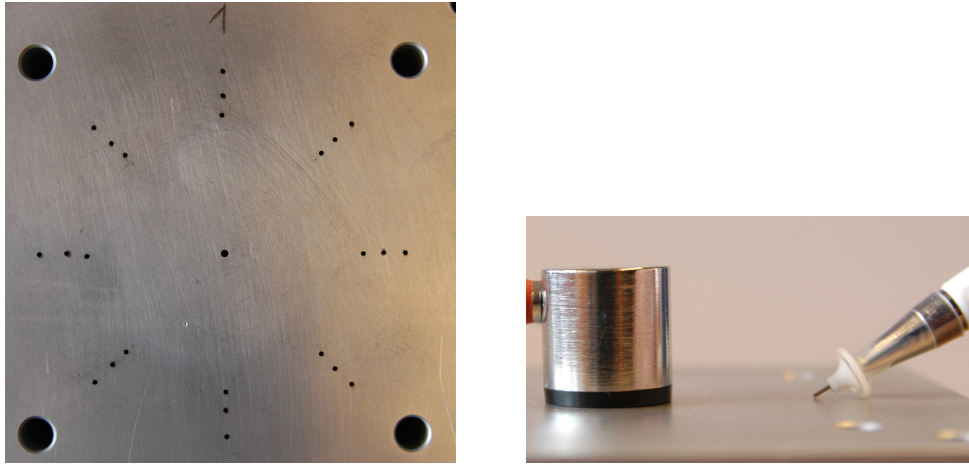


Figure 5.1: Photograph of an aluminium test block prepared for the transducer performance test (left). The concentrically arranged points mark the breaking points. Due to different transducer diameters, circles of three radii are drawn. On the right hand side is shown a customized mechanical pencil from the manufacturer *Physical Acoustics*, which enables a constant breaking angle of 45° (right) [172].

a defined direction, so that the pencil and the center of the circle are in-line. With a preamplification of 40 dB five out of eight lead breaks should generate hits with amplitudes larger than 90 dB. If the test fails, a malfunction must be concluded. Unfortunately, the conclusion cannot be reached the other way round: A passed test can testify the quality of the transducer, but not necessarily guarantee the correct operation of the preamplifier. If the test is passed, but the experiments reveal nevertheless abnormal results, the preamplifier should be inspected separately.

Besides the pure quality test, the lead breaking test can reveal useful characteristics of the transducer under investigation. The recorded amplitude and peak frequency distribution provide a fingerprint of the characteristics of the transducer with respect to sensitivity and resonance frequencies.

5.2 Temperature calibration

An accurate measurement of the sample temperature would need an embedded temperature sensor inside the sample. To avoid drilling a hole into the sample, the temperature is not measured in the sample but in the sample holder. Because of measurements with a varying temperature, the system, which has a limited thermal conductivity λ and a finite thermal mass, is not in thermodynamic equilibrium. As a result, there is a temperature offset between the real sample

temperature T_B and the measured sample holder temperature T_A . The estimation of the real sample temperature T_B derived from the measured sample holder temperature is the objective of the temperature calibration.

The temperature offset between sample holder temperature T_A and the sample temperature T_B leads to a heat transfer flux \dot{q} which is described by *Fourier's law*

$$\dot{q} = -\lambda \nabla T, \quad (5.1)$$

where λ is the characteristic thermal conductivity and ∇T is the temperature gradient in the corresponding volume.

Understanding the reasons for the temperature offset between T_A and T_B , two cases have to be distinguished. In the stationary case with a constant sample holder temperature T_A , the heat exchange rate \dot{q} of the sample with its surroundings is a function of the non-covered surfaces of the sample and the transducer. The surfaces of both components are thermally coupled to the (reduced) atmosphere and they emit and absorb heat radiation (for a further analysis see section 5.3.1, where the equilibrium (static) temperature distribution is simulated).

In the dynamic case with a changing T_A temperature, the thermal capacities and conductances should be additionally taken into account (for a further analysis see section 5.3.2, which describes a dynamic temperature and heat flux simulation of the relevant components).

5.2.1 Setup and measurement procedure

For the calibration of the sample temperature a dummy sample is constructed, which displays similar features as the original sample and has an embedded temperature sensor (figure 5.2). The outer dimensions of each dummy sample are the same as the original one. The material of the dummy sample should have a comparable heat capacity c_p as the original sample c^* . In contrast to the specific heat capacity of Ni-Al [109], the specific heat capacity of Au-Cd is not reported in literature. However, it can be assessed by Dulong–Petit's law ($c = 3R \approx 3 \cdot 8.3 \text{ J}/(\text{mol} \cdot \text{K})$), due to the fact that its Debye temperature of approximately 200 K [17] is far below the temperature interval of the measurements (see table 6.1). An overview of all heat capacities can be found in table 5.1.

Dummies are only built for $\text{Ni}_{63}\text{Al}_{37}$, and $\text{Au}_{50.5}\text{Cd}_{49.5}$. Both $\text{Fe}_{68.8}\text{Pd}_{31.2}$ samples (single crystal and polycrystal) are of the same size as the temperature sensor itself. In these two cases the calibration is performed only with the Pt-100 sensor, which displays the most important features of a dummy, such as a small heat capacity and two flat surfaces at the bottom and at the top for a thermal coupling to the sample respectively to the transducer. For calibrating the $\text{Au}_{50.5}\text{Cd}_{49.5}$ sample an Al dummy and for $\text{Ni}_{63}\text{Al}_{37}$ a Cu dummy has been used (see table 5.1).

For the calibration measurements a sensor is embedded in the center of the dummy. The dummy itself is placed on the sample holder and the transducer is

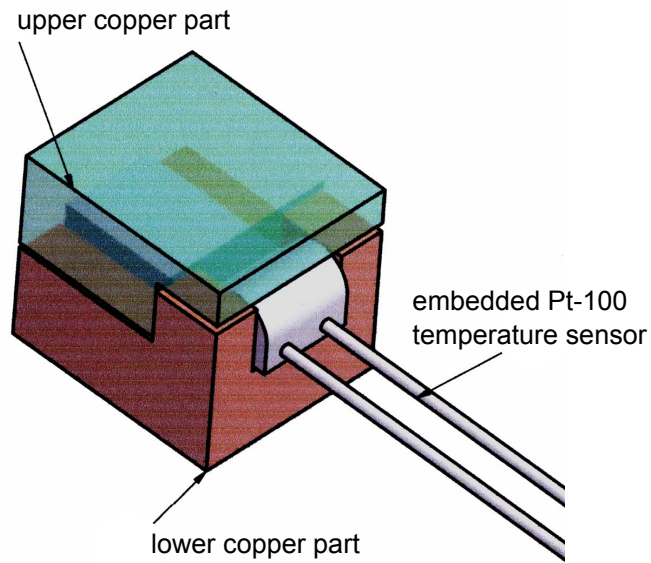


Figure 5.2: Three-dimensional *computer-aided design* (CAD) model of the $\text{Au}_{50.5}\text{Cd}_{49.5}$ dummy sample, consisting of two copper parts and a temperature sensor. The upper and the lower part, which perfectly match, have a gap for the Pt-100 sensor. With the temperature data from the embedded sensor the real sample temperature can be calculated (c.f. equation 5.2).

Table 5.1: Overview of the specific heat capacities of the alloys, of the dummy samples, and for comparison, of the elements. The specific heat capacity of $\text{Au}_{50.5}\text{Cd}_{49.5}$ is assessed by Dulong–Petit’s law. In order to facilitate an application to a sample of a given size the heat capacities are expressed in $\text{J}/(\text{cm}^3\text{K})$. This allows an easy calculation of the heat capacities per sample J/K .

element	$c_p \left[\frac{\text{J}}{\text{cm}^3\text{K}} \right]$	sample	$c^* \left[\frac{\text{J}}{\text{cm}^3\text{K}} \right]$	dummy	$c_p \left[\frac{\text{J}}{\text{cm}^3\text{K}} \right]$
Cu	3.456 [55]	$\text{Ni}_{0.63}\text{Al}_{0.37}$	3.6 [109]	Cu	3.456 [55]
Au	2.434 [177]	$\text{Au}_{0.505}\text{Cd}_{0.495}$	2.15	Al	2.430 [55]
Ni	3.81 [193]				
Cd	2.127 [193]				
Al	2.430 [55]				

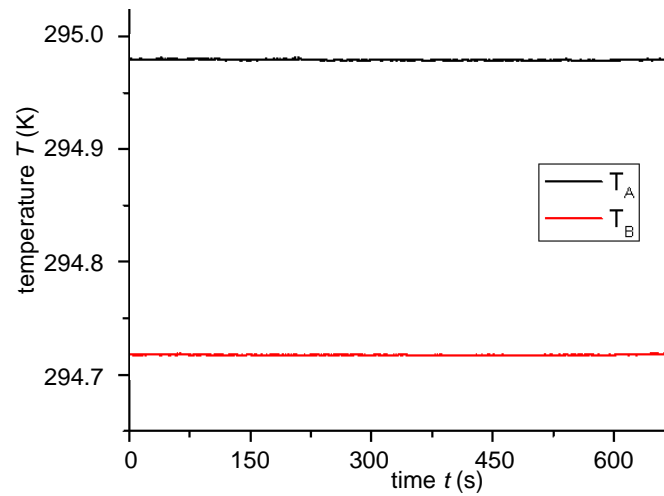


Figure 5.3: The plot shows temperature T_A , which is measured inside the sample holder, and temperature T_B , which is measured on top of the sample holder. Both temperatures are measured at equilibrium conditions with a homogenous temperature in order to estimate the constant offset between both sensors.

placed on its top. The whole design is analog to the regular measurements. For a good thermal respectively acoustic coupling the corresponding grease is applied to both interfaces. The typical measurement temperature cycles are performed with all dummy samples at all rates between 0.1 K/min and 10 K/min that have been used during the real measurements. Both temperatures of the sample holder T_A and of the dummy sample T_B are recorded for the analysis.

The calibration of the sample temperature itself requires calibrated temperature sensors. It is known from the tolerance class of the sensors that the only relevant variation of the temperature is a static offset. For the adjustment of this offset the dummy sensor is thermally coupled with the surface of the sample holder next to the embedded sensor. The whole system remains at a constant temperature. After a while the system is thermally equilibrated and the relevant part of the setup has a homogeneous temperature. The static offset, which is the difference between both recorded equilibrium temperatures, can be seen in figure 5.3. For all following calibrations the offset has been corrected.

5.2.2 Analysis and results

Over a wide temperature range the temperature of the dummy sample T_B shows a linear dependence on the temperature of the sample holder T_A (figure 5.4)

$$T_B = A \cdot T_A + B. \quad (5.2)$$

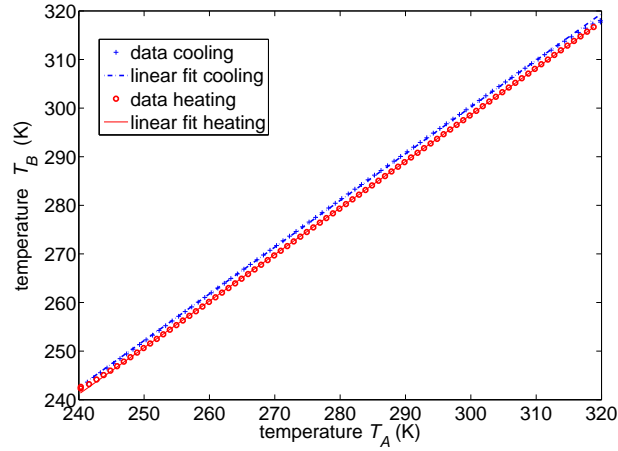


Figure 5.4: The temperature of the dummy sample T_B and the temperature of the sample holder T_A show a linear dependence. The represented data belong to the $\text{Ni}_{63}\text{Al}_{37}$ calibration, which spreads over a wide temperature range because of the relatively broad transition. For clarity reasons, only every sixth point is plotted (adapted from [172]).

At the end points of the temperature interval, where the rate changes sign, the linear relation does not hold. This limitation is not relevant because all measured phase transitions occur within the linear range. For the estimation of A and B two cycles (cooling and heating) of each used rate (0.1 K/min, 0.5 K/min, 1 K/min, 2 K/min, 3 K/min, 4 K/min, 5 K/min, and 10 K/min) are measured within the relevant temperature interval. To secure equilibrium conditions, the second cycle is used.

For the analysis T_A is plotted against T_B and a linear regression is performed using $T_B = A \cdot T_A + B$ (figure 5.4). Exemplarily the calibration results for the $\text{Au}_{50.5}\text{Cd}_{49.5}$ sample are shown in figure 5.5. It is worth noting that apart from the linear dependence between T_A and T_B the coefficients A and B themselves show a linear dependence on the rate.¹

With the coefficients A and B the corrected sample temperature has been calculated using the linear dependence from equation 5.2. All presented measurement results use the calibrated sample temperature which will be called temperature T or sample temperature T . The numerical values of the temperature calibration can be found in the appendix (section A.1).

¹A linear dependence between the coefficients A and B is not found in every calibration.

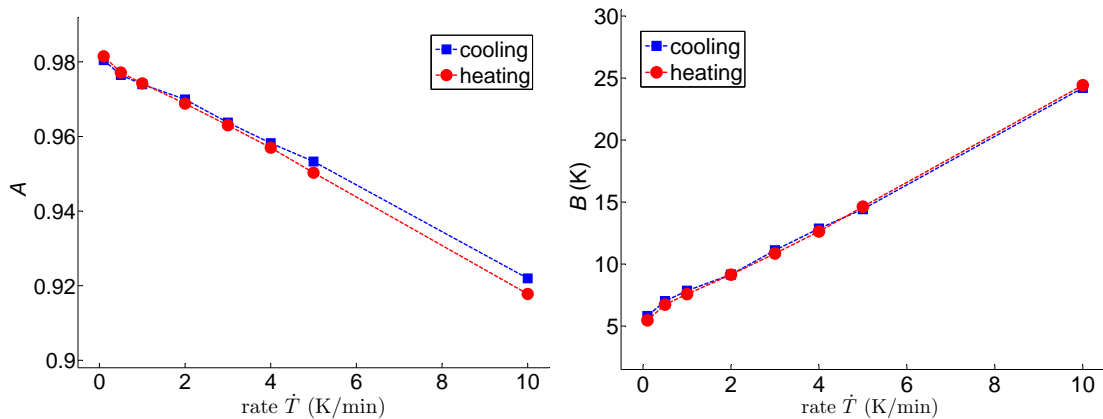


Figure 5.5: Exemplary results of the temperature calibration with the AuCd dummy sample using the relation $T_B = A \cdot T_A + B$, where T_A is the temperature of the sample holder and T_B the temperature inside the dummy sample. Results are depicted as a function of the rate for both cooling and heating.

5.3 Temperature simulation and evaluation

In order to obtain a better understanding of the static and dynamic (rate-dependent) temperature behavior of the sample, the sample holder and its surrounding components, two types of simulations are performed [86]. The *finite element method* (FEM)² provides a spatially resolved temperature distribution of all components inside the vacuum chamber in the thermal equilibrium limit. Using the results from the FEM computation a temperature rate-dependent, dynamic simulation is performed which analyzes the heat flux between the sample and its environment and calculates the temperature of all involved components. A qualitative and quantitative comparison between the performed temperature calibration and the simulated temperature behavior is given in section 5.3.2.

5.3.1 Static simulation

The aim of the FEM analysis is to provide insights into the temperate distribution of the sample and its environment as well as to identify the areas of the largest temperature gradients. To obtain input data for the simulation, the temperature of all critical components is measured, i. e. the temperature of the sample holder, the teflon (PTFE) and brass compound disk, the thermal reservoir, and the housing of

² The *finite element method* (FEM) is a numerical technique for finding approximate solutions of integral equations as well as of partial differential equations. It is a modern simulation technique which requires much computing power and is widely used in engineering and science.

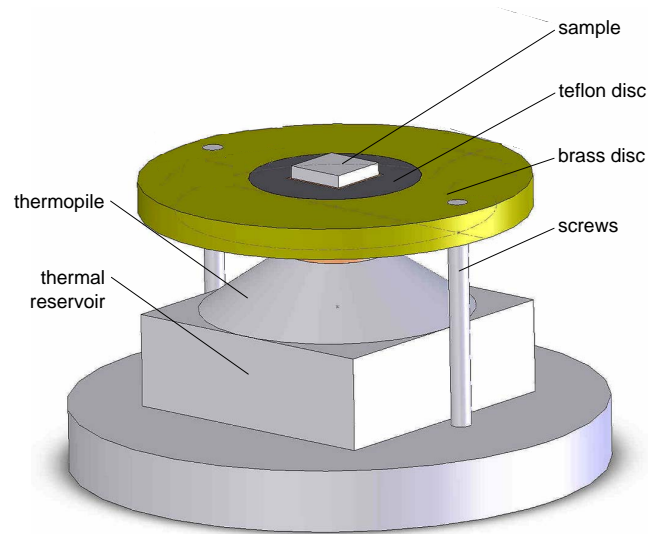


Figure 5.6: Three-dimensional model of the inner components of the vacuum chamber.

the chamber. For a later comparison with simulation results, the temperatures of the points of interest are measured at different sample holder temperatures, which is the only component in the chamber connected to an active temperature control. The temperatures are measured several times in order to receive reliable mean temperature data.

The preparation of the simulation process continues with the development of a three-dimensional model of the vacuum chamber and its components (the inner components are shown in figure 5.6). In order to keep the model manageable some simplifications are introduced. The upper square part of the chamber (figure 4.5) and some inner components are modeled with a rotational symmetry instead of their square shape.³ For all components the thermal mass and the thermal conductivity (which are known from literature) are applied to the system. As a consequence of this simplification the material constants of the corresponding parts are averaged. I. e., instead of computing the thermal influence of every single window and its surrounding steel housing, the thermal mass and conductivity of glass (for the windows) and steel (for the body) are proportionally averaged and used in the simulation as values for a quasi-homogenous fictitious material. In the following step a grid is adjusted to the geometry of the chamber model where critical areas are represented with higher node densities than other areas (figure 5.7). The highest node density is located where the highest gradients are expected, here at the interface between two objects, e. g. at the interface between sample

³Rotational symmetries in areas of less importance leave out large temperature gradients that occur at square architectures and need a lot of computing power.

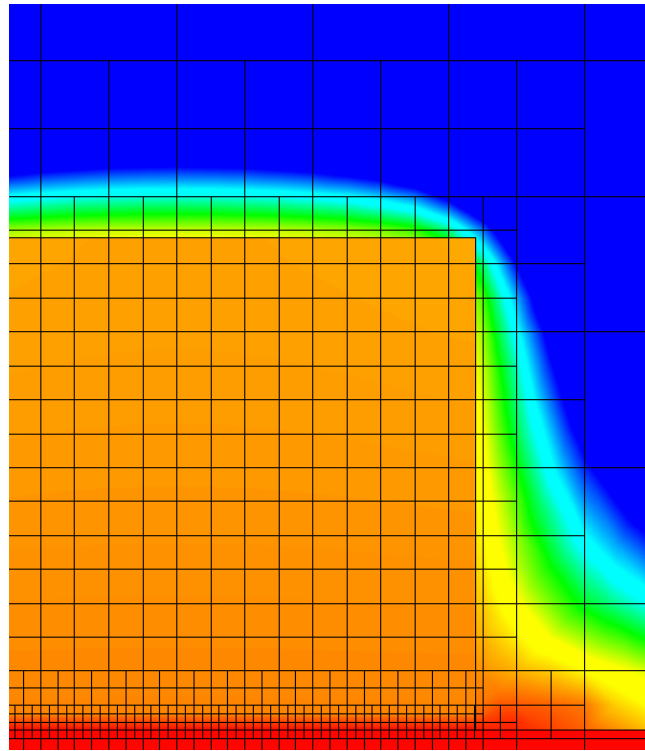


Figure 5.7: Exemplary part of the grid for the FEM simulation at the sample/sample holder interface. Note the different node densities with a maximum at the interface between the sample and the sample holder where the highest temperature gradients are expected.

and sample holder. The next input is the thermal resistance at the interfaces of the components which is estimated after a literature research. The last step of preparing the analysis is the introduction of the measured temperature data into the system and the test of its basic functionalities. For this reason, the system is fed with all but one temperature input data. The missing input temperature (which is already known from the measurement) is computed and the outcome is compared with the experimental data. In case of a mismatch the estimated system parameters are adjusted. The thermal resistance at the interfaces is most critical because it is the main reason for temperature gradients. It can only be estimated from literature. The iteration process stops when the described testing delivers acceptable results for all areas. Figure 5.8 shows the results of the simulation for two selected sample holder temperatures.

One surprising result is the microclimate that develops (in spite of the medium vacuum) around the sample. The microclimate of the sample environment, which

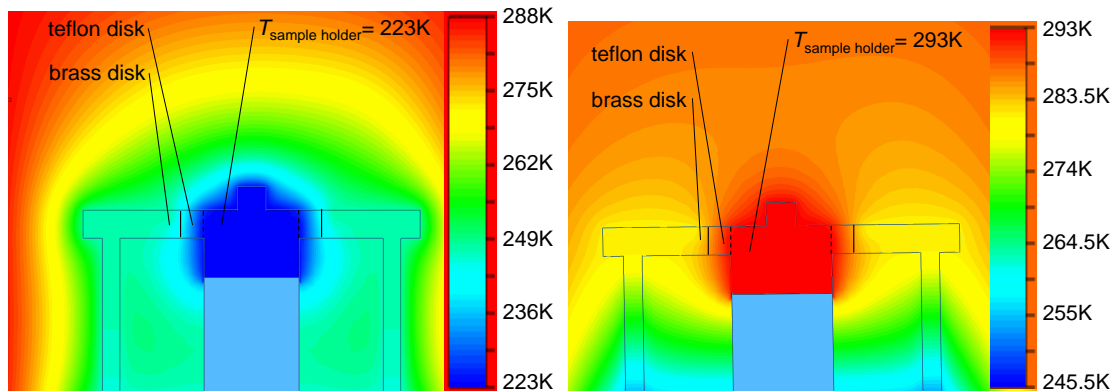


Figure 5.8: Results of an FEM temperature simulation of the sample environment. The figures show the temperature distribution at different sample holder temperatures T_A . At $T_A = 223\text{K}$ a small temperature gradient between the sample holder and the reservoir can be seen (left). As the sample is the coolest point in the chamber, a positive heat flux into the sample occurs. At $T_A = 293\text{K}$ the sample holder is the hottest point in the chamber, resulting in a large temperature difference to the thermal reservoir (right). A different microclimate develops, showing large gradients. The thermal bypass of the screws and the thermal mass of the sandwich brass plate can be identified by the deformed microclimate.

can be clearly seen in figure 5.8, is an interplay between the variable temperature of the sample holder and the fixed temperatures of the temperature reservoir and the chamber. If there is a difference between these temperatures the microclimate works as a thermal bypass. Another result of the FEM simulation can be found in figure 5.9, which depicts the interface between sample and sample holder, where the largest temperature gradient occurs. Good thermal conductors, like the metal components, have a rather homogenous temperature. In a composite system the temperature changes appear at the interfaces, because their thermal resistivities are at least a factor 500 larger (see section 5.3.2).

Besides the better understanding of the dominant components of the setup the findings lead to some hardware changes. To reduce the negative influence of the thermal bypass the material of the screws connecting the reservoir with the brass disk are changed from metal to PVC. For a better thermal coupling between the sample and the sample holder the surface of the sample holder has been lapped⁴. Furthermore, a high quality thermal grease, which can be constantly used under vacuum conditions over a large temperature interval, has been applied (see footnote 8).

⁴Lapping is a polishing technique which reaches optical flatness

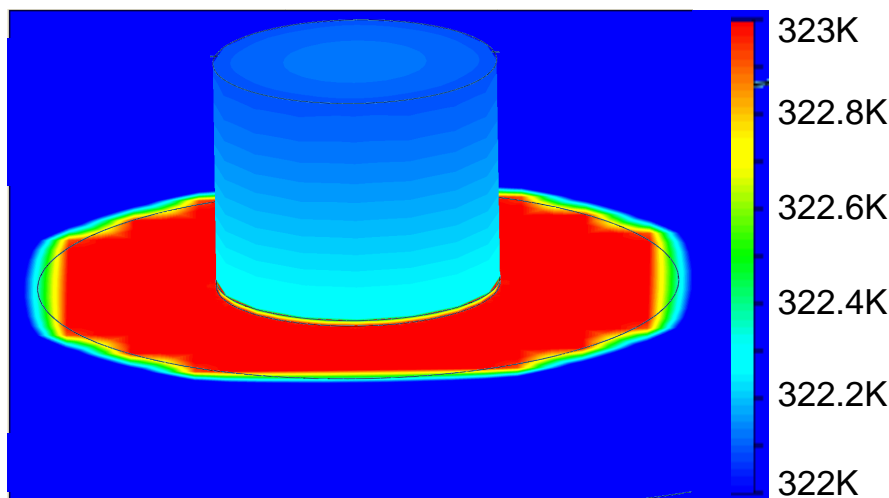


Figure 5.9: Temperature distribution calculated by an FEM simulation. The (almost) unicolored areas of the sample holder, the surrounding tefflon disk, and the sample show that the temperature gradients appear at the interfaces. This behavior is reflected by the abrupt temperature changes between the components.

5.3.2 Dynamic simulation

After the evaluation of the FEM simulation, which is performed for static conditions with constant temperatures, a dynamic model based on the static results is developed. The model uses the analogy between thermal and electrical circuits and consists of thermal capacities representing thermal masses of the relevant components and thermal resistances (figure 5.10). The aim of the model is to check if our understanding of the thermal characteristics and the involved quantities of the sample surroundings is correct. Furthermore, the simulation provides information about the network, e. g. the temperature of all components and the heat flux which cannot be derived easily by measurements. Additionally it provides the possibility, supposing that the network reveals useful results for the existing setup, to simulate new designs before constructing them, e. g. the influence of a new sample holder, a different transducer, or a better vacuum.

Because of the close physical and mathematical relation between an electrical circuit and its thermal analogon, the thermal model was built on an electronic workbench named *LTSpice*. The model consists of a network of wires, capacities, and resistors. The calculation basically works with exponential charge- and discharge-functions resulting in a system of coupled differential equations. Table 5.2 gives an overview of the electrical and thermal quantities that are used analogously. The components of the model are: sample, sample holder, AE transducer, thermal reservoir, screws (part of the sandwich construction see figure

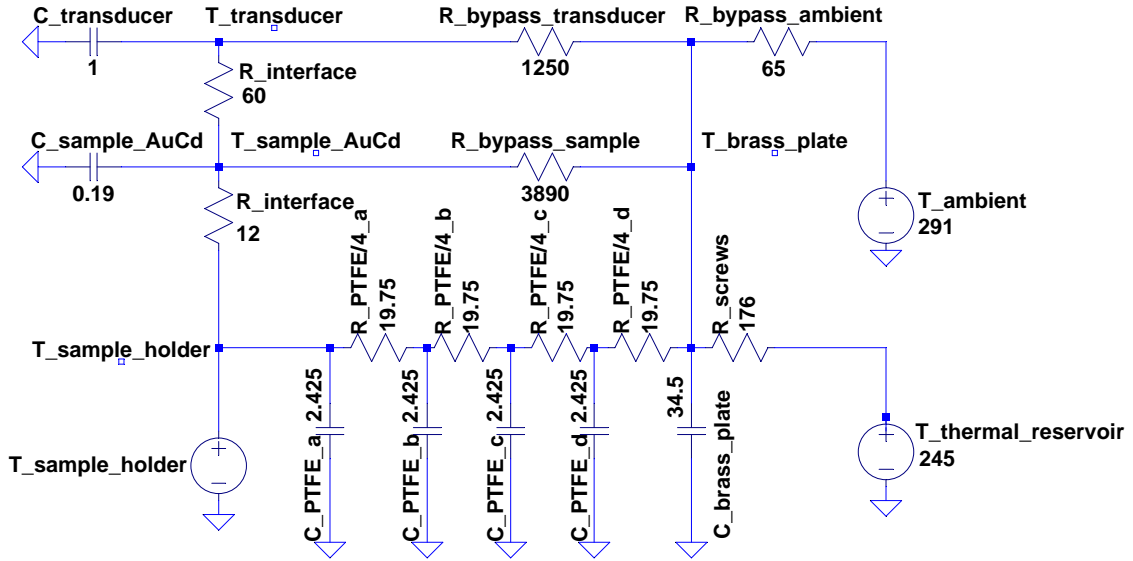


Figure 5.10: Thermal network representing the components of the AE setup, including thermal masses and resistivities of the components sample, sample holder, AE transducer, thermal reservoir, screws, brass-teflon disk, and the chamber. All components named with a leading C are thermal capacities. Their numerical values have the unit J/K . Thermal resistances are named with a leading R and are measured in K/W . The temperatures of the components are located at the intersection points, named with a leading T and are given in Kelvin.

Table 5.2: Analogous electrical and thermal quantities used in the dynamic simulation.

quantity	electrical	thermal
driving force	voltage U (V)	temp. difference ΔT (K)
flux	current I (A)	thermal flux \dot{Q} ($W = J/s$)
resistance	resistance $R = U/I$ ($\Omega = V/A$)	resistance $R_{th} = \Delta T/\dot{Q}$ ($K/W = K \cdot s/J$) ^a
capacity	capacity $C = Q/U$ (As/V)	thermal mass $C_{th} = Q/T$ (J/K)
RC-time constant	$RC = \tau$ (V/A \cdot As/V = s)	$R_{th}C_{th} = \tau_{th}$ (Ks/J \cdot J/K = s)

^aspecific thermal resistance $R_{spec\ th} = m \cdot K/W$.

5.8), brass-teflon disk, and the chamber. Every mentioned part is represented by a thermal capacity and each qualitatively different thermal contact is taken into account by an individual thermal resistivity. In case of the sample there are implemented e. g. three resistances, representing the thermal coupling to the sample holder, to the transducer and to the microclimate. The differentiation between thermal masses and resistors is artificial. In real systems the capacity and the resistance are inherently connected. For low resistances and high capacities (which applies for all metals) this fact can be easily ignored, because the only relevant thermal resistance is located at the interface ($\rho_{interface} = 0.7 \text{ W/mK}$ at 309 K and $\rho_{metal} \geq 10^2 \text{ W/mK}$), which applies for the cases named above. For bad thermal conductors such as the teflon disk, which serves as a thermal insulator between the brass disk and the sample holder, the situation is different and both features should be integrated (see below). The following paragraph describes how input values are estimated for the thermal equivalent circuit diagram, which is depicted in figure 5.10.

The thermal resistivity of the microclimate bypass from the chamber to the sample $R_{bypass\ sample}$ is derived from the FEM simulation. The ratio of the thermal resistivity to the transducer bypass $R_{bypass\ sample}$ is

$$\frac{R_{bypass\ sample}}{R_{bypass\ transducer}} \approx \frac{1}{3}. \quad (5.3)$$

This ratio mirrors the ratio of the "non-covered" surfaces of sample and transducer which is

$$\frac{A_{sample}}{A_{transducer}} = \frac{80 \text{ mm}^2}{250 \text{ mm}^2} \approx \frac{1}{3}. \quad (5.4)$$

The ratio between the coupling of the sample to the sample surface and the coupling of the transducer to the sample

$$\frac{R_{interface\ sample\ holder}}{R_{interface\ transducer}} = \frac{12 \text{ K/W}}{60 \text{ K/W}} = \frac{1}{5} \quad (5.5)$$

is derived from the ration between the thermal conductivities of the used thermal respectively acoustic grease

$$\frac{\rho_{thermal\ grease}^{-1}}{\rho_{acoustic\ grease}^{-1}} = \frac{(0.7 \text{ W/m}\cdot\text{K})^{-1}}{(0.2 \text{ W/m}\cdot\text{K})^{-1}} = \frac{1}{3.5}. \quad (5.6)$$

The difference between $1/5$ and $1/3.5$ is probably related to the excellent polish of the sample holder surface. The thermal bypass from the ambient temperature ($R_{bypass\ ambient} + R_{bypass\ sample}$ and $R_{bypass\ ambient} + R_{bypass\ transducer}$), which is 291 K, is deduced from the FEM calculation. The thermal resistance of the screws connecting the reservoir with a temperature of 245 K and the brass disk are known from literature and checked with the FEM approach.

For the teflon disk the thermal capacity and the resistivity should not be separated, because the thermal resistance of the material has the same order as the resistance of the interface. For a precise mathematical modeling both features should be integrated. As building a sum is the first approximation of an integral, the total thermal capacity and conductivity is divided into parts that are connected in series. In the model, the thermal flux first has to cross a partial resistance and to load a partial capacity and then has to cross another resistance and so on. In order to get a realistic and less complex model, the teflon disc is divided into four parts ($R_{PTFE/4a}$ until $R_{PTFE/4d}$ and $C_{PTFE/4a}$ until $C_{PTFE/4d}$). The thermal masses of the transducer and the brass disk are represented by single capacities which are found in literature. The thermal mass of the sample is derived from an estimation (see table 5.1). It is worth mentioning that all used thermal capacities and conductivities are treated as constant without any temperature-dependence. In the relevant temperature range the approximation seems to be reasonable because the corresponding changes of other metals are reported to be only a few percent.

Before running the network simulation the temperature range, rate, and profile are prompted. The dynamic simulations principally can be applied to many temperature profiles. Here temperature cycles ranging from 0.1 K/min to 10 K/min are of special interest because the presented experiments show the same profile. The temperatures of all components and all heat fluxes can be displayed against time. However, in this analysis the sample temperature (see section 5.2) and the sample holder temperature are of main interest. Representative results for Au-Cd are shown in figures 5.11, 5.12, and 5.13. A qualitative comparison between the measurement and the simulation at a rate of 10 K/min is shown in figure 5.11, where the measured temperature is represented by open circles and the simulated temperature by lines. The central features are displayed in both plots. The sample and the sample holder show a temperature-dependent offset. Both temperatures cross each other around 300 K for heating and 310 K for cooling. At the end points of the temperature interval, the temperature offsets are maximal and the sample temperature shows a small time delay of a few seconds. Besides the temperature the heat flux, which is not easily accessible in the presented setup by measurements, can be analyzed as well. Figure 5.12 shows the heat flux into the sample and the transducer against time. Both heat flux curves show clear differences. While the heat flux into the sample quickly reaches an almost constant level, the curve of the transducer has a much larger slope. This behavior is a result of the different heat capacities ($C_{transducer}^{th} = 5 \cdot C_{sample}^{th}$) and thermal conductivities (see above). The temperature increase of the sample is, because of a small thermal mass and good conductivity, almost at equilibrium condition. By contrast, the transducer falls behind the excitation and the charging function turns into a discharging function before an equilibrium condition is

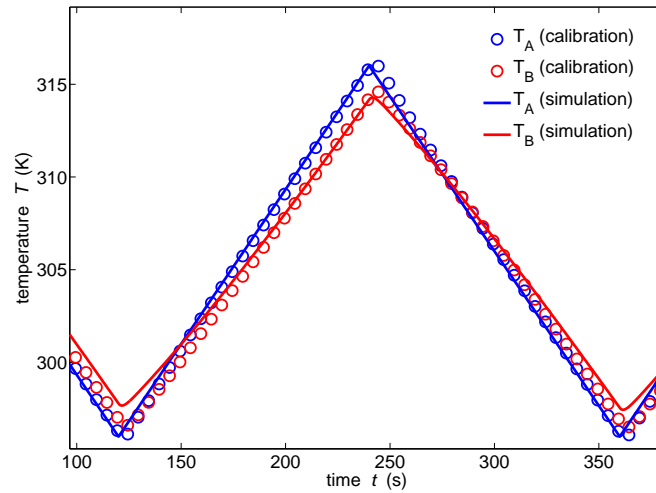


Figure 5.11: Qualitative comparison between experimental and simulated data for $\text{Au}_{50.5}\text{Cd}_{49.5}$. The experimental data are measured with the dummy Au-Cd sample (see section 5.2) For clarity reasons, only every 5th point is plotted. Both curves show similar features. A quantitative comparison can be found in figure 5.13.

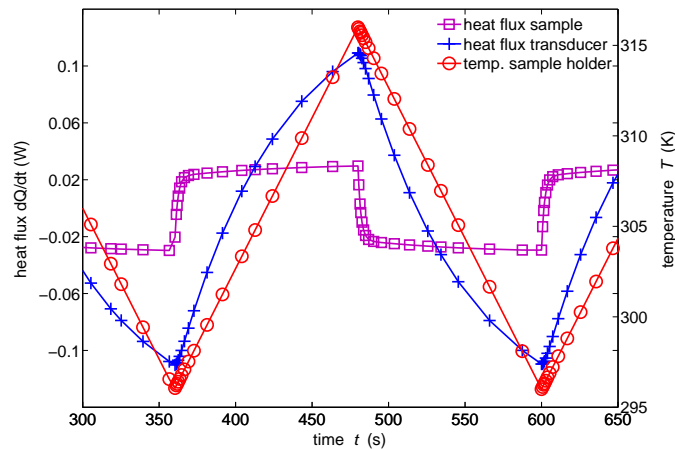


Figure 5.12: Simulated heat fluxes into the sample and the transducer and the temperature of the sample holder for $\text{Au}_{50.5}\text{Cd}_{49.5}$. The different thermal masses of the sample and the transducer result in largely varying time constants. To ensure the absence of transient effects the second cycle is depicted. For clarity reasons, only every 4th point is plotted.

reached. Comparing the time constants $\tau_{sample}^{th} \approx 2s$ and $\tau_{transducer}^{th} \approx 60s$ with the heating/cooling time of 120s for 10K/min the qualitative difference can be quantitatively confirmed.

A quantitative analysis is derived by the condensation of the temperature-dependence into the linear relation $T_B = A \cdot T_A + B$ which is already used for the temperature calibration in equation 5.2. A comparison between measurement and simulation, which are in very good agreement for both coefficients for all cooling and heating rates, can be found in figure 5.13. Based on the convincing qualitative and quantitative matching between measurement and simulation, some conclusions can be derived.

In the given configuration, the following components have the strongest influence on the behavior of the sample temperature T_B (with decreasing importance):

1. Thermal contact between the sample and the sample holder.
2. Thermal contact of the sample and the transducer.
3. Thermal mass of the transducer, which varies a lot between different transducer types (see table 4.1).
4. Thermal coupling of the sample and the transducer via the established microclimate to the thermal reservoir, the brass disk, and the screws. The importance of this thermal bypass mainly scales with the non-covered surface of the transducer, the temperature of the reservoir, and the atmosphere pressure.
5. Thermal coupling of the sample and the transducer with the housing of the chamber by the microclimate. The bypass scales with the non-covered surface of the sample and the transducer.

For a moderate change of the setup (new sample, transducer, or sample holder) the order of importance is not very likely to change. Nevertheless the relative importance of the listed influences may vary.

As a general result it can be summarized that a good thermal contact between sample holder and sample is crucial for a small temperature offset. From a thermal point of view, the transducer should be chosen as small as possible, because it is the most thermally inert component of the system. A better vacuum (high vacuum or ultrahigh vacuum) would improve the thermal control by closing the thermal bypasses and reducing the importance of uncovered surfaces (see section 4.2.1); however, its overall influence is limited. By setting the temperature of the thermal reservoir close to the operation range of the sample temperature, large temperature gradients can be avoided without changing the vacuum conditions. Sufficiently low temperature gradients lead to the absence of convection.

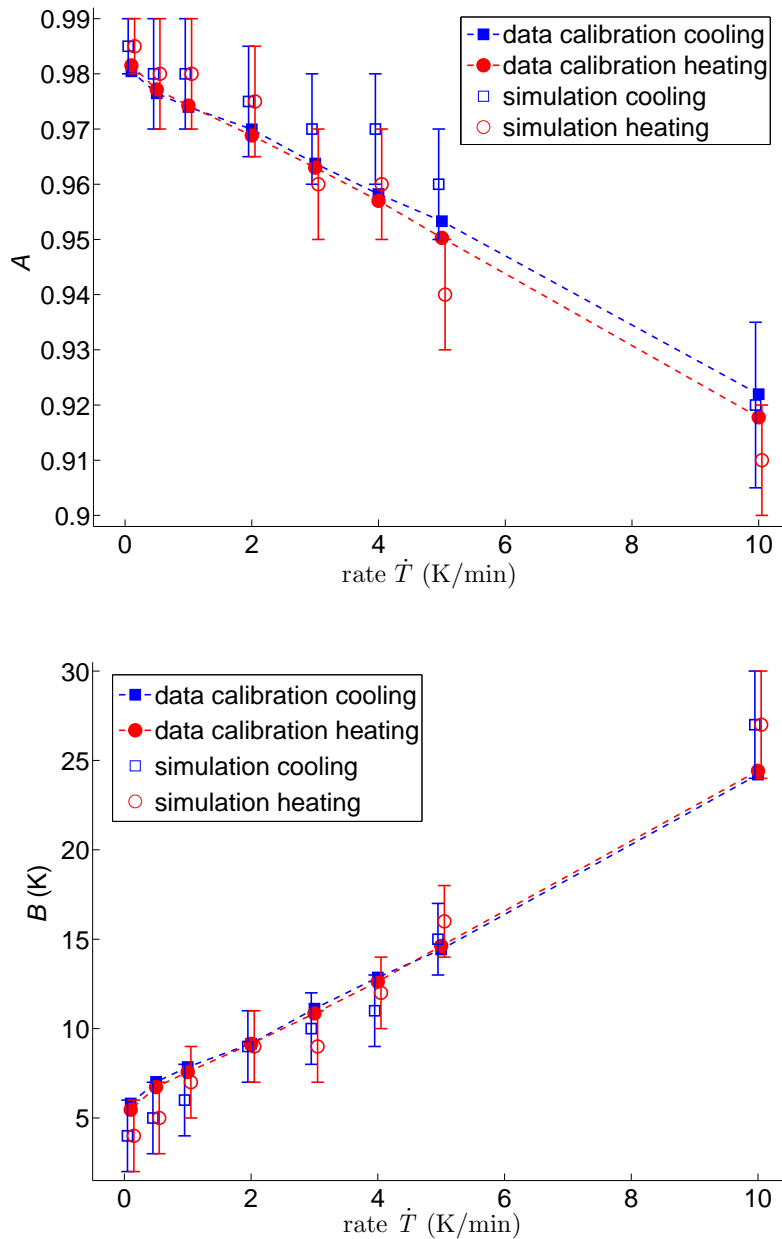


Figure 5.13: Quantitative comparison between experimental data from the temperature calibration with the AuCd dummy sample and simulated data. All rates are represented using the linear relation $T_B = A \cdot T_A + B$. A qualitative comparison can be found in figure 5.11. Despite of the large error bars, the simulation results are robust, because the errors on A and B stabilize each other. A smaller factor A leads in agreement with the error bar to a small increment of B and vice versa.

6 Measurement procedures

To prepare the measurements, the sample is placed on the sample holder and thermal grease is applied. The acoustic transducer is placed on top of the sample. In case of the vacuum setup, the sample and the sample holder are fixed by a PVC or plexiglass disk. The preparation finishes with the evacuation of the vacuum chamber. In case of field-dependent measurements the transducer is fixed by a rubber band and, in some cases additionally with a small weight, which in sum, applies a small pressure of 0.15 MPa. The Hall probe is then positioned next to the sample between the magnet coils.¹

Before starting the measurement, the acoustic emission program is prepared. The following settings need to be introduced into the AE system: gain, bandpass filter, sampling frequency, threshold, hit definition time, peak definition time, and hit lockout time. The only hardware setting to be chosen is the gain of the preamplifier, which should be identical with the software input. For the temperature control a temperature profile $T(t)$ is programmed or loaded. In case of the vacuum setup this profile can be programmed directly on the computer containing the AE data acquisition card. In case of the field setup this is done via a program panel as part of the *Lauda proline* cooling system. In both cases the temperature profile consists of ramps and plateaus. Programming a ramp the starting temperature T_{start} , the ending temperature T_{end} and the rate \dot{T} are necessary, in case of plateaus a constant temperature T_{hold} and a holding time t_{hold} are prompted. Field-dependent measurements additionally require a time-field profile, which can be introduced using the computer controlling the electromagnet. Only plateaus of different field strengths can be programmed. A ramp-like increase/decrease of the field can be simulated by introducing a large amount (approximately 600) of short plateaus with only little increment. This leads effectively to a smooth field increase/decrease at a constant rate. The order of all runs of an experiment is randomized to guarantee the absence of pseudo-dependencies.

¹For the calibration of the Hall probe approximately ten different currents are applied and their corresponding magnetic fields are measured with the Hall probe. The recorded fields, which show a linear relation, are fitted and the coefficients are determined. At a constant pole distance the magnetic field is known and listed from earlier calibrations. Based on this information the offset between the measured and the listed field is corrected by the adjustment of the coefficients.

Table 6.1: Overview of all experiments. The randomized order displays the chronology of the measurements as well as the order of the applied rates respectively fields. The randomized rate respectively field order is mirrored as well in the rate respectively field order in the legends of the subsequent figures in chapters 7 and 8. Cycle numbers and rates apply to either temperature or magnetic cycles.

sample	transducer	threshold (dB)	HDT (μ s)	T-interval (K)	rates K/min]	fields (T)	direc.	cycle number
Ni ₆₃ Al ₃₇	NANO 30	23	200	320 - 240	10	0	[001]	152
Au _{50,5} Cd _{49,5}	NANO 30	22	200	316 - 296	1, 2, 0.5, 10, 5, 0.1, 3, 4	0	[001]	20 (10 for 0.1 K/min)
Ni ₆₃ Al ₃₇	NANO 30	22	30	320 - 240	3, 0.5, 10, 2, 1, 4, 5, 0.1	0	[110]	20 (12 for 0.1 K/min)
Fe _{68,8} Pd _{31,2} ^{single}	PICO	22	30	265 - 200	10, 0.1, 3, 2, 4, 5, 1, 0.5	0	[110]	20 (10 for 0.1 K/min)
Fe _{68,8} Pd _{31,2} ^{Poly}	PICO	22	30	265 - 200	0.1, 3, 0.5, 5, 4, 2, 1, 10	0	[001]	20 (10 for 0.1 K/min)
Ni ₅₂ Mn ₂₃ Ga ₂₅	R15-LT	25	100	300 - 195	≤ 1	0.0, 0.2, 0.1, 0.15, 0.05, 0.25	[001]	3
Ni ₅₂ Mn ₂₃ Ga ₂₅	R15-LT	25	100	195	1300 μ /field cycle	0 - 1	[001]	46
Ni ₅₂ Mn ₂₃ Ga ₂₅	R15-LT	25	100	195	130 μ /field cycle	0 - 0.8	[110]	20
Ni ₅₂ Mn ₂₃ Ga ₂₅	R15-LT	25	100	300 - 195	≤ 1	0.0, 0.8, 0.4, 0.6, 0.2	[110]	3
Ni ₅₂ Mn ₂₃ Ga ₂₅	R15-LT	25	100	300 - 195	≤ 1	0.0, 0.2, 0.15, 0.1, 0.25, 0.05	[110]	3
Ni ₅₂ Mn ₂₃ Ga ₂₅	R15-LT	25	100	300 - 195	≤ 1	0.0, 0.4, 0.2, 0.6, 0.8	[001]	3

Table 6.1 gives an overview of all performed measurements. Measurements with the $\text{Ni}_{63}\text{Al}_{37}$, $\text{Au}_{50.5}\text{Cd}_{49.5}$, $\text{Fe}_{68.8}\text{Pd}_{31.2}^{\text{single}}$, and $\text{Fe}_{68.8}\text{Pd}_{31.2}^{\text{poly}}$ samples are conducted with the vacuum setup without an external magnetic field. The focus of these measurements lies on the rate-dependence in order to analyze kinetic aspects. Using the $\text{Ni}_{63}\text{Al}_{37}$ sample additional multi-cycle measurement have been conducted to analyze the behavior during many temperature cycles at a fixed rate. The rate-dependent measurements are performed at eight different rates between 0.1 K/min and 10 K/min (0.1 K/min, 0.5 K/min, 1 K/min, 2 K/min, 3 K/min, 4 K/min, 5 K/min, 10 K/min). 20 cycles are conducted at each rate. For the lowest rate the cycle number is on the order of 10. The temperature interval of the cycles (T_{start} and T_{end}) is adapted to the temperature range of the transition. The multi-cycle measurement has been performed at a constant rate of 10 K/min with a cycle number of 152.

With the ferromagnetic Heusler alloy $\text{Ni}_{52}\text{Mn}_{23}\text{Ga}_{25}$ field-dependent measurements are performed with the field setup. Two different measurement procedures occur: temperature cycles at constant fields in order to analyze the magneto-structural coupling as well as cycles of the magnetic field after zero-field cooling ($T < M_s$), in order to analyze the field-induced rearrangement of structural variants which is associated with the effect of magnetic-field-induced strain (MFIS). Both procedures are performed with an applied magnetic field parallel to the crystallographic directions [001] and $[\bar{1}10]$.

The effect of an applied magnetic field on the martensitic and the premartensitic (or intermediate) transition is analyzed by temperature cycles, which are conducted at constant fields between $\mu_0 H = 0.0 \text{ T}$ and $\mu_0 H = 0.8 \text{ T}$ ($\mu_0 H = 0.2 \text{ T}$, $\mu_0 H = 0.4 \text{ T}$, $\mu_0 H = 0.6 \text{ T}$, $\mu_0 H = 0.8 \text{ T}$). Three cycles are repeated at a constant field in order to check the reproducibility. The analysis of the premartensitic transition requires smaller fields with a smaller increment because large fields of $\mu_0 H > 0.25 \text{ T}$ suppress the transition. The applied field is varied in 0.05 T steps between zero field and $\mu_0 H = 0.25 \text{ T}$. To ensure reasonable statistics three cycles are performed per field. Table 6.1 additionally lists the transducer type, the used threshold (th), and the hit definition time.

Measurements using the vacuum setup allow a very low threshold because of the low noise, thermopile-based cooling system, which is situated inside the vacuum chamber. The field setup works with a different cooling system (see section 4.2.2). It has in a certain temperature interval of approximately 230 K - 260 K a high noise level. A threshold of 25 dB turns out to be the best tradeoff between noise and transition signals, which maximizes the signal to noise ratio.

The procedure of calorimetric measurements can be found as part of the description of the experimental setup in section 4.2.3.

7 Results

In this chapter the experimental results of the acoustic emission (AE) measurements are presented. The analyzed material systems are Ni-Al, Au-Cd, Fe-Pd, and Ni-Mn-Ga. Each system is represented by a single crystal and in case of Fe-Pd additionally by a polycrystal. All material systems except Ni-Mn-Ga are analyzed by rate-dependent ($0.1 \text{ K/min} \rightarrow 10 \text{ K/min}$) temperature cycle measurements. In addition, a multi-cycle measurement with approximately 150 cycles at a constant rate of 10 K/min has been performed with the material system Ni-Al. Ni-Mn-Ga has been analyzed with magnetic-field-dependent measurements. Furthermore, calorimetric measurements have been conducted with all samples using a differential scanning calorimeter as a reference method for the AE technique. A detailed description of the measurement procedures can be found in section 6.

First, this chapter will give a description of the data processing and evaluation process. Subsequently, the results of the analyzed material systems will be presented, each in a separate subsection.

7.1 Data processing and evaluation procedures

The raw data have been processed and evaluated in order to convert them into a usable format. This process consists of data filtering, the separation into cooling and heating runs respectively magnetic field increase and decrease runs, and the computation of histograms of several AE features such as activity, energy, amplitude, or duration. Afterwards, power law distribution fits have been computed using the maximum likelihood method.

Both the filter and the data evaluation processes are executed by custom-made Matlab programs with integrated C++ routines. After reading all data of a measurement sequence, every single AE signal runs through a multi-level filter. The first criterion of the filter is the peak frequency of the wave packets (see section 4.1). All hits with a peak frequency outside the hardware frequency bandpass are discarded (vacuum setup: $100 \text{ kHz} \rightarrow 1 \text{ MHz}$; field setup: $20 \text{ kHz} \rightarrow 2 \text{ MHz}$; for more information see section 4.1). Next, the temperature is tested where the hit occurs. Only hits inside the relevant temperature interval are considered.¹ A third filter corrects a subtle error of the AE-acquisition system

¹The relevant temperature intervals have been estimated by calorimetric results.

concerning only amplitude histograms and leaving activity histograms unaffected. This systematic error² arises in the detection of the lowest amplitude above the threshold. All these hits are ignored in the power law evaluation process of the amplitude distribution. All hits that pass the described filters are accurately processed by the AE system.³ However, some of the detected signals can be noise signals that have their origin in processes other than the transition. In order to estimate the characteristics of the noise signals noise measurements have been performed in both setups using a dummy sample material that does not show any phase transition in the relevant temperature range or any magnetic interaction at all. For both setups typical measurement sequences have been conducted analyzing the dummy sample. After the introduction of the data evaluation process, which is applied as well to the dummy measurements, the following paragraphs will describe the results of the noise measurements.

The data evaluation process continues with the computation of histograms of AE features. Histograms of the acoustic activity use linear temperature bins with a well adapted bin width. The narrower the transition temperature range and the more acoustically active the sample, the smaller the bins. $\text{Au}_{50.5}\text{Cd}_{49.5}$ is processed with a bin width of 50 mK, $\text{Ni}_{52}\text{Mn}_{23}\text{Ga}_{25}$ with 100 mK, the $\text{Fe}_{68.8}\text{Pd}_{31.2}$ samples with 200 mK, and $\text{Ni}_{63}\text{Al}_{37}$ with 250 mK.

The logarithmic binning of the amplitude histograms is predefined by the AE-acquisition system which measures the amplitude in decibel (dB). The relation between the voltage released by the piezoelectric transducer and the detected amplitude in dB is given in equation 4.1. In order to display the amplitude against the original observable on a logarithmic scale the amplitude values are converted back into voltage values using equation 4.1. The histograms of the duration as a function of the amplitude show color-coded "iso-activity areas" on a log-log-log scale.

The hit energy and duration are presented in logarithmic histograms, too. The advantage of logarithmic histograms over linear histograms lies in their large bins in areas of little distribution probability. The bin width is given by the equation

$$\text{dB}x = A_{\text{bw}} \cdot \log_{10}(x/x_{\text{ref}}), \quad (7.1)$$

where x is an AE feature like the energy or duration, A_{bw} indicates how many dB equal one order of magnitude, and x_{ref} is a reference value which controls the resolution. The parameters A_{bw} and x_{ref} are well adapted to each investigated feature.

The power law fits of each AE feature are realized with the maximum likelihood method, which is the most suitable technique because it is independent of the

²The origin of the error is neither known to the author nor to the manufacturer *Physical Acoustics*.

³In regular measurements only a few percent of the AE signals (or even less) are rejected by the filters.

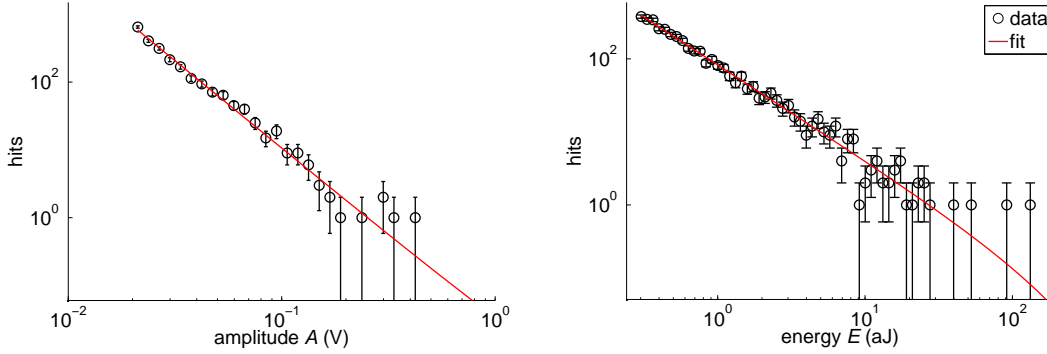


Figure 7.1: Exemplary histograms of the amplitude (left) and energy (right) distribution with exponentially corrected power law fits (red line). The data originate from a martensitic transition in $\text{Au}_{50.5}\text{Cd}_{49.5}$ at a rate of 1 K/min .

histogram representation (linear or logarithmic scales) and of the chosen bin width [48]. The fits of the power law behavior with an exponential correction of the AE features energy, amplitude, and duration can be described by

$$\begin{aligned}
 p(E) &= \frac{1}{Z(\epsilon, \lambda_E)} E^{-\epsilon} e^{-\lambda_E E} \\
 p(A) &= \frac{1}{Z(\alpha, \lambda_A)} A^{-\alpha} e^{-\lambda_A A} \\
 p(D) &= \frac{1}{Z(\delta, \lambda_D)} D^{-\delta} e^{-\lambda_D D},
 \end{aligned} \tag{7.2}$$

where E , A , and D are the values of energy, amplitude, and duration; ϵ , α , and δ are the corresponding exponents; $1/\lambda_E$, $1/\lambda_A$, and $1/\lambda_D$ the scales on which corrections become appreciable; and Z is a normalization factor. The exponential correction factor λ is an indicator of the distance to criticality (details in section 3.2.1). Figure 7.1 exemplarily shows the distributions of the amplitude and the energy with the corresponding power law fits concerning equation 7.2.

In the following the noise measurements starting with the vacuum setup are described. V2A steel has been used as the reference material of the dummy sample. Because of the absence of a phase transition, the only activity under thermal cycling should result from thermal expansion. Figure 7.2 shows the acoustic activity as a function of the temperature. It can be seen that only at temperatures below 210 K a significant noise level arises. All measurements of

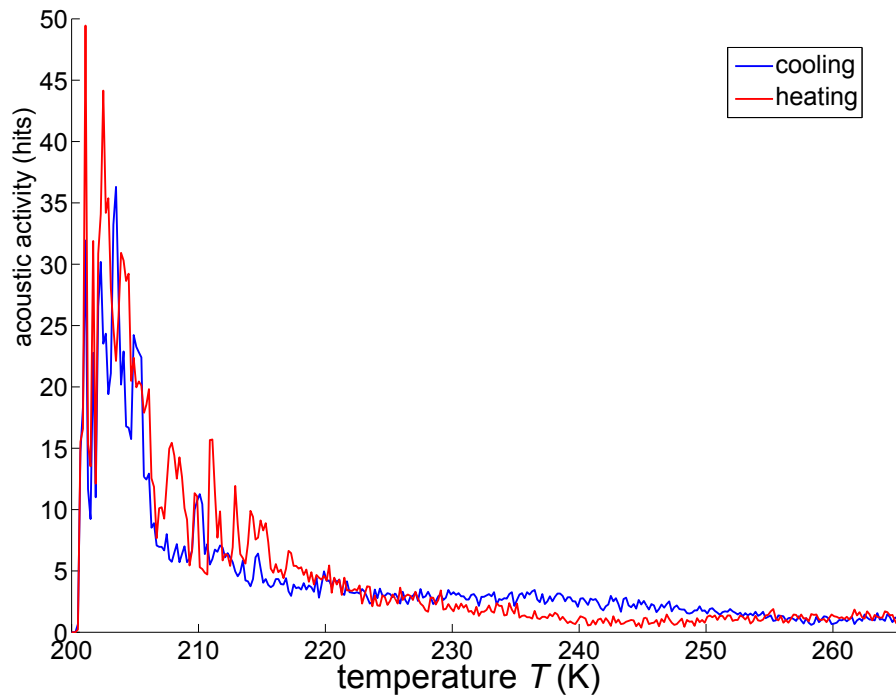


Figure 7.2: Noise measurement with the vacuum setup using a steel dummy sample and the PICO AE transducer. The diagram shows the acoustic activity with a bin width of 200 mK. Several runs at selected rates are averaged for cooling (blue line) and heating (red line). The acoustic activity of the analyzed martensitic transitions is much higher than this noise level. Depending on the sample the signal to noise ratio lies between 100 and 2000.

this setup are conducted at higher temperatures. This guarantees an excellent signal to noise ratio larger than 100.⁴

Due to a different cooling system the magnetic field measurements have a more complicated noise profile. The noise distribution shown in figure 7.3 has its maximum at approximately 300 K, which is of the same order as the transition signal. Under cooling the noise decreases, and at approximately 230 K it reaches an irrelevant level. The martensitic transition of the analyzed $\text{Ni}_{52}\text{Mn}_{23}\text{Ga}_{25}$ sample starts at approximately 210 K and is not affected by noise. By contrast, the premartensitic transition occurs in a temperature interval between 245 K and 220 K, which lies inside the noisy region. For the acoustic activity distributions the subtraction of the noise background from the data would be sufficient. In case of power law distributions of amplitude, energy, and

⁴The noise measurement has been performed at an amplitude threshold of 23 dB, which is, regarding the specification, the lowest possible value [1].

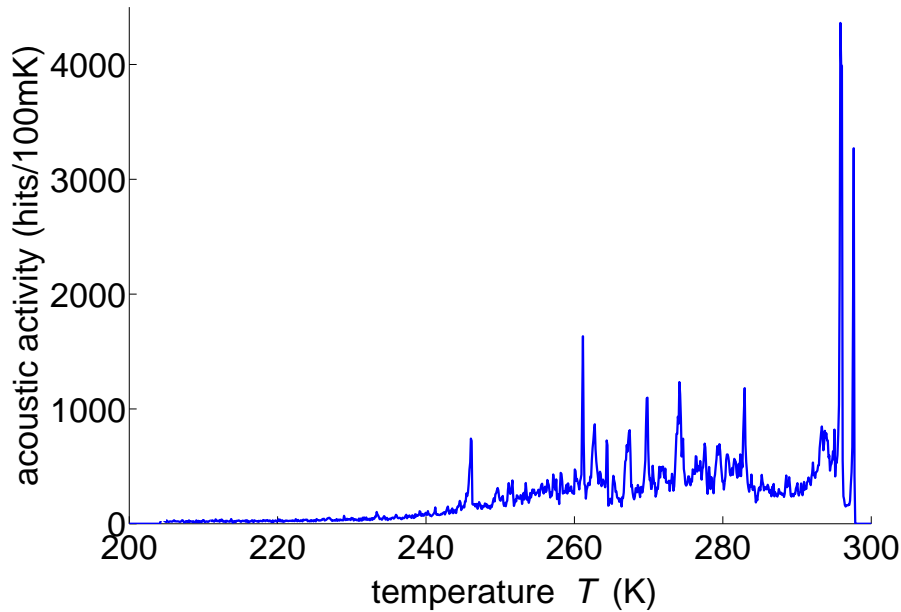


Figure 7.3: Noise measurement with the magnetic field setup using a copper dummy sample and the R15-LT AE transducer. The diagram shows the acoustic activity histogram with a bin width of 100 mK in analogy to the real measurements with $\text{Ni}_{52}\text{Mn}_{23}\text{Ga}_{25}$. In the range of the martensitic transition below 210 K the noise can be neglected. At higher temperatures in the region of the premartensitic transition the noise level is comparable to the transition activity.

duration such an approach is not useful because every single hit needs to be classified as noise or as a transition signal. To identify an appropriate classification criterion a comprehensive comparison between noise and transition data has been undertaken. A comparison of pure noise data from noise measurements (figure 7.4) with an unfiltered transition (figure 7.5 (left)) reveals that noise signals of the same amplitude as transition AE signals have much larger durations. In a log-log histogram of amplitude against duration, as shown in figures 7.5 and 7.6, it can be seen that noise and transition AE signals occur in two distinct regimes. This allows their separation by an adequate amplitude-duration noise filter, as indicated by the white dotted line in figure 7.5. The filter results have been confirmed by comparing unfiltered and filtered transition data. It can be easily seen that the amplitude distribution of the unfiltered data (figure 7.5) shows dramatic deviations from power law behavior whereas the filtered data are in good agreement with a power law distribution (figure 7.6). All data presented in the next sections have been previously filtered in order to suppress noise arising from the cooling device.

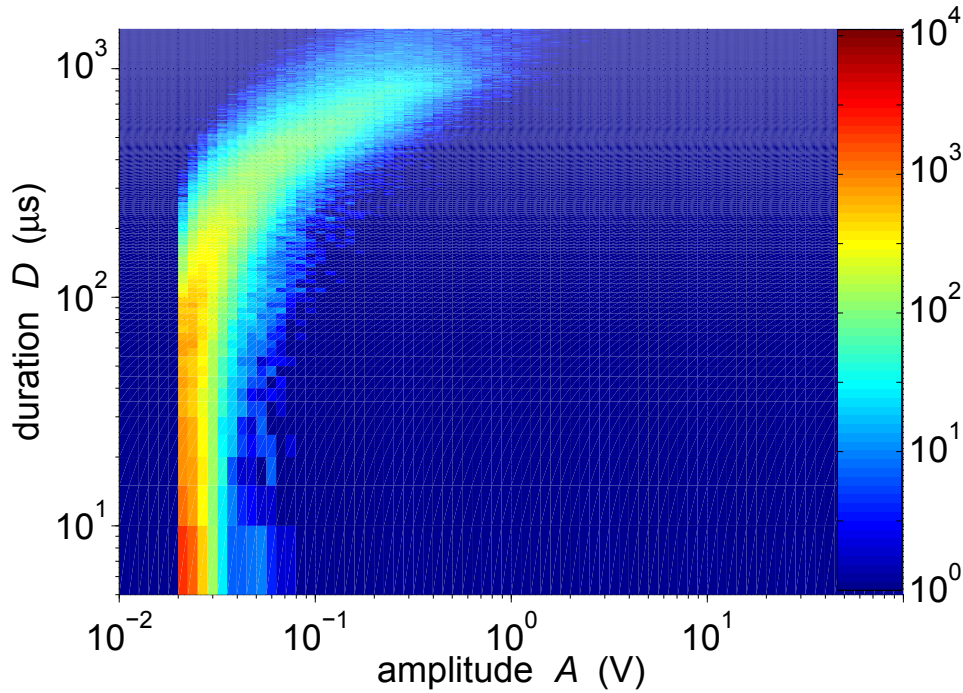


Figure 7.4: Noise measurement with the field setup using a copper dummy sample and the R15-LT AE transducer. The figure shows the color-coded acoustic activity in a log-log histogram of the amplitude-duration distribution. The comparison with figure 7.5 reveals that the noise displays a special pattern, which allows to distinguish between transition and noise signals.

It has to be mentioned that another systematic error lies in the energy measurement of a hit, which is inherently coupled to the detection process (for the calculation of the energy see equation 4.2). Figure 7.7 shows a stylized waveform. It can be seen how the vertical cutoff at the estimated start and finishing time rejects the rising and falling edges of the waveform. The energy of the lateral parts of the waveforms is not included in the integral. It is worth noticing that this effect becomes smaller for longer hit durations. In hits with an ordinary waveform shape (see e. g. figure 4.3) this cutoff-error is rather small and has no relevance.

7.2 Sample characterization

In this work five shape memory samples have been analyzed, from which four are single crystals and one is a polycrystal (see figure 7.8). The samples are $\text{Ni}_{63}\text{Al}_{37}$,

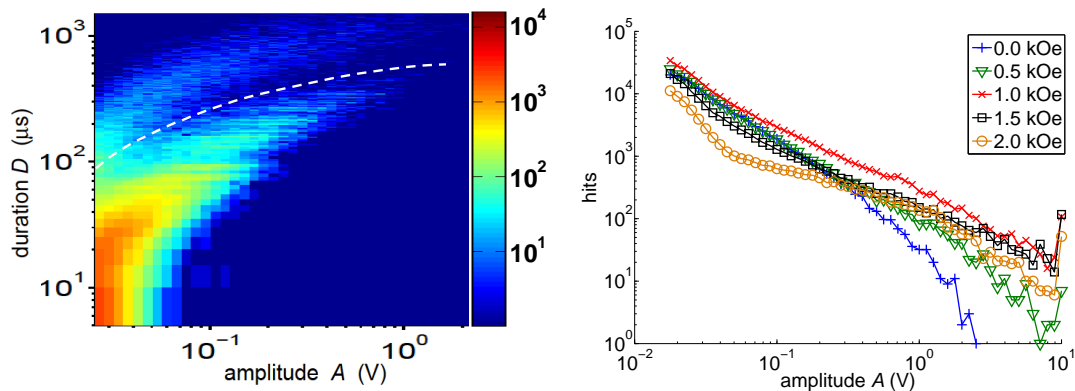


Figure 7.5: On the left can be seen the color-coded acoustic activity in a log-log histogram showing the duration against the amplitude of useful AE events and noise, which can be separated by an amplitude-duration filter as indicated by the white dotted line (noise above and transition signal below). On the right hand side is depicted a histogram of the unfiltered amplitude data from the premartensitic forward transition of the Ni_2MnGa sample at selected applied magnetic fields. The distributions show marked deviations from power law behavior.

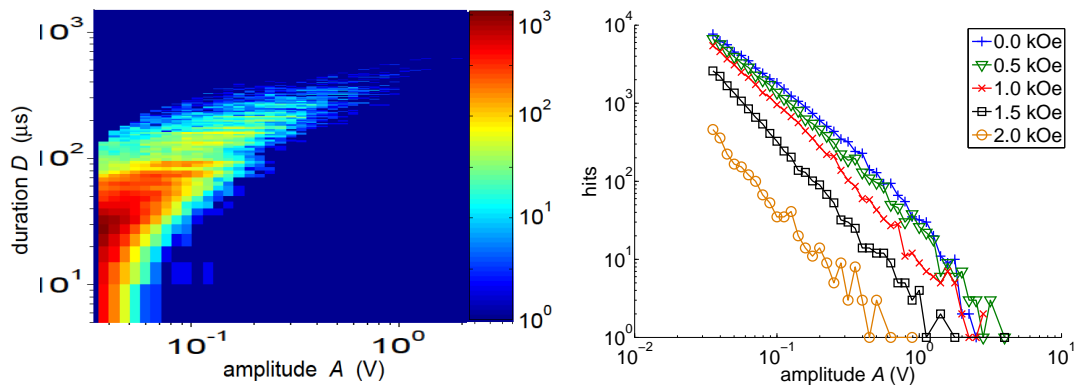


Figure 7.6: On the left hand side is shown the color-coded acoustic activity in a log-log histogram showing the filtered signal distribution of the duration against the amplitude (analog figures of the unfiltered data set can be seen in figure 7.5). The right hand side shows the corresponding histogram of the filtered amplitude distribution of the premartensitic forward transition of the Ni_2MnGa sample. In contrast to the unfiltered data the distributions now can be described by power laws over more than three orders of magnitude, providing evidence for a consistent filtering procedure.

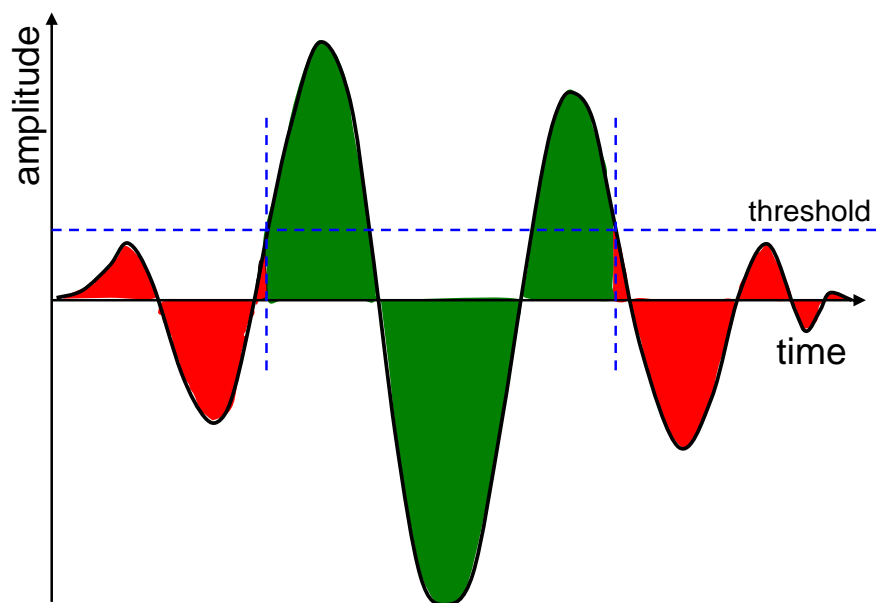


Figure 7.7: Schematical depiction of the hit energy detection process where the vertical cutoff at the threshold leads to a smaller hit energy. The energy integral includes the green colored oscillations and excludes the red edge regions. In real waveforms, the fraction of rejected areas is usually very small (see figure 4.3).

$\text{Au}_{50.5}\text{Cd}_{49.5}$, $\text{Fe}_{68.8}\text{Pd}_{31.2}^{\text{single}}$, $\text{Fe}_{68.8}\text{Pd}_{31.2}^{\text{poly}}$, and $\text{Ni}_{52}\text{Mn}_{23}\text{Ga}_{25}$. The general properties of the different systems are given in section 3.5. The following description is sample specific and starts with the sample preparation process (as far as it is known to the author). Additionally, the sample properties such as the dimensions, the weight, the transition enthalpy, and characteristic temperatures are given, which are gathered by calorimetric and acoustic emission measurements. A tabular overview of the relevant properties summarizes the corresponding section. Subsequently, the main experimental results of this work originated from rate or magnetic-field-dependent AE measurements will be presented. The results will be discussed in chapter 8.

7.2.1 $\text{Ni}_{63}\text{Al}_{37}$

The $\text{Ni}_{63}\text{Al}_{37}$ single crystal analyzed in this work is a fragment of a crystal grown at the *Ames Laboratory* of the *United States Department of Energy*. It has a mass of 184.2 mg and a plate-like shape with dimensions of 8.9 mm x 4.4 mm x 0.98 mm. The sample has been cut in the high temperature phase along its high symmetry



Figure 7.8: Photograph showing the analyzed samples in their parent phase at room temperature and a 1-eurocent coin as a reference. From left to right: $\text{Au}_{50.5}\text{Cd}_{49.5}$, $\text{Ni}_{63}\text{Al}_{37}$, $\text{Cu}_{68}\text{Zn}_{16}\text{Al}_{16}$ (which will serve as a reference in section 8.5 and in the introduction of chapter 8), and $\text{Fe}_{68.8}\text{Pd}_{31.2}^{\text{single}}$ (both the single crystal and the polycrystal have identical shapes). In the upper right corner a photograph of the $\text{Ni}_{52}\text{Mn}_{23}\text{Ga}_{25}$ sample has been added according to scale.

directions ([100], [010], and [001]) and its (001) surface has been electropolished. The high temperature lattice constant was measured to be $a = 2.856 \text{ \AA}$ [111].

Figure 7.9 shows the surface relief in the low temperature phase, which is highly oriented. On a superficial examination the relief looks qualitatively the same during different runs. Nevertheless, on a closer inspection different patterns can be found to occur. Due to the exposure to several hundreds of cooling and heating cycles, which involve large internal strains during the phase transitions, the sample reveals some cracks. In the parent phase these cracks are not visible to the naked eye for they are closed (figure 7.10 top). In the low temperature phase these cracks open due to the occurring strains (figure 7.10 center and bottom) and their width can be estimated to be approximately $25 \mu\text{m}$, which is in good agreement with results of Finlayson *et al.*, published in reference [43]. For further details on the thermal treatment of the sample and its influence on fatigue and aging processes (martensite stabilization and rubber-like behavior) see [111].

Figure 7.11 shows the acoustic emission and the calorimetric data of the forward and reverse transition of $\text{Ni}_{63}\text{Al}_{37}$. Both curves, which are in very



Figure 7.9: Micrograph showing the Ni₆₃Al₃₇ sample surface in the martensitic phase. The surface relief, originating from the self-accommodation process, is highly oriented.

good agreement with each other, show a broad transition interval with a double peak structure that originates presumably from a stoichiometric gradient. Here and in the following the martensitic start (M_s) and finish temperatures (M_f) have been respectively determined from the first significant rise of the acoustic activity above the noise threshold and the last significant threshold crossing. The definition of the austenitic start (A_s) and finish temperatures (A_f) is analogous. The following characteristic temperatures have been determined for Ni₆₃Al₃₇: $M_s = 298 \pm 1$ K, $M_f = 251 \pm 1$ K, $A_s = 264 \pm 1$ K to $A_f = 314 \pm 1$ K. The hysteresis width, which is calculated as the temperature offset between the activity peaks of the forward and reverse transition, can be estimated to be approximately 5 K and the thermodynamic equilibrium temperature T_0 to be $T_0 = 306 \pm 1$ K. T_0 has a considerably high value because of the long tail of AE signals towards high temperatures. A rough estimate of the stoichiometric gradient throughout the sample from the transition temperature interval leads to a compositional difference of about 0.4 at.% across the sample (for the stoichiometry dependence of M_s see [25, 166]). The double peak structure indicates that the sample mainly consists of two stoichiometries, which can be confirmed by video observation of the surface relief during the transition [90].

In addition to the acoustic activity, the distribution of the acoustic energy (as well a function of the temperature) emitted during the forward and reverse

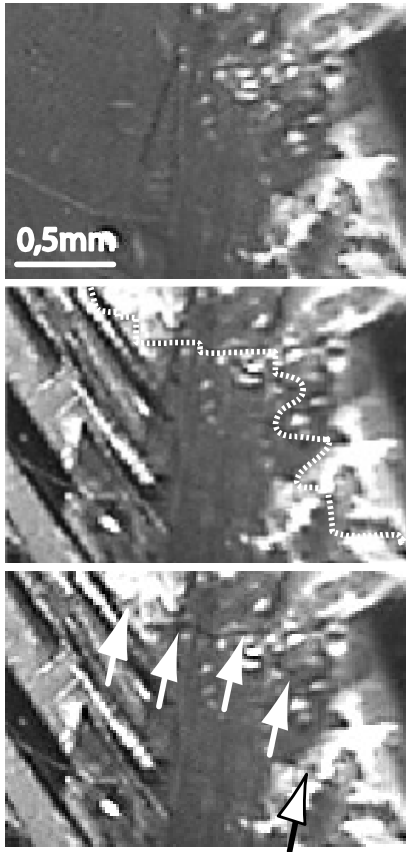


Figure 7.10: Micrographs showing a section of the $\text{Ni}_{63}\text{Al}_{37}$ sample surface in the high temperature phase (top) and in the low temperature phase (center and bottom). In the low temperature phase cracks can be identified. The dotted white line is a guide to the eye tracing a crack. In the micrograph at the bottom the same crack is highlighted by arrows [90].

transition can be analyzed. In general, both distributions show similar results. In some cases, as can be seen in figure 7.12, the acoustic energy has a more abrupt character. This can be understood by the fact that the energy scales with the hit amplitude and duration, whereas the activity is the number of hits independent of their characteristics. However, both distributions are correlated with each other and display the same characteristic temperatures and the double peak structure.

Furthermore, the AE feature duration shows a correlation with the amplitude. Figure 7.13 depicts the color-coded acoustic activity in an amplitude-duration distribution on a log-log scale. The arrow-shaped distribution indicates a positive correlation - the higher the amplitude the higher the duration.

The acoustic activity of the martensitic and the austenitic transition at selected rates spanning over two decades (0.1 K/min, 1 K/min, and 10 K/min) can be seen in figure 7.14. The nearly identical acoustic activity curves of the reverse transition at different rates indicate the absence of any rate-dependence. By contrast, the forward transition only shows qualitatively similar behavior without scaling.⁵ In fact, the amount of acoustic activity is reduced by a factor of 0.5 between

⁵In this work scaling refers to a data collapse without any normalization.

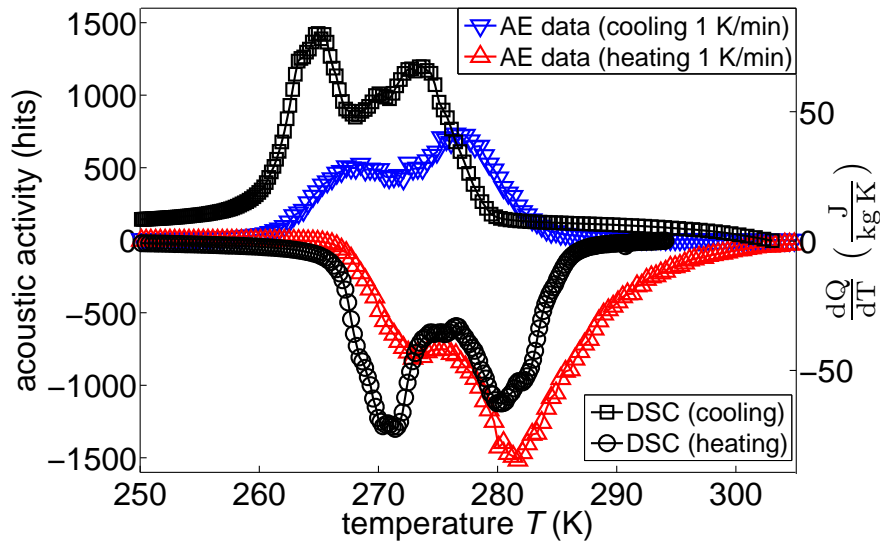


Figure 7.11: Comparison between the mean acoustic activity and calorimetric data during the martensitic forward and reverse transition of the $\text{Ni}_{63}\text{Al}_{37}$ sample. For clarity reasons, the data of the reverse transition have been plotted with negative values. The temperature offset between the acoustic and calorimetric data can be explained by the absent temperature calibration of the calorimetric measurement.

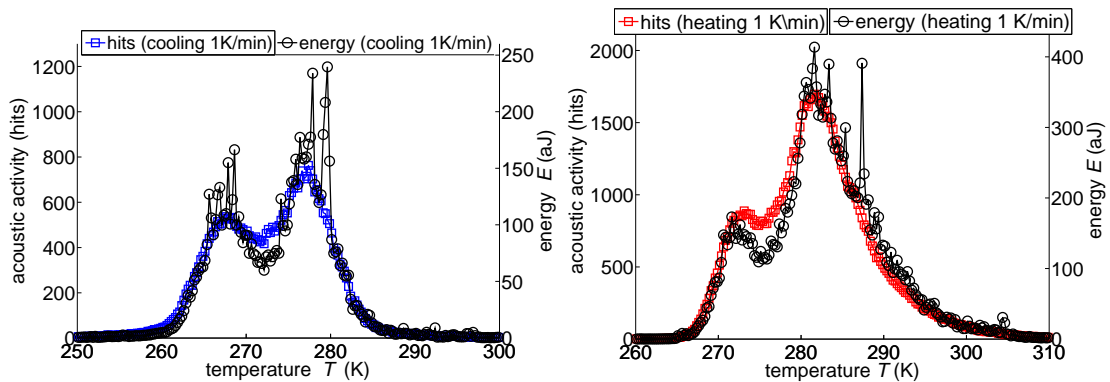


Figure 7.12: Comparison of the mean energy distribution and the acoustic activity of the $\text{Ni}_{63}\text{Al}_{37}$ sample as a function of temperature, exemplarily shown at a rate of 1 K/min. With adequately chosen ordinates both curves show a high degree of scaling. The forward transition can be seen on the left and the reverse transition on the right.

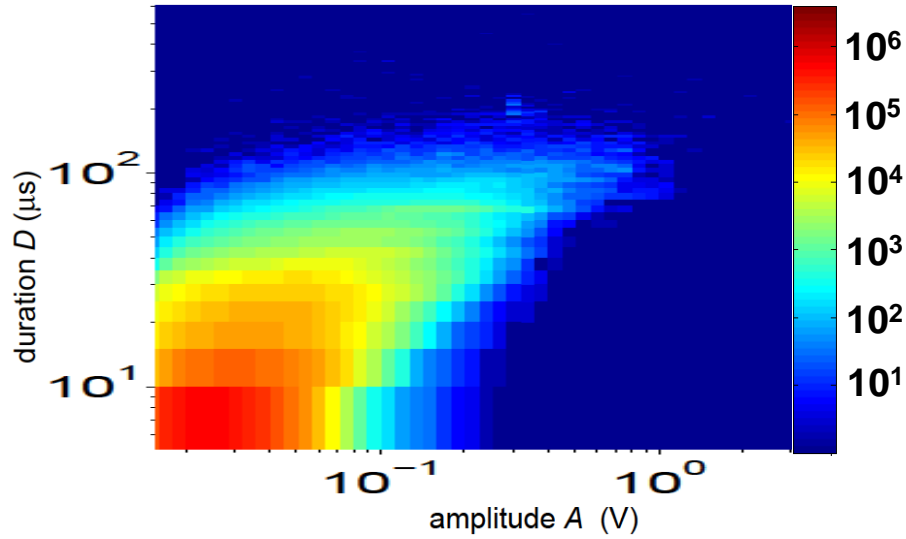


Figure 7.13: Color-coded acoustic activity in an amplitude-duration histogram of all rate-dependent measurements of the $\text{Ni}_{63}\text{Al}_{37}$ sample. Amplitude and duration show a positive correlation centered at low amplitudes and small durations.

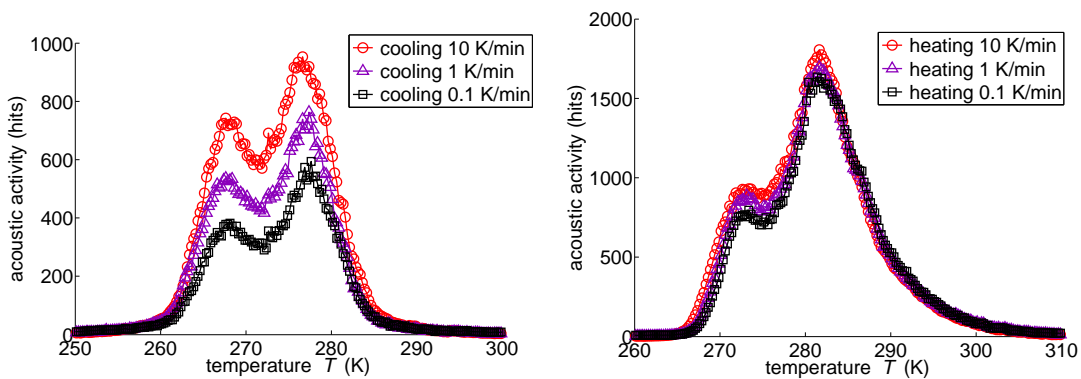


Figure 7.14: Mean acoustic activity of the forward (left) and reverse transitions (right) of the $\text{Ni}_{63}\text{Al}_{37}$ sample at three selected rates (0.1 K/min, 1 K/min, and 10 K/min).

Table 7.1: Characteristic quantities of the analyzed $\text{Ni}_{63}\text{Al}_{37}$ sample. 7 R structures are reported for $\text{Ni}_x\text{Al}_{1-x}$ with $x \lesssim 63\%$. The martensite phase structure of the sample under investigation has not been determined.

phase	start temp.	finish temp.	enthalpy	structure
austenite	$A_s \approx 264\text{K}$	$A_f \approx 314\text{K}$	$\approx 4.4\text{J/g}$	B2
martensite	$M_s \approx 298\text{K}$	$M_f \approx 251\text{K}$	$\approx 4.4\text{J/g}$	3R or 7R

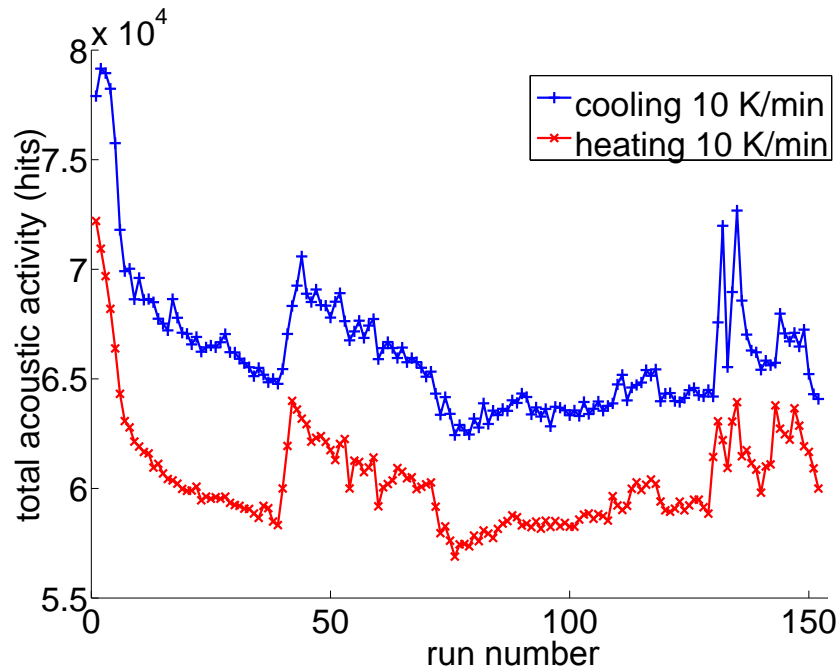


Figure 7.15: Total acoustic activity of the forward (blue) and reverse transitions (red) of the $\text{Ni}_{63}\text{Al}_{37}$ sample during a multi-cycle measurement (152 cycles at a rate of 10K/min). For clarity reasons, the acoustic activity of the forward transition has been divided by two.

the highest and the lowest rate. The energy versus temperature distributions show the same results. The four characteristic temperatures M_s , M_f , A_s , and A_f remain constant at all rates. Table 7.1 summarizes the characteristic temperatures, the structures, and the enthalpy of the $\text{Ni}_{63}\text{Al}_{37}$ sample.

Figure 7.15 shows the total acoustic activity recorded during a multi-cycle measurement consisting of 152 full temperature cycles at a rate of 10K/min . It can be seen that the total acoustic activity as a function of the run number is not constant, neither for cooling nor for heating cycles. During the first approximately 80 cycles a marked decrease is visible, which levels out at a value approximately

20 % lower than the start value. This trend and the superimposed fluctuation can be found in both cooling and heating runs, demonstrating a strong correlation (see discussion in section 8.1).

The probability distributions of the AE features amplitude and energy can both be described by power laws (see figure 7.16 (top)). The exponents α and ϵ describing the amplitude and energy distributions show different numerical values, although their behavior is very similar. The forward transitions show a weak but significant increase of the exponents with decreasing rates. The reverse transitions show constant exponents within the error bars without any rate-dependence (see figure 7.16 (center)). In all cases the exponential correction term has little relevance, as can be seen in figures 7.16 (top and bottom). The inverse of λ indicates the scale on which exponential corrections become relevant (with $\lambda_A^{-1} \hat{=} A \rightarrow e^{-\lambda_A \cdot A} = e^{-1} \approx 0.37$). The values $\lambda_A \approx 2 \text{ V}^{-1}$ and $\lambda_A^{-1} \approx 1/2 \text{ V}$, exemplarily for cooling runs, indicate that the amplitude data deviate at $A = 0.5 \text{ V}$ from the power law behavior by a factor of $e^{-1} = 0.37$. Thus the amplitude can be described by a power law over more than one and a half decades in amplitude and over four decades in number of corresponding hits for all forward transitions and over more than one decade in amplitude and four decades in corresponding hits for all reverse transitions. The energy distributions follow a power law distribution in energy over more than two and a half decades (and three decades in hits) for all cooling runs and over more than two decades in energy (and three decades in hits) for all heating runs.

7.2.2 Au_{50.5}Cd_{49.5}

The Au_{50.5}Cd_{49.5} sample is a single crystal with an almost cubic shape of the dimensions 4.83 mm x 4.4 mm x 4.11 mm and a mass of 1157.2 mg. The sample has been cut in the high temperature phase along its high symmetry directions. In the same phase the (001) sample surface has been polished, which allows a good acoustical coupling to the AE transducer. In the martensitic phase the sample shows a highly oriented surface relief, which is barely visible to the naked eye. In comparison to the Ni₆₃Al₃₇ sample the relief has shorter length scales, as can be seen in the illustration of a very similar sample in figure 7.17.

Before running the AE measurements the sample has been trained by several hundreds of temperature cycles across the phase transition. This training period leads to a (certain) stabilization of the transition characteristics, such as the transition temperatures.

The acoustic activity emitted by the Au_{50.5}Cd_{49.5} sample is strongly correlated with the emitted latent heat (see figure 7.18). Both curves exhibit a single maximum. The larger width of the DSC curves results from the large thermal mass of the measurement system. The temperature offset originates from the absent temperature calibration of the DSC measurement.

7. Results

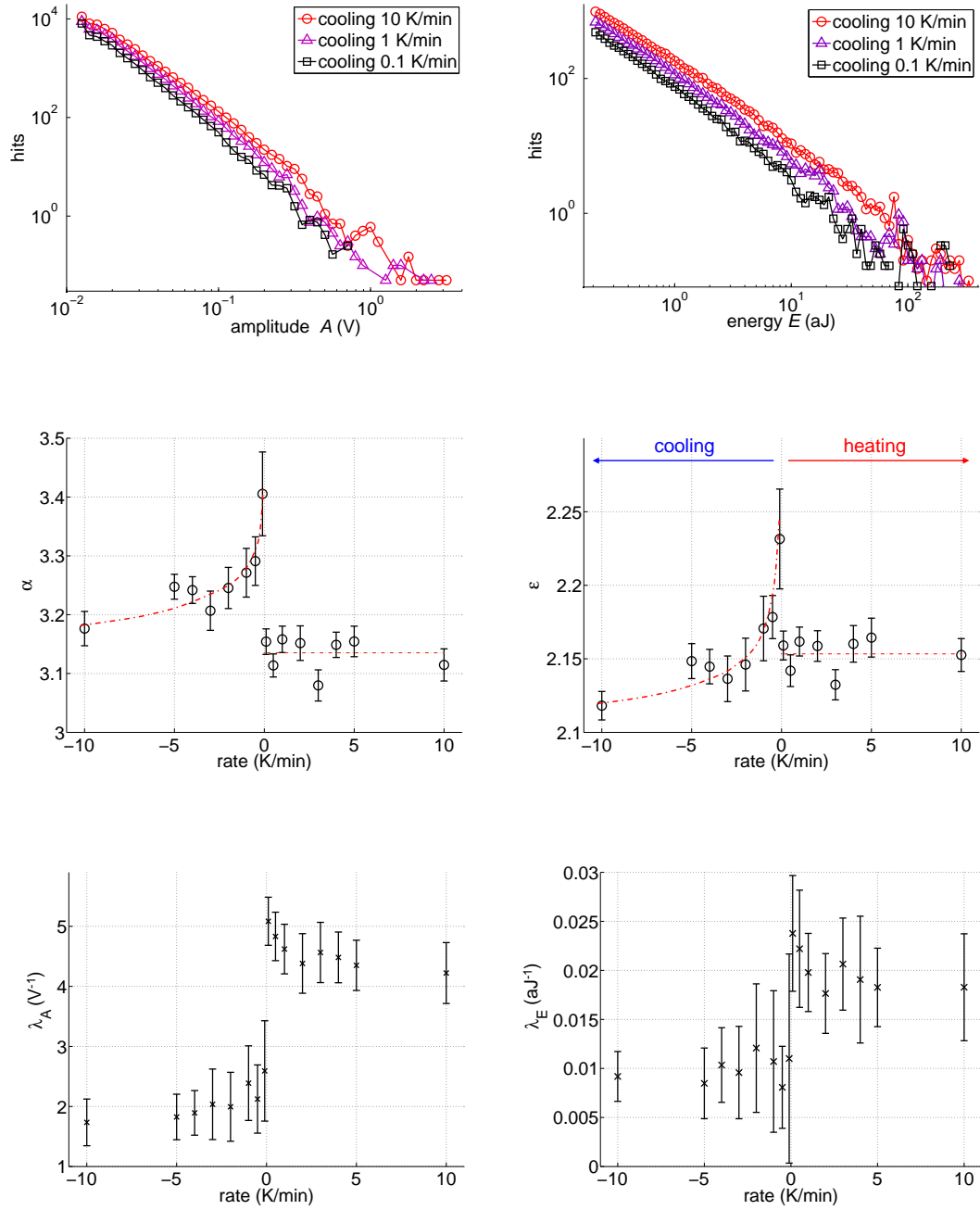


Figure 7.16: Power laws, exponents, and exponential corrections for the forward and reverse transition of the $\text{Ni}_{63}\text{Al}_{37}$ sample at selected rates.

Top: Log-log histograms of the mean amplitude (left) and energy distribution (right).

Center: Amplitude and energy exponents α (left) and ϵ (right). The exponents have been determined by the maximum likelihood method using the equations $p(A) \propto A^{-\alpha} e^{-\lambda_A A}$ and $p(E) \propto E^{-\epsilon} e^{-\lambda_E E}$. The red dotted lines are guides to the eye indicating the trends or the mean values, respectively.

Bottom: λ -values of the exponential correction terms $e^{-\lambda_A A}$ (left) and $e^{-\lambda_E E}$ (right) of the amplitude and energy distributions.

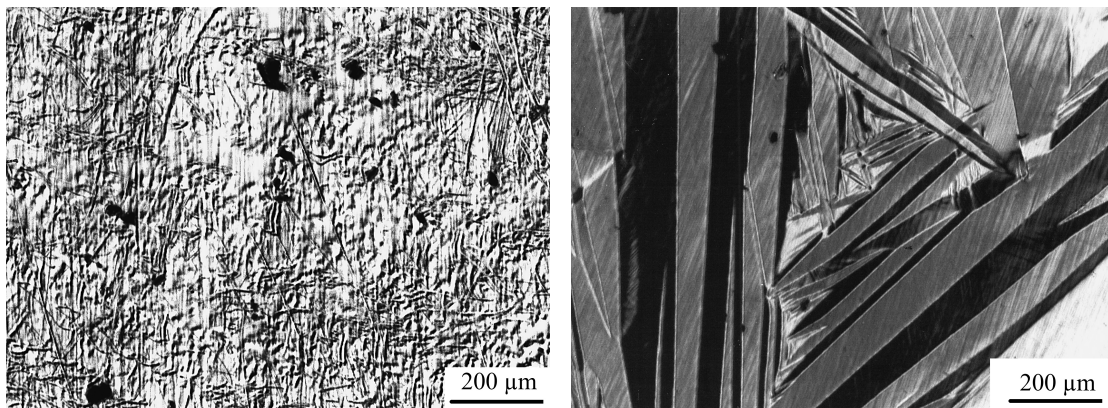


Figure 7.17: Micrographs showing the sample surface in the high temperature phase (left) and the low temperature phase (right) of a Au-Cd sample with a stoichiometry of $\text{Au}_{52.5}\text{Cd}_{47.5}$, which is very similar to the analyzed sample. The polished sample surface of the high temperature phase solely shows some scratches whereas the low temperature surface is characterized by a highly oriented relief. Note the different length scales of the martensitic relief in the center and near the edges of the micrograph [111].

Figure 7.19 compares the acoustic activity with the energy distribution of $\text{Au}_{50.5}\text{Cd}_{49.5}$. Scaling can be observed for both transition directions. The comparison of the acoustic activity respectively energy between the forward and reverse transition reveals a higher activity during the forward transition (more than a factor of two). The transition is considerably sharp with a peak width of approximately 1 K. As it is the case for $\text{Ni}_{63}\text{Al}_{37}$, the AE features amplitude and duration are correlated in the case of $\text{Au}_{50.5}\text{Cd}_{49.5}$, too. The color-coded log-log histogram can be found in figure 7.20.

In order to analyze the rate-dependence of the martensitic transition the mean acoustic activity at each rate is plotted in figure 7.21. These curves do not scale but show two trends at higher rates: a temperature-shift of the peak temperature towards lower values and a peak broadening. The acoustic activity of the reverse transition shows a similar rate-dependence, but with a shift towards higher temperatures. For both cooling and heating, the energy-temperature distribution shows the same rate-dependent behavior as the corresponding acoustic activity data.

Table 7.2 gives an overview of the characteristic temperatures at low rates.

The analysis of the rate-dependent exponents of the amplitude and energy distributions can be found in figure 7.22. Both, the amplitude and the energy distributions show power law behavior, as can be seen for three selected rates in figure 7.22 (top). The exponents of the cooling runs do not show any rate-

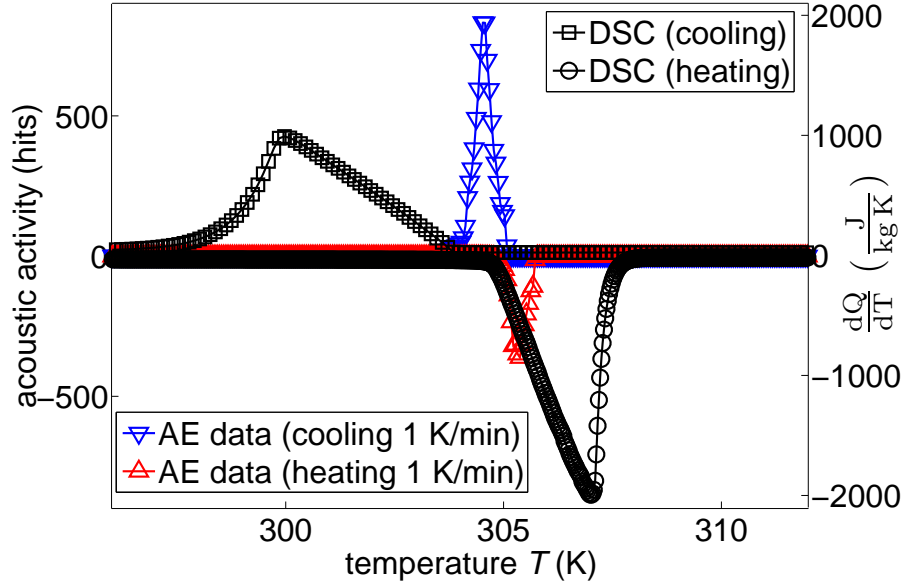


Figure 7.18: Comparison between the mean acoustic activity and calorimetric data during the forward and reverse transition of the $\text{Au}_{50.5}\text{Cd}_{49.5}$ sample. For clarity reasons, the data of the reverse transition have been plotted with negative values. The temperature offset and the different peak widths between the acoustic and calorimetric data can be explained by the absent temperature calibration of the calorimetric measurement and a much larger thermal mass of the calorimetric setup. Note the different temperature scale compared to figure 7.11 for the $\text{Ni}_{63}\text{Al}_{37}$ sample.

Table 7.2: Characteristic quantities of the analyzed $\text{Au}_{50.5}\text{Cd}_{49.5}$ sample.

phase	start temp.	finish temp.	enthalpy	structure
austenite	$A_s \approx 304.8 \text{ K}$	$A_f \approx 305.7 \text{ K}$	$\approx 2.46 \text{ J/g}$	B2
martensite	$M_s \approx 305.1 \text{ K}$	$M_f \approx 303.7 \text{ K}$	$\approx 2.46 \text{ J/g}$	ζ'_2

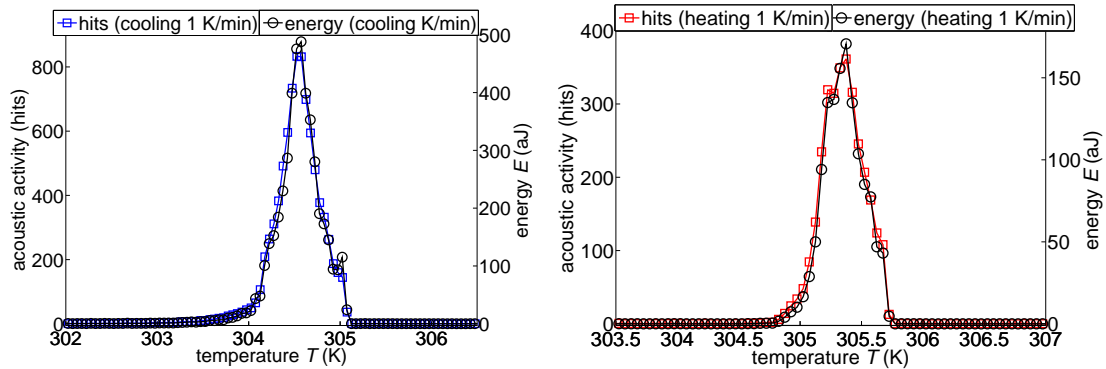


Figure 7.19: Comparison of the mean energy distribution and the acoustic activity of the $\text{Au}_{50.5}\text{Cd}_{49.5}$ sample as a function of the temperature exemplarily shown at a rate of 1 K/min. With adequate ordinates both curves show an excellent scaling. The forward transition can be seen on the left and the reverse transition on the right.

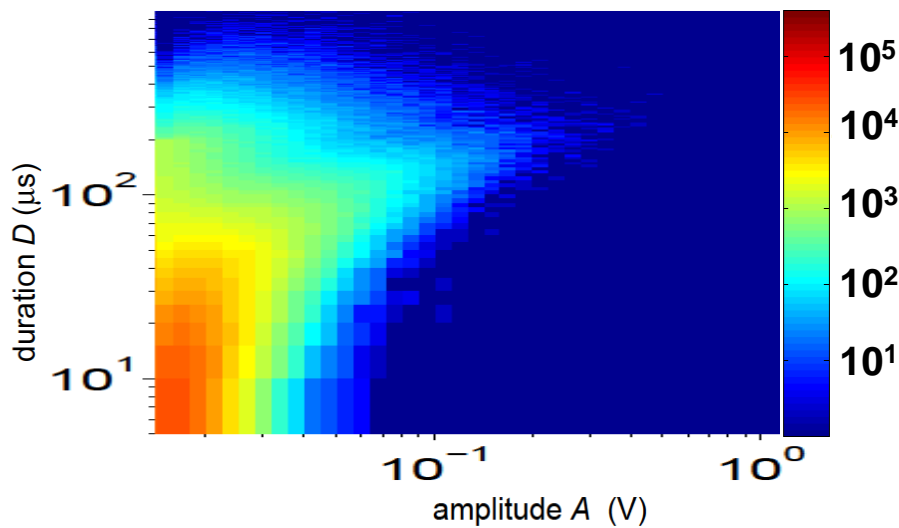


Figure 7.20: Color-coded acoustic activity in an amplitude-duration histogram of all rate-dependent measurements of the $\text{Au}_{50.5}\text{Cd}_{49.5}$ sample. The characteristic color distribution indicates the positive correlation between the two features.

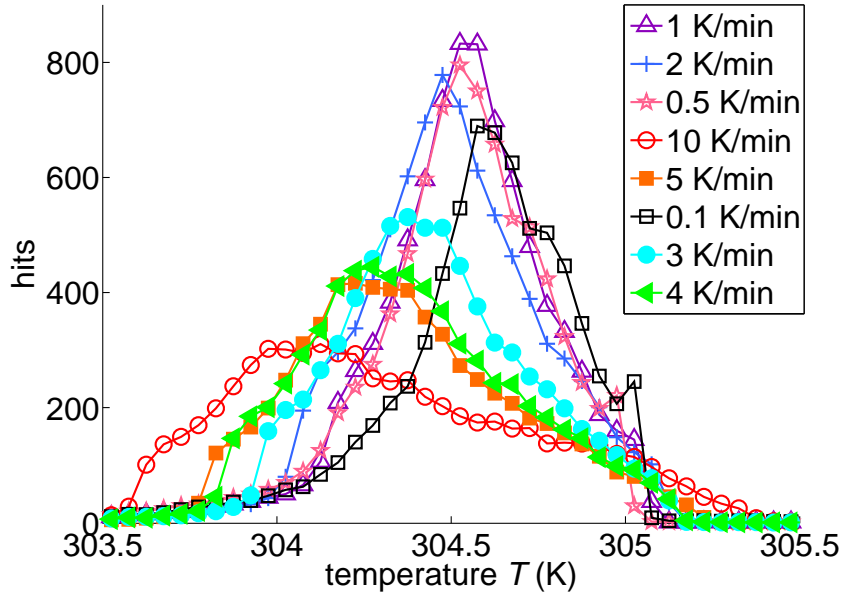


Figure 7.21: Mean acoustic activity of the forward transition of the $\text{Au}_{50.5}\text{Cd}_{49.5}$ sample at eight rates ranging from 0.1 K/min to 10 K/min.

dependence within their error bars and the exponential correction terms have little relevance, i. e. great $1/\lambda$ -values occur. The cooling amplitude power laws span over two decades and the cooling energy power laws cover more than two and a half orders of magnitude.

By contrast, the exponents of the reverse transition show an explicit time dependence. Increasing heating rates lead to increasing values of the amplitude and energy exponents, i. e. a shift towards weaker signals. For low rates and in case of the energy for the highest rate, the exponential correction becomes important. Due to the exponential correction, these power laws only spread over an interval of approximately one order of magnitude. Power laws of the reverse transition with intermediate rates cover the same number of decades as the corresponding power laws of the forward transitions.

7.2.3 $\text{Fe}_{68.8}\text{Pd}_{31.2}^{\text{single}}$ and $\text{Fe}_{68.8}\text{Pd}_{31.2}^{\text{poly}}$

The two Fe-Pd samples analyzed in this work are a single crystal and a polycrystal with the same nominal composition of $\text{Fe}_{68.8}\text{Pd}_{31.2}$. The single crystal was grown by the floating zone method, homogenized in vacuum, and then quenched in iced water. The sample was cut from an ingot parallel to its high symmetry directions $\{100\}$ to the dimensions of 3.098 mm x 2.966 mm x 1.138 mm and

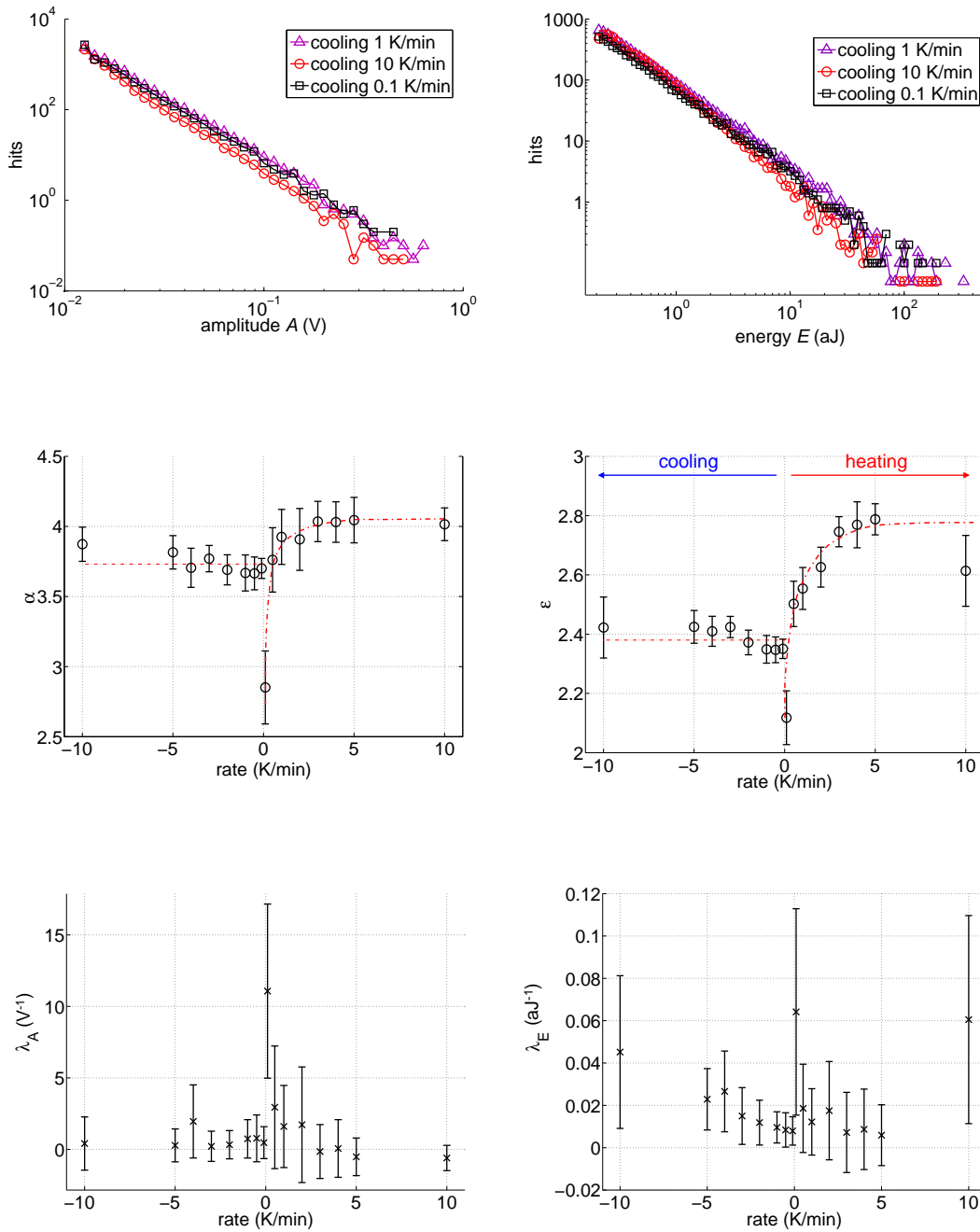


Figure 7.22: Power laws, exponents, and exponential corrections for the forward and reverse transition of the $\text{Au}_{50.5}\text{Cd}_{49.5}$ sample at selected rates.

Top: Log-log histograms of the mean amplitude (left) and energy distributions (right).

Center: Rate-dependence of the amplitude and energy exponents α (left) and ϵ (right). The exponents have been determined by the maximum likelihood method using the equations $p(A) \propto A^{-\alpha} e^{-\lambda_A A}$ and $p(E) \propto E^{-\epsilon} e^{-\lambda_E E}$. The red dotted lines are guides to the eye indicating the trends or the mean values, respectively.

Bottom: λ -values of the exponential correction terms $e^{-\lambda_A A}$ (left) and $e^{-\lambda_E E}$ (right) of the amplitude and energy distributions.

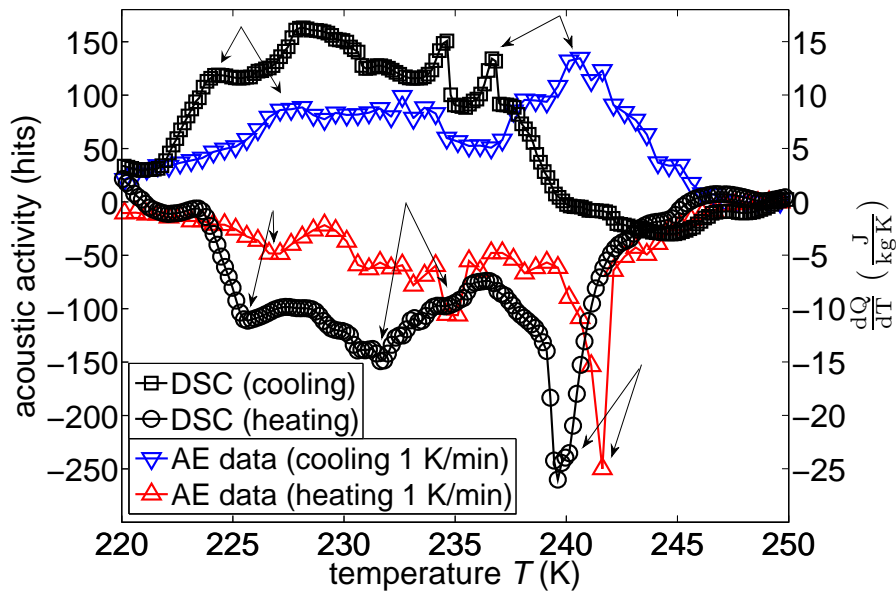


Figure 7.23: Comparison between the mean acoustic activity and calorimetric data during the martensitic forward and reverse transition of the $\text{Fe}_{68.8}\text{Pd}_{31.2}^{\text{single}}$ sample. The arrows point at transition patterns which can be identified in both the AE and calorimetric data. For clarity reasons, the data of the reverse transition have been plotted with negative values. The temperature offset between the acoustic and calorimetric data can be explained by the absent temperature calibration of the calorimetric measurement.

a mass of 0.088160 g. After cutting the sample it was further homogenized at 1373 K for one hour and quenched into iced water to eliminate possible remanent deformations [20].

The polycrystalline sample was prepared with the technique of arc fusion, using a tungsten electrode in combination with a water cooled copper crucible under a purified argon atmosphere. The grain size was determined by optical microscopy to be $\approx 200 \mu\text{m}$ on average. From the ingot a parallelepiped sample was cut with the dimensions of 3.14 mm x 2.95 mm x 1.09 mm and a mass of 0.0865508 g. Note that both samples have basically the same shape, dimensions, and mass [20].

The figures 7.23 and 7.24 show the acoustic activity and the calorimetric data as a function of temperature for the single crystal and the polycrystal. For each crystal the heat flux and the AE data show very similar characteristics. This becomes particularly obvious for the single crystal due to its complex activity respectively heat flux structure. Characteristic patterns occurring in both observables are marked by arrows. Interestingly, the peak temperatures

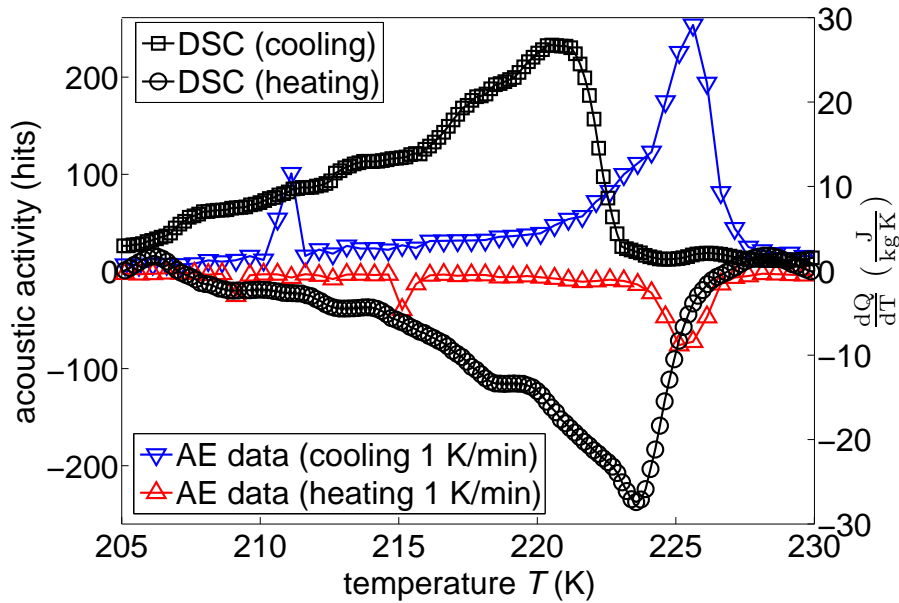


Figure 7.24: Comparison between the mean acoustic activity and calorimetric data during the martensitic forward and reverse transition of the $\text{Fe}_{68.8}\text{Pd}_{31.2}^{\text{poly}}$ sample. For clarity reasons, the data of the reverse transition have been plotted with negative values. The temperature offset between the acoustic and calorimetric data can be explained by the absent temperature calibration of the calorimetric measurement.

T_{peak} of the acoustic activity are the same for cooling and heating for each sample within a small error (single crystal: $T_{\text{peak}} = 241 \pm 0.5$ K and polycrystal: $T_{\text{peak}} = 225 \pm 0.5$ K). The very small hysteresis width indicated by these results can be confirmed by magnetic susceptibility measurements,⁶ conducted with the same samples [20].

It is worthwhile to enlarge the temperature region where the transition starts in order to identify the exact martensitic start respectively austenitic finish temperatures. Figure 7.25 displays these regions for both crystals on four identically scaled histograms. It turns out that in all four cases the corresponding temperatures have the same value, i. e. $M_s^{\text{single}} = A_f^{\text{single}} = M_s^{\text{poly}} = A_f^{\text{poly}} = 247 \pm 1$ K (see the discussion in section 8.3). The characteristic temperatures and enthalpies of both samples are summarized in table 7.3.

The mean acoustic activity of cooling and heating runs at three selected rates between 0.1 K/min and 10 K/min can be found for both samples in figures 7.26 and

⁶A hysteresis width of 2 K has been found with susceptibility measurements for $\text{Fe}_{68.8}\text{Pd}_{31.2}^{\text{poly}}$ [20].

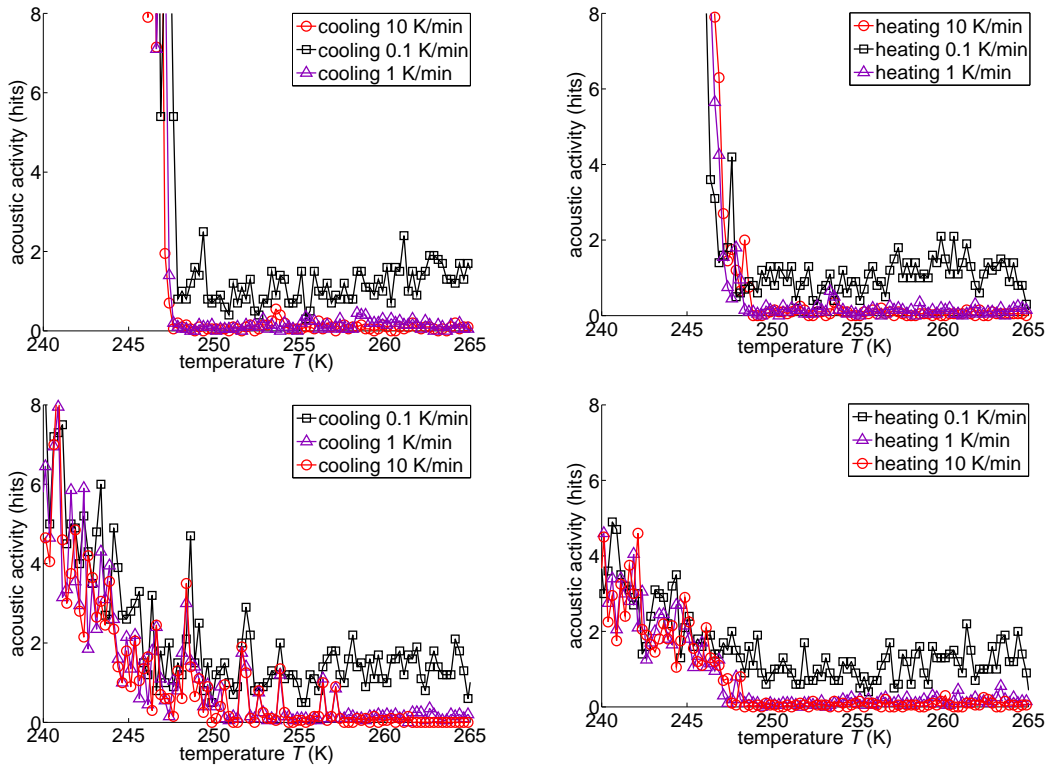


Figure 7.25: Details of the mean acoustic activity of the $\text{Fe}_{68.8}\text{Pd}_{31.2}^{\text{single}}$ (top) and the $\text{Fe}_{68.8}\text{Pd}_{31.2}^{\text{poly}}$ samples (bottom) at three selected rates (0.1 K/min, 1 K/min, and 10 K/min). The forward transitions are plotted on the left and the reverse transitions on the right.

7.27. The martensitic transitions of both crystals and the austenitic transition of the single crystal show scaling behavior. For all heating rates the acoustic activity of the austenitic transition of the polycrystal reveals similar curve shapes but with varying activity maxima.

The histograms corresponding to the amplitude and energy distributions of both samples exhibit in all cases power law behavior, as can be seen in figures 7.28 (top) and 7.29 (top). In case of the single crystal λ -values close to zero (see figure 7.28 (bottom)) give rise to power laws covering more than two decades in amplitude and four decades in energy. The amplitude distributions of the polycrystal merely follow a power law over approximately one decade (a bending of the curves cannot be neglected). By contrast, the power law of the energy distributions cover four decades (see figure 7.29 (bottom)).

The exponents of the amplitude and the energy do not show any rate-dependence neither for the single nor the polycrystal, as shown in figures 7.28 (center) and 7.29 (center). It is worth mentioning that the exponents of the polycrystal show

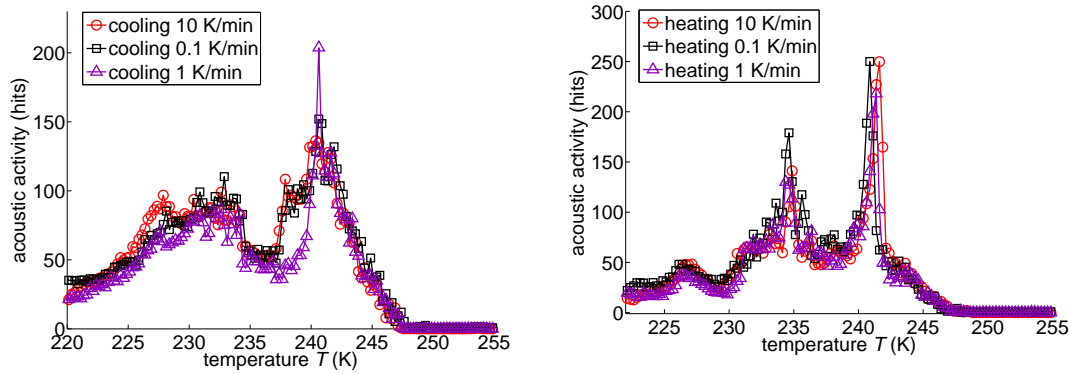


Figure 7.26: Mean acoustic activity of the forward (left) and reverse transitions (right) of the $\text{Fe}_{68.8}\text{Pd}_{31.2}^{\text{single}}$ sample at three selected rates (0.1 K/min, 1 K/min, and 10 K/min).

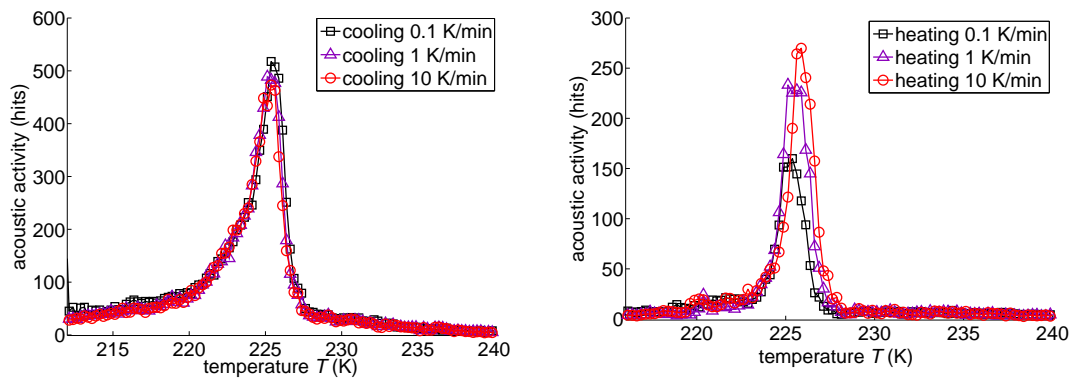


Figure 7.27: Mean acoustic activity of the forward (left) and reverse transitions (right) of the $\text{Fe}_{68.8}\text{Pd}_{31.2}^{\text{poly}}$ sample at three selected rates (0.1 K/min, 1 K/min, and 10 K/min).

a huge offset between the forward and the reverse transition. By contrast, the exponents of the single crystal have almost the same value for both cooling and heating runs. Only the highest and the lowest cooling rates show exceptional behavior. This is not an effect of the rate but can be explained by a training effect (see section 3.2). A training effect occurs during repeated thermal cycling when the sample probes the optimal path through the high dimensional energy landscape. Due to a randomized order, the rates 10 K/min and 0.1 K/min have been performed (by chance) first (for a further discussion see section 8.3).

7. Results

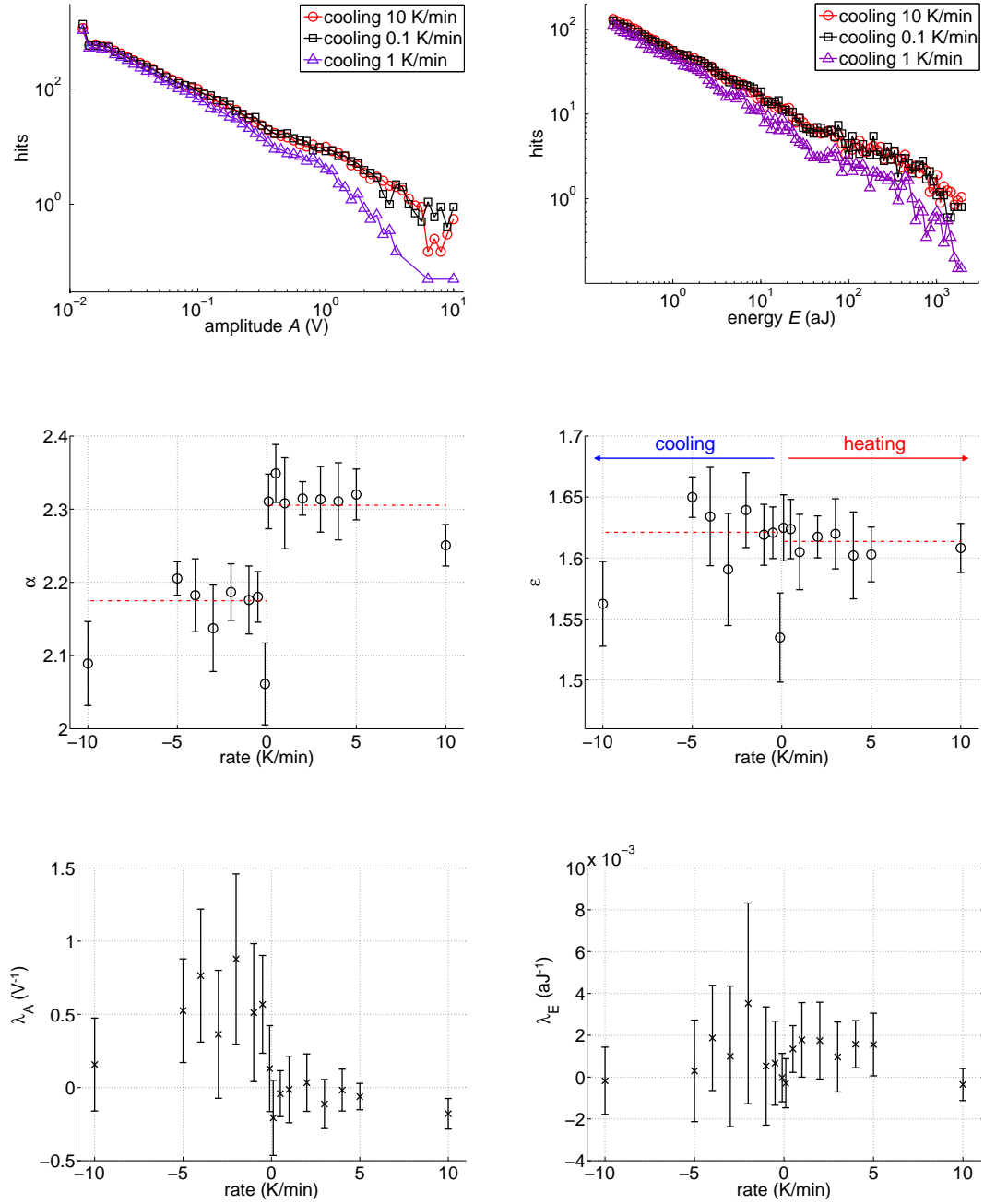


Figure 7.28: Power laws, exponents, and exponential corrections for the forward and reverse transition of the $\text{Fe}_{68.8}\text{Pd}_{31.2}^{\text{single}}$ sample at selected rates.

Top: Log-log histograms of the mean amplitude (left) and energy distributions (right).

Center: Amplitude and energy exponents α (left) and ϵ (right). The exponents have been determined by the maximum likelihood method using the equations $p(A) \propto A^{-\alpha} e^{-\lambda_A A}$ and $p(E) \propto E^{-\epsilon} e^{-\lambda_E E}$. The red dotted lines are guides to the eye indicating the mean values.

Bottom: λ -values of the exponential correction terms $e^{-\lambda_A A}$ (left) and $e^{-\lambda_E E}$ (right) of the amplitude and energy distributions.

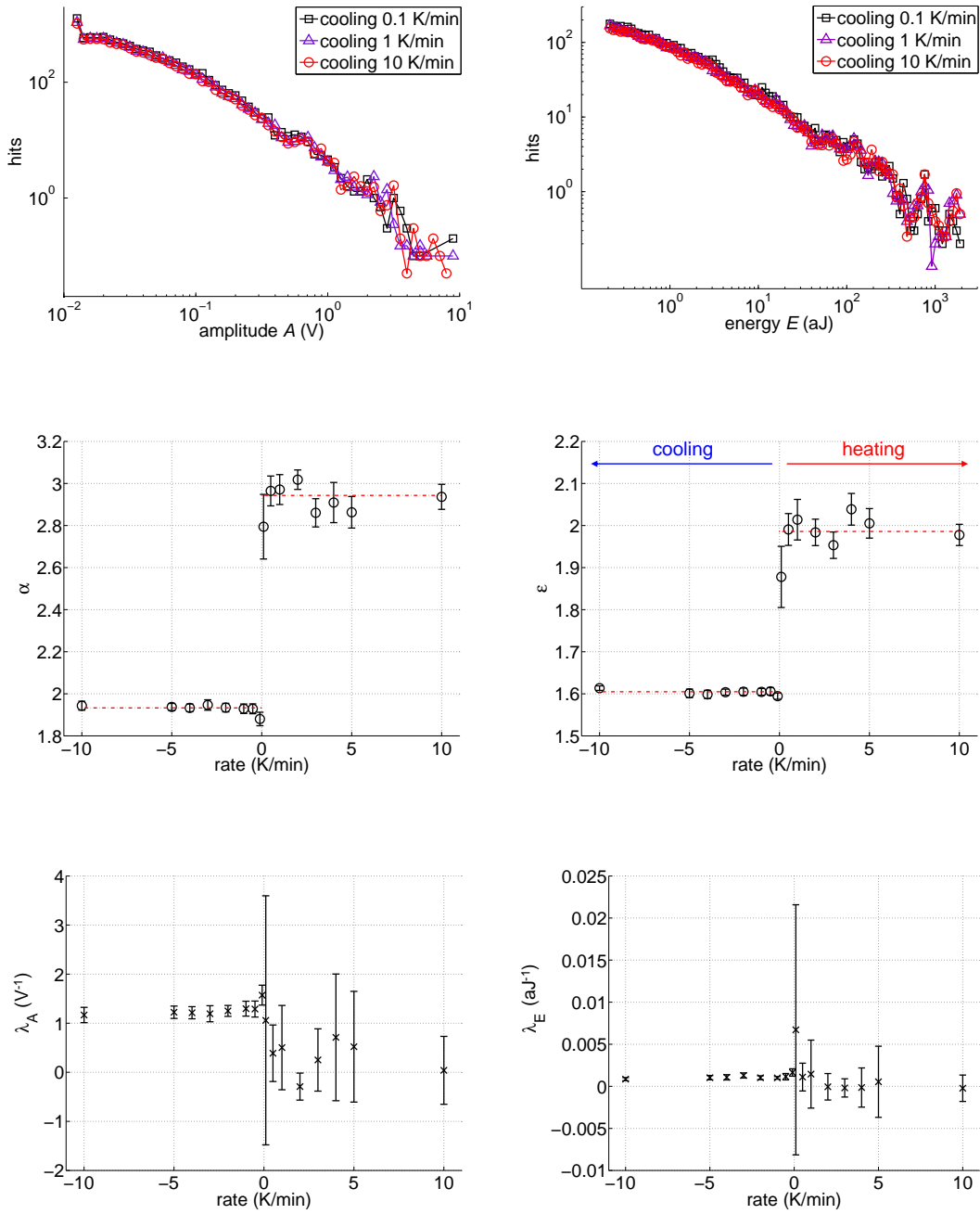


Figure 7.29: Power laws, exponents, and exponential corrections for the forward and reverse transitions of the $\text{Fe}_{68.8}\text{Pd}_{31.2}^{\text{poly}}$ sample at selected rates.

Top: Log-log histograms of the mean amplitude (left) and energy distributions (right).

Center: Amplitude and energy exponents α (left) and ϵ (right). The exponents have been determined by the maximum likelihood method using the equations $p(A) \propto A^{-\alpha} e^{-\lambda_A A}$ and $p(E) \propto E^{-\epsilon} e^{-\lambda_E E}$. The red dotted lines are guides to the eye indicating the mean values.

Bottom: λ -values of the exponential correction terms $e^{-\lambda_A A}$ (left) and $e^{-\lambda_E E}$ (right) of the amplitude and energy distributions.

Table 7.3: Characteristic quantities of the analyzed single- (top) and polycrystalline (bottom) Fe_{68.8}Pd_{31.2} sample.

phase	start temp.	finish temp.	enthalpy	sample	structure
austenite	$A_s \approx 210 \pm 1$ K	$A_f \approx 247 \pm 1$ K	≈ 0.52 J/g	single	fcc
martensite	$M_s \approx 247 \pm 1$ K	$M_f \approx 210 \pm 1$ K	≈ 0.52 J/g	single	fct
austenite	$A_s \approx 210 \pm 1$ K	$A_f \approx 247 \pm 1$ K	≈ 0.28 J/g	poly	fcc
martensite	$M_s \approx 247 \pm 1$ K	$M_f \approx 204 \pm 1$ K	≈ 0.28 J/g	poly	fct

7.2.4 Ni₅₂Mn₂₃Ga₂₅

The Ni₅₂Mn₂₃Ga₂₅ sample analyzed in this work was grown at the *Ames Laboratory* in Iowa using appropriate quantities of nickel (99.99 % pure), electronic grade gallium (99.999 %), and electrolytic manganese (99.9 %). The compounds are cleaned and, for several times, arc melted under argon as inert gas. In order to ensure compositional homogeneity throughout the samples the buttons were remelted. For the Bridgman-like crystal growth the as-cast ingots were placed in alumina crucibles and placed in a refractory metal resistance furnace. For homogenization reasons the ingots are heated to 1620 K for 1 h and are then slowly cooled by withdrawing the sample from the furnace with 2.0 mm/h. In order to minimize vaporization of the manganese, the crystal growth process is run under a certain pressure of purified argon after the chamber and the sample have been outgassed at 1620 K. The mean composition of the sample to be studied has been determined by chemical analysis to be Ni₅₂Mn₂₃Ga₂₅ with an electron per atom concentration of $e/a = 7.56$. The sample shows a composition gradient which leads to a relatively broad martensitic and intermediate transition temperature interval of $M_s = 213$ K and $M_f = 195$ K respectively $M_s^I = 245$ K and $M_f^I = 220$ K for the intermediate transition (without an applied magnetic field or pressure). The crystal has been cut to the dimensions of 10.25 mm x 10.5 mm x 8.2 mm (mass ≈ 7.33 g) with faces parallel to the [001], $[\bar{1}10]$ and [110] crystallographic directions in the parent phase. In the parent phase the crystal has an L₂₁ structure. The martensitic transition is preceded by an intermediate (or premartensitic) transition to a 3M modulated phase [40, 209]. In the product phase the crystal has a 10M pseudo-tetragonal 5-layered modulated structure [142]. The unit cell has the following parameters: $a = 4.2$ Å, $b = 5.5$ Å, $c = 21$ Å; $\alpha = 90^\circ$, $\beta = 91^\circ$, $\gamma = 90^\circ$ [142]. Selected sample properties are summarized in table 7.4. For further details on the preparation process, calorimetric characterization, x-ray analysis of the grain alignment, and neutron scattering experiments on the softening of anomalous phonons see [98, 139].

Figure 7.30 shows the acoustic activity and the heat flux of both the premartensitic transition and the martensitic transition at zero magnetic field. It can be

Table 7.4: Characteristic quantities of the analyzed $\text{Ni}_{52}\text{Mn}_{23}\text{Ga}_{25}$ sample. The temperature values have been estimated from the AE measurements. All values have been taken without an applied field.

phase	start temp.	finish temp.	enthalpy	structure
reverse premar.	$A_s^I = 225 \text{ K}$	$A_f^I \approx 242 \text{ K}$	$\approx (0.15 \pm 0.05) \text{ J/g [142]}$	cubic
premartensite	$M_s^I = 245 \text{ K}$	$M_f^I = 220 \text{ K}$	$\approx (0.15 \pm 0.05) \text{ J/g [142]}$	3M modulated
austenite	$A_s = 200 \text{ K}$	$A_f = 217 \text{ K}$	$\approx 4.13 \text{ J/g}$	$L2_1$
martensite	$M_s = 213 \text{ K}$	$M_f \approx 195 \text{ K}$	$\approx 4.13 \text{ J/g}$	10M pseudo-tetragonal modulated
ferromagnetic	$T_c = 359.5 \text{ K}$	n/a	n/a	n/a

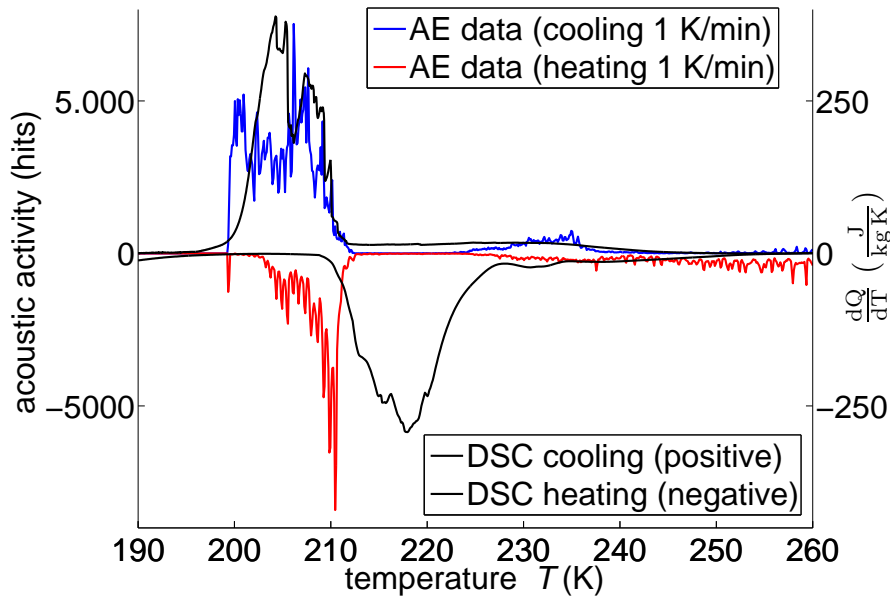


Figure 7.30: Comparison between the acoustic activity and calorimetric data during the premartensitic and martensitic forward and reverse transition of the $\text{Ni}_{52}\text{Mn}_{23}\text{Ga}_{25}$ sample. The temperature cycles have a rate of 1 K/min. An enlargement of the region of the premartensitic transitions can be found in figure 7.31. For clarity reasons, the data of the reverse transition have been plotted with negative values. The excellent matching of the AE data and the DSC data in case of the forward transition must be regarded as accidental as the DSC data is not temperature calibrated.

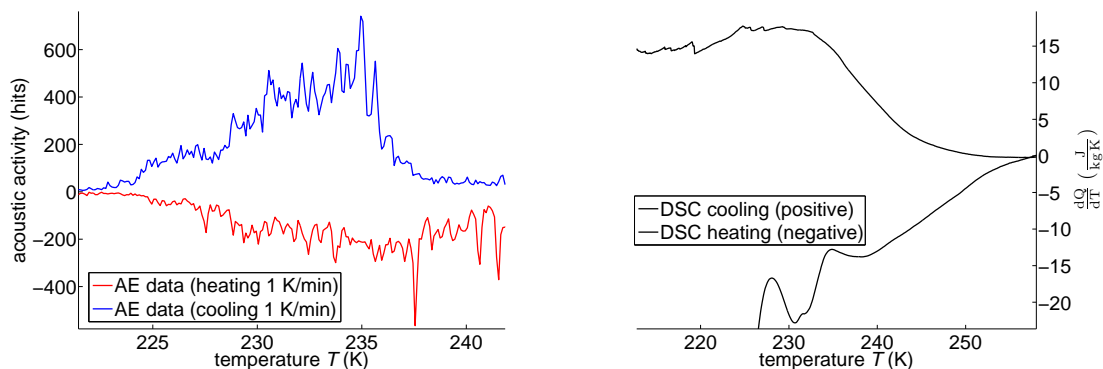


Figure 7.31: Enlargement of the premartensitic region of the $\text{Ni}_{52}\text{Mn}_{23}\text{Ga}_{25}$ sample with the acoustic activity on the left and the calorimetric data on the right. The maximum, arising during cooling, appears to be more pronounced than the maximum during heating. The same holds for the calorimetric data after a proper baseline correction. The cycles have been performed without an applied magnetic field.

seen that both curves are strongly correlated. Furthermore, the calorimetric data are in very good agreement with results of a similar sample [142]. Figure 7.31 shows an enlargement of the premartensitic region of the acoustic activity and the calorimetric data. In the following section the premartensitic and the martensitic transition will be discussed first both as a function of the applied magnetic field, followed by a discussion of the magnetic-field-induced reorientation of martensitic variants. It is worth mentioning that the forward and reverse transition both show monotonic decrease of the total acoustic activity with increasing field. However, in any case the reverse transition exhibits less total acoustic activity than the forward transition, inhibiting further analysis owing to poor statistics.

The analysis of $\text{Ni}_{52}\text{Mn}_{23}\text{Ga}_{25}$ has been performed with an applied magnetic field in two orthogonal orientations along the crystallographic directions $[001]$ and $[\bar{1}10]$. In general, both orientations show similar results. In the following the results with a field applied along the $[001]$ direction will be exemplarily shown. Cases where the field orientation has a significant influence, will be explicitly mentioned and discussed.

Premartensitic transition

The premartensitic transition shows, in analogy to the martensitic transition of the samples discussed before, a strong correlation between the distribution of the acoustic activity and the distribution of the enthalpy released/absorbed during the transition. In addition, the distribution of the amplitude is coupled to the hit duration. This correlation is of special importance, because it enables a filter

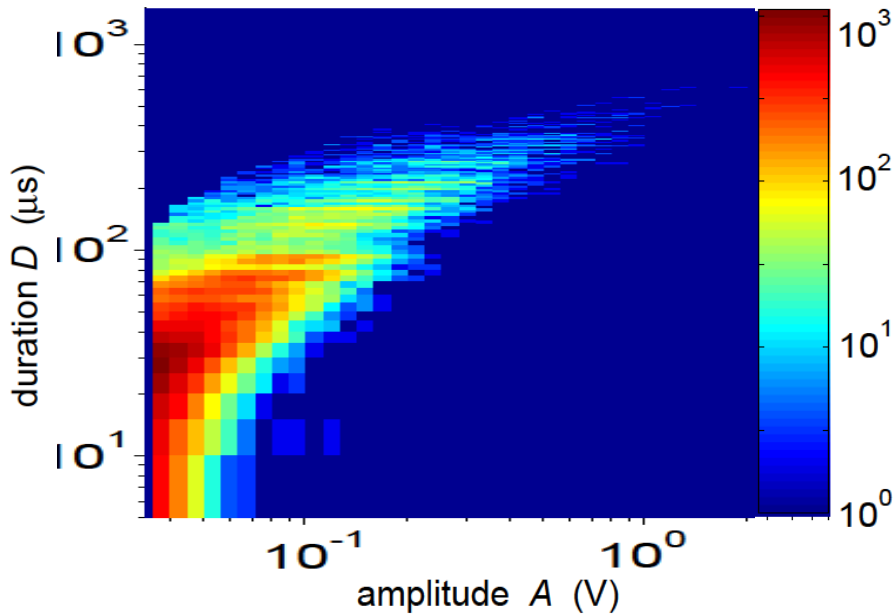


Figure 7.32: Color-coded acoustic activity in a log-log histogram showing the filtered signal distribution of the duration against the amplitude during the forward pre-martensitic transition of the $\text{Ni}_{52}\text{Mn}_{23}\text{Ga}_{25}$ sample.

procedure to discriminate between transition signals and noise (see section 7.1). The typical arrow-like distribution of the filtered signals can be seen in figure 7.32.

Figure 7.33 (a) shows an example of the acoustic activity of the premartensitic transition as a function of temperature during cooling at selected values of the magnetic field applied along the [001] direction. Results show that the acoustic activity is already strongly reduced by small applied fields. Due to the fine binning of 0.1 K, the jerky and intermittent character of the transition dynamics becomes evident, which is a consequence of the interplay of pinning and depinning processes resulting in avalanche kinetics. The total amount of acoustic energy released during the complete intermediate forward transition shows a strict monotonic decrease with increasing fields and leads to a complete suppression at moderate fields of approximately 2.5 kOe (see figure 7.33 (b)). At higher fields no acoustic activity was detected (fields up to 10 kOe have been tested).

The temperature interval, over which AE is detected during cooling, can be associated with the transition region. This enables us to determine a start (M_s^I) and finish (M_f^I) temperature of the forward intermediate transition. These temperatures have been estimated from the first rise of the AE activity above the

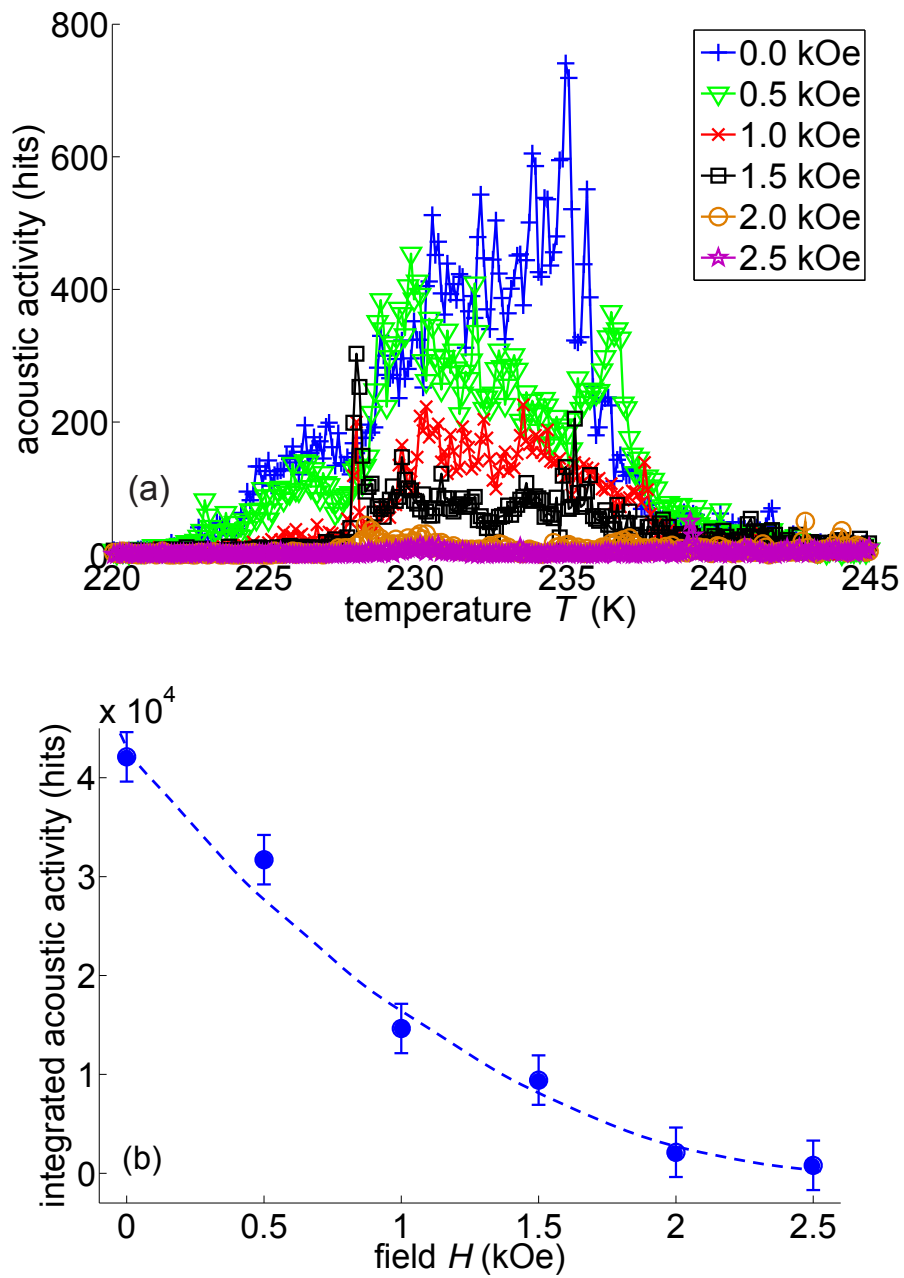


Figure 7.33: Exemplary acoustic activity during the premartensitic forward transition of the $\text{Ni}_{52}\text{Mn}_{23}\text{Ga}_{25}$ sample at selected magnetic fields (a). Integrated acoustic activity during the forward transition at selected fields of the same sample (b). The dotted line is a guide to the eye. In both cases the field was applied along the [001] direction.

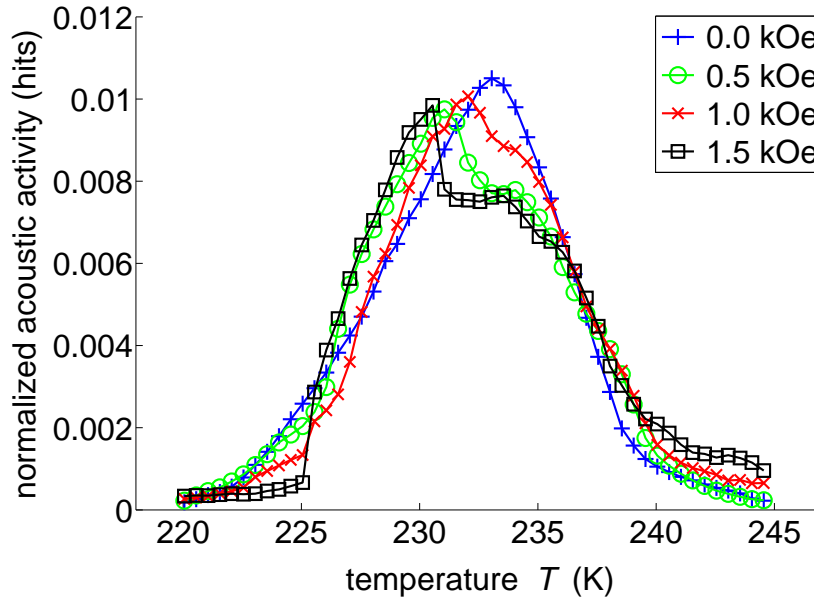


Figure 7.34: Smoothed acoustic activity of the premartensitic forward transition of the $\text{Ni}_{52}\text{Mn}_{23}\text{Ga}_{25}$ sample at selected magnetic fields applied along the $[001]$ direction (normalized to a total acoustic activity of one).

noise threshold and the last significant threshold crossing, respectively. Within error bars the start and finish temperatures are not affected by the applied field and can be estimated to be $M_s^I = 244 \pm 1$ K and $M_f^I = 222 \pm 1$ K. In order to detect a possible shift of the premartensitic transition with the applied magnetic field a normalized and smoothed acoustic emission has been computed from data given in figure 7.33 (a). The normalization factor is the total amount of AE given by $\int_{M_s^I}^{M_f^I} \text{hits}(T) dT$. Smoothing includes 50 bins which is equivalent to ± 2.5 K around the center. This normalized and smoothed acoustic activity at selected magnetic fields is shown in figure 7.34. Interestingly, the maximum of this smoothed acoustic activity shows a shift of about 3 K towards lower temperatures at higher magnetic fields before the AE activity is completely suppressed.

Figure 7.35 shows this shift as a function of the applied field. Because measurements with a magnetic field applied in both directions $[001]$ and $[\bar{1}10]$ revealed very similar results, the peak temperatures T_p of the smoothed AE curves corresponding to both directions have been averaged.

It is worth mentioning that the suppression of the acoustic activity at fields above 2.5 kOe is not an artifact related to the temperature shift towards lower temperatures, resulting in a hypothetical masking of the intermediate transition

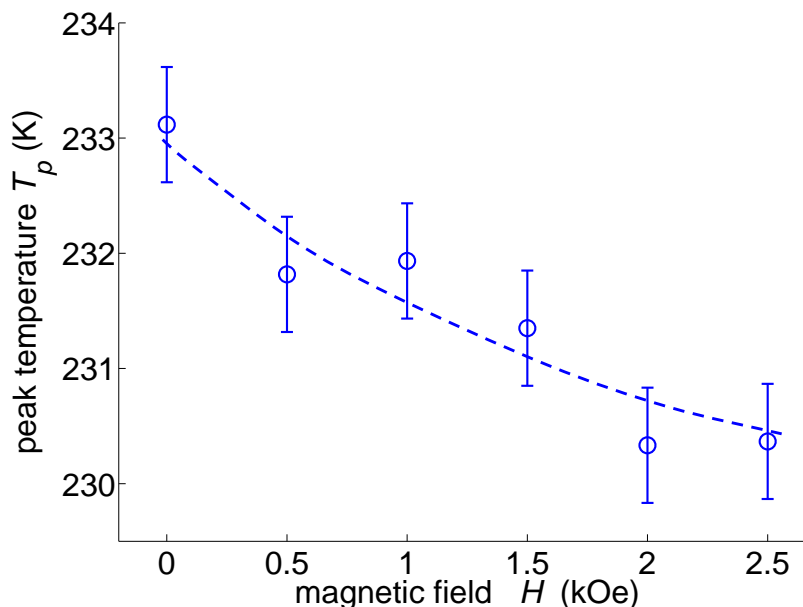


Figure 7.35: Temperature shift of the premartensitic transition of the $\text{Ni}_{52}\text{Mn}_{23}\text{Ga}_{25}$ sample as a function of the applied magnetic field. The dotted line is a guide to the eye.

by the martensitic transition. Both transitions remain well separated by several Kelvin at all applied fields. In fact, in the range of the applied magnetic field, the martensitic transition also shows a shift of a few Kelvin towards lower temperatures (see section 7.2.4 and [91]).

Figure 7.36 shows the distribution of the extracted characteristic AE signal features (duration, amplitude, and energy) at selected applied magnetic fields on a log-log scale. All features show a power law behavior (amplitude and energy over more than two decades) for fields up to 1.5 kOe. For higher applied fields the acoustic activity is either absent or so low that the poor statistics does not allow quantitative conclusions.

A fit of the power-law behavior of the regions unaffected by the window effect⁷ has been performed using the maximum likelihood method. The fitted exponents δ , α , and ϵ of the duration, amplitude, and energy as a function of the magnetic field are shown in figure 7.37. It is worth mentioning that the exponents of all corresponding features increase with increasing fields and saturate at approximately 1.5 kOe where the acoustic activity is already very low (almost suppressed). Therefore, the exponents show that higher fields lead to signals of

⁷The window function effect describes the impact of non-detectable hits due to hardware limitations on the results (for more details see the discussion in section 8.1).

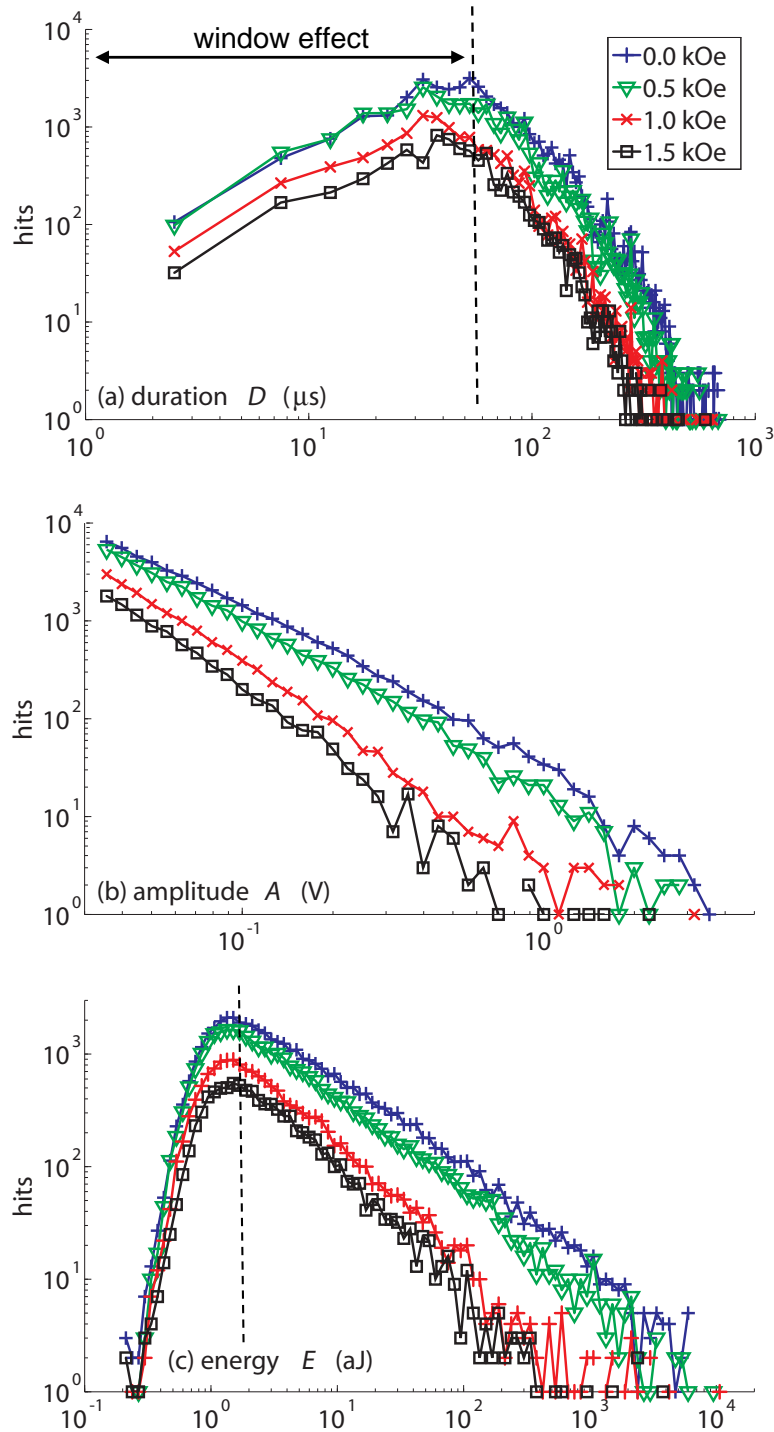


Figure 7.36: Duration (a), amplitude (b), and energy (c) distributions of the premartensitic forward transition of the $\text{Ni}_{52}\text{Mn}_{23}\text{Ga}_{25}$ sample at selected fields applied along the [001] direction. Because of an amplitude threshold, the amplitude distribution shows a sharp cutoff whereas the duration and energy distributions show a window effect. Data affected by the window effect cannot be used for statistical analysis (see introduction of chapter 8).

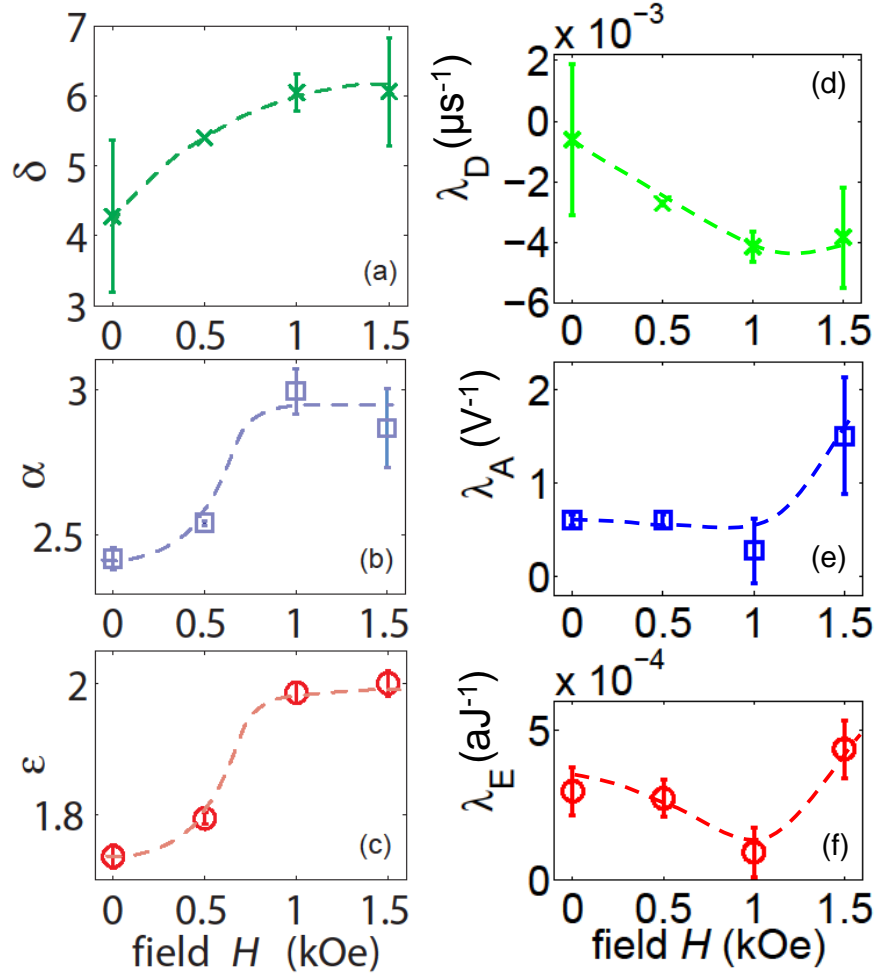


Figure 7.37: Exponents and exponential corrections for the premartensitic transition of the $\text{Ni}_{52}\text{Mn}_{23}\text{Ga}_{25}$ sample. Exponents with error bars for the duration (a), the amplitude (b), the energy (c), and the corresponding λ -values (d - f) as a function of the magnetic field applied in [001] direction. The values have been determined by the maximum likelihood method using the equation $p(X) \propto X^{-x} e^{-\lambda_x X}$. The dotted lines serve as guides to the eye.

Table 7.5: Zero field exponents for the AE distributions of the premartensitic transition obtained by a maximum likelihood fit. The inverse of λ indicates where the exponential correction becomes relevant.

feature	exponent at zero field	λ^{-1}
duration	4.3 ± 1.1	$(353 \pm 146) \mu\text{s}$
amplitude	2.44 ± 0.03	$(1.34 \pm 0.49) \text{V}$
energy	1.73 ± 0.02	$(3620 \pm 1060) \text{aJ}$

smaller amplitudes and energies with shorter durations. It is noteworthy that in case of the amplitude a zero field exponent $\alpha = 2.3 \pm 0.15$ has been reported [139], which is in very good agreement with the result of this work. The zero field exponents are listed in table 7.5. The λ -values of the exponential correction terms to the power law behavior are plotted in figure 7.37. In order to estimate the importance of the exponential correction the inverse of λ_X has been calculated and compared with the corresponding value X . For all features λ_X^{-1} is of the same order as the highest occurring values X_{max} . For these high values, power laws naturally have poor statistics and the exponential term consequently has no relevance (see table 7.5 and figure 7.37).

Results for applied fields along both crystallographic directions [001] and $[\bar{1}10]$ are quantitatively in good agreement with each other. In contrast to results from the martensitic transition, where the effect of a field is considerably more pronounced when applied along [001] than along $[\bar{1}10]$ (see section 7.2.4 and [91]), here the cubic symmetry is preserved (at least on average) and no variants are formed. Consequently the field direction cannot couple to any anisotropies.

Martensitic transition

In the following section, the magnetic field-dependence of the martensitic transition will be studied. Figure 7.38 (a) shows examples of the acoustic activity as a function of temperature during the forward martensitic transition on cooling at selected values of the magnetic field applied along the [001] direction. The acoustic activity is obtained as the number of AE events (hits) recorded per temperature interval of 0.1 K. Results show that the energy released in the form of acoustic waves is emitted intermittently, thus confirming the jerky character of the transition. The accumulated number of hits as a function of temperature is depicted in figure 7.38 (b). It shows that the integrated number of hits over the whole transition increases with the applied magnetic field for the forward transitions. It is worth mentioning that the obtained values represent a lower bound to the total amount of possible AE events since it was not possible to guarantee that the temperature was sufficiently lowered to complete the transition,

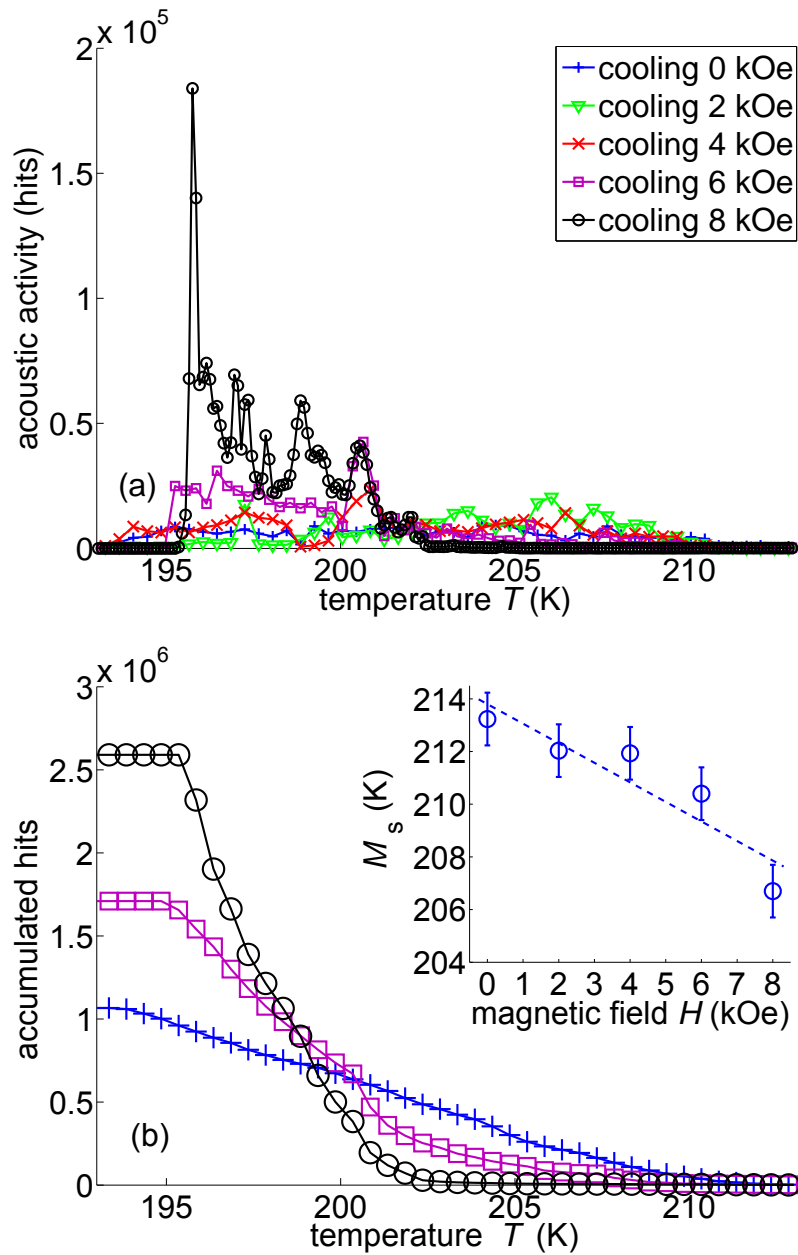


Figure 7.38: Acoustic activity of the $\text{Ni}_{52}\text{Mn}_{23}\text{Ga}_{25}$ sample during the martensitic forward transition on cooling at selected values of the field applied along the [001] direction (a). Accumulated acoustic activity during forward transition at selected fields applied along the [001] direction (b). Inset: Martensitic start temperature M_s as a function of the applied magnetic field with a dotted line as a guide to the eye.

especially at higher magnetic fields. For the reverse transition on heating the integrated amount of hits is smaller than for the forward transition and remains basically independent of the applied field. The transition temperature M_s was estimated as usual from the first detected rise in AE above the noise threshold. The dependence of M_s on the applied magnetic field is shown in the inset of figure 7.38 (b). The obtained decrease of M_s with increasing the field is consistent with results reported in [74] where transition temperatures were estimated from resistivity measurements.

The distributions of hit amplitudes (A) and energies (E) corresponding to the forward transition at selected values of the applied magnetic field are shown in figure 7.39 (top) on a log-log scale. In all cases, the distributions display power law behavior over more than two and a half decades in amplitude and over more than six decades in energy. Fitted values of α and ϵ describing the amplitude and energy distribution are shown in figure 7.39 (center). The corresponding λ -values of the exponential correction terms are without exception equal or close to zero and depicted in figure 7.39 (bottom).

For both forward and reverse transitions the exponents α and ϵ decrease with increasing the field. Results essentially indicate that by increasing the field, signals of higher amplitude and energy are emitted. This behavior is consistent with the reported increase of dissipated energy with increasing the applied field obtained from calorimetric measurements [100].

Magnetic-field-induced variant rearrangement

In this section, the magnetic-field-induced rearrangement of martensitic variants at constant temperature will be studied. The magnetic field has been applied either along the crystallographic direction $[001]$ or $[\bar{1}10]$. As will be shown in the discussion in section 8.4.3, both field directions give rise to similar results. The field cycles between 0 kOe and 10 kOe have been performed either at a high or at a low rate with periods of $\tau_{mf} = 130$ s (quick cycles) respectively $\tau_{mf} = 1300$ s (slow cycles). The different field cycle rates have been found to influence the results considerably.

Figure 7.40 shows the acoustic activity, the energy, and the applied magnetic field as a function of time with a time binning of 1 s. The cycles of the magnetic field applied along the $[\bar{1}10]$ crystallographic direction extend from 0 kOe to 10 kOe (no field inversion) with $\tau_{mf} = 130$ s. Results show the highest acoustic activity and energy during the first cycle. With increasing run numbers the acoustic activity decreases monotonically. It is important to note that the recorded amount of AE during the first cycle represents a lower bound to the total activity due to memory overflow hardware limitations of the AE acquisition system. During slow cycles and for higher cycle numbers (2, 3, ...) of quick cycles this problem does not arise anymore. It is worth mentioning that AE is not only

7. Results

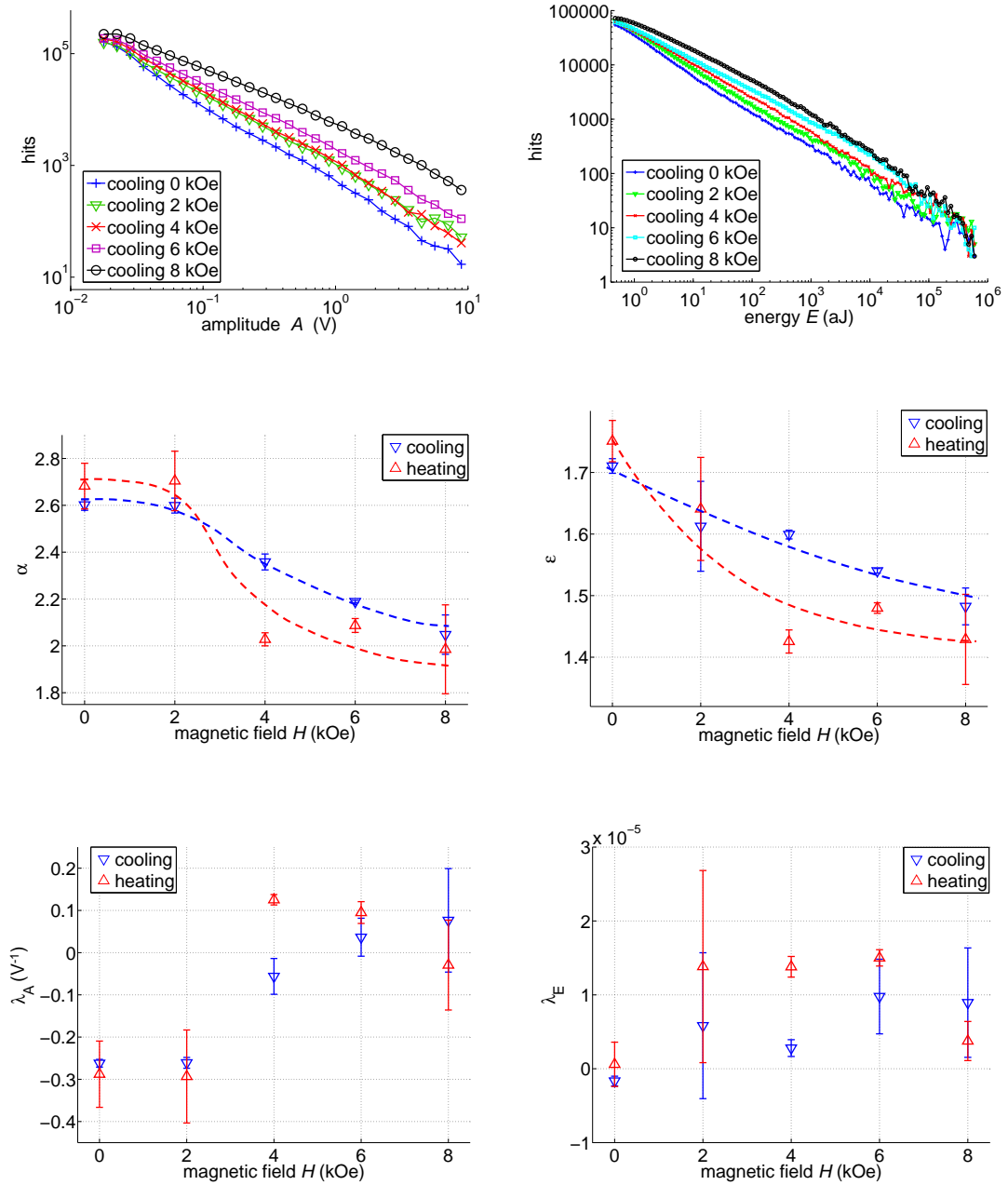


Figure 7.39: Power laws, exponents, and exponential corrections for the forward and reverse martensitic transition of the $\text{Ni}_{52}\text{Mn}_{23}\text{Ga}_{25}$ sample at selected magnetic fields applied along the [001] direction.

Top: Amplitude (left) and energy (right) distributions of the forward transition. Note that the energy distributions cover more than 6 decades.

Center: Amplitude α (left) and energy exponents ϵ (right). The dotted lines serve as a guide to the eye indicating the trends.

Bottom: λ -values of the exponential correction terms $e^{-\lambda_A A}$ (left) and $e^{-\lambda_E E}$ (right) of the amplitude and energy distributions.

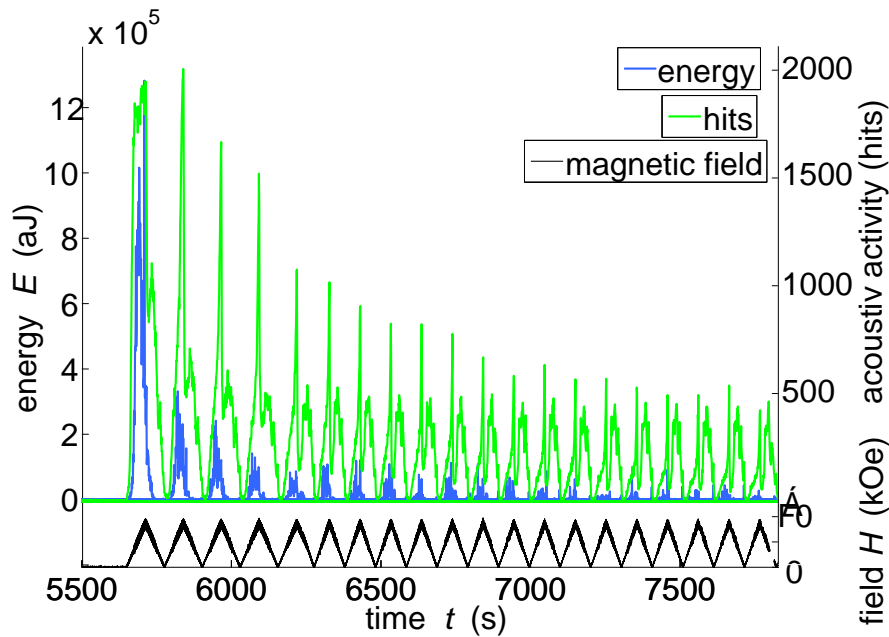


Figure 7.40: Acoustic emission by the magnetic-field-induced rearrangement of martensitic variants in the martensitic phase of the $\text{Ni}_{52}\text{Mn}_{23}\text{Ga}_{25}$ sample measured in acoustic activity and energy versus time. The maximal acoustic activity and energy detected during the first field cycle represent a lower bound due to hardware restrictions. The lower part of the figure displays the magnetic field applied along $[\bar{1}10]$ with a period of $\tau_{mf} = 130$ s.

measured during increasing fields, which is associated with variant alignment, but as well during decreasing fields, which is assumed to be associated with a back rotation of some variants due to a bias force, as reported in literature, e. g. [113]. The observation of AE detected in higher run numbers (cycle 2, 3, ...) supports this assumption.

The distributions of the amplitude and the energy display power law behavior for increasing and decreasing fields and for both slow and quick cycles, as can be seen in figure 7.41 (top) for the quick cycles and in figure 7.42 (top) for the slow cycles. Due to λ -values, which are in all cases equal or close to zero, the exponential terms are essentially irrelevant and the power laws cover more than two and a half decades in amplitude and more than four decades in energy.

Figure 7.41 (bottom) and 7.42 (bottom) show the amplitude exponents determined by the maximum likelihood method corresponding to quick and slow cycles. The energy exponents (not depicted here) show similar results. The amplitude exponents of the quick cycles have a constant value within the error bars and

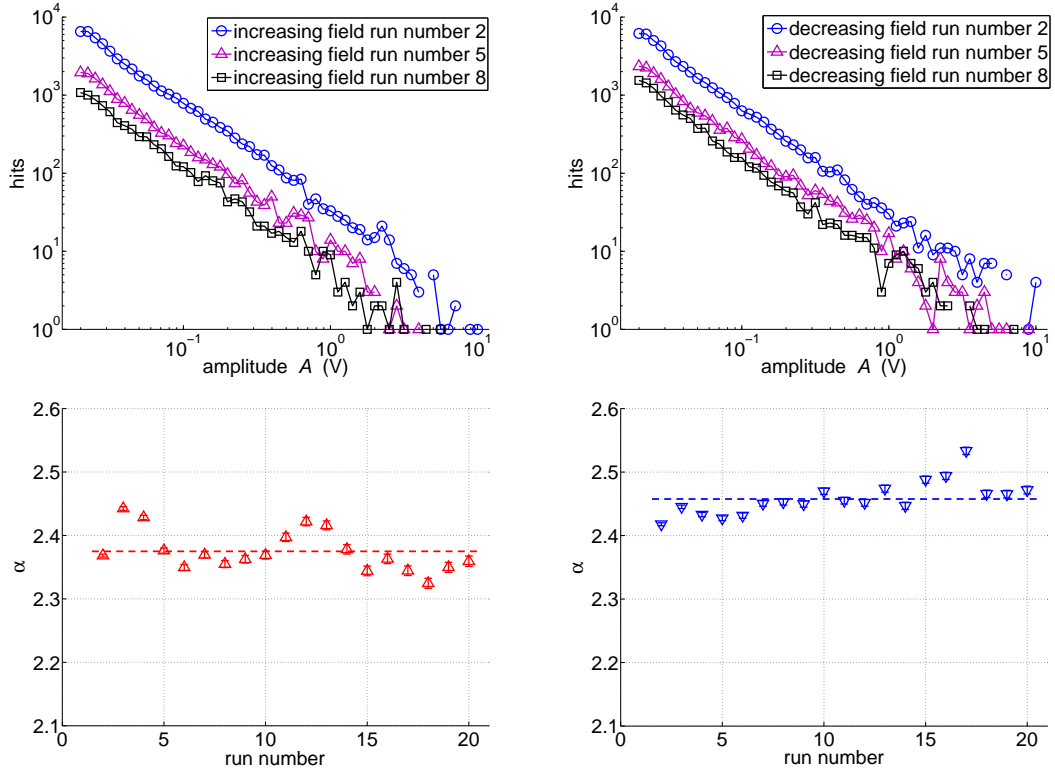


Figure 7.41: Amplitude distributions (top) and corresponding exponents (bottom) detected during quick cycles of the magnetic field in the martensitic phase of the $\text{Ni}_{52}\text{Mn}_{23}\text{Ga}_{25}$ sample. The quick magnetic field cycles have an amplitude of 10 kOe, a period of $\tau_{mf} = 130$ s, and are applied along the [001] direction.

Top: The amplitude distributions on the left belong to increasing fields, the distributions on the right to decreasing fields.

Bottom: Exponents of the amplitude distribution with increasing fields on the left and decreasing fields on the right. The exponents of the first cycle have been ignored due to a memory overflow arising from hardware limitations. The exponent values have been determined by the maximum likelihood method using the equation $p(A) \propto A^{-\alpha} e^{-\lambda_A A}$. The dotted lines are guides to the eye and represent a mean value.

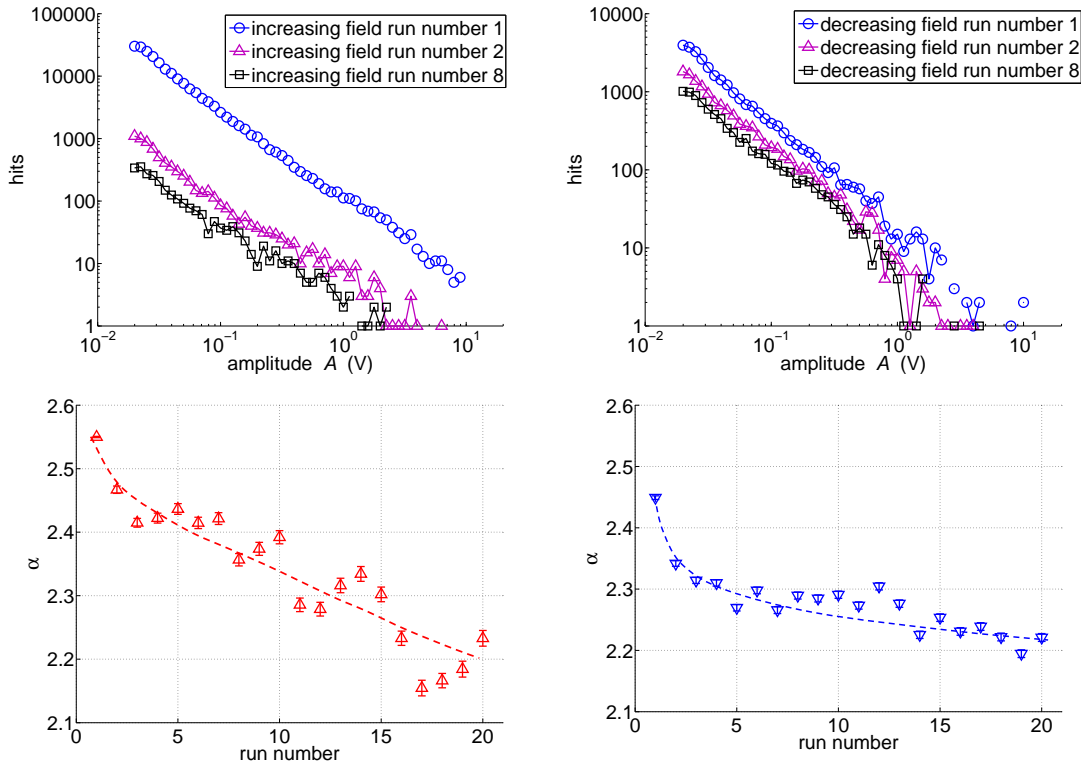


Figure 7.42: Amplitude distributions (top) and corresponding exponents (bottom) detected during slow cycles of the magnetic field in the martensitic phase of the $\text{Ni}_{52}\text{Mn}_{23}\text{Ga}_{25}$ sample. The slow magnetic field cycles have an amplitude of 10 kOe, a period of $\tau_{mf} = 1300$ s, and are applied along the [001] direction.

Top: The amplitude distributions on the left belong to increasing fields, the ones on the right to decreasing fields.

Bottom: Exponents of the amplitude distribution with increasing fields on the left and decreasing fields on the right. The values of the exponents have been determined by the maximum likelihood method using the equation $p(A) \propto A^{-\alpha} e^{-\lambda_A A}$. The dotted lines serve as guides to the eye.

do not depend on the cycle number.⁸ By contrast, the amplitude exponents of the slow cycles decrease with increasing run numbers, indicating a shift of the signal towards higher amplitudes and energies. A new approach explaining the rate-dependent exponent behavior within the framework of martensite stabilization will be discussed in section 8.4.3.

⁸The exponents of the first cycle have been ignored due to the memory overflow hardware limitation.

8 Discussion

In this chapter, the results presented in chapter 7 will be discussed. Additionally, the results gained in this work are compared with each other and with literature.

First, this chapter deals with a few observations that are shared by all analyzed samples and can be understood as general characteristics of martensitic shape memory materials. Afterwards the results of each material class will be discussed in a separate section. For the sample of $\text{Ni}_{63}\text{Al}_{37}$, the rate-dependence of the total acoustic activity and the exponents will be explained by an interaction of isothermal kinetics and the different driving rates in the presence of inherent disorder. Additionally, it will be shown that fingerprint-like changes arising in the AE signals first occur in the forward transition and are then inherited by the reverse transition (see section 8.1). Dealing with the sample of $\text{Au}_{50.5}\text{Cd}_{49.5}$, the author proposes that a martensite stabilization process is responsible for stronger AE signals under decreasing heating rates (see section 8.2). The discussion on the $\text{Fe}_{68.8}\text{Pd}_{31.2}$ samples concentrates on the common characteristics and differences between the single and the polycrystalline sample (see section 8.3). The results of $\text{Ni}_{52}\text{Mn}_{23}\text{Ga}_{25}$ will be reviewed in three subsections: First, the effect of the magnetic field on the premartensitic transition, which suppresses the acoustic activity and leads to an overall weakening of the first order character, will be discussed (see section 8.4.1). Next, modifications of the martensitic transition under an applied field will be analyzed (see section 8.4.2). Finally, it will be dealt with the magnetic-field-induced rearrangement of martensitic variants and the influence of twin stabilization (see section 8.4.3).

AE experiments and calorimetric measurements are interesting techniques for analyzing structural first order phase transitions. On the one hand they are sensitive towards different observables. Nevertheless they reveal very similar results on the other hand. Due to this strong correlation, which has been confirmed for all samples analyzed in this work, they can both serve as reference measurements. Furthermore, quantitative correlations between both techniques can be found by comparing curve peak ratios (see for example $\text{Fe}_{68.8}\text{Pd}_{31.2}^{\text{single}}$ or $\text{Ni}_{63}\text{Al}_{37}$). This observation is in agreement with results presented in literature (see e. g. [21]). AE experiments are particularly suitable for the analysis of structural phase transitions due to their high sensitivity to small transforming domains and their high time resolution. Owing to this high time resolution the jerky and intermittent character of the transition can be uncovered. Figure 8.1 exemplarily shows the

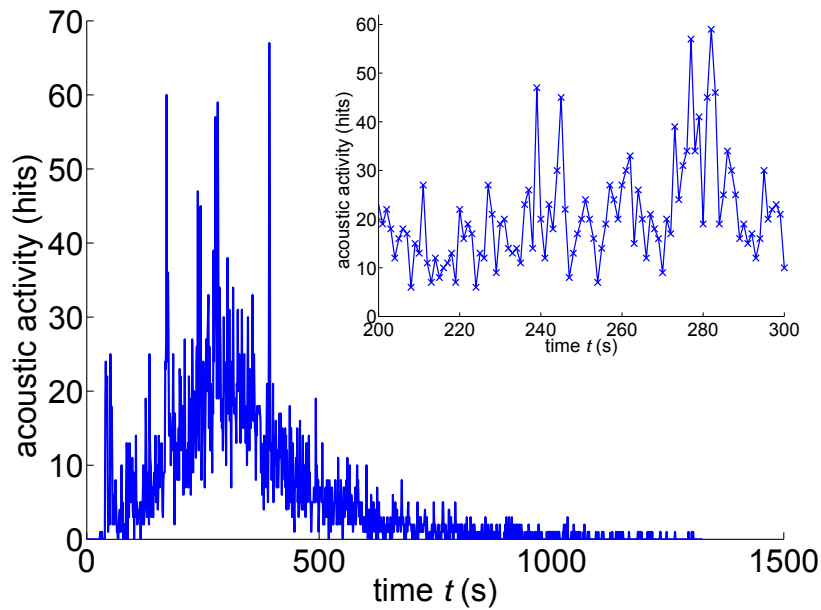


Figure 8.1: Acoustic activity of the martensitic transition of the $\text{Au}_{50.5}\text{Cd}_{49.5}$ sample at a rate of 0.1 K/min . The bin width of 1 s is equivalent to a temperature bin width of 1.667 mK . The inset shows a section of the activity between 200 s and 300 s . Due to the fine binning the jerky transition character is evident.

jerky acoustic activity of $\text{Au}_{50.5}\text{Cd}_{49.5}$ during the martensitic transition at a rate of 0.1 K/min with a fine time binning of 1 s , which is equivalent to a temperature binning of 1.667 mK .

For a further analysis of the intermittent transition dynamics a comparison is carried out between total time without signal (*silence*) and total time with signal. The former is the sum of all waiting times between hits and the latter the sum of all hit durations. This comparison is as well interesting for the evaluation whether

a pile up of AE events¹ is a relevant mechanism and needs to be considered for the interpretation of the results [135, 201].

The total sum of the durations of all AE hits occurring during a transition can be calculated to be less than one second regardless of the sample. The ratio of the sum of all hit durations to the total silence time is influenced by three factors: (i) the temperature rate, (ii) the width of the transition interval, and (iii) the acoustic activity of the sample. Exemplarily the ratios are given for $\text{Au}_{50.5}\text{Cd}_{49.5}$ and $\text{Ni}_{63}\text{Al}_{37}$, which have very distinct characteristics. Because of its narrow transition interval and a high acoustic activity $\text{Au}_{50.5}\text{Cd}_{49.5}$ has a signal to silence ratio of approximately $1/30$ at a rate of 10 K/min , which is the largest value of all analyzed samples. By contrast, $\text{Ni}_{63}\text{Al}_{37}$ has a ratio of approximately $1/500$ at a rate of 10 K/min and approximately $1/50000$ at a rate of 0.1 K/min , because of a quite broad transition interval. These numbers show that the sample response to constant cooling respectively heating is discontinuous in nature. Moreover, it reveals that the transition does not move on until a sufficiently large undercooling is realized to enable jumps towards the next metastable state.

Besides this integrated information of total signal and silence times it is important to analyze whether the AE signals cluster or show a homogeneous distribution. A very fine time binning of 1 ms , which is equivalent to a temperature binning of 0.16 mK at a rate of 10 K/min and $1.6\text{ }\mu\text{K}$ at a rate of 0.1 K/min , has been chosen to answer this question. Results show a rather uniform distribution of the AE signals. Clustering is very unlikely to occur, even at the highest rates in the areas of most activity. In an interval of 1000 bins of 1 ms , exemplarily analyzed, clustering of three or more events could not be found more than five times.

It can be concluded that under given experimental parameters a pile up of AE events is not relevant and cannot be considered the reason for rate-dependent behavior of the acoustic activity (see discussion on $\text{Ni}_{63}\text{Al}_{37}$ in section 8.1) or the rate-dependence of exponents (see discussion on $\text{Au}_{50.5}\text{Cd}_{49.5}$ in section 8.2).

In contrast to the irrelevant impact of a signal pile up, hardware limitations can cause a window effect that potentially affects the AE results. Figure 8.2 shows the window effect concerning the AE results of this work in a four-quadrant-histogram

¹Higher rates lead to a reduction of the time between successive signals which can cause a pile up of two or more acoustic events. This overlap can have the following consequences: (i) A constructive interference, leading to an increase of the signal energy. (ii) A destructive interference leading to a decrease of the signal energy. (iii) A superposition of both effects. The constructive pile up can have two opposing effects: On the one hand, it can lead to a smaller number of hits because two or more hits above the threshold merge and form a new hit. Consequently, the detected hits have a higher energy resulting potentially in smaller exponents. On the other hand, it is possible that two or more hits below the threshold pile up and form a hit that exceeds the threshold. In this scenario the total number of hits increases and new hits have a lower energy leading to higher exponents. In the case of destructive interference the hit number and energy is always reduced. The resulting effect in real measurements is assumed to be a mixture of constructive and destructive interference.

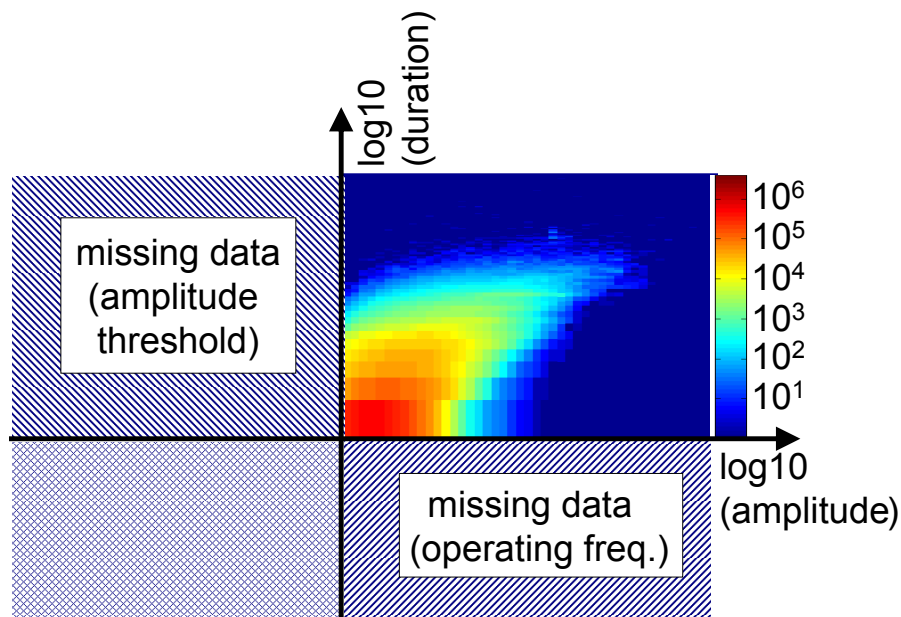


Figure 8.2: The four quadrants of all possible amplitude and duration values in a log-log histogram of the martensitic transition in the $\text{Ni}_{63}\text{Al}_{37}$ sample. The first quadrant shows the color-coded amplitude-duration distribution including all accessible data. The other three quadrants are not accessible due to hardware limitations.

of duration versus amplitude. As indicated by the blue hatched areas only one of the four quadrants contains measurable data, whereas the other three quadrants contain signals that are not accessible due to amplitude and/or time window function effects. It is worth mentioning that the amount of hits discriminated due to the amplitude threshold is much larger than the number of hits discriminated due to their short duration (see figure 8.3 and its discussion below).

The amplitude threshold is an adjustable parameter in order to distinguish between noise and signal (see figure 4.3). The duration hardware limitation arises from the maximal transducer operating frequency of 750 kHz, which leads to a minimal duration of approximately $1.3 \mu\text{s}$. Due to its high sampling frequency of 40 MHz the time resolution of the AE acquisition system is no additional limiting factor. Because of the correlation between duration and amplitude, as can be seen in figure 4.3, and the amplitude and the energy as will be shown later (see equation 8.2), each window function has an influence on the other AE features. The amplitude threshold of approximately $15 \mu\text{V}$ (see section 4.1) leads to a deviation from power law behavior both in duration and amplitude. Whereas the duration distribution shows a rather large deviation, the energy distribution is only affected over a small energy interval, as can be exemplarily seen in figure 8.3

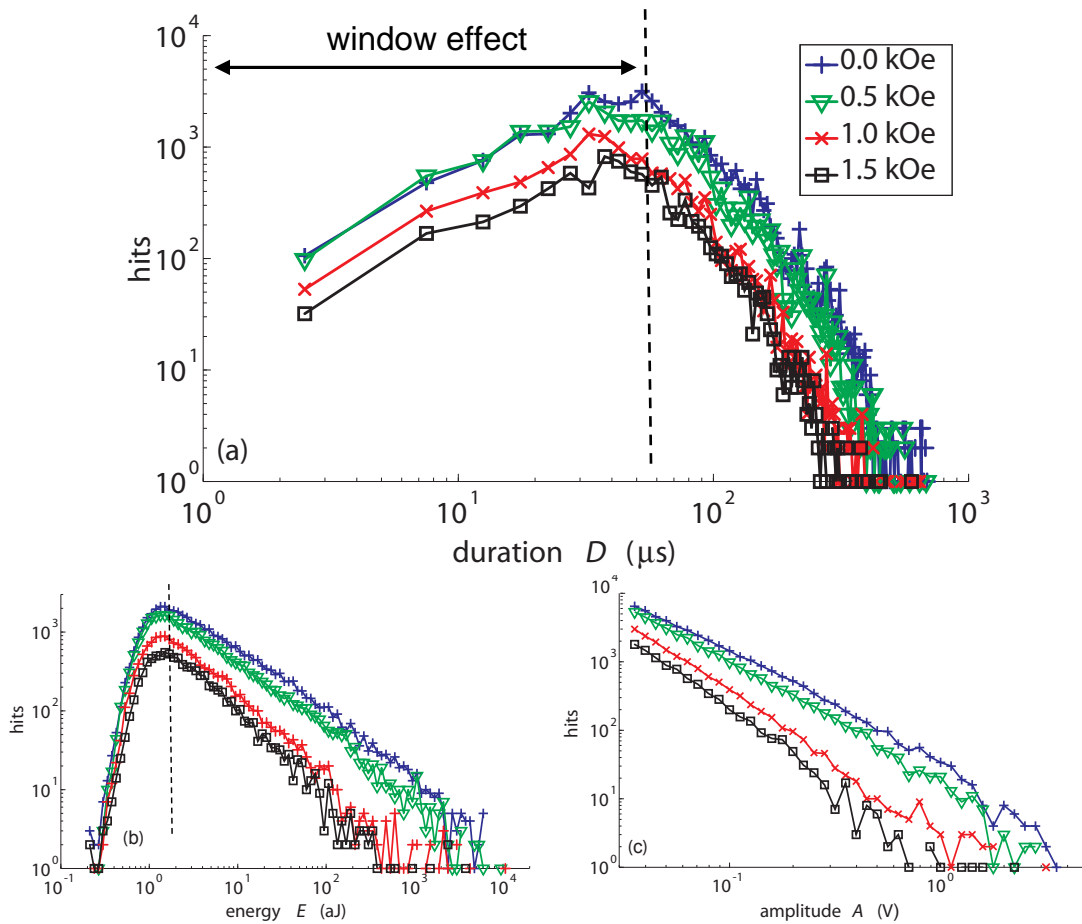


Figure 8.3: Amplitude window effect and its influence on the power law distributions of the duration (a), the energy (b), and the amplitude (c).

(a) and (b). The cutoff due to time or energy window functions has no measurable influence on the amplitude data, as can be seen by the well defined amplitude power laws in figure 8.3 (c). As a summary figure, 8.4 indicates by the red hatched area which type of data is most influenced by the window functions.

AE features reveal correlated behavior, as shown by the duration-amplitude histograms, indicating that hits with large amplitudes are accompanied by large durations. Because of the arrow-like broad shape of these histograms, which look qualitatively the same for all samples, the correlation is not strict and cannot be formulated as a scaling relation. By contrast, the values of the amplitude and energy exponents α and ϵ suggest the existence of a generic statistical dependence $E \propto A^2$. For simplicity reasons and due to their limited influence, the exponential correction terms will not be considered in the following calculation yielding a

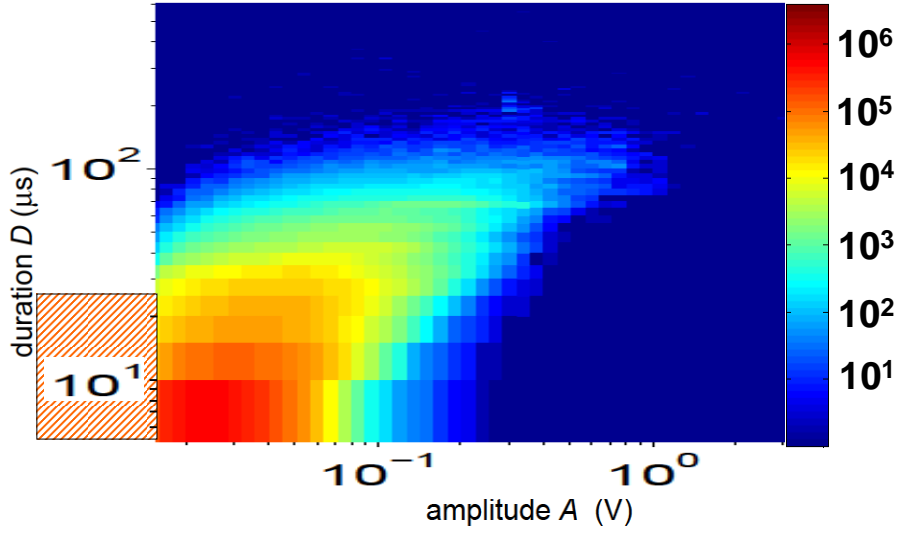


Figure 8.4: Color-coded acoustic activity in a log-log histogram showing the duration against the amplitude of all measurable AE events. The red hatched area indicates a region of strong acoustic activity with low amplitudes and short durations, which cannot be detected owing to hardware settings causing a window effect.

change of variables of the power law probability densities. Thus, the amplitude A can be described by $p(A)dA \propto A^{-\alpha}dA$ and the energy E by $p(E)dE \propto E^{-\epsilon}dE$. The approach $E \propto A^z$ leads to

$$\begin{aligned}
 p(E)dE &\propto E^{-\epsilon}dE \\
 &\propto A^{-z\epsilon}dE \\
 &\propto A^{-z\epsilon}A^{z-1}dA \\
 &\propto A^{-z(\epsilon-1)-1}dA.
 \end{aligned} \tag{8.1}$$

By comparing the expression with $p(A)dA \propto A^{-\alpha}$ the following scaling relation can be deduced

$$z = \frac{\alpha - 1}{\epsilon - 1}. \tag{8.2}$$

The mean z value of all measurements can be calculated to be $z = 1.99 \pm 0.19$, as can be seen in tables 8.1 and 8.2, which summarize all exponents determined experimentally in this work.

The resulting dependence of $E \propto A^2$ can directly be tested with experimental data by plotting a cloud map of E versus A . Figure 8.5 shows a typical example originating from cooling runs of $\text{Fe}_{68.8}\text{Pd}_{31.2}^{\text{single}}$, which is in very good agreement with the proposed scaling relation $E \propto A^z$. Similar plots for other samples and heating runs reveal the same good agreement.

Table 8.1: Part I of the overview of the experimentally determined mean exponents of the rate-dependent measurements. In cases of detected significant rate-dependence ($\text{Au}_{50.5}\text{Cd}_{49.5}$, $\text{Ni}_{63}\text{Al}_{37}$) the corresponding values are listed explicitly. The z value describes the scaling relation between amplitude and energy $\alpha^{-1}/\epsilon^{-1} = z$. Abbreviations: r = rate, fwd = forward transition, and rev = reverse transition.

sample	transition	rate	α	ϵ	z
$\text{Ni}_{63}\text{Al}_{37}$	fwd	0.1 K/min	3.41 ± 0.07	2.23 ± 0.03	1.95 ± 0.11
$\text{Ni}_{63}\text{Al}_{37}$	fwd	0.5 K/min	3.29 ± 0.04	2.18 ± 0.01	1.94 ± 0.06
$\text{Ni}_{63}\text{Al}_{37}$	fwd	1 K/min	3.27 ± 0.04	2.17 ± 0.02	1.94 ± 0.07
$\text{Ni}_{63}\text{Al}_{37}$	fwd	2 K/min	3.25 ± 0.04	2.15 ± 0.02	1.96 ± 0.06
$\text{Ni}_{63}\text{Al}_{37}$	fwd	3 K/min	3.21 ± 0.03	2.14 ± 0.02	1.94 ± 0.06
$\text{Ni}_{63}\text{Al}_{37}$	fwd	4 K/min	3.24 ± 0.02	2.14 ± 0.01	1.96 ± 0.04
$\text{Ni}_{63}\text{Al}_{37}$	fwd	5 K/min	3.25 ± 0.02	2.15 ± 0.01	1.96 ± 0.04
$\text{Ni}_{63}\text{Al}_{37}$	fwd	10 K/min	3.18 ± 0.03	2.12 ± 0.01	1.95 ± 0.04
$\text{Ni}_{63}\text{Al}_{37}$	rev	mean all r	3.14 ± 0.05	2.15 ± 0.02	1.86 ± 0.08
$\text{Au}_{50.5}\text{Cd}_{49.5}$	fwd	mean all r	3.732 ± 0.04	2.38 ± 0.05	1.98 ± 0.10
$\text{Au}_{50.5}\text{Cd}_{49.5}$	rev	0.1 K/min	2.85 ± 0.26	2.12 ± 0.09	1.66 ± 0.37
$\text{Au}_{50.5}\text{Cd}_{49.5}$	rev	0.5 K/min	3.76 ± 0.23	2.50 ± 0.08	1.84 ± 0.25
$\text{Au}_{50.5}\text{Cd}_{49.5}$	rev	1 K/min	3.93 ± 0.20	2.55 ± 0.07	1.88 ± 0.21
$\text{Au}_{50.5}\text{Cd}_{49.5}$	rev	2 K/min	3.91 ± 0.22	2.63 ± 0.07	1.79 ± 0.21
$\text{Au}_{50.5}\text{Cd}_{49.5}$	rev	3 K/min	4.04 ± 0.14	2.75 ± 0.05	1.74 ± 0.13
$\text{Au}_{50.5}\text{Cd}_{49.5}$	rev	4 K/min	4.03 ± 0.14	2.77 ± 0.08	1.71 ± 0.16
$\text{Au}_{50.5}\text{Cd}_{49.5}$	rev	5 K/min	4.05 ± 0.16	2.79 ± 0.05	1.70 ± 0.14
$\text{Au}_{50.5}\text{Cd}_{49.5}$	rev	10 K/min	4.02 ± 0.12	2.61 ± 0.12	1.87 ± 0.21
$\text{Fe}_{68.8}\text{Pd}_{31.2}^{\text{single}}$	fwd	mean all r	2.18 ± 0.1	1.62 ± 0.01	1.90 ± 0.19
$\text{Fe}_{68.8}\text{Pd}_{31.2}^{\text{single}}$	rev	mean all r	2.31 ± 0.1	1.61 ± 0.01	2.13 ± 0.19
$\text{Fe}_{68.8}\text{Pd}_{31.2}^{\text{poly}}$	fwd	mean all r	1.93 ± 0.05	1.61 ± 0.02	1.54 ± 0.13
$\text{Fe}_{68.8}\text{Pd}_{31.2}^{\text{poly}}$	rev	mean all r	2.943 ± 0.02	1.99 ± 0.01	1.97 ± 0.05
$\text{Cu}_{68}\text{Zn}_{16}\text{Al}_{16}$	fwd	mean all r	2.74 ± 0.1	1.99 ± 0.05	1.75 ± 0.19
$\text{Cu}_{68}\text{Zn}_{16}\text{Al}_{16}$	rev	mean all r	2.46 ± 0.06	1.85 ± 0.02	1.72 ± 0.11

Table 8.2: Part II of the overview of the experimentally determined mean exponents of the magnetic-field-dependent measurements. The value z describes the scaling relation between amplitude and energy $\alpha^{-1/\epsilon-1} = z$. Abbreviations: r = rate, fwd pm = forward premartensitic transition, and rev pm = reverse premartensitic transition.

sample	transition	field	α	ϵ	z
Ni ₅₂ Mn ₂₃ Ga ₂₅	fwd	0 kOe	2.60 ± 0.02	1.71 ± 0.01	2.25 ± 0.07
Ni ₅₂ Mn ₂₃ Ga ₂₅	fwd	2 kOe	2.60 ± 0.03	1.61 ± 0.07	2.61 ± 0.36
Ni ₅₂ Mn ₂₃ Ga ₂₅	fwd	4 kOe	2.36 ± 0.03	1.60 ± 0.01	2.27 ± 0.08
Ni ₅₂ Mn ₂₃ Ga ₂₅	fwd	6 kOe	2.19 ± 0.01	1.540 ± 0.004	2.20 ± 0.03
Ni ₅₂ Mn ₂₃ Ga ₂₅	fwd	8 kOe	2.05 ± 0.08	1.48 ± 0.03	2.17 ± 0.31
Ni ₅₂ Mn ₂₃ Ga ₂₅	rev	0 kOe	2.68 ± 0.10	1.75 ± 0.03	2.24 ± 0.23
Ni ₅₂ Mn ₂₃ Ga ₂₅	rev	2 kOe	2.70 ± 0.13	1.64 ± 0.08	2.66 ± 0.55
Ni ₅₂ Mn ₂₃ Ga ₂₅	rev	4 kOe	2.03 ± 0.03	1.43 ± 0.02	2.42 ± 0.17
Ni ₅₂ Mn ₂₃ Ga ₂₅	rev	6 kOe	2.09 ± 0.03	1.48 ± 0.01	2.27 ± 0.10
Ni ₅₂ Mn ₂₃ Ga ₂₅	rev	8 kOe	1.99 ± 0.19	1.43 ± 0.07	2.30 ± 0.84
Ni ₅₂ Mn ₂₃ Ga ₂₅	pm fwd	0 kOe	2.42 ± 0.04	1.74 ± 0.02	1.93 ± 0.10
Ni ₅₂ Mn ₂₃ Ga ₂₅	pm fwd	0.5 kOe	2.54 ± 0.01	1.79 ± 0.01	1.94 ± 0.03
Ni ₅₂ Mn ₂₃ Ga ₂₅	pm fwd	1 kOe	2.99 ± 0.08	1.99 ± 0.02	2.02 ± 0.11
Ni ₅₂ Mn ₂₃ Ga ₂₅	pm fwd	1.5 kOe	2.87 ± 0.13	2.00 ± 0.02	1.87 ± 0.17

z mean value of all exponents (table 8.1 and 8.2): 1.99 ± 0.19

Despite the excellent experimental verification the found relation is in contradiction to some hypotheses, proposed in the context of theoretical models of criticality in disordered systems [82] and in the context of Barkhausen noise [106]. According to these publications, criticality implies a scaling of the average pulse shape in a universal way. Thus, a pulse with amplitude A and duration D should be described by

$$V_{A,D}(t) = A\Phi(t/D), \quad (8.3)$$

where Φ is a universal function. In addition to this hypothesis a scaling relation between amplitude and duration is assumed to be $A \propto D^x$. Combining these two hypotheses with the definition of the energy given in equation 4.2, the energy can be written as

$$E \propto \int_0^D A^2 \Phi^2(t/D) dt \propto A^2 D \propto A^{2+1/x}. \quad (8.4)$$

The experimentally obtained value $z = 2$ is not compatible with any reasonable value of the exponent x . However, the relation of amplitude and duration has been evaluated several times in this work and an arrow-like shape of the distribution has been found in all cases (see e. g. figure 8.4). Because of the bend at large

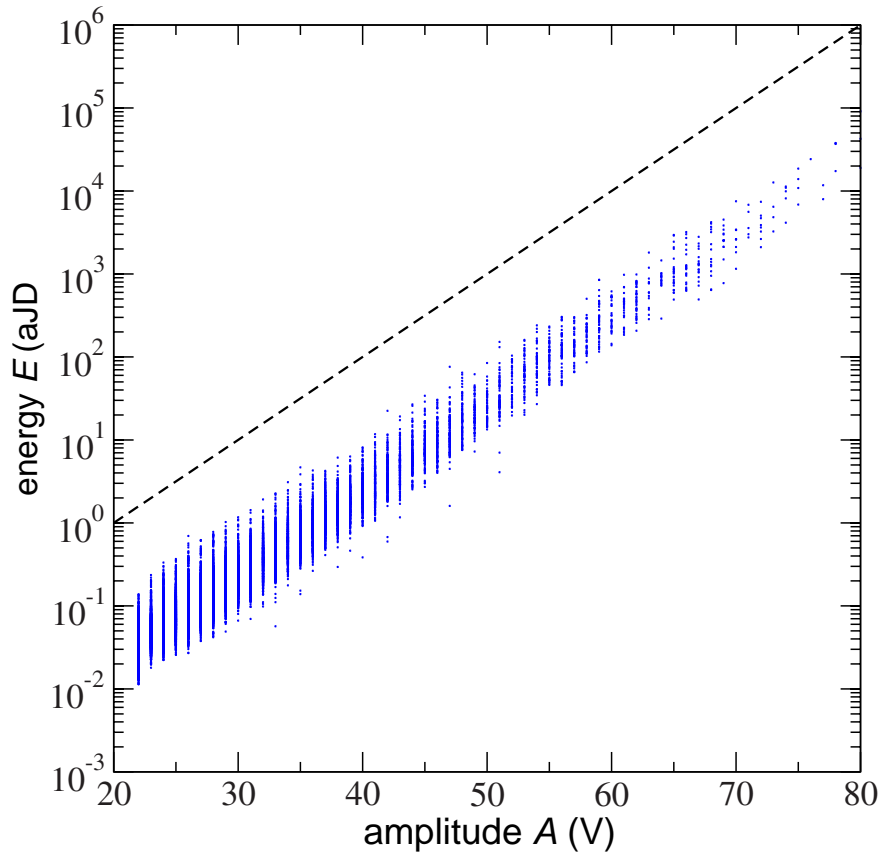


Figure 8.5: Exemplary hit energy versus hit amplitude cloud map corresponding to cooling ramps of the $\text{Fe}_{68.8}\text{Pd}_{31.2}^{\text{single}}$ sample. Data have been averaged over 20 ramps at a cooling rate of 1 K/min. The amplitude is given in dB with 20 dB being equal to one decade ($\text{dB} = 20 \log(\frac{U_0}{1\mu\text{V}})$). The dashed line indicates the behavior $E \propto A^2$.

amplitudes the hypothesis $A \propto D^x$ is not compatible with the experimental results.²

Because of the strong relation between amplitude and energy, signals with high amplitudes always have high energies, too. Therefore, hits with high energies will be subsequently referred to as strong hits and hits with small energies will be called weak hits.

The analysis of all samples includes both the forward transition under cooling as well as the reverse transition under heating. Although literature primarily concentrates on the forward transition, both transition directions are interesting

²In earlier publications [192] [147], in which the poorer quality of the statistics did not allow to distinguish the bend at large amplitude regions, Vives *et. al.* proposed a relation of $A \propto D^x$ with $x = 1$.

Table 8.3: Overview of the transition enthalpy of the analyzed samples.

sample	Ni ₆₃ Al ₃₇	Au _{50.5} Cd _{49.5}	Fe _{68.8} Pd _{31.2} ^{single}	Fe _{68.8} Pd _{31.2} ^{poly}	Cu ₆₈ Zn ₁₆ Al ₁₆
enthalpy	4.4 J/g	2.46 J/g	0.52 J/g	0.28 J/g	5.05 J/g
sample	Ni ₅₂ Mn ₂₃ Ga ₂₅ (premar)		Ni ₅₂ Mn ₂₃ Ga ₂₅		
enthalpy	0.15 J/g		4.13 J/g		

because their mechanisms show fundamental differences. During the martensitic forward transition the high temperature phase with a high (cubic) symmetry transforms under spontaneous symmetry-breaking into a low-symmetry phase with a domain structure. It is evident that the AE technique is very sensitive to these structural changes. Whether one of the transition directions is associated with a higher amount of AE can be answered by the comparison of the mean acoustic activity divided into cooling and heating runs, as shown in figure 8.6.³ The amount of acoustic activity and energy is normalized to a sample mass of 1 g in order to compare material characteristics instead of sample characteristics.

The sample overview allows for some general remarks: First, the total amount of acoustic activity and energy released during a transition varies significantly between the different samples. Cu₆₈Zn₁₆Al₁₆ and Ni₆₃Al₃₇ belong to the most active samples, whereas Au_{50.5}Cd_{49.5} and the premartensitic transition of Ni₅₂Mn₂₃Ga₂₅ reveal the lowest activities. Second, the acoustic energy scales with the acoustic activity in all cases. Third, the activities show diverse results depending on the transition direction. In Ni₆₃Al₃₇ and Cu₆₈Zn₁₆Al₁₆ more AE arises during the reverse transition whereas for the other samples more AE arises in the forward transitions.

However, results have been reported from three polycrystalline samples Au_{0.525}Cd_{0.475}, Au_{0.51}Cd_{0.49}, and Ni_{62.7}Al_{37.3} where the ratio of the AE is inverse to what has been found in this work [14, 15]. This difference can be probably explained by the different stoichiometries. Furthermore, several publications [41, 99, 140, 191] report that the forward transition of CuZnAl shows less AE than the reverse transition, in agreement with the results of this work. In addition, no correlation can be found between the amount of AE and the transition enthalpy, as can be estimated by comparing table 8.3 with figure 8.6. It can be concluded that no obvious systematic relation exists between the acoustic activity and the transition enthalpy.

³Due to its high acoustic activity the Cu₆₈Zn₁₆Al₁₆ sample has been measured with an amplitude threshold of 29 dB, which leads to a lower amount of AE. Under equal system parameters the activity differences would have been even larger.

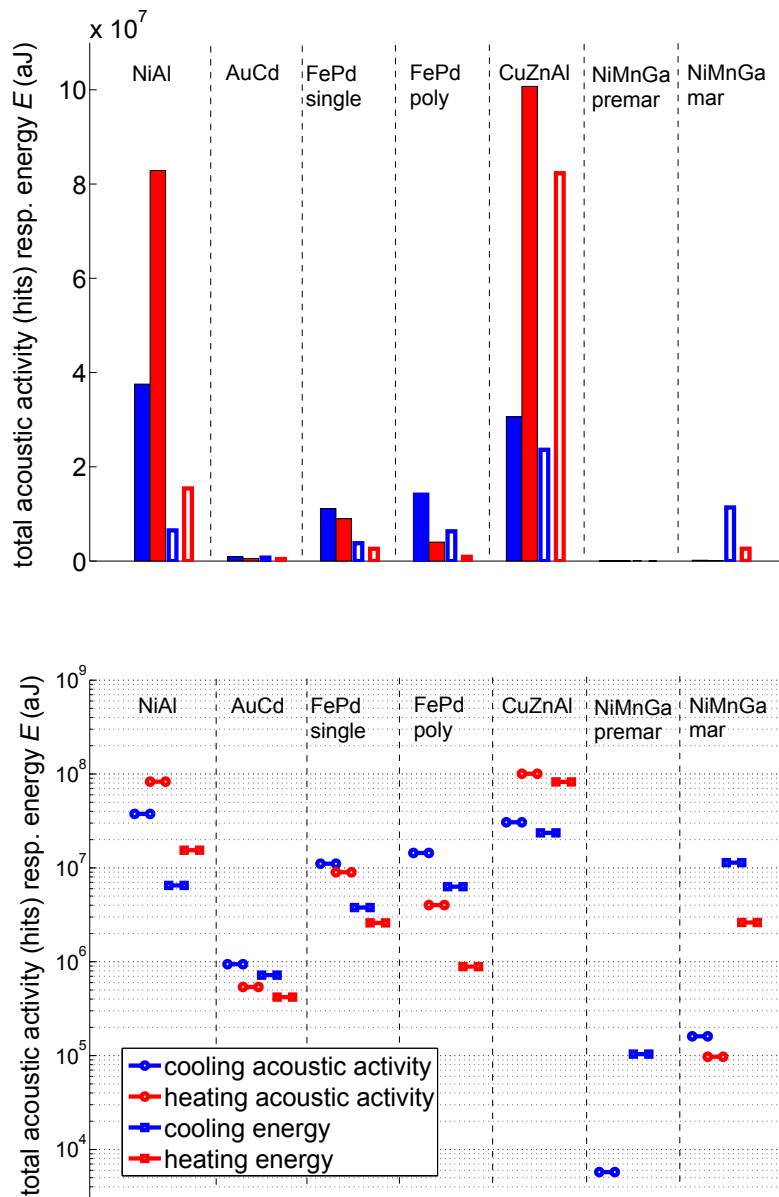


Figure 8.6: Mean total acoustic activity and mean total energy of the forward and reverse transitions of all analyzed samples on a linear scale (top) and a log scale (bottom). Cooling runs are colored in blue and heating runs in red. The acoustic activity is represented by the first two columns respectively symbols. The energy is represented by the last two columns respectively symbols. For a better comparison, the mean total activity has been normalized to a sample mass of 1 g.

Table 8.4: Overview of the crystal structures in the high and low temperature phase. In the high temperature phase all shape memory samples exhibit a cubic symmetry. If all atoms of the B2, L2₁, DO₃ structures were the same they would form a bcc structure.

sample	structure austenite	structure martensite	higher activity at
Ni ₆₃ Al ₃₇	B2	3R, 7M or 7R	reverse transition
Cu ₆₈ Zn ₁₆ Al ₁₆	L2 ₁ or DO ₃	18R	reverse transition
Au _{50.5} Cd _{49.5}	B2	ζ ₂ ' (trigonal)	forward transition
Fe _{0.688} Pd _{0.312}	fcc	fct	forward transition
Ni ₅₂ Mn ₂₃ Ga ₂₅	L2 ₁	10M	forward transition

In the austenitic phase all shape memory alloys have a cubic structure, whereas in the low-symmetry phase the structures differ from each other. In table 8.4 the low temperature structures of the samples analyzed in this work are listed together with the transition direction which emits more AE. It worth noting that those samples showing more AE in the reverse transition have a monoclinic ($\alpha \neq 90^\circ$ and $\beta = \gamma = 90^\circ$ and $a \neq b \neq c$) low temperature phase (Ni₆₃Al₃₇ and Cu₆₈Zn₁₆Al₁₆), whereas the samples emitting more AE under cooling transform into a tetragonal ($\alpha = \beta = \gamma = 90^\circ$ and $a = b \neq c$; Fe_{0.688}Pd_{0.312} and Ni₅₂Mn₂₃Ga₂₅) or a trigonal ($\alpha, \beta, \gamma \neq 90^\circ$ and $a = b = c$; Au_{50.5}Cd_{49.5}) structure. This relation suggests that the symmetry of the low temperature phase is responsible for the amount of AE during the transition. A similar hypothesis has been reinforced by Carillo *et al.*, who have reported two universality classes of exponents for Cu based Hume-Rothery alloys transforming either into an 18R (monoclinic structure) or into a 2H (hexagonal) structure. As will be shown in section 8.5, the amplitude exponents of Ni₆₃Al₃₇ and Cu₆₈Zn₁₆Al₁₆ determined in this work are in agreement with the proposed universality classes. It is worth mentioning that difficulties in comparing experimentally determined exponents with reported values can arise either because of different fit routines, or due to driving rate effects [135]. In order to achieve comparable exponents their values should be examined under adiabatic conditions [135], leading to two implications: On the one hand, the rate should be slow enough to prevent an overlap of the signals corresponding to independent transformation events [201]. On the other hand, for systems that do not behave athermally, the driving should be fast enough to prevent nucleation due to thermal fluctuations.

As proposed by Carillo *et al.*, the amplitude exponents of the samples analyzed in this work indicate that the symmetry of the low temperature phase is a relevant parameter for the transition. Both samples, which show less AE in the forward than in the reverse transition (Ni₆₃Al₃₇ and Cu₆₈Zn₁₆Al₁₆ with an orthorhombic low temperature phase), have as well a higher amplitude exponent

Table 8.5: Comparison of the acoustic activity ratio and the signal strength ratio of the forward and reverse transition. Samples that transform into an orthorhombic low temperature symmetry have in their forward transition more acoustic activity with stronger signals than in their reverse transition. For samples with a tetragonal or trigonal low temperature symmetry the situation is inverse.

samples	forward transition		reverse transition
NiAl and CuZnAl	acoustic activity	<	acoustic activity
NiAl and CuZnAl	signal strength	<	signal strength
AuCd, FePd, and Ni ₂ MnGa	acoustic activity	>	acoustic activity
AuCd, FePd, and Ni ₂ MnGa	signal strength	≥	signal strength

α in the forward than in the reverse transition. By contrast, the other samples (Au_{50.5}Cd_{49.5}, Fe_{0.688}Pd_{0.312}, and Ni₅₂Mn₂₃Ga₂₅), which have more AE in the forward than in the reverse transition, in general show stronger signals in this forward transition.⁴ It can be concluded that the transition direction with more AE has stronger signals. Table 8.5 summarizes this correlation. In the scaling behavior of the acoustic activity both samples with an orthorhombic low temperature phase again differ from the other samples, as they exhibit the largest rate-dependence. Interestingly, in both samples one of the transition directions shows excellent scaling, whereas the other transition direction shows time-dependent results.⁵

8.1 Ni₆₃Al₃₇

Ni₆₃Al₃₇ has been analyzed by rate-dependent measurements and by a multi-cycle measurement. The multi-cycle measurement consists of approximately 150 temperature cycles. Figure 8.7 (top) shows the total acoustic activity of this multi-cycle measurement as a function of the run number. The total activity shows for cooling and heating a decreasing trend with some superimposed jumps of approximately 10 % of the total activity. The decreasing trend can be explained by a training effect, which optimizes the transition path and leads to a saturation of the transition characteristics (see e. g. [136]). The discontinuity around run number 40, which can be observed in both transition directions, is not associated with such a training effect and will be discussed in the following.

Figure 8.7 (bottom) shows the numerical derivative and the correlation of

⁴For samples showing an explicit rate or field-dependence, the amplitude exponents of forward and reverse transition overlap but still show the described asymmetry.

⁵Although the data of this work as well as experimental and theoretical results from literature suggest a strong correlation between transition characteristics and symmetry aspects a general model, which incorporates these results, is still missing.

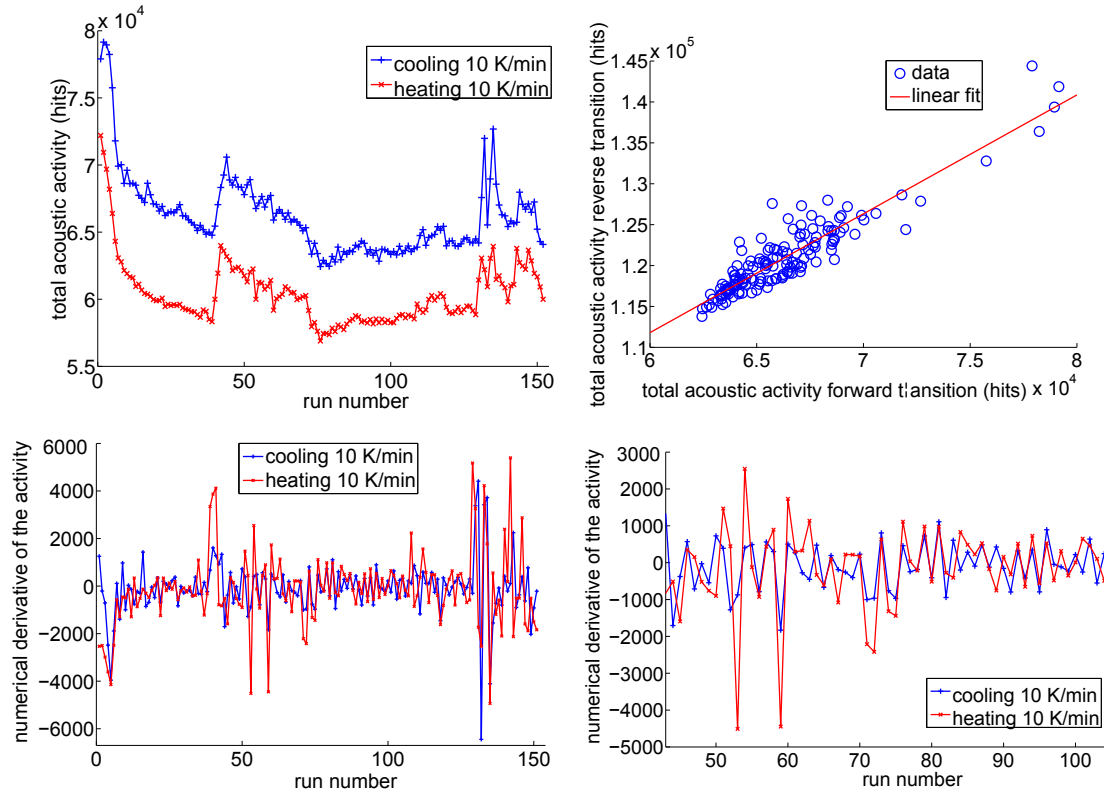


Figure 8.7: Analysis of the correlation of the total activity of the forward (blue) and the reverse transition (red) of the $\text{Ni}_{63}\text{Al}_{37}$ sample during a multi-cycle measurement of approximately 150 temperature cycles at a rate of 10 K/min.

Top: The acoustic activities of both transition directions show a strong correlation. For clarity reasons, the acoustic activity (left) of the forward transition has been divided by two. Note that the abrupt activity changes first occur in the martensitic transition and subsequently in the austenitic transition (cooling run i is followed by heating run i). Scatter plot of the total acoustic activity of each cooling and heating run i (right). The linear shape with a positive slope indicates a high positive correlation with a correlation coefficient of $\rho = 0.922$.

Bottom: Numerical derivative of the activity (left). Enlargement of a selected interval of the activity derivative where the high positive correlation can be explicitly observed (right).

the cooling and the heating data set. A strong correlation between the acoustic activities of cooling and heating runs can be observed. The correlation coefficient can be determined to be $\rho = 0.922$ (with 1 indicating a perfect correlation, 0 absence of correlation, and -1 a perfect negative correlation). It is worth mentioning that the jumps first occur in the martensitic and subsequently in the austenitic transition, for this behavior reveals some information about the transition process.

In the carried out experiment all externally controlled parameters and, in particular, the rate of 10 K/min are constant. Consequently, the change of the total amount of AE events is supposed to be related to the partly irreversible transition character during repeated cycling. It is known that the transition path proceeds through a complex high dimensional energy landscape, where pinning-depinning processes are responsible for the occurrence of a series of metastable states that lead to avalanche dynamics (see e. g. [21]). It is further assumed that the defect structure and the associated disorder are mainly responsible for the self-accommodation of the martensitic variants during the transition, which is known to be very sensitive towards changes in the local strain fields (see section 3.2.1). Thus, the local strain fields can support or hinder the self-accommodation process as well as the phase boundary propagation, which is proposed to be reflected in the released AE (see section 3.4.1 and e. g. [21]).

On this basis it becomes very likely that the observed jumps in the acoustic activity are related to changes in the local strain fields arising from changes in the microstructure of the system. This hypothesis can be corroborated by the observation of a training effect, which modifies the "untrained" path through the changed energy landscape and results in a decreasing acoustic activity, as can be seen between run number 40 and 80. The fact that the changes in the AE first arise in the forward transition and subsequently in the reverse transition indicates that the changes in the microstructure (in comparison to the previous cycle) are triggered during the symmetry-breaking martensitic transition. Taking the asymmetry between the forward and reverse transition into account (single crystal into multi-domain state and vice versa), it is remarkable that this new microstructure has such a pronounced effect on the heating process, too. This gives rise to the assumption that the martensitic transition drives changes in the defect microstructure, leading to higher energy barriers because of enhanced pinning processes. The new microstructure of the austenitic phase is inherited from the martensitic phase, which gives rise to stricter boundary conditions and leads to an AE increase.

The author assumes that the less optimized way through the energy landscape is reflected by higher energy barriers separating the metastable states. This hypothesis can be experimentally tested by observing the exponent behavior, where higher barriers are associated with stronger AE signals. Indeed, it can be seen in figure 8.8 that the large change of the exponents towards lower values

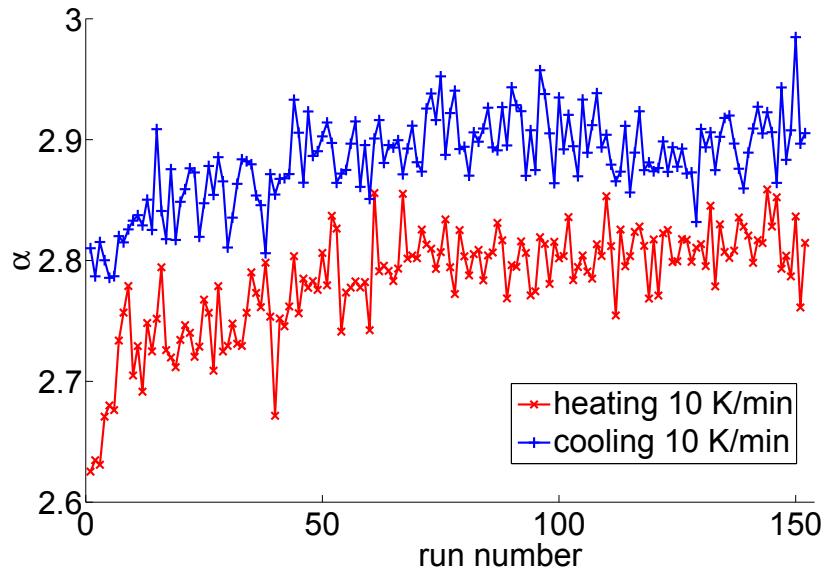


Figure 8.8: Amplitude exponents of cooling and heating runs during a multi-cycle measurement with the $\text{Ni}_{63}\text{Al}_{37}$ sample at a rate of 10 K/min.

occurs in both transition directions at the same run number where the activity shows strong increase. In addition, a general correlation can be found between the decreasing trend of the acoustic activity and the increasing trend of the exponents. This indicates that cycles of less activity produce hits of lower strength. To validate this observation a correlational analysis between the total acoustic activity of a cooling run and the corresponding amplitude exponents has been run. Results are shown in figure 8.9 (left). The shape of the scatter plot and the correlation coefficient $\rho = -0.508$ for cooling and $\rho = -0.466$ for heating confirm this negative correlation: the higher the activities the smaller the amplitudes. Furthermore, the amplitude exponents of subsequent cooling and heating runs positively correlate with $\rho = 0.644$, as shown in figure 8.9 (right). It can be concluded that the forward transition with its symmetry-breaking character is the driving force of irreversible changes, manifesting themselves in the defect microstructure.

Rate-dependent AE experiments with $\text{Ni}_{63}\text{Al}_{37}$ reveal an ambivalent scaling behavior of the acoustic activity. The reverse transition shows excellent scaling over all tested rates between 0.1 K/min and 10 K/min, which indicates athermal transition dynamics and can be described by $\frac{dN(T,T/r)}{dT} = f(T)$. Furthermore, the exponents of the amplitude and energy distributions each have a constant value without any rate-dependence.

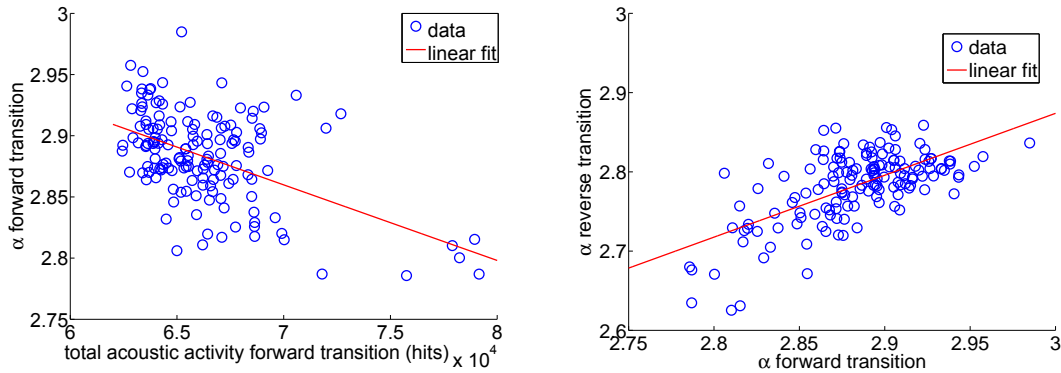


Figure 8.9: Correlations between AE transition characteristics of the Ni₆₃Al₃₇ sample during a multi-cycle measurement at a rate of 10 K/min. On the left can be seen a scatter plot of the total acoustic activity of the forward transition and the corresponding exponents of the amplitude distribution. The oval shape with a negative slope and the correlation coefficient of $\rho \approx -0.5$ for cooling and heating indicate a negative correlation. On the right is shown a scatter plot of the amplitude exponents of the forward and reverse transition. The oval shape with a positive slope and the correlation coefficient of $\rho \approx 0.644$ indicate a rather strong correlation.

By contrast, the activities of the forward transitions do not show any scaling due to a strongly decreased acoustic activity at lower rates (see figure 8.11 (left)). However, all curves have a similar shape, as can be seen in the depiction of the normalized activity curves in figure 8.10. The isothermal behavior of Ni₆₃Al₃₇ is a special case of $\frac{dN(T,r)}{dT} = f(T,r)$, because $f(T,r)$ can be written as $f(T)g(r)$, with $g(r)$ being an almost monotonic function that can be used to normalize the measured activities. However, earlier experiments have proven the isothermal character of the forward transition of the same sample by optical and AE incubation time measurements [31, 90].

In order to make sure that the rate-dependent activity does not originate from measurement artifacts, it has been proven that window effects due to hardware limitations can be neglected. Furthermore, the merging of avalanches as proposed in [135] and similar rate-dependent effects can be ruled out, too (for a detailed analysis see the introduction to this chapter).

In order to explain the increased activity with increasing cooling rates, the author proposes an interplay of the time scale associated with thermal activation τ_{th} (due to the isothermal dynamics), with the rate-dependent time scale τ_{dr} , and with the high degree of intrinsic disorder of the material system. As reported in [135], driving rate effects are closely related to all time scales related to the dynamics. Relevant time scales are here: (i) The time scale of the avalanche

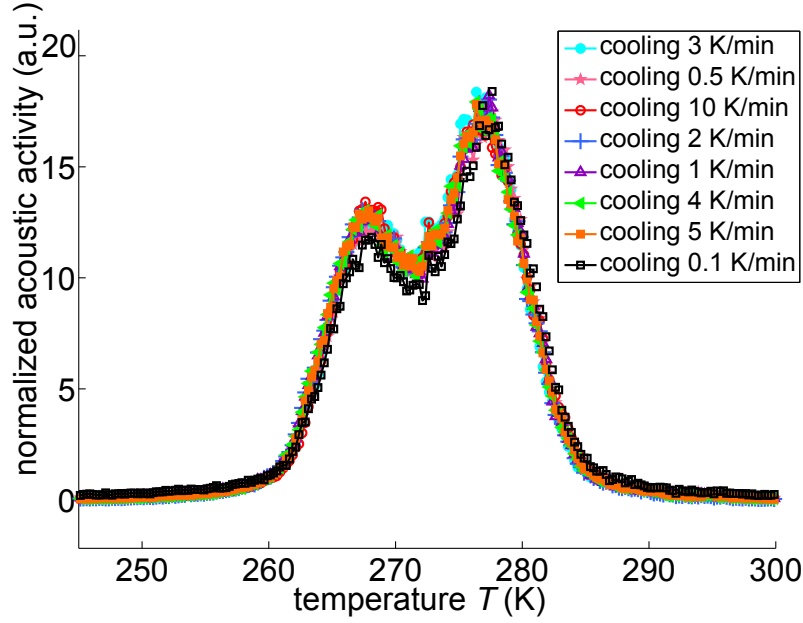


Figure 8.10: Normalized acoustic activity of the $\text{Ni}_{63}\text{Al}_{37}$ forward transition at selected rates.

relaxation τ_{av} that has been determined for $\text{Ni}_{63}\text{Al}_{37}$ (see figure 8.12) to lie between $2 \mu\text{s}$ and $10^3 \mu\text{s}$ (which is supported by [77]). (ii) The time scale τ_{dr} that arises from the driving rate r and the transition interval $\Delta T \approx 50 \text{ K}$. It can be calculated by $\tau_{dr} = \Delta T/r$ and it ranges between 5 min and 500 min. (iii) The time scale τ_{th} associated with the thermal activation by fluctuations.⁶

Figure 8.11 shows the mean total acoustic activity per cycle as a function of the driving time τ_{dr} . A decreasing trend with the largest changes occurring at small driving times i. e. highest driving rates is visible. The isothermal aspects of the dynamics under cooling implies that thermal fluctuations play a relevant role during the transition process. Under cooling, the high symmetry phase transforms into the low-symmetry phase of martensitic variants. As already shown for the multi-cycle measurement (see figure 8.7), the forward transition can take place under a relatively low amount of AE when the transition path has been trained several times. By contrast, a high amount of AE occurs when the transition propagates under large changes in the strain fields [21], which can arise e. g. from an imperfect self-accommodation [91]. As an explanation of the rate-dependent behavior of this measurement the author proposes that slower rates provide sufficient time to the fluctuation-controlled system for

⁶The adiabatic limit, where fluctuations are irrelevant, can be characterized by $\tau_{dr}/\tau_{th} \rightarrow 0$ and $\tau_{av}/\tau_{dr} \rightarrow 0$, which is equivalent to well separated time scales $\tau_{av} < \tau_{dr} < \tau_{th}$.

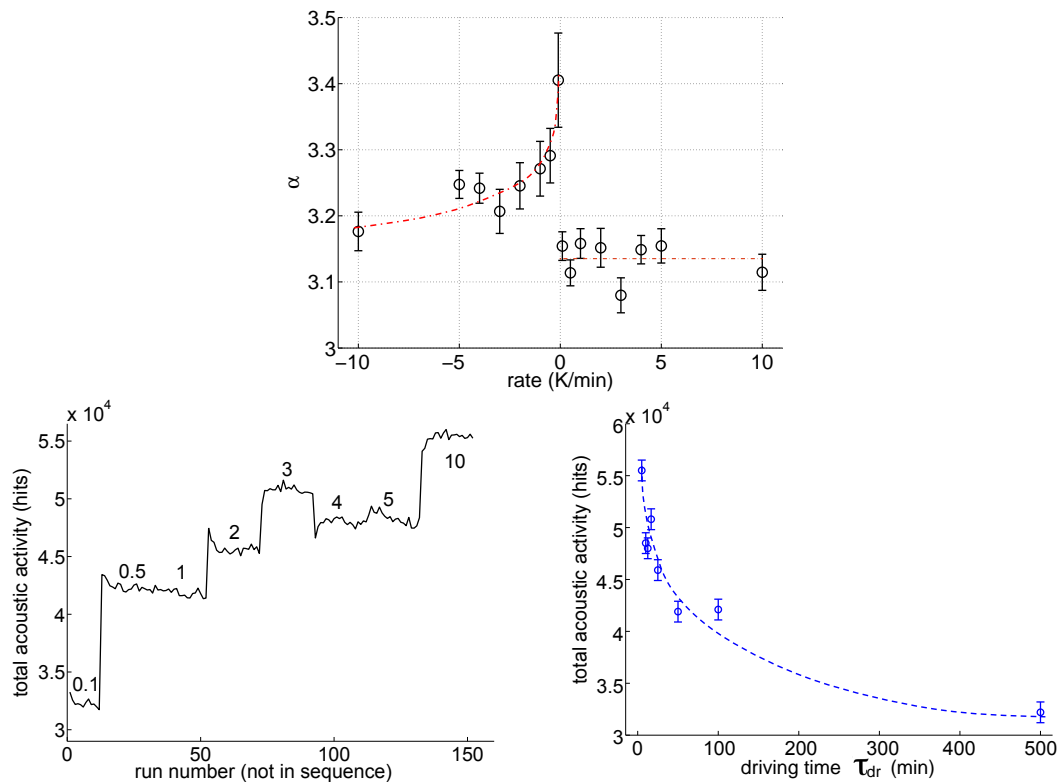


Figure 8.11: Rate-dependent behavior of the Ni₆₃Al₃₇ sample. Amplitude exponents of cooling and heating runs (top). Total acoustic activity of the forward transition under cooling sorted according to the rate (left). Mean total activity as a function of the driving time τ_{dr} (right). The dotted line is a guide to the eye.

testing several configurations until an appropriate accommodation is found. At higher rates, less time is available for optimizing the accommodation process, because a rapid further undercooling forces the system to transform immediately. This interpretation assumes that the driving time τ_{dr} and the characteristic time scale to trigger avalanches by fluctuations τ_{th} are of the same order. This assumption can directly be tested by incubation time experiments. The isothermal incubation times, measured with the same sample, reveal athermal activation times τ_{th} between some minutes and about one and a half days.⁷ This indicates that, instead of being close to the adiabatic limit, where the time scales are well

⁷Short incubation times have to be taken carefully because a temperature shift, after reaching the temperature plateau cannot be completely neglected, for long times this limitation is absent. However, according to Kakeshita *et al.* short incubation times have higher probability than long incubation times when the system is close to the next transition step. This is always guaranteed in the two phase coexistence regime during a transition [67, 70].

separated $\tau_{av} < \tau_{dr} < \tau_{th}$ [135], the time of the thermal activation in the case of $\text{Ni}_{63}\text{Al}_{37}$ is of the same order as the driving time $\tau_{av} \ll \tau_{dr} \approx \tau_{th}$.

The approach can further be corroborated by the rate-dependent signal strength, as can be seen in figure 8.11 (top). At high rates, the system fluctuations have limited attempts to minimize the internal strains, which leads to high energy barriers and strong AE signals (low exponents). At slow rates, in contrast, the rather perfect accommodation associated with low internal strains leads to low energy barriers, resulting in weak AE signals and high exponents. In $\text{Ni}_{63}\text{Al}_{37}$, the probing of an optimal accommodation seems to be particularly difficult, due to its high amount of intrinsic disorder, which arises from the non-stoichiometric composition and the frozen-in vacancy distribution from elevated temperatures (see section 3.5.1). A similar behavior of the rate-dependent amount of AE during heating is found in the polycrystalline $\text{Fe}_{68.8}\text{Pd}_{31.2}$ sample, which underlines the importance of disorder (see figure 7.27 in section 8.3). It is worth mentioning that the observed rate-dependence does not fit into the model of driving rate effects proposed in [135]. Nevertheless, the suggested interpretation could be a useful supplement to it. It can be concluded that the thermal activation in combination with the different driving rates provides a potential explanation for the rate-dependent acoustic activity and signal strength in the highly disordered material class Ni-Al.

Transition kinetics played a central role in previous considerations. Especially the avalanche trigger mechanism, either athermal or isothermal in nature, has been discussed. However, the propagation dynamics, once the metastable barrier is overcome, still has to be considered in detail. Figure 8.12 shows the distributions of the hit durations of $\text{Ni}_{63}\text{Al}_{37}$ at different rates with the normalized cooling runs showing isothermal aspects on the left and the heating runs exhibiting athermal behavior on the right. These results confirm that both distributions show scaling, regardless of the transition direction.

This scaling further shows that the time scale of the avalanches τ_{av} (i. e. duration of AE events) is not coupled to the time scale of the driving rate τ_{dr} or the mechanism that is responsible for the nucleation process. Once the new transformation step has been triggered, it occurs with its intrinsic duration independently of the driving rate or the transition mechanism, be it athermal or isothermal. In agreement with what has been shown before, it can be concluded that the time scale of the avalanche relaxation τ_{av} is much shorter than the time scale of the driving force τ_{dr} at all chosen rates.⁸

From a broader perspective the data collapse, the decoupled scales, and the identified power laws⁹ in both transition directions support the concept of a scale-

⁸The case of $\tau_{av} \approx \tau_{dr}$, would lead to correlated time scales. As a consequence event pile up would occur and scaling would be absent [201].

⁹Keeping in mind the existence of a window effect (see section 8.)

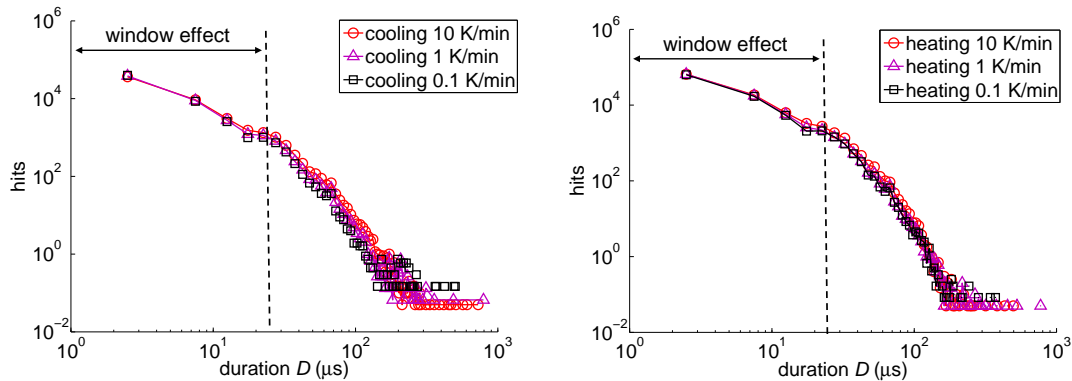


Figure 8.12: Distribution of the hit duration of the forward (left) and reverse (right) transition of the $\text{Ni}_{63}\text{Al}_{37}$ sample at three selected rates. For a better comparison the cooling curves have been normalized to compensate the rate-dependent hit number. Both transition directions show each a high degree of scaling in spite of their different classification as partly isothermal (forward transition) and athermal (reverse transition).

free process as well. Interestingly, no scaling of the duration distributions can be found between cooling and heating, which seems to result from the asymmetry between the forward and the reverse transition.

8.2 $\text{Au}_{50.5}\text{Cd}_{49.5}$

The discussion on $\text{Au}_{50.5}\text{Cd}_{49.5}$ starts with the absent activity scaling observed during cooling and heating runs. Next, the rate-dependence of the signal strength during heating will be explained within the framework of martensite stabilization. This section will end with some statistical considerations by a detrended fluctuation analysis (dfa).

The acoustic activity of $\text{Au}_{50.5}\text{Cd}_{49.5}$ shows a strong rate-dependence under both cooling and heating, as can be exemplarily seen in figure 7.21 for cooling runs. The curves that differ considerably in their shape show a common trend: the higher the rate, the broader and lower the curves. Additionally, a displacement of the cooling curves towards lower temperatures can be observed. The fact that a contrary displacement can be noted during heating runs suggests that the described effects originate from the transition enthalpy, which has not been taken into account in the temperature calibration procedure. This explanation is supported by the large enthalpy and quite narrow transition interval (approximately one Kelvin; equivalent to a 6 s time interval at 10 K/min) of $\text{Au}_{50.5}\text{Cd}_{49.5}$. By comparison with the other samples, $\text{Au}_{50.5}\text{Cd}_{49.5}$ shows by far the smallest transition

interval and the second largest absolute enthalpy (see table 8.3), which reveals the relevance of this consideration. The author proposes that the combination of these two characteristics leads to a temporary offset of the real and the measured sample temperature. Due to a limited heat transfer between the sample and the cooling device, the emitted respectively absorbed enthalpy leads to the described temperature shift. Only the martensitic and austenitic start temperatures (M_s and A_s) should not be influenced, as indicate the very beginning of the transition, where no enthalpy has been exchanged before. However, assuming that the influence of the enthalpy has been correctly described, the conventional representation of the acoustic activity as a function of the temperature is inapplicable to decide whether the transition behaves isothermally or athermally.

In order to analyze the degree of scaling, a new normalization procedure is applied to the data which eliminates the rate-dependent (enthalpy) effects. The new procedure consists of a data normalization to its maximum activity $A(r)$ and of a temperature shift $(T - T_{max}(r))$ that moves all maxima to the same temperature $T_{max}(r)$. The described rescaling leaves the areas under the activity curves invariant. It is evident that the normalization procedure leaves the sharpest curve (of the lowest rate) unchanged, whereas the lowest curve receives the largest changes. The following equations describe the approach:

$$\frac{dN}{dT} \rightarrow \frac{dN}{dT} \frac{1}{A(r)} \quad (8.5)$$

$$T \rightarrow (T - T_{max}(r)) \frac{A(r)}{A_{max}}$$

Figure 8.13 shows the rescaled acoustic activity of the cooling runs with the corresponding rate-dependent values of $A(r)$ and $T_{max}(r)$. The recalculated curves scale much better, although they do not reach a perfect data collapse. Differences can be especially noted at the M_f temperatures, which indicates a certain degree of isothermal behavior. This explicit rate-dependence can as well be evidenced by the rescaling parameters. They do not show a monotonic trend, as would be the case for fully athermal behavior. The verified degree of isothermal behavior is in good agreement with earlier experiments that revealed an explicit time dependence of $\text{Au}_{50.5}\text{Cd}_{49.5}$ by incubation time measurements [158].

Even under rescaling, a data collapse for the reverse transition of $\text{Au}_{50.5}\text{Cd}_{49.5}$ cannot be realized, which reflects a high degree of isothermality. This can be evidenced as well by the curve shapes, as can be seen in figure 8.15 (top). However, the total amount of acoustic activity remains basically constant in spite of the varying curve shapes.

The evidenced explicit time dependence of $\text{Au}_{50.5}\text{Cd}_{49.5}$ is in contrast to results of Baram *et al.* who reported a purely athermal transition dynamics of $\text{Au}_{0.525}\text{Cd}_{0.475}$ and $\text{Au}_{0.51}\text{Cd}_{0.49}$ by incubation time measurements [15]. This

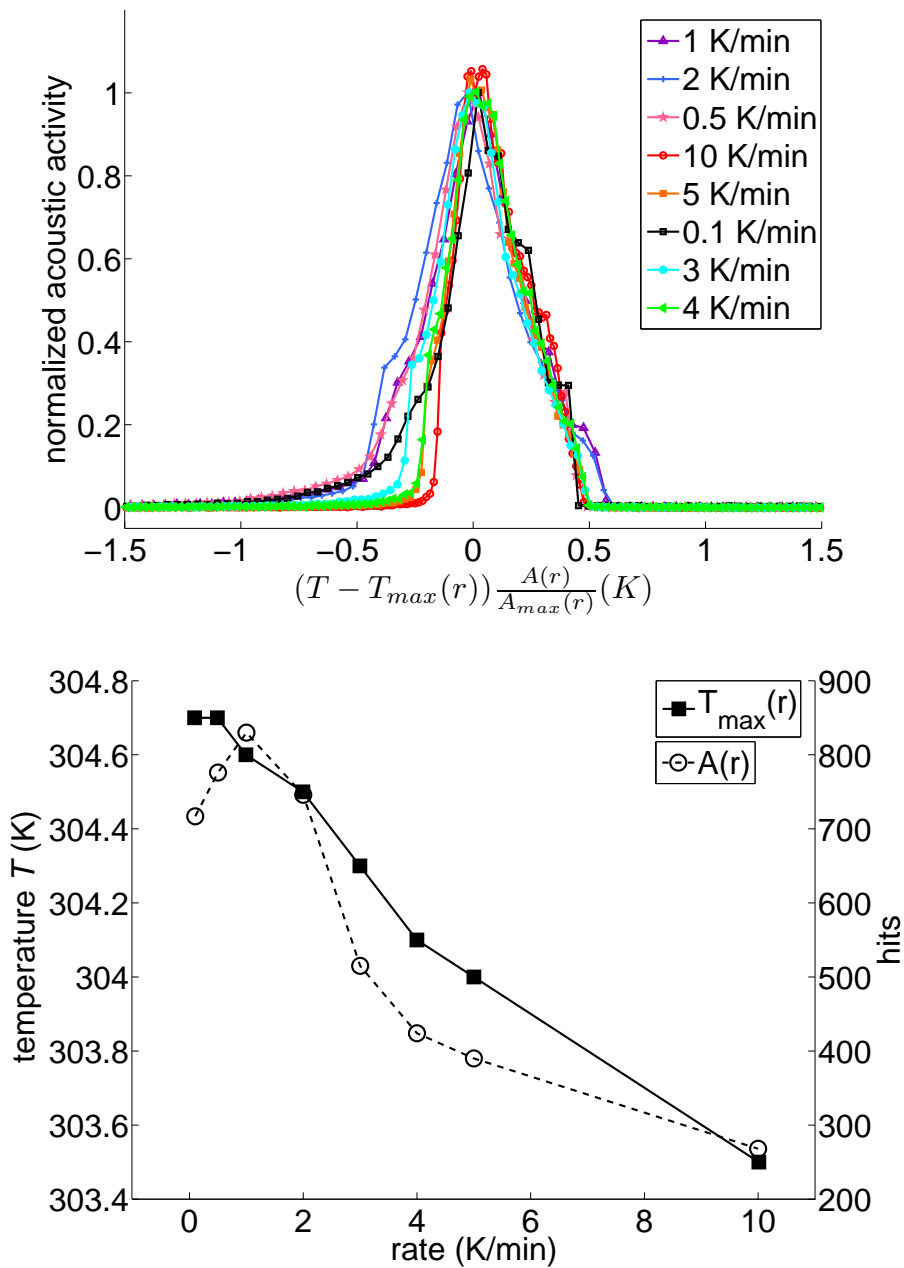


Figure 8.13: (top) Rescaling of the acoustic activity of the forward transition of the $\text{Au}_{50.5}\text{Cd}_{49.5}$ sample at selected rates. An incomplete data collapse of the rescaled activity can be seen. The legend displays the randomized order of the rates. (bottom) Rate-dependent rescaling coefficients as defined in equation 8.5. The non-monotonic behavior indicates partly isothermal kinetics.

apparent contradiction can probably be solved by taking the differing stoichiometries into account as well as the fact that the above-mentioned samples were polycrystals. Moreover, the absence of AE under isothermal holding is only a compelling argument if no incubation is observed after very long waiting times at many temperatures close to M_s ; both criteria not being fulfilled in [15].

Besides the rate-dependence of the acoustic activity, $\text{Au}_{50.5}\text{Cd}_{49.5}$ shows a clear rate-dependence of the α and ϵ exponents during the reverse transition. It has been found to be the largest driving rate-dependent variation of all analyzed samples. A pile up of the AE signals can be neglected because, even at the highest rate of 10 K/min, the ratio between signal and waiting time is smaller than $1/30$ (for a further discussion see the introduction to this chapter in section 8).

In the following the author proposes a new approach by taking martensite stabilization into account as a factor influencing the rate-dependent AE signal strength. A convincing model for martensite stabilization has been introduced by Otsuka *et al.* and is called *symmetry-conforming short-range order model*. This model explains aging effects, such as rubber-like behavior and martensite stabilization, with the help of local short-range diffusion on a sublattice or associated defect microstructures, which follows the long-range ordered lattice structure (see e. g. [127, 149, 151]). A schematical depiction of this model can be found in figure 8.14.

Aging is considered to be relevant in rate-dependent measurements with $\text{Au}_{50.5}\text{Cd}_{49.5}$ because of two reasons: First, the experimental temperature interval¹⁰ implies that the sample remains in the martensitic state in the range of 180 min at a rate of 0.1 K/min and approximately 1 min at a rate of 10 K/min. Second, the characteristic time constant for martensite stabilization effects in Au-Cd is reported to be approximately 30 min, as can be found in table 8.6. This implies that at slow rates martensite stabilization should be expected, whereas at high rates the aging time is too short to exert any relevant influence.

Consequently, the author assumes that martensite stabilization modifies the transition dynamics in two ways: First, as proposed in [151], a stabilized marten-

¹⁰The arbitrarily chosen temperature interval of $\text{Au}_{50.5}\text{Cd}_{49.5}$ ranges from 296 K to 316 K and the characteristic temperatures are $M_s \approx A_s \approx 305$ K.

Table 8.6: Overview of experimentally observed characteristic times for martensite stabilization t_g of different materials at room temperature. Additionally, the martensitic transition temperature reduced by the melting temperature M_s/T_m is given, which correlates with the stabilization times [149].

alloy	Ni-Ti	Cu-Al-Ni	Cu-Zn-Al	Au-Cd	In-Tl
M_s/T_m	≈ 0.19	≈ 0.23	≈ 0.27	≈ 0.34	0.5–0.79
t_g	$\approx \infty$	≈ 10 months	≈ 5 h	≈ 0.5 h	< 1 s

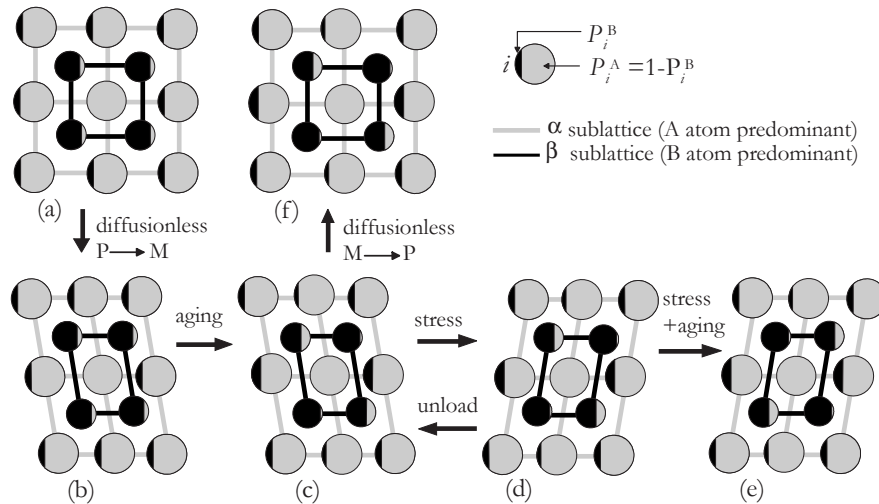


Figure 8.14: Illustration of the aging process as explained by the symmetry-conforming short-range order model. The black and grey areas symbolize the probability of finding an A atom (P_i^A grey) or a B atom (P_i^B black) at lattice site i .

(a) High temperature phase of an alloy A-B with disorder.

(b) Low temperature phase immediately after the martensitic phase transition with an inherited local structure ("microstructure").

(c) Diffusion leads to new equilibrium configurations of the sublattices A and B.

(d) The stress-induced reorientation of the variants leads to new out-of-equilibrium sublattices. If the stress is only applied for a short time, the variant jumps back into the old orientation due to the constraints arising from the preserved local atomic configuration. This time-dependent out-of-equilibrium effect is called rubber-like behavior or twin stabilization.

(e) In case of a stress applied for a sufficiently long time, diffusion leads to a new equilibrium situation that stabilizes the new variant orientation.

(f) Under increasing temperatures the stabilized martensite is exposed to constraints from the equilibrated sublattices that hinder the sample from starting the reverse transition immediately. A larger driving force, i. e. a larger superheating, is required to start the reverse transition, leading to higher A_s and A_f temperatures. This effect is called martensite stabilization (adapted from [151] and [127]).

site needs a larger superheating to start the reverse transition than a non-stabilized martensite. This hypothesis can be confirmed by the acoustic activity of the reverse transition, shown in figure 8.15. Both the A_s and the A_f temperature show a shift towards higher values (larger superheating) with lower rates. $A_s^{0.1\text{K/min}}$ is shifted against $A_s^{10\text{K/min}}$ by approximately $(0.4 \pm 0.025)\text{K}$, which is comparable to temperature shifts reported in [127]. It is important to keep in mind that the transition enthalpy does not affect A_s as it marks the transition start where no enthalpy has been absorbed before. Second, lower rates and the associated martensite stabilization give rise to higher energy barriers dividing the metastable states. Besides the larger superheating this should lead as well to stronger AE signals manifested in lower amplitude and energy exponents. As expected, results show strongly decreasing amplitude and energy exponents with decreasing rates. Figure 8.16 exemplarily depicts this behavior for α by plotting the exponent as a function of the time spent in the low temperature phase, which is anti-proportional to the rate. The black dotted line indicates the stabilization time of approximately 30 min. In agreement with the explanation approach it sets apart the areas of large and low influence of the stabilization process. It is worth mentioning that the characteristic aging time of half an hour, as reported in literature, is not only confirmed by this work but additionally by X-ray photo correlation spectroscopy (XPCS) measurements. This modern technique uses a coherent synchrotron beam for the detection of diffusive dynamics in $\text{Au}_{50.5}\text{Cd}_{49.5}$ by correlating changes in the speckle patterns at $M_s - 0.05\text{K}$. This temperature corresponds to the phase coexistence regime [111].

Baram *et al.* analyzed the effect of varying cooling rates on the microstructure and the acoustic emission of Au-Cd [13]. They found signals of higher energies at slower cycles, which is in full agreement with the results of this work. Additionally, an optical analysis of the martensitic microstructure shows that the surface patterns associated with slow cycles have a finer structure than the surface patterns which are emerged during quick cycles. Whereas Baram *et al.* did not provide a further interpretation, the author proposes that the effect of martensite stabilization is responsible for their results. This hypothesis can be supported by the reported (but not explained) microstructure changes under higher rates, which probably result from an inherited high temperature microstructure [150].

An interesting counterexample to the discussed martensite stabilization is the absent rate-dependence of $\text{Cu}_{68}\text{Zn}_{16}\text{Al}_{16}$. This material neither shows rate-dependent exponents nor undercooling or overheating effects (results of $\text{Cu}_{68}\text{Zn}_{16}\text{Al}_{16}$ can be found in [172]). This rate independent behavior fits well into the framework of martensite stabilization: The characteristic time of aging effects of Cu-Zn-Al is reported to be approximately 5 h (see table 8.6), which exceeds the largest remaining time in the low temperature phase at the lowest rate. Consequently, no rate-dependence is observed. Furthermore, $\text{Ni}_{63}\text{Al}_{37}$ does not show any rate-

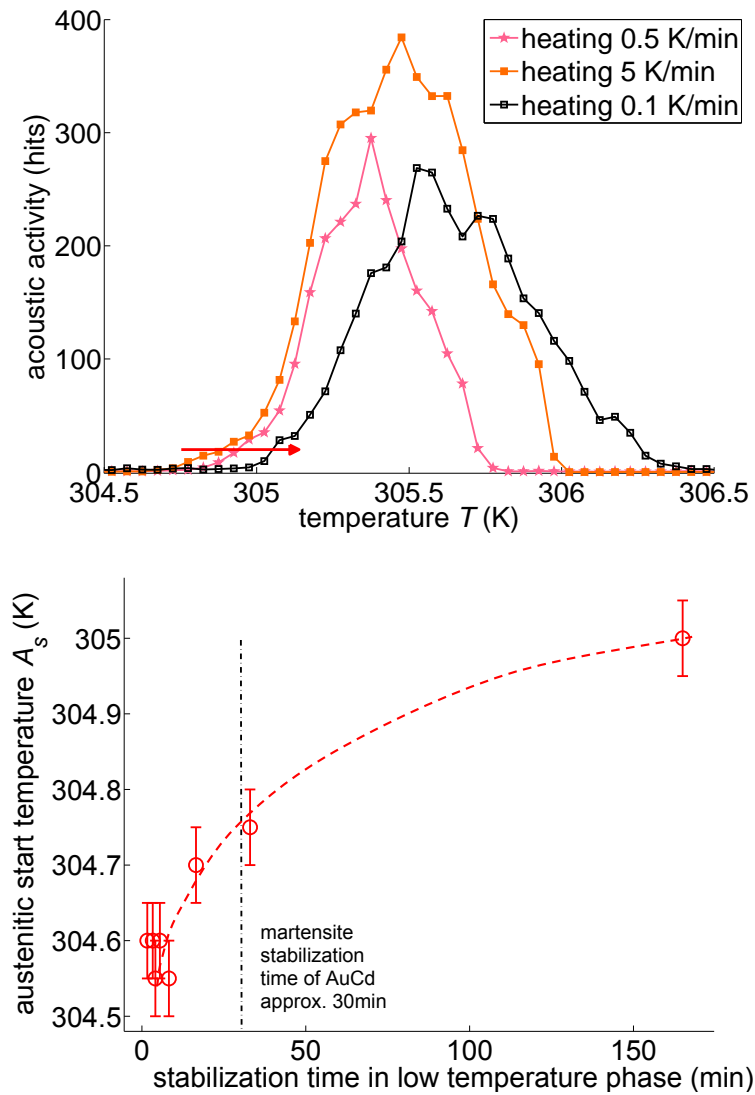


Figure 8.15: Acoustic activity (top) and start temperature (bottom) of the reverse transition of the $\text{Au}_{50.5}\text{Cd}_{49.5}$ sample at selected rates. The acoustic activity curves show absent scaling and a shift of A_s towards higher temperatures with lower rates, i. e. longer aging times. The austenitic start temperature shows a shift towards higher temperatures with longer aging times.

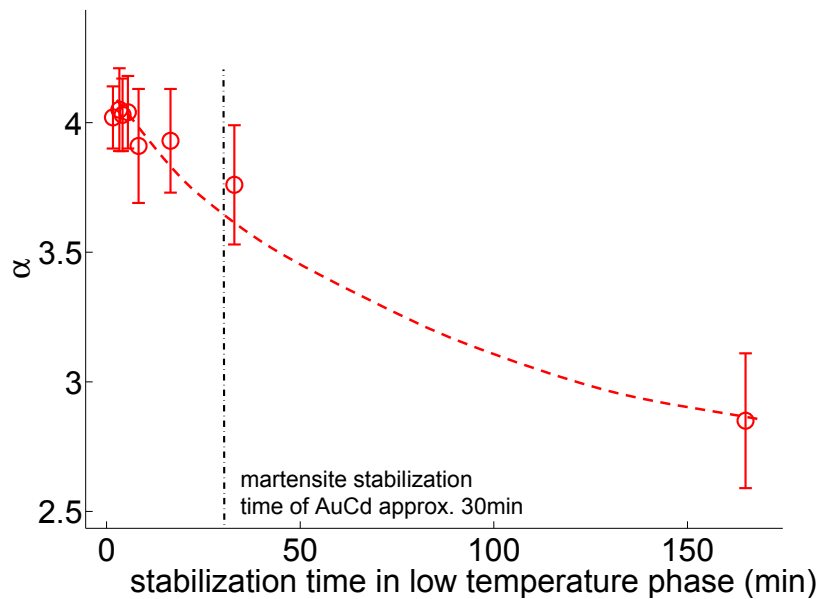


Figure 8.16: Amplitude exponents of $\text{Au}_{50.5}\text{Cd}_{49.5}$ during heating cycles after staying for different time periods in the low temperature phase owing to different driving rates. The black dotted line indicates the characteristic time for martensite stabilization in Au-Cd which is fully consistent with the fact that the two exponents belonging to larger times are considerably lower than the others. The red dotted line is a guide to the eye.

dependence during heating (see section 7.2.1 and 8.1), which is fully compatible with the infinite aging times proposed for that material system.

In the last section it has been shown that the time lag of the short-range order following the new symmetry after sudden changes in the crystal structure has a considerable influence on the signal strength during heating. However, due to symmetry considerations, the forward transition should be influenced by an inherited martensite short-range order as well. In fact, this effect has been observed by Ren *et al.* using transmission electron microscopy (TEM) and optical microscopy. Additionally, it is manifested in the macroscopic two-way shape memory effect [150]. However, the results of this work only show a significant effect in heating runs. This asymmetry can be explained by taking two aspects into consideration: First, the time, which the sample remains in the high temperature phase, is (at all rates) about 20 % longer than the respective time in the low temperature phase. Second, due to the higher temperature of the parent phase diffusion is thermally activated and leads to a shorter time lag between short-range and long-range order. The diffusion-controlled relaxation

time is given by $\tau_{re} = \tau_0 \exp(\Delta H/kT)$, where τ_0 and ΔH are the attempt time and the activation enthalpy of diffusion [36]. As a consequence, the author concludes that the characteristic austenite stabilization time for Au-Cd is much shorter than the martensite stabilization time - an assumption that is supported by similar observations in different materials (see e. g. [160, 161, 205]). A stabilization time of a few minutes would lead to a stabilized austenite at all measured rates and would provide an explanation for the absent rate-dependence.

The observation of jerky dynamics as a fundamental character of phase transitions in shape memory alloys (see figure 8.1 in the introduction to this chapter) calls for an analysis of the fluctuation behavior of the dynamics in some more details, which was exemplarily done with Au_{50.5}Cd_{49.5}. A simple autocorrelation analysis would not be meaningful because of an instationary time series (see figure 8.1). A suitable technique is the detrended fluctuation analysis (dfa), which first eliminates a polynomial trend from the data distribution. The dfa method, which has been introduced by Peng *et al.* for the analysis of long-range correlation in DNA sequences [132, 133], analyzes the degree of correlation of the data points of a timeline and can estimate the relevant timescales and statistics of fluctuations. The dfa was used for the first time by Stadler *et al.* to analyze dynamics in solids by computing the correlation between X-ray speckles. A comprehensive overview of the dfa technique can be found in [111].

Figure 8.17 depicts the result of the dfa analysis.¹¹ The slope in the log-log representation, i. e. the exponent of the power law, slightly changes its value at approximately $10^{2.07} \text{ s} \approx 117 \text{ s}$. This change indicates that the fluctuations of the system show different characteristics on short time scales ($t \lesssim 120 \text{ s}$) and on long time scales ($t \gtrsim 120 \text{ s}$). The two occurring exponents indicate which statistics describe the analyzed fluctuations. A tabular overview of the exponents and their meaning extracted from [59, 132, 133] can be found in table 8.7. The exponent $\alpha = 0.88$ for small time scales indicates that the distribution basically follows a pink noise distribution, i. e. $1/\nu$ -noise. The exponent of $\alpha = 0.55$, corresponding to longer fluctuation time scales, indicates an almost randomly distributed signal (white noise: $p(\nu) \propto \nu^0$).

The analysis points out that AE signals emitted during a relatively short time interval of approximately 2 min or respectively 0.2 K have a higher degree of correlation than data that are more separated in time respectively temperature. Supposing a single habit plane, these results indicate that AE processes originating from the same sample region are highly correlated. The different degrees of correlation probably reflect varying defect configurations depending on the sample section. This would be of essential significance as defects are known as a

¹¹The logarithmic abscissa values indicate the width of the time intervals, which are fitted by an polynomial of the 6th order. The F-value, which is plotted logarithmically at the ordinate, represents the square of the deviation of the data from the fit. The positive slope of the curve shows that larger fit intervals lead to larger root mean square values.

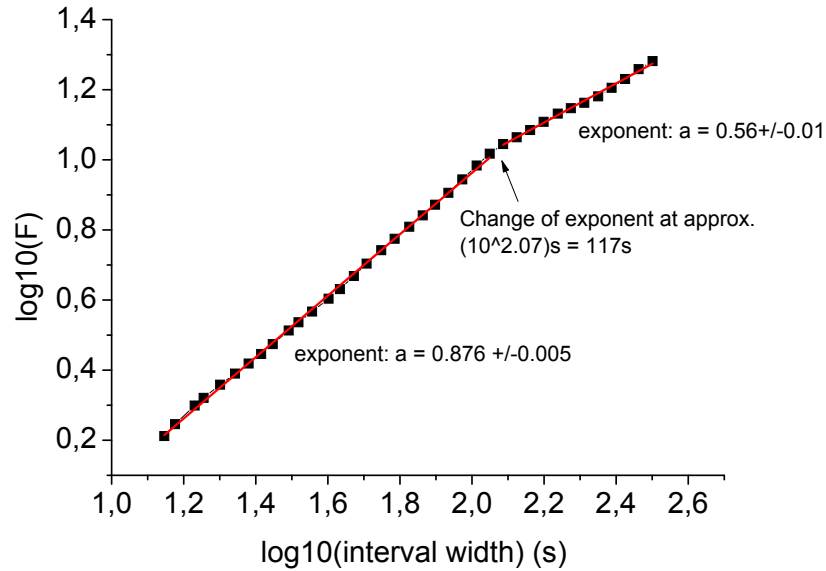


Figure 8.17: Results of the detrended fluctuation analysis applied to the acoustic activity of the $\text{Au}_{50,5}\text{Cd}_{49,5}$ sample at a cooling rate of 0.1 K/min (see figure 8.1). The log-log plot reveals a correlated behavior of the data over short time intervals of less than 117 s and a rather uncorrelated distribution over longer time scales. Red lines indicate the fits of the two regimes.

Table 8.7: Overview of the exponents determined by the detrended fluctuation analysis and the corresponding statistics [59, 132, 133].

exponent α	statistics
$\alpha < 0.5$	negative correlation (anti-correlation)
$\alpha = 0.5$	white noise ($p(\nu) \propto \nu^0$)
$0.5 < \alpha < 1$	correlation with power law behavior ($p(\nu) \propto \nu^{-x}$)
$\alpha = 1$	pink noise ($p(\nu) \propto \nu^{-1}$)
$\alpha = 1.5$	Brownian noise ($p(\nu) \propto \nu^{-2}$)

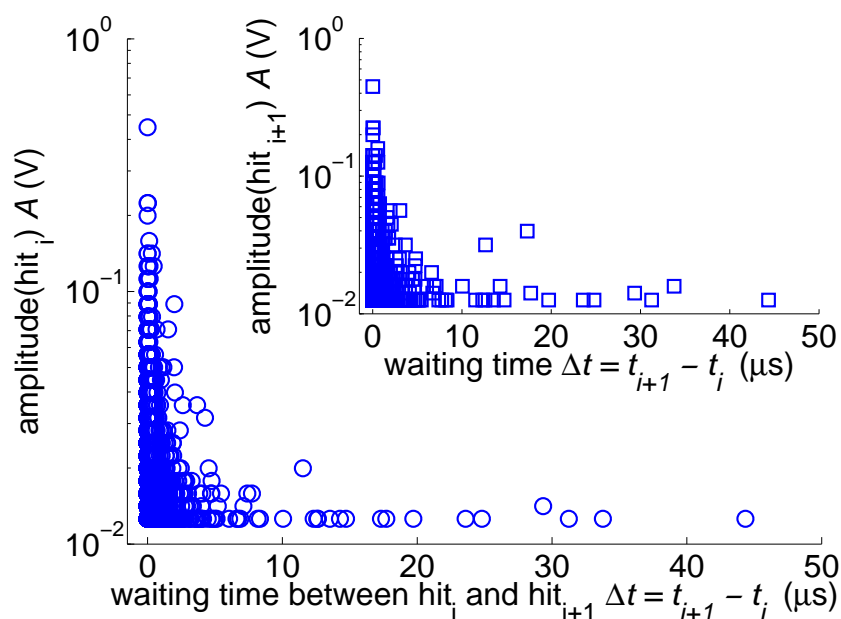


Figure 8.18: Hit amplitude as a function of the waiting time between subsequent hits of the forward transition of the Au_{50.5}Cd_{49.5} sample at a rate of 0.1 K/min. The main plot shows the correlation of hit_{*i*} with the waiting time between hit_{*i*} and hit_{*i+1*}. The inset shows the amplitude of hit_{*i+1*} with the waiting time between hit_{*i*} and hit_{*i+1*}.

main source of AE (see e. g. [12, 191]). In order to prove this assumption, further investigations are needed in this field. However, connecting characteristic time scales (found by dfa) with transition mechanisms (that give rise to AE) seems to be a promising approach.

The following brief analysis focuses on the correlation between the waiting time between successive signals hit_{*i*} and hit_{*i+1*} and the corresponding signal strength of hit_{*i*} and hit_{*i+1*}. It intuitively seems evident that longer waiting times, i. e. larger undercooling, lead to stronger signals. However, the analysis shows opposing results. Large amplitudes have only been found after short waiting times (see figure 8.18).

Vives proposes a positive correlation between the amplitude of a hit and the subsequent waiting time until the next hit occurs [188]. This hypothesis has been tested with the same data set and the results are shown in the inset of figure 8.18. Both figures display the same negative correlation of waiting times and amplitudes, which is in contrast to the hypothesis.

A possible explanation of the results is given by figure 8.19. It shows the histogram of the acoustic activity and a scatter plot of the amplitude distribution. Large amplitudes predominantly arise in regions of very high activity, where

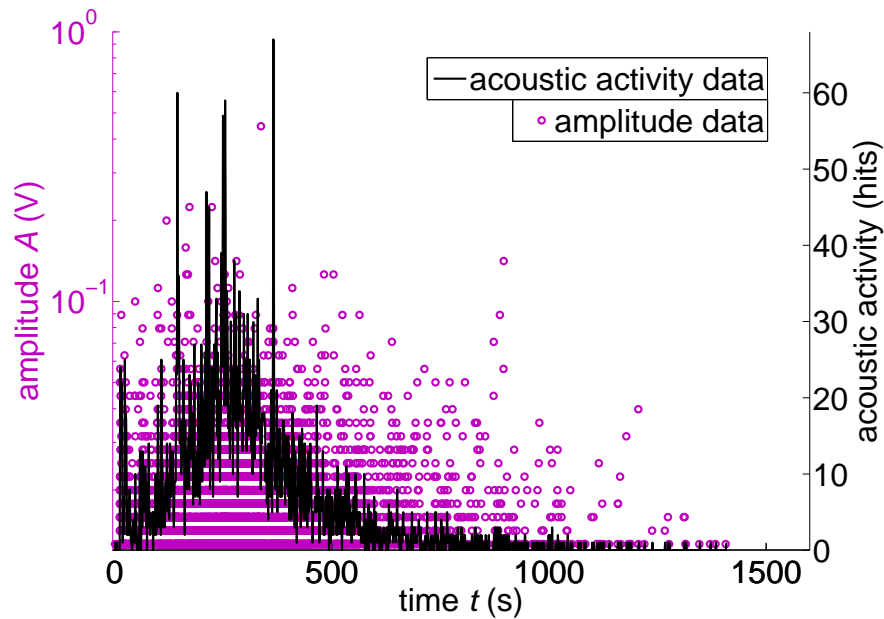


Figure 8.19: Acoustic activity and amplitude distributions of the martensitic transition of the $\text{Au}_{50.5}\text{Cd}_{49.5}$ sample at a rate of 0.1 K/min. The acoustic activity is represented in a time-histogram with a bin width of 1 s, which corresponds to a temperature bin width of 1.667 mK. The amplitude is depicted in a scatter plot. The similar distribution of the features indicates that high amplitudes occur predominantly in regions of high activity.

waiting times between successive hits are naturally short. For an experimental design with one AE transducer, the spatial origin of the signals cannot be detected. As a consequence, it is not possible to identify whether the AE signals originate from the propagation of a single or from more than one interface, as has been found for Cu-Zn-Al by Bonnot *et al.* [21]. The occurrence of more than one parallel source of AE would result in the detection of too short waiting times. Keeping this in mind, the real waiting time distribution may vary and the above presented results have to be taken with care.

8.3 $\text{Fe}_{68.8}\text{Pd}_{31.2}^{\text{single}}$ and $\text{Fe}_{68.8}\text{Pd}_{31.2}^{\text{poly}}$

The discussion in this chapter focuses on the similarities and differences between the single and the polycrystalline sample of $\text{Fe}_{68.8}\text{Pd}_{31.2}$. To the best knowledge of the author no AE experiments have been reported on Fe-Pd so far.¹²

¹²The AE measurements presented in [20] originate from this work.

The figures 7.23 and 7.24 (see section 7.2.3) depict the acoustic activity and the calorimetric data of the single crystal and polycrystal as a function of temperature. What catches the eye first is the strong similarity between the acoustic activity and the calorimetric curves, an observation that applies to all materials of this work and that is reported for many other martensitic transitions [140]. Nevertheless, the acoustic activity allows a much better resolution of the details of the transition kinetics in temperature. As a consequence, large differences can arise between the transition temperatures determined with calorimetric and AE experiments. In the case of the polycrystal the higher resolution of the AE data allows to detect the beginning of the martensitic transition at a temperature more than 25 K above the value estimated by the DSC standard procedure.

A second interesting observation, in agreement with calorimetric and AE data, is that the single crystal exhibits a much more structured transition than the polycrystal (see figures 7.23 and 7.23 in section 7.2.3). In contrast to the single peak curve shape of the polycrystal, the single crystal shows two to three prominent peaks on cooling and three to four prominent peaks on heating. This peak structure does not depend on the driving rate, as is illustrated in figures 7.26. Note that the rate has been changed by two orders of magnitude. Although the scaling is not as good as that found for other martensitic systems [137], it indicates pronounced athermal character of the single crystal transition. Additionally, a similar structure and especially the high peak obtained at the final part of the heating process have been reported from calorimetric measurements in a $\text{Fe}_{70.4}\text{Pd}_{29.6}$ single crystal [33]. This means that this structure is, to some extent, not a sample-dependent property and that it can be observed in a broad range of compositions.

In contrast to the athermal dynamics of the single crystal, the reverse transition of the polycrystal shows a rate-dependent acoustic activity, as has been observed in $\text{Ni}_{63}\text{Al}_{37}$ for cooling. The interpretation of the monotonic activity increase with increasing rates is analogous to the interpretation proposed for $\text{Ni}_{63}\text{Al}_{37}$ because again, isothermal dynamics meets different driving rates in a crystal with large disorder due to grain boundaries. However, different to $\text{Ni}_{63}\text{Al}_{37}$, here a constant signal strength can be observed and the isothermal behavior occurs in the reverse transition. The constant signal strength probably results from the (isothermal) transition direction, which is exhibited without accommodation processes. Moreover, the athermality of the forward transition leads to the storage of a constant amount of strain energy at all rates. Consequently, the signal strength does not depend on the rate [13]. The increase of AE with higher rates is supposed to be related to the reduced strain field relaxation times after pinning-depinning interactions because of quicker super-heating. The decoupling of the rate-dependence of the activity and the exponents suggest that rate-dependent exponents are a sufficient but not a necessary condition for explicitly time-dependent dynamics.

The single peaked and quite smooth transition of the polycrystal is probably owed to the fact that grains exhibit a distribution of internal strains and boundary conditions that smooth out the diverse structure of the acoustic activity from the various grains. An interesting observation is that, although the activity peaks of the polycrystal and the single crystal show a temperature offset of approximately 15 K, there are tails of activity that clearly extend many degrees above and below the peak position. The tails of the AE above 240 K can be seen in figure 7.25 in section 7.2.3. The first observation is that the beginning of the transition on cooling and the end of the transition on heating coincide for both the single crystal and the polycrystal ($M_s^{\text{single}} = A_f^{\text{single}} = M_s^{\text{poly}} = A_f^{\text{poly}} = 247 \pm 1$ K). Moreover, the acoustic activity also reveals that there is almost no hysteresis (< 2 K), which is in agreement with calorimetry and magnetic-susceptibility measurements [20].

In this context, the absence of measurable acoustic activity above 250 K is worth noticing. It indicates that, if AE associated with pretransitional effects exists, it is below the limit of detectability. Moreover, the temperature intervals, where the nonlinear behavior of the lattice parameters has been reported, are much larger than the transition temperature interval found by AE and calorimetry measurements.¹³ Based on this finding it can be inferred that AE is strictly related to first-order phase transitions and occurs all over the coexistence of tetragonal and cubic phases.

As can be seen in figures 7.28 and 7.29 in section 7.2.3, none of the crystals shows a significant rate-dependence of the exponents. Moreover, the single crystal does not show any relevant dependence of the exponents when comparing cooling and heating ramps, whereas for the polycrystal this difference is obvious for both the amplitude and energy exponents.

The value $\alpha = 2.25$ obtained for the single crystal can be compared with the values found for other single-crystalline samples. A few years ago, it was proposed that this exponent is universal and characteristic of all the martensitic transitions with the same symmetry change [22]. Different Cu-based alloys transforming from a cubic structure to a monoclinic one (18R) had $\alpha = 3.1 \pm 0.2$ and those transforming from cubic to orthorhombic (2H) had $\alpha = 2.4 \pm 0.2$. Later, it was realized [135] that the true universal value is only obtained when the thermal driving of the sample is adiabatic. This has two implications: on the one hand,

¹³Measurements of the dependence of the lattice parameter on temperature [33, 110] reveal that the transition is first order, spreading over a temperature range of approximately 25 K. Within this range a coexistence of the x-ray peaks of the two phases exists. Moreover, for temperatures well below this coexistence region the a and c lattice parameters of the tetragonal lattice exhibit a remarkable monotonous increase on cooling, which extends more than 75 K up to 100 K. This monotonous increase has been found to be nonlinear and similar to the increase expected for a second-order-like behavior for an alloy similar to the one of this work [64]. Actually, in previous work, the transition was classified as nearly second order [33], also because of its small latent heat compared to that of other shape-memory alloys.

the rate should be slow enough to prevent an overlap of the signals corresponding to independent transformation events [201]. On the other hand, for systems that do not behave athermally, the driving should be fast enough to prevent nucleation due to thermal fluctuations. Supposing that the materials analyzed in [22] were less athermal and driven too slow, this last point suggests that the value proposed for the transformation from cubic to orthorhombic can be potentially higher than $\alpha = 2.4 \pm 0.2$. In the Fe_{68.8}Pd_{31.2} case, corresponding to a transition from cubic to tetragonal symmetry, the independence of the exponent from the driving rate (while changing it by two orders of magnitude) provides ample evidence that the exponent is close to the adiabatic one.

Figure 8.20 shows the amplitude exponents of all approximately 150 temperature cycles during cooling. It can be seen that the change of the exponents is rather large during the first approximately 50 cycles before it reaches saturation after approximately 80 runs. It is worth mentioning that this behavior reveals interesting insights into the training effect. First, the exponent shift towards higher values can be identified with the establishment of an easier transition path. This interpretation is also in agreement with the experimental results for Ni₆₃Al₃₇, showing that a well trained sample needs less undercooling to start the martensitic transition than an untrained sample (for details, see [90]). Second, the fluctuation of the exponent can be viewed as a manifestation of the attempt of the system to find a new transition path. The clustering of the exponents at values of approximately 2.2 after 80 cycles is consistent with the idea that a rather optimal path has been found.

8.4 Ni₅₂Mn₂₃Ga₂₅

This section deals with the discussion on the AE generated during the premartensitic and the martensitic transition in a Ni–Mn–Ga ferromagnetic Heusler alloy. Associated with the transitions, these materials display magnetic shape-memory properties [186]. These properties are related to the ability of magnetically inducing large deformations, which is a consequence of the existence of strong coupling between elastic and magnetic degrees of freedom. Due to this coupling nucleation and growth of the intermediate and the martensitic phase are expected to be affected by the presence of an applied field. Moreover, these transitions show jerky character, which means that the growth process occurs through a sequence of discontinuities related to sudden changes of the local strain field [134]. These discontinuities can be understood as jumps from a marginally stable state to a metastable state within a complex free energy landscape. These changes in the strain field give rise to the AE waves, which carry the dissipated energy in the process [21]. Indeed, owing to the mentioned coupling an applied field could modify these barriers and thus influence the nucleation and growth processes.

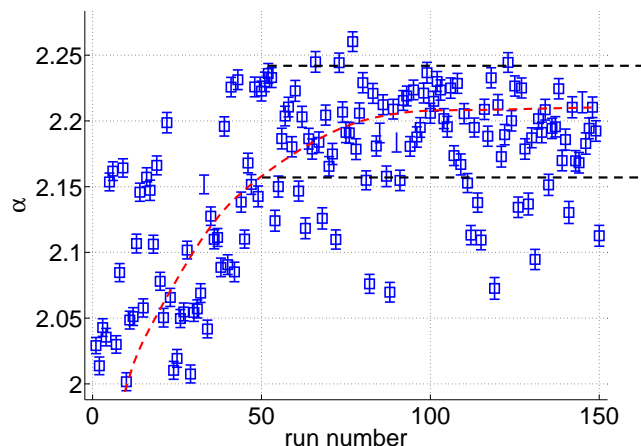


Figure 8.20: Development of the exponent α of the amplitude distribution of $\text{Fe}_{68.8}\text{Pd}_{31.2}^{\text{single}}$ as a function of the cooling run number. The trend of the exponent is visualized by the red dotted line. The black dotted lines indicate the saturation range of the majority of the exponents. The exponent ϵ of the energy distribution shows a similar behavior.

The discussion on $\text{Ni}_{52}\text{Mn}_{23}\text{Ga}_{25}$ closes with an analysis of the AE during the field-induced rearrangement of variants, which has, to the best knowledge of the author, not been analyzed before.

8.4.1 Premartensitic transition

Acoustic activity has been detected during the forward and reverse intermediate transition in a range of weak applied magnetic fields. The occurrence of AE for sufficiently low applied fields shows that the intermediate transition displays jerky character. Amplitude, energy, and duration of AE signals show power law distributions which reflect the absence of characteristic length and time scales associated with the transition process. This behavior is common to a broad class of processes [164], which occur through a sequence of discontinuous steps of the order parameter. Each step is supposed to be related to a fast relaxation from a marginally stable configuration towards a new metastable one. This relaxation can be understood as taking place in a complex energy landscape determined by disorder, long-range effects, or the coupling to a secondary (inhomogeneous) field. In the case of structural transitions, such as martensitic transitions, these discontinuous steps are related to sudden changes of the local strain field that occur due to the interplay between transition and some pinning effects and are responsible for the observed acoustic activity. The author suggests that for the intermediate transition studied here, the magnetic field plays essentially the role

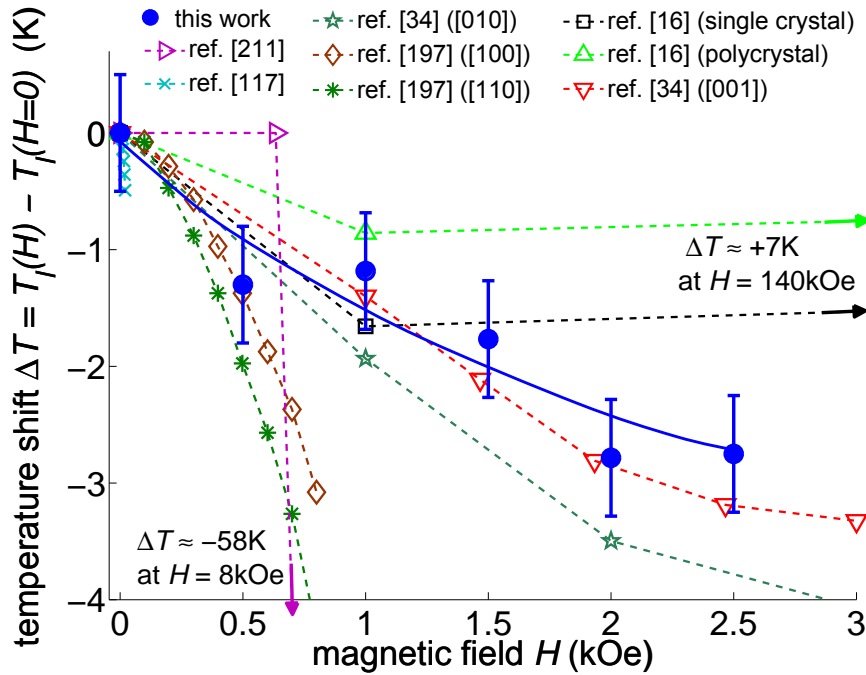


Figure 8.21: Comparison of the temperature shift of the premartensitic transition as a function of the applied magnetic field, in the field range relevant here, reported by various authors. Note that directions of the applied field as well as results from single and polycrystals are displayed together (see legend and table 8.8).

of an ordering field that controls pinning effects. This is supported by the fact that the acoustic activity during forward and reverse intermediate transitions decreases with increasing the field and is suppressed for fields larger than about 2.5 kOe, which is close to the magnetization saturation field (see e. g. [16, 34, 197]). This effect is accompanied by a decrease of the temperature T_{max} at which a maximum acoustic activity is detected ($dT_{max}/dH \simeq 1 \text{ K/kOe}$). By identifying T_{max} with an effective transition temperature T_I of the forward premartensitic transition, results indicate that the intermediate transition shifts to lower temperatures when a weak magnetic field is applied. The decrease of T_I at low applied fields is consistent with all previous reported results (see figure 8.21). For comparison, values of the intermediate transition temperature, reported in the literature for alloys of slightly different compositions, are included in the figure. In the depicted field range of 0 kOe–3 kOe all authors consistently report a decreasing transition temperature with the applied field, independent of the direction of the field. However, the maximum temperature shift varies between less than one Kelvin [16] and approximately 40 Kelvin [211]. Table 8.8 summarizes these

Table 8.8: Published values for the temperature shift from various authors.

composition	crystal	field direction	T_I (K)	shift ΔT at $H=0.5$ kOe	max. shift ΔT_{\max} at H	reference
Ni _{49.5} Mn _{25.4} Ga _{25.1}	single	-	244	-0.8 K	+8.5 K at 140 kOe	[16]
Ni _{51.1} Mn _{24.9} Ga _{24.0}	poly	-	261	-0.4 K	+7.5 K at 140 kOe	[16]
Ni _{50.5} Mn _{24.5} Ga _{25.0}	single	[001] / [010]	202	-0.7 K / -1.0 K	-3.5 K / -5 K at 16 kOe	[34]
Ni ₅₀ Mn ₂₅ Ga ₂₅	single	[100] / [110]	251	-1.4 K / -2.0 K	-3 K / -4.25 K at 0.8 kOe	[197]
Ni ₅₀ Mn ₂₅ Ga ₂₅	-	-	270	0 K	-58 K at 8 kOe	[211]
Ni ₅₀ Mn ₂₅ Ga ₂₅	single	[100]	230	-	-0.5 K at 0.02 kOe	[117]
Ni ₅₂ Mn ₂₃ Ga ₂₅	single	[001] and [110] (average)	233	-1.3 K	-3 K at 2.5 kOe	this work

results. In some cases, much larger fields up to 140 kOe are applied and the sign of the temperature shift even changes [16].

The results clearly show that the transition path strongly depends on the applied magnetic field. This is corroborated by the fact that the exponents characterizing the distributions of amplitude, energy, and duration of AE signals increase as the field is increased. This increase means that signals of lower energy and duration occur when a magnetic field is applied, which suggests that the magnetic field leads to an overall weakening of the first order character of the transition.

The effect of the field on the transition path can be understood from the change of the micromagnetic structure taking place at the intermediate transition. In most shape-memory alloys precursor texture known as tweed, which consists of cross-hatched nanoscale modulated structural domains, occurs far above the martensitic phase transition [71]. In magnetic shape-memory alloys, magnetic nanodomains are formed inside these domains [157]. Moreover, modulated nanoscale domains play the role of nucleation embryos at the intermediate transition where tweed texture locks into the intermediate micromodulated phase [209]. In the absence of an applied magnetic field, the distribution of magnetic domains gives rise to a distribution of local magnetic moments in the intermediate phase [131], which is mainly determined by magnetocrystalline anisotropy. Note that compared to the cubic phase, the intermediate phase shows larger uniaxial anisotropy [197]. It can be argued that this larger magnetocrystalline anisotropy is responsible for the coupling of transition and magnetization in this system. Therefore, under an applied magnetic field, the distribution of magnetic moments will be modified which in turn should affect the transition path. Moreover, it is also responsible for the (weak) decrease of magnetization taking place during the transition. Actually, this scenario for the intermediate transition is similar to the picture of martensitic transition under an applied magnetic field where coupling between transition and magnetism is acknowledged to be driven by magnetic anisotropy (see section 8.4.2 and [125]). There is, however, an important difference: the intermediate transition is not accompanied by a uniform distortion of the lattice as happens in the case of the martensitic transition [210]. Therefore, the transition is not constrained by an invariant plane condition necessary to

minimize the elastic strain energy arising from the crystal lattice misfit along interfacial boundaries. Thus, for the intermediate transition, selective growth of those variants with magnetic moments parallel to the applied magnetic field is possible. Hence it is expected that when magnetization saturation is reached, energy barriers that have to be overcome for the transition to progress should have a minimal value. This scenario explains the overall decrease of the acoustic activity as well as the decrease of the exponents characterizing the amplitude, energy, and duration distributions of AE signals. Whether the reduction of energy barriers due to the ordering field is able to yield a second order transition remains an open question. In case this occurs, the absence of interfacial energies would exclude all pinning-depinning processes and would explain the suppression of AE with increasing the magnetic field.

8.4.2 Martensitic transition

In the martensitic transition the applied magnetic field not only modifies the relative stability between parent and martensitic phases due to their different magnetic moments but, and more importantly here, breaks the degeneracy of the low temperature martensitic phase as a consequence of its strong uniaxial magnetocrystalline anisotropy. Thus, the martensitic variant with an easy axis forming a lower angle with the applied magnetic field will be favored in relation to other variants [4, 125].

In the following will be discussed the amplitude distribution of the AE signals recorded during the martensitic transition at selected values of the applied magnetic field. These distributions, which are shown in figure 7.39, reflect the distribution of energy barriers, which separate metastable states and thus provide information on the transition path and dissipated energy. Interestingly, in a number of systems undergoing martensitic transitions, after some amount of cycling through the transition (which increases the density of lattice defects), the distribution of AE amplitudes displays power law behavior. This reflects the absence of any characteristic scale, which is a typical feature of criticality [134]. Note that the power laws found in transitions of Ni₅₂Mn₂₃Ga₂₅ can exceed more than six decades (see figure 7.39). It has been suggested that such a criticality is related to the athermal character of the transition and an intrinsic amount of disorder [163]. The idea has been substantiated by the study of simple lattice models that exhibit fluctuationless first-order phase transitions [35, 163]. However, as has been shown in the last sections, explicit time-dependent processes can be characterized by power laws, too.

It has been suggested that the amplitude exponent α depends on the degeneracy of the martensitic phase, which in turn depends on its crystallographic structure [20, 22]. Actually, the obtained value $\alpha \approx 2.5$ at zero field (consistent with a previous estimate [139] for a system which transforms to a 10 M structure) fits

well within this framework [20]. As the field is increased, the system has the tendency to transform into a single variant martensite with associated reduced degeneracy, which is due to the symmetry-breaking effect of the magnetic field. In accordance with this a decrease in the exponent α can be found. It is worth pointing out that in addition to the amplitude distribution, the distribution of hit energies has also been studied. The energy E of hits has been obtained, as described above, from the integration of the square of the voltage signals over their time duration divided by a reference resistance. Obtained results are qualitatively similar to those obtained from the analysis of amplitudes. At zero field an exponent of $\epsilon = 1.75 \pm 0.1$, characterizing the energy distribution, has been found. This value is compatible with the relationship $\epsilon = (\alpha + 1)/2$ between ϵ and α , which results from the scaling relation $E \propto A^2$ (see equation 8.2 at the beginning of this chapter).

Results for the field applied in the $[\bar{1}10]$ direction are also qualitatively similar to those reported for fields applied along the $[001]$ direction, but the effect of the magnetic field is more pronounced when applied along the $[001]$ direction. This is the expected result, taking into account that, when the field is parallel to the $[001]$ direction, a single variant with easy axis (short c-axis) parallel to the field is favored while more than one variant is equally likely to develop when the field is applied along the $[\bar{1}10]$ direction (see, e. g. [118]).

The analysis of the distributions of hit amplitudes and energies shows that AE events of higher energy occur by increasing the field. This reflects the existence of higher barriers to be overcome for the transition to proceed as the temperature is decreased/increased. This result can be understood by taking into account that in these systems, nucleation gives rise to plates formed by parallel strips of twin-related variants with an appropriate amount of each variant so that the parent-martensite interface satisfies the invariant plane condition [73]. This configuration minimizes the elastic strain energy arising from the crystal lattice misfit along interfacial boundaries. Under an applied magnetic field it has been shown [125] that nucleation still requires two different variants to form simultaneously. However, in this case the two variants are not energetically equivalent, which gives rise to higher barriers to be overcome. At the late stages of the forward transition process, rearrangement of variants (with tendency to form a single variant martensite) is expected, which is responsible for the increase in the total amount of AE associated with the transition with increasing magnetic field (see figure 7.38). In order to confirm this result, it has been proven that this increase in acoustic activity corresponds, to a good approximation, to the acoustic activity generated during isothermal rearrangement of martensitic variants under magnetic field in a zero-field cooled martensitic state (see results in section 7.2.4 and the discussion in the subsequent section).

By contrast, the acoustic activity of the reverse transition remains practically constant regardless of the applied field, as can be seen in figure 8.22. At suf-

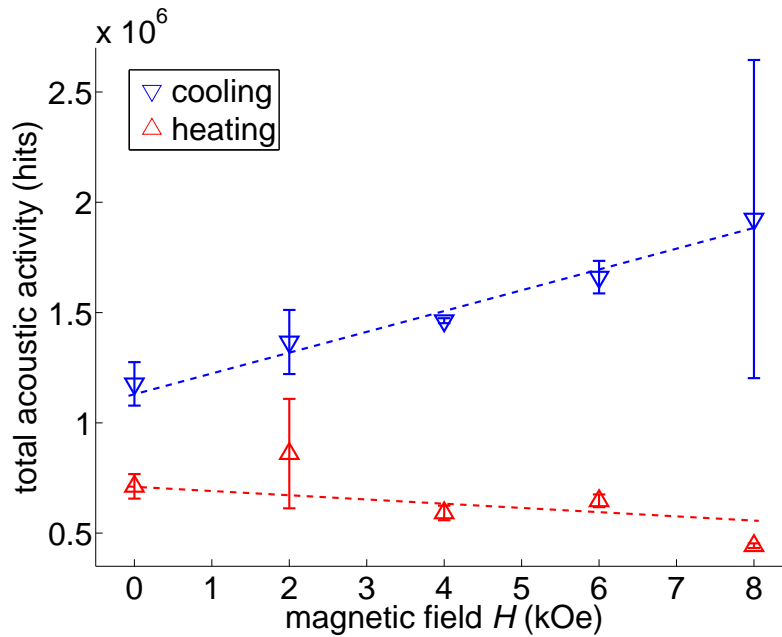


Figure 8.22: Total acoustic activity during the forward and the reverse transition at selected fields applied along the [001] direction. The acoustic activity under heating shows, in contrast to the cooling runs, essentially no field-dependence.

ficiently high fields all variants are aligned and a single variant martensite is achieved. Okamoto *et al.* observed that under field heating twinning occurs in order to satisfy the invariant habit plane condition prior to the transformation into the high temperature phase [125]. From the constant amount of acoustic activity it can be inferred that under heating, in contrast to the forward transition, the variant reorientation and the transition, i. e. the twin and phase boundary motion, occur in a single step instead of proceeding as a twofold process. This assumption would explain the constant activity. However, higher fields are expected to exert larger magnetic constraints on the process, leading to higher energies. This assumption can be supported by the observation of strongly increased acoustic energy associated with the reverse transition under applied fields. Figure 8.23 compares the constant amount of acoustic activity with the field-dependent energy distribution, both belonging to the same reverse transitions.

The discussion about the martensitic transition closes with a brief analysis of the emitted frequency spectrum.¹⁴ Neither the spectrum of the premartensitic transition nor the spectrum of the martensitic transition show any dependence on the applied field. The mean peak frequency, including the forward and reverse

¹⁴Note that the frequency spectrum strongly depends on the resonance frequency of the used AE transducer (R15-LT: nominal resonance frequency 150 kHz).

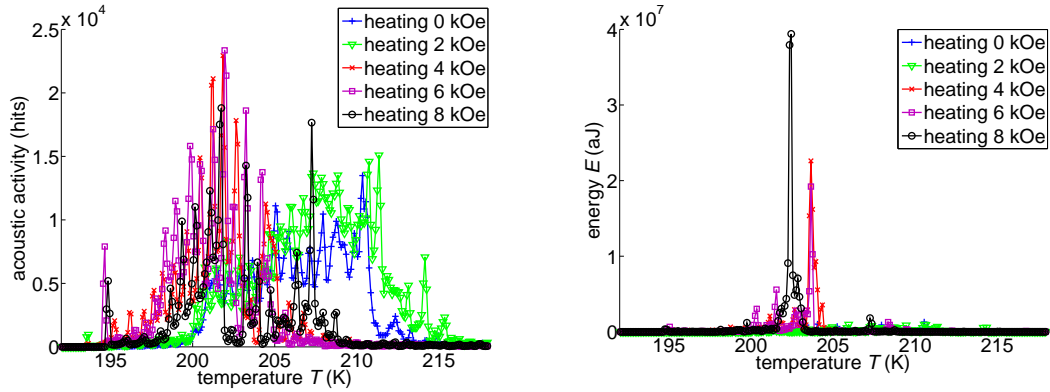


Figure 8.23: Acoustic activity (left) and energy (right) versus temperature during the reverse transition on heating at selected values of the field applied along the [001] direction. Note that the acoustic activity is basically field independent, whereas the acoustic energy strongly increases with increasing fields and that both plots originate from the same heating runs. This observation is consistent with the rate-dependent signal strength, as depicted in figure 7.39.

transition, at all applied fields, and both for field directions, can be determined to be 128 ± 4.6 kHz (see figure 8.24). As can be seen in the small standard deviation, all martensitic transitions show the same frequency distribution within a small error. However, the premartensitic transition shows a significantly lower mean frequency of 112 ± 2.4 kHz.

8.4.3 Rearrangement of variants under magnetic field

This section discusses the effects observed under field-induced rearrangement of martensitic variants, which have to the best knowledge of the author not been analyzed before by AE spectroscopy.

It can unmistakably be proven that the magnetic-field-induced rearrangement of martensitic variants occurs under large amounts of AE.¹⁵ Figure 8.25 shows the acoustic activity detected during the first magnetic field cycles after zero-field cooling at a high rate with a cycle period of $\tau_{mf} = 130$ s and at a low rate with a cycle period of $\tau_{mf} = 1300$ s. It is important to note that during the first cycle at $\tau_{mf} = 130$ s a certain amount of acoustic events has not been detected by the AE acquisition setup because the high number of AE events per time step exceeded the buffer capacity of the AE acquisition system. As shown in figure 8.25 (right), the hardware limit results in a sudden decrease of the activity during the first

¹⁵Interestingly, during an similar experiment with $\text{Fe}_{68.8}\text{Pd}_{31.2}^{\text{single}}$, no AE could be detected associated with magnetic field cycles.

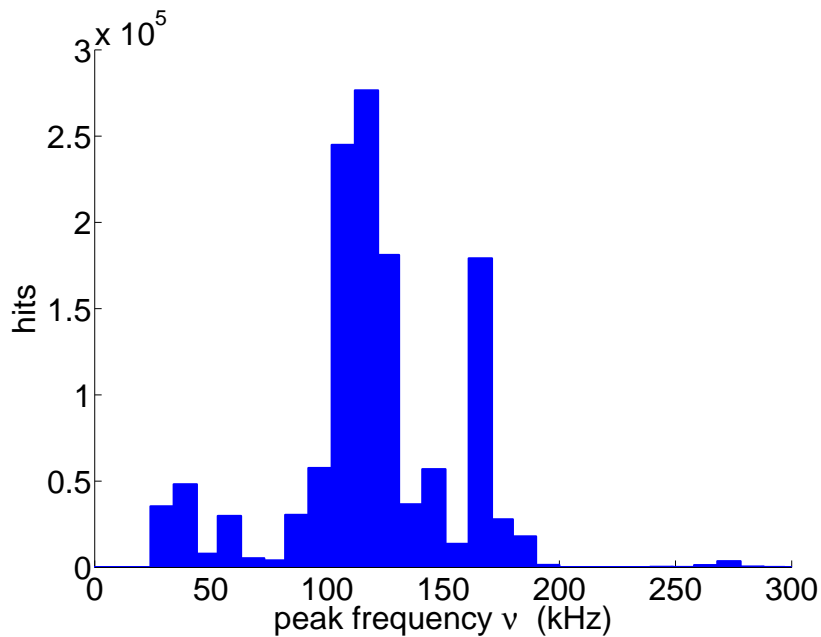


Figure 8.24: Frequency spectrum detected with an AE transducer resonant at 150 kHz during the martensitic transition of the $\text{Ni}_{52}\text{Mn}_{23}\text{Ga}_{25}$ sample without applied magnetic field. Note that the discrete spectra result from a 10 kHz binning of the AE acquisition system.

field increase. However, it can be guaranteed that only the first quick cycle is affected by this limitation. It has further been proven that all hits have been detected during all slow cycles.

The shape of the acoustic activity curve under the first field increases after zero-field cooling reveals useful information about the rearrangement process. As can be seen in figure 8.25, the maximum activity occurs at approximately 5 kOe. Under further increasing field the activity decreases and reaches almost zero at approximately 10 kOe. In agreement with literature it is shown that saturation of the variant alignment, i. e. a single variant state, is reached at approximately 10 kOe (see e. g. [186]).

Moreover, the comparison of the total activities during increasing cycle numbers reveals for both quick and slow cycles that the by far largest amount of AE occurs during the first cycle. After the strong activity decrease from cycle number one to two a further weak decrease is visible.

In a stress- and bias-free sample it is assumed that, after applying a sufficiently large field of approximately 10 kOe, all variants form a single variant state and remain in this aligned configuration after removing the field due to absent restoring forces. However, as shown in literature, even a small applied stress

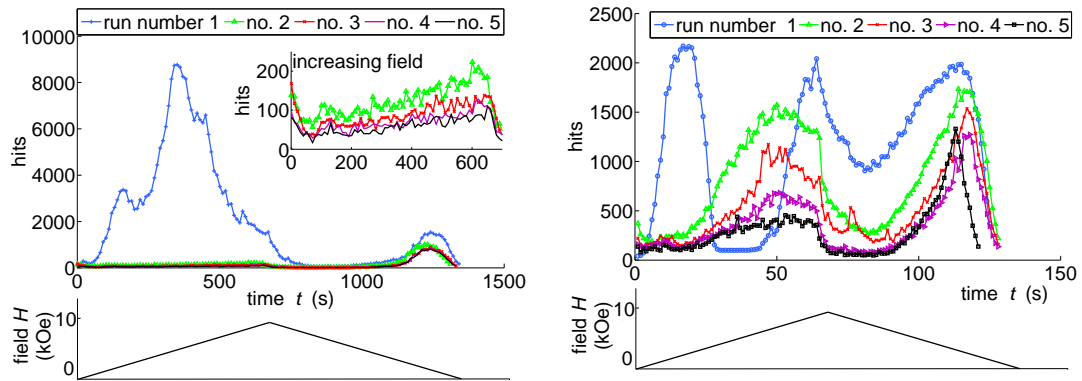


Figure 8.25: Acoustic activity during magnetic-field-induced rearrangement of martensitic variants under increasing and decreasing fields. For a better comparison the subsequent cycles have been plotted within the same time frame. On the left, the acoustic emission is shown for slow cycles with $\tau_{mf} = 1300$ s and on the right for quick cycles with $\tau_{mf} = 130$ s. The bin width of 10 s in case of the slow cycle and 1 s in case of the quick cycle compensate the different rates and are both equivalent to a field change of approximately 0.15 kOe. The inset (left) enlarges the region of small activity during increasing fields of the cycle numbers 2, 3, 4, and 5. Note that the drop in AE during the first quick cycle between 25 s and 50 s is caused by hardware limitations of the AE acquisition system.

can lead to the back rotation of a certain number of variants during the removal of the field [113]. For those variants the repeated application and removal of a field during field cycles would lead to a repeated variant alignment with the field and a subsequent back orientation without field. In fact, the detected AE is fully consistent with the described process. The field-free self-accommodation process during cooling leads to the formation of appropriate amounts of each variant (see equation 3.7 and [125]). During the subsequent first field increase the highest amount of activity arises due to an alignment of all variants that were not aligned before. During the removal of the field only those variants flip back that are exposed to the largest bias forces arising from internal strain fields and in addition from the sample mounting, which applies a small stress of approximately 0.05 Mpa perpendicular to the applied field. It is important to keep in mind that the magnetic easy axis lies parallel to the short c-axis. During the second cycle only those variants which rearranged under field removal align again with the field. This can be detected by a certain amount of AE. Based on these observations the author assumes that the amount of AE is an indicator of the amount of rotating variants. Moreover, the assumption that under field removal only those variants flip back that are subjected to large constraints can

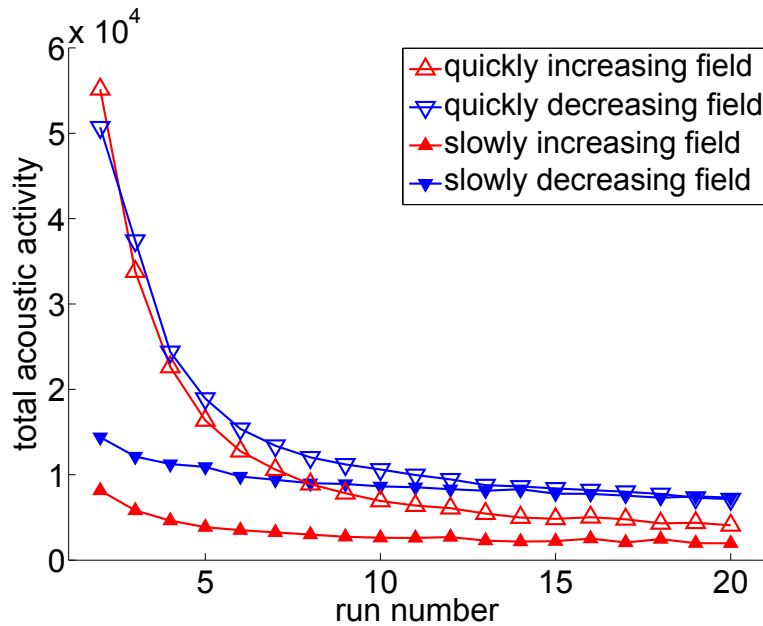


Figure 8.26: Total acoustic activity of increasing and decreasing magnetic fields at a slow rate with a period of 1300 s and at a high rate with a period of 130 s. The figure starts with run number two to exclude a problem arising from hardware restrictions.

be corroborated by the following observation: In contrast to the first cycle, the maximum of the acoustic activity during the following field increase is found to be close to 10 kOe. This shows that only the strongest field is sufficiently large to overcompensate the constraints and to reach a realignment.

Taking all aspects described above into account, the slow and the quick magnetic field cycles show similar results. However, a closer look at figure 8.25 reveals differences in the amount of AE occurring at higher field cycle numbers. As can be seen in figure 8.26, quick cycles show a higher amount of AE during the cycles 2, 3, ..., than slow cycles. After approximately 20 cycles both activities saturate at comparable values. With the proposed correspondence of AE events with the number of reorientating variants it can be concluded that under slow cycles the amount of variants that remain in the single variant state after field removal is larger than under quick cycles.

An explanation of this rate-dependent behavior can be given within the framework of martensite respectively twin stabilization, which are aging phenomena. A general model for martensite stabilization is given by Ren and Otsuka (see e. g. [127, 149, 151] and section 8.2, where the symmetry-conforming short-range

order model is presented).¹⁶ For magnetic shape memory alloys as Ni₂MnGa a second approach exists that considers twin stabilization as a consequence of the time-dependent adaptation of the nanosized short-range magnetic cluster to the martensite symmetry [36]. In high-temperature Ni₂MnGa samples aging times ranging from minutes to several days have been found [36] [161] [205].

The author proposes that the different cycle times of $\tau_{mf} = 130$ s and $\tau_{mf} = 1300$ s lead to different degrees of twin stabilization, which in turn lead to varying total AE amounts between slow and quick cycles.

After zero-field cooling and before applying a magnetic field, the samples were held in the martensitic phase for approximately one hour, which stabilized the self-accommodated variant configuration. In spite of the stabilization the application of a magnetic field leads to a rearrangement of martensitic variants reaching a single variant state at 10 kOe. Once the single variant state is realized, the large total time of the slow cycles leads to a stabilization of the new configuration because of lowered twin boundary mobility [35]. Under field removal only those variants flip back that are exposed to sufficiently large (local) constraints, which are not compatible with the single variant state. Under the subsequent field increase of the second cycle only the small fraction of variants that have already flipped back realign. For subsequent cycles this process of realignment and back orientation is repeated, which is fully consistent with the observed AE behavior.

For quick cycles the situation is different: Due to the rather short cycle time $\tau_{mf} = 130$ s the single variant state is not stabilized. By contrast, the microstructure of the self-accommodated variant distribution after zero-field cooling is passed on to the single variant state [127, 149, 151] and leads to the back rotation of a considerable large number of variants under field removal. This effect is known from the two-way shape memory effect [150]. As a consequence, the amount of AE under quick field removal is considerably higher than under slow removal. During the second cycle the number of variants to realign with the field is relatively large, which leads again to a high amount of AE.¹⁷

An observation that accounts for both slow and quick cycles is the monotonically reduced AE as a function of the cycle number, which can be identified with a constantly decreasing number of variants that flip back from the single variant state (see figure 8.26). Here again, the twin stabilization offers an explanation: All variants that remain aligned after field removal will not flip back during subsequent cycles, because the time without rotation leads to a further stabilization. Moreover, it can be assumed that the higher degree of stabilization leads to a smaller misfit between long-range and short-range order, which lowers the local strain fields [35]. The author supposes that because of the reduced constraints the

¹⁶Ni₅₂Mn₂₃Ga₂₅ has a relatively low ratio of $M_s = 210$ K to the melting point $T_m \approx 1380$ K $M_s/T_m \approx 0.15$ (see table 8.6).

¹⁷It is evident that the stabilization of the self-accommodated variants, i. e. the two-way shape memory effect gets lost with increasing cycle numbers.

stabilized variants adopt the role of a catalyst for further variant alignment and subsequent stabilization. Due to this positive feedback the amount of flipping variants is constantly reduced, which is reflected by the decreasing amount of AE. The observation that the saturation-like level is reached after a smaller cycle number for low rates supports this interpretation.

Moreover, the lower twin boundary mobility due to stabilization effects is expected to be associated with higher energy barriers separating different twin respectively variant orientations. A main conclusion of the last chapter has been that higher energy barriers are manifested in stronger AE signals, i. e. lower exponents. In this case, the lower twin boundary mobility due to higher stabilization is expected to have the same effect on the signal strength.

During slow cycles with long stabilization times a variant selection process is supposed to occur due to the reduced twin boundary mobility: After each field removal the number of variants that flip back is reduced by those variants where the twin stabilization exceeds the bias forces and constraints. This is expected to occur predominantly for those variants that are exposed to the lowest constraints and whose reorientation process is associated with the weakest AE events. Consequently, the variant selection with increasing cycle numbers filters small events and results in decreasing exponents. The constraints are known to hinder the alignment during field application and to drive the back rotation during field removal. This turns out to be the reason why both exponents of increasing and decreasing fields show lower values with higher cycle numbers (see figure 8.27 (top)).

The stabilization hypothesis can be tested by the opposite case of quick cycles. Due to the absent twin stabilization¹⁸ and associated low energy barriers, even variants exposed to small constraints can flip back to their energetic minimum position under a decreasing field. Without stabilization and associated higher energy barriers no selection process is active and the amplitude distribution remains constant under increasing cycle numbers, as reflected by the exponents (see figure 8.27 (bottom)).

It can be concluded that the effect of twin stabilization in magnetic-field-induced variant rearrangement leads to a reduced number of flipping variants under field cycles which are accompanied by stronger signals. The observed characteristics are fully compatible with the reported time-dependent reduction of the twin boundary mobility [36].

Besides the influence of the different field driving rates the influence of the field direction on the reorientation process has been analyzed. According to O'Handley (see reference [118]), the force on the variants is largest with a magnetic field applied along the twin boundary, i. e. along the $[\bar{1}10]$ direction. This has been

¹⁸The stabilized martensite after zero-field cooling cannot be identified in the exponent, because the exponents of the first cycle are missing due to memory overflow problems.

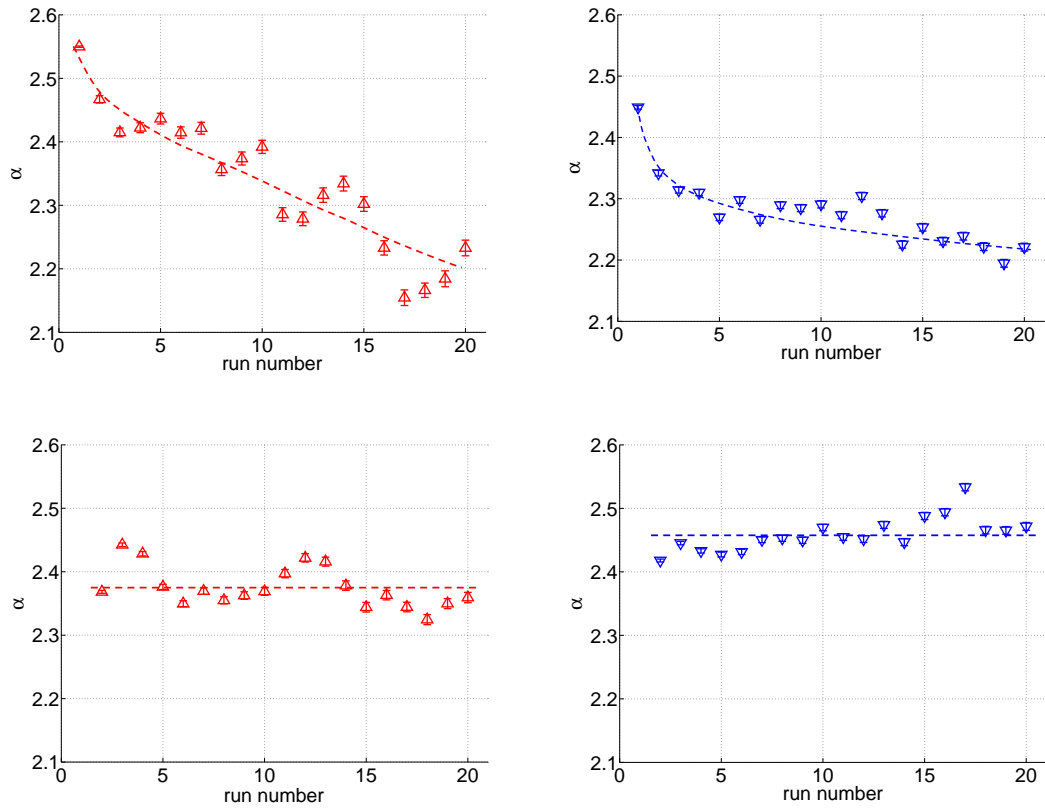


Figure 8.27: Amplitude exponents α as a function of the run number obtained during magnetic-field-induced rearrangement of martensitic variants of $\text{Ni}_{52}\text{Mn}_{23}\text{Ga}_{25}$ under increasing fields (left) and decreasing fields (right). The field is applied in $[001]$ direction. Results of the energy exponents ϵ are similar and follow the scaling relation $\epsilon = \alpha + 1/2$.

Top: Decreasing amplitude exponents during slow field increase (left) and slow field decrease (right) with a cycle period $\tau_{mf} = 1300$ s.

Bottom: Constant amplitude exponents during quick field increase (left) and quick field decrease (right) with a cycle period $\tau_{mf} = 130$ s. Experiments with an applied field in $[\bar{1}10]$ direction yield comparable results.

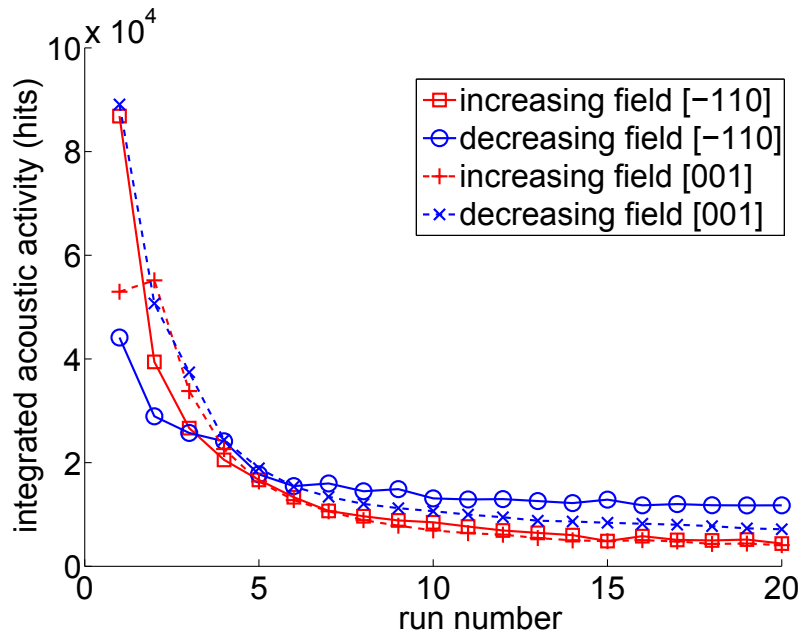


Figure 8.28: Comparison of the integrated acoustic activities as a function of the cycle number of both field orientations $[001]$ and $[\bar{1}10]$. In contrast to O’Handley’s prediction that the strain should be maximized by a field applied along $[\bar{1}10]$ (see reference [118]), both directions show the same total amount of AE.

tested by applying identical field cycles along the directions $[001]$ and $[\bar{1}10]$. As can be seen in figure 8.28 both field directions reveal comparable amounts of AE, which is not in line with the calculations of O’Handley. Moreover, results confirm the occurrence of aging effects during the rearrangement of variants regardless of the orientation of the applied field.

8.5 Comparison of results

This chapter ends with a brief comparison of the discussed results of the different samples and the corresponding exponents.

Athermality or time-dependent sample characteristics such as aging or isothermality can be analyzed by acoustic activity. The absence of scaling during rate-dependent temperature or magnetic field cycles indicates explicit time dependence.

The analysis of the exponents has a different focus. Because of the positive correlation between amplitude, energy, and duration, a change of the exponents draws a specific picture of the acoustic emission events: Smaller exponents

Table 8.9: Overview of cooling amplitude exponents of materials that transform into the same low temperature symmetry. Two universality classes are proposed, which are compatible with literature [22]. The exponents of Ni₂MnGa have been determined at zero magnetic field, the exponents of the other materials in the adiabatic limit at a cooling rate of 10 K/min (see the tables 8.1 and 8.2).

material system	low temp. symmetry	cooling amplitude exp.	class
NiAl	monoclinic	3.18 ± 0.03	3.1 ± 0.2
CuZnAl	monoclinic	2.85 ± 0.05	3.1 ± 0.2
Ni ₂ MnGa	(pseudo) tetragonal	2.60 ± 0.02	2.4 ± 0.2
FePd	tetragonal	2.18 ± 0.1	2.4 ± 0.2

indicate longer acoustic signals with higher amplitudes and energies. In short they indicate stronger signals.

As has been confirmed by this work, the strength of the AE events reveals information about the transition path through the complex energy landscape which is dominated by metastable states giving rise to jerky avalanche dynamics. The signal strength provides a useful tool for analyzing the modifications of energy barriers, which have been shown to depend on several sample properties. These properties are: (i) disorder, which in case of the premartensitic transition of Ni₅₂Mn₂₃Ga₂₅ can be controlled by a magnetic field, (ii) strain fields arising from a biased self-accommodation process that satisfies the invariant plane condition during the martensitic transition of Ni₅₂Mn₂₃Ga₂₅ under an applied magnetic field, (iii) the defect microstructure and the disorder during a multi-cycle experiment with Ni₆₃Al₃₇, (iv) the local diffusion and domain relaxation giving rise to martensite and twin stabilization in Au_{50.5}Cd_{49.5} and Ni₅₂Mn₂₃Ga₂₅, and (v) the pinning at grain boundaries in the polycrystalline Fe_{68.8}Pd_{31.2} sample.

Figure 8.29 gives an overview of all amplitude and energy exponents determined in this work. Exponents showing an explicit time or field-dependence are included by colored bars sufficiently large to include all values found experimentally. In spite of the seemingly unsystematically varying exponent distributions, some conclusions can be drawn: (i) The signal strength of the forward and the reverse transitions of single crystalline shape memory alloys only show small differences. By contrast, rather large differences occur between the transition directions of the analyzed polycrystalline Fe_{68.8}Pd_{31.2} sample. (ii) The exponents of different material classes have different values ranging from 2 to 4 in case of the amplitude and from 1.5 to 2.75 in case of the energy, satisfying the scaling relation $\epsilon = (\alpha+1)/2$, given in equation 8.2. (iii) The amplitude exponents during cooling can be grouped into universality classes according to the symmetry of the low temperature phase. Table 8.9 gives an overview of the material systems, their low temperature symmetries, the exponents (in the adiabatic limit at 10 K/min and

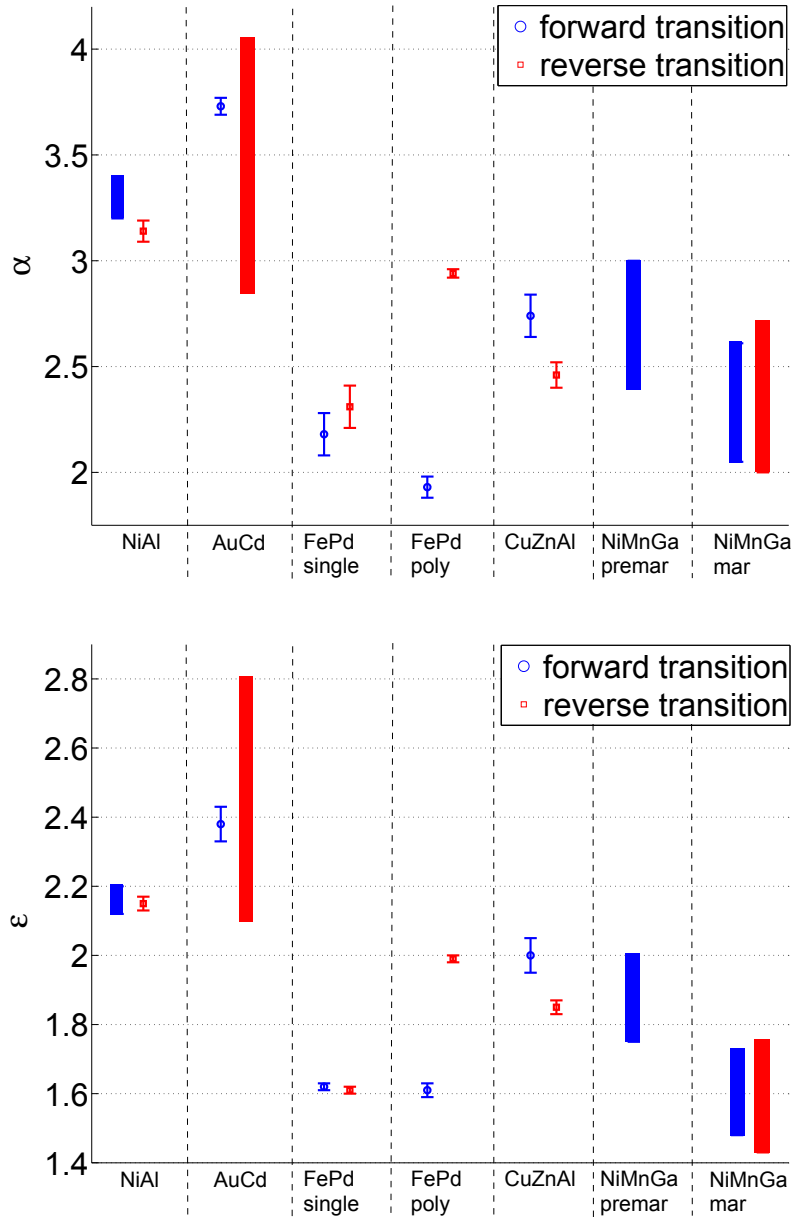


Figure 8.29: Overview of all experimentally determined amplitude (top) and energy exponents (bottom) of all analyzed samples. Exponents with an explicit time- ($\text{Ni}_{63}\text{Al}_{37}$ and $\text{Au}_{50.5}\text{Cd}_{49.5}$) or field-dependence ($\text{Ni}_{52}\text{Mn}_{23}\text{Ga}_{25}$) are included in a sufficiently large bar.

without applied field), and the proposed universality class. The polycrystalline $\text{Fe}_{68.8}\text{Pd}_{31.2}$ sample, the $\text{Au}_{50.5}\text{Cd}_{49.5}$ sample, and the premartensitic transition of the $\text{Ni}_{52}\text{Mn}_{23}\text{Ga}_{25}$ sample are not listed because they each represent a single group and cannot be compared with a reference. As shown in table 8.9, $\text{Ni}_{63}\text{Al}_{37}$ and $\text{Cu}_{68}\text{Zn}_{16}\text{Al}_{16}$, both have a monoclinic low temperature symmetry and fit into the universality class proposed by Carillo *et al.* Moreover, both samples with the tetragonal low temperature symmetry are covered by an exponent value of 2.4 ± 0.2 . Interestingly, this is exactly the value of the universality class proposed for systems transforming into a hexagonal 2H structure [22]. In the case the results of this work can be confirmed by experiments with other samples of the same symmetry, the universality classes of hexagonal and tetragonal structures could probably be merged. Presuming the adequacy of the proposed classification, it is no surprise that the exponents of $\text{Ni}_{52}\text{Mn}_{23}\text{Ga}_{25}$ range at the upper border of its universality class. The structure is described as pseudo-tetragonal with a slight deviation of one angle from 90° ($a \approx b \neq c$, $\alpha = \gamma = 90^\circ$ and $\beta = 91^\circ$, see table 3.2), i. e. the symmetry of $\text{Ni}_{52}\text{Mn}_{23}\text{Ga}_{25}$ is close to both structures.

In addition to the proposed universality classes, matching can be found with simulated amplitude exponents proposed in literature [2]. The simulated value of $\alpha = 2.6$ is very similar to the exponents of $\text{Ni}_{52}\text{Mn}_{23}\text{Ga}_{25}$ and $\text{Cu}_{68}\text{Zn}_{16}\text{Al}_{16}$ determined in this work. Furthermore, the simulated exponent $\delta = 3.2$, describing the hit duration distribution [2], is similar to the corresponding value found in $\text{Ni}_{52}\text{Mn}_{23}\text{Ga}_{25}$ and to the experimental result $\delta = 3.5 \pm 0.8$ obtained for CuZnAl [192].

From all observed effects martensite stabilization seems to have the largest influence on the signal strength. It is followed by the effect of the magnetic field on the premartensitic and martensitic transition strength. The isothermal aspect of the forward transition in $\text{Ni}_{63}\text{Al}_{37}$ has the smallest noticeable influence on the signal strength. This hierarchy can be supported by the fact that the isothermal character of the reverse transition of $\text{Fe}_{68.8}\text{Pd}_{31.2}^{\text{poly}}$ has no measurable influence on the signal strength.

It is worth mentioning that $\text{Ni}_{63}\text{Al}_{37}$ and $\text{Au}_{50.5}\text{Cd}_{49.5}$ reveal opposing rate-dependent behavior with respect to their AE signal strength. $\text{Ni}_{63}\text{Al}_{37}$ shows weaker signals at smaller cooling driving rates than $\text{Au}_{50.5}\text{Cd}_{49.5}$. This has been explained by an interplay of isothermal transition dynamics, the varying time scales of the temperature cycles, and the intrinsic disorder. The increasing transition signal strength of $\text{Au}_{50.5}\text{Cd}_{49.5}$ with longer cycle periods has been explained by an approach taking martensite stabilization as a relevant factor into account. Because Ni-Al and Cu-Zn-Al are known to have long aging times, they fit as counterexamples into the framework of martensite stabilization. Furthermore, both material systems $\text{Ni}_{63}\text{Al}_{37}$ and $\text{Au}_{50.5}\text{Cd}_{49.5}$ show unconventional behavior which is not part of the classical martensite theory. The martensitic transition

dynamics, formally known to be athermal and diffusionless, can either be dramatically influenced by local diffusion as in the case of aging in Au-Cd, or show a thermal activation providing a better accommodation as in Ni-Al.

It is noteworthy that an applied magnetic field has opposing effects on the acoustic fingerprints of the premartensitic and the martensitic transition in $\text{Ni}_{52}\text{Mn}_{23}\text{Ga}_{25}$. The acoustic activity of the premartensitic transition is suppressed by relatively low fields, whereas the acoustic activity of the martensitic transition is strongly increased by an applied field. In case of the premartensitic transition, fields have an ordering character which leads to a reduction of pinning-depinning processes. By contrast, the martensitic transition occurs with more AE under applied fields due to field-induced rearrangement of variants after the spontaneous symmetry-breaking. A decrease of the signal strength can be detected during the premartensitic transition under increasing fields, which is interpreted to be an indicator for an overall weakening of the first order transition character. Due to the associated symmetry-breaking the situation is different in the martensitic transition. The applied magnetic field lifts the degeneracy of the system during the accommodation process and modifies the energy barriers arising from the invariant plane condition, which leads to stronger transition signals.

9 Conclusions and summary

In this work the avalanche dynamics of five shape memory samples has been analyzed by acoustic emission spectroscopy. The acoustic emission spectroscopy is particularly suitable for this analysis as it couples with high sensitivity to small structural changes caused by nucleation processes, interface movements, or variant rearrangements [91]. Owing to its high time resolution it provides a statistical approach to describe the jerky and intermittent character of the avalanche dynamics [20].

Rate-dependent cooling and heating runs have been conducted in order to study time-dependent aspects of the transition dynamics of the single crystals $\text{Ni}_{63}\text{Al}_{37}$, $\text{Au}_{50.5}\text{Cd}_{49.5}$, and $\text{Fe}_{68.8}\text{Pd}_{31.2}^{\text{single}}$, and the polycrystalline sample $\text{Fe}_{68.8}\text{Pd}_{31.2}^{\text{poly}}$. Moreover, a ferromagnetic $\text{Ni}_{52}\text{Mn}_{23}\text{Ga}_{25}$ single crystal has been studied by temperature cycles under applied magnetic field and additionally by magnetic-field cycles at a constant temperature in the martensitic phase. The access to the amplitude, energy, and duration power law spectra of the acoustic emission data allows a further investigation of energy barriers separating the metastable states, which give rise to avalanche transition dynamics.

By performing rate-dependent experiments under both temperature and magnetic field cycles the importance of thermal fluctuations and the impact of martensite respectively twin stabilization processes have been examined. It has been found out that the named processes co-occurring with the associated structural changes lead to modifications in the acoustic emission fingerprint: In the case of the $\text{Ni}_{52}\text{Mn}_{23}\text{Ga}_{25}$ sample, the magnetic-field-induced variant rearrangement at slow field cycles leads to stronger signals than the rearrangement at quick cycles. This rate-dependent behavior can be explained by twin stabilization processes, which are accompanied by a reduction of the twin boundary mobility. For $\text{Ni}_{63}\text{Al}_{37}$ the combination of relevant thermal fluctuations, different involved time scales, and a high degree of intrinsic disorder leads to a lower acoustic activity and weaker signals under decreasing cooling rates. By contrast, for $\text{Au}_{50.5}\text{Cd}_{49.5}$ the low rates allow aging to become significant leading to higher energy barriers and, as a consequence, to stronger acoustic emission signals. The excellent agreement of this result with a martensite stabilization model introduced by Otsuka *et al.* [127], suggests that aging should be included into the framework of driving rate effects in avalanche-mediated phase transitions [135].

In contrast to what has been stated earlier [20, 172], the author concludes (on the base of $\text{Au}_{50.5}\text{Cd}_{49.5}$, $\text{Ni}_{63}\text{Al}_{37}$, and $\text{Fe}_{68.8}\text{Pd}_{31.2}^{\text{poly}}$ data) that only the detection of rate-dependent acoustic activity curves or the detection of incubation times are necessary and sufficient conditions for time-dependent dynamics. Rate-dependent exponents are a sufficient but not necessary condition for time-dependent behavior, as shown by the example of $\text{Fe}_{68.8}\text{Pd}_{31.2}^{\text{poly}}$, where rate-dependent curves can be observed at constant exponents.

All samples analyzed in this work show power law behavior in the acoustic emission features amplitude, energy, and duration. This indicates scale-free behavior. The determination of power law exponents has been proven to be a reliable tool for the characterization of the transition dynamics and associated energy barriers, because they are robust and do not depend on experimental details, as far as they are determined in the adiabatic limit [135]. The occurrence of power laws covering several decades regardless of the chosen experimental window in frequency,¹ signal strength, rate, or magnetic field suggest a universal nature of the scale-free behavior for structural phase transitions in shape memory alloys. Moreover, the existence of scale-free behavior in first-order structural transitions, which does not depend on certain experimental settings or a specific tuning of experimental parameters, reveals a close relation to the concept of self organized criticality [9, 10].

In this work it has been shown for the first time by the evaluation of power law exponents how an applied magnetic field alters energy barriers during structural transitions of magnetic shape memory alloys. Depending on the product phase symmetry, phase transitions under applied magnetic fields can lead to opposing results: The symmetry-breaking process of a martensitic transition under an applied magnetic field leads to an increase of the activity due to a twofold process, including phase and twin boundary motion. Furthermore, the satisfaction of the invariant habit plane condition under an applied field which breaks the degeneracy leads to larger constraints reflected in stronger signals. By contrast, less acoustic activity and weaker signals appear in association with the symmetry-conserving premartensitic transition under an applied field. The application of a field leads to an alignment of the magnetic moments, lowering the disorder. Lower energy barriers are supposed to be a consequence of the lower disorder, which lead to less acoustic activity and weaker signals. At (moderate) fields equal to or higher than 2.5 kOe the acoustic activity is completely suppressed. These observations suggest an overall weakening of the first order character of the premartensitic transition.

¹The frequency window during the measurements arises from the acoustic emission transducers, which have a relatively small resonance frequency interval on the order of 30 kHz (see section 8.4.2).

The amplitude and energy exponents for the material systems NiAl, FePd, and Ni₂MnGa under applied magnetic field (premartensitic and martensitic transition) have been, to the best knowledge of the author, for the first time experimentally determined in this work. The following amplitude exponents of NiAl and CuZnAl (3.1 ± 0.2) and of Ni₂MnGa and FePd (2.4 ± 0.2), determined in this work and reported in literature (see section 8.5 and [22, 94, 139]) can be grouped by similar values. This reinforces the universality hypothesis [52] and the assumption that the symmetry of the product phase determines the universality class of the exponents [22]. However, the pronounced rate-dependence of the AuCd exponents and the large difference between the exponents of the single and polycrystalline Fe_{68.8}Pd_{31.2} samples (see section 7.2.3 and 8.3) suggests that further criteria, such as the degree of disorder or rate-dependent aging effects, should be taken into consideration as well.

10 Outlook

The presented results of this work recommend a continuation of research activities in several directions. New approaches can either arise from the combination of the established AE technique with complementary experimental methods or from the analysis of additional material systems.

Small modifications of the AE acquisition setup would allow the use of two AE transducers. The resulting linear design would enable a localization of the source of the AE events (see e. g. [21, 97]). Assuming a speed of sound in the sample on the order of 1000 m/s, the high time resolution¹ of $5 \cdot 10^{-8}$ s enables a localization within a small sample section of approximately 10 μm thickness. This could reveal valuable information on nucleation and growth processes. Spatial information is especially useful to examine whether AE signals have a high degree of correlation if they originate from a narrow sample region as opposed to events resulting from different sample regions (see results of the detrended fluctuation analysis of $\text{Au}_{50.5}\text{Cd}_{49.5}$ in section 8.2).

The application of stress to the sample provides the possibility to study the transition under biased conditions and to analyze its effect on the transition temperature and the signal strength. In addition to this, the use of strain gauges enables the detection of length and volume changes occurring during the martensitic transition. This is particularly valuable in combination with magnetic-field-induced strain measurements, as it can prove or disprove some of the assumptions presented in section 8.4.3.

The combination of AE and optical measurements is an interesting approach as it compares surface and volume aspects of the transition. This is especially interesting for the identification of the potent defect relevant for the formation of a supercritical nucleus that starts the heterogeneous nucleation process. In-situ imaging of the sample surface combined with the AE technique² would provide new means to correlate the surface pattern resulting from the self-accommodation process with associated acoustic events during multi-cycle measurements. A detailed analysis could help to further verify the hypothesis that changes in the self-accommodation process can be observed in the total acoustic activity and the associated signal strength, as described for $\text{Ni}_{63}\text{Al}_{37}$ in section 8.1.

¹The sampling frequency of the AE acquisition system operating with two AE transducers is 20 MHz.

²The combination of optical surface imaging and the AE technique has already been used to analyze the front propagation process in a CuZnAl single crystal [21].

An in-situ measurement of AE spectroscopy during an XPCS experiment is a promising approach due to the high sensitivity of both techniques towards avalanche dynamics. It is in particular compelling since both techniques work on complementary time and length scales: The AE technique monitors structural changes occurring in the whole sample with a very high time resolution (see above). By contrast, state-of-the-art measurements with coherent X-rays directly monitor the sample dynamics on long time scales in the range of 1 s. Due to a small spot size and a low penetration depth the X-ray technique only integrates over a small sample volume of approximately $1000 \mu\text{m}^3$.

Besides the combination of different in-situ measurement techniques it would be interesting to evaluate further the adequacy of the universality classes proposed in section 8.5. This would require experiments with additional shape memory alloys that reveal different low temperature symmetries. The influence of the sample dimension on the power law exponents as well as on the universality class appear to be an interesting field of study with shape memory samples of reduced dimensions such as thin-layer samples or nano-wires. Furthermore, the study of new material classes that transform under AE such as ferroelectrics can broaden the understanding of avalanche interface dynamics in multi-domain systems. The measurement and evaluation procedures, proposed in this work, will help to achieve comparable results in this context. Finally, a further analysis of the proposed scaling relation $E \propto A^2$ would be interesting. This study should be undertaken by comparing curve shapes of different AE signals by means of the transient AE signal, instead of the extracted AE features, which have been mainly analyzed in this work.

A Appendix

A.1 Results of temperature calibration

In this section are given all parameters for the sample temperature calibration (see section 5.2). With the temperature calibration it is possible to estimate the (unknown) sample temperature T_B from the measured sample holder temperature T_A . The two temperatures show the linear dependence:

$$T_B = A \cdot T_A + B \quad (\text{A.1})$$

and should be measured in Kelvin.

NiAl

rate (K/min)	10	5	4	3	2	1	0.5	0.1
cooling, B	11.7445	9.8603	9.4585	9.0890	8.7073	8.0022	7.3357	6.9472
cooling, A	0.9629	0.9680	0.9690	0.9701	0.9712	0.9734	0.9756	0.9766
heating, B	11.0458	9.5209	9.1372	8.7975	8.4186	7.7794	7.3231	6.9947
heating, A	0.9597	0.9661	0.9676	0.9690	0.9706	0.9732	0.9750	0.9764

AuCd

rate (K/min)	10	5	4	3	2	1	0.5	0.1
cooling, B	24.2087	14.4267	12.8603	11.1108	9.1559	7.8484	7.0125	5.8094
cooling, A	0.9220	0.9533	0.9582	0.9638	0.9700	0.9740	0.9765	0.9805
heating, B	24.4182	14.6264	12.6262	10.8493	9.1446	7.5722	6.7285	5.4626
heating, A	0.9178	0.9503	0.9570	0.9630	0.9688	0.9742	0.9772	0.9815

FePd

rate (K/min)	10	5	4	3	2	1	0.5	0.1
cooling, B	3.1012	3.4527	2.8389	3.3668	3.2425	2.9363	2.6700	3.5355
cooling, A	0.9898	0.9884	0.9907	0.9889	0.9892	0.9902	0.9912	0.9884
heating, B	2.9614	3.3739	2.6988	3.2766	3.1460	2.9358	2.6891	3.4810
heating, A	0.9901	0.9877	0.9909	0.9878	0.9884	0.9895	0.9906	0.9863

CuZnAl								
rate (K/min)	10	5	4	3	2	1	0.5	0.1
cooling, B	1.9411	1.7242	2.1187	2.0990	1.9209	2.1686	1.7243	1.5394
cooling, A	0.9937	0.9943	0.9931	0.9932	0.9937	0.9932	0.9943	0.9949
heating, B	1.9442	1.7096	2.0881	2.0581	1.9107	2.1058	1.7254	1.5992
heating, A	0.9931	0.9941	0.9922	0.9922	0.9929	0.9916	0.9937	0.9946

List of Figures

2.1.	Phase diagram of water with the triple point (A), the critical point (C), the sublimation line (D), the vaporization line between (A) and (C), and the melting line (B).	5
2.2.	Representation of the free energies of two phases in the vicinity of the phase transition. At the thermodynamic equilibrium temperature T_0 both phases have the same free energy. At a lower temperature, the low temperature phase is energetically favored whereas at a higher temperature the high temperature phase is favored. The temperature is only one example of a possible control parameter.	7
2.3.	Representation of the free energy G calculated within a Landau theory as a function of the order parameter η at selected temperatures. (Left for a continuous, right for a discontinuous phase transition.) Note the different local and global energy minima for both transitions at the relevant temperatures, which reveal the continuous respectively the discontinuous character of the transitions (adapted from [78] and [172]).	8
2.4.	Nucleation energy barrier as a result of competing interfacial and volume energies (left). A generic radius dependence is supposed, $G \propto r^2$ for the interfacial term (blue line) and $G \propto r^3$ for the volume term (red line). The resulting nucleation barrier (black line) has its maximum at the critical radius r_c , which has to be overcome for a successful nucleation. On the right hand side is shown the non-equilibrium temperature-density phase diagram of a fluid. The area of coexistence is divided into an unstable and a metastable region between the phase boundary curve and the (dotted) spinodal curve. By quenching outside the critical point the system crosses a metastable state of undercooling and reaches the (unstable) area of spinodal decomposition, which is the separation of two macroscopic phases inside the coexisting region.	12
2.5.	Comparison of the discontinuous (left) and the continuous (right) phase transition. The figure shows the behavior of the free energy and its first and second derivative as a function of the temperature.	13

2.6.	Temperature-density phase diagram of several fluids including a discontinuous (blue isotherms with short bars) and a continuous phase transition (red isotherm with long bars) at and below the critical point. After normalizing the data of all substances to their critical values all curves collapse on an universal curve. The fitted line represents a power law $(\rho - \rho_c) \propto (T - T_c)^\beta$ with $T \leq T_c$ and a critical exponent $\beta = 1/3$ (adapted from [53]).	14
2.7.	A power law $f(x) = x^\alpha$ is form-invariant under a linear rescaling of x . Graphically, this can be understood by comparing the two scaled functions $f(x) = x^\alpha$ and $f(n \cdot x) = (n \cdot x)^\alpha$ normalized by their maxima $\max(f(x))$ and $\max(f(n \cdot x))$, respectively. By contrast, exponential functions cannot be normalized in a way that they scale after a rescaling of x	15
3.1.	All forms of ferroic order and their characterization under parity operations of space and time (adapted from [185]).	22
3.2.	Classification of solid-solid phase transitions by their symmetry characteristics [80, 178] (and adapted from [75]).	23
3.3.	Classification of heterogeneous solid-solid phase transitions with regard to their predominant growth processes. The characteristics marked in red are typical for martensitic transitions (adapted from [27] and [75]). Some numerical values of characteristic properties of typical classical martensitic transitions and of shape memory alloys can be found in table 3.1.	24
3.4.	Classification of diffusionless phase transitions in solids by energetic considerations. The path marked in red is characteristic for shape memory alloys (adapted from [30] and [75]).	25
3.5.	Formation of martensitic variants under cooling in two dimensions (left) and three dimensions (right). The transition leaves the orientation relationship and nearest neighbors unchanged. Nevertheless, the distortion results in a reduction of the symmetry of the unit cell. On the left hand side is shown the distortion of the square two-dimensional elementary cell into the two possible variants. Note that the two occurring variants cannot be converted into each other by a rotation. On the right hand side can be seen a three-dimensional cubic unit cell in the parent phase and one possible variant in the product phase. In higher dimensions more variants are available to be formed.	26

3.6. Hysteretic dependence of the amount of transformed martensite as a function of the temperature. The blue line represents the cooling and the red line the heating process. The hysteresis widths vary between 100 K in case of classical ferrous alloys and 10 K in case of shape memory alloys (see as well table 3.1).	27
3.7. The minimization process of strain energies during the martensitic transformation leads to a spontaneous self-arrangement of strain domains resulting in a highly oriented surface relief.	28
3.8. Schematic representation of self-accommodated variants during the martensitic transition separated by the habit plane from the high temperature phase. The variant pairs V_1 and V_2 , and V_3 and V_4 each share a twin boundary [54].	28
3.9. Microscopic delineation of a half-transformed crystal with the martensitic variant structure on the right (twin boundaries) and the parent phase on the left. The atoms situated along the interfacial boundary store elastic energy due to the crystal lattice misfit, which is indicated by small springs.	29
3.10. The martensitic transition implies a change of shape and sound (see definition of Clapp [29]), which allows for both optical and acoustical experimental methods. Several experimental methods (x-ray techniques, neutron scattering, AE-techniques and optical reflection methods) are possible, from which two suitable techniques are schematically depicted. The optical method (top) works with the reflection of a laser beam which is scattered in a characteristic pattern by the martensitic surface relief (e. g. [77, 90, 111]). The acoustic emission (AE) technique (bottom) used in this work is a volume-sensitive method measuring the acoustic emission generated during the martensitic transition (for details see section 4.1 and 6).	30
3.11. Depiction of the concise definition of a martensitic transition given by Christian, Olsen, and Cohen [28], which serves as a summary of the main characteristics of martensitic transitions described in this section.	31
3.12. Depiction of nucleation thermodynamics for both isothermal and athermal transitions [68]. The nucleation barrier and driving force ΔG are displayed at the thermodynamical equilibrium temperature T_0 , at the martensitic transition temperature M_s , and at a temperature T in between [68].	32

3.13. Thermodynamics of isothermal transitions. On the left is shown a schematic depiction of two opposing effects leading to a maximum of the transition rate. High temperatures enable thermal activation but reduce the driving force of the transition. Low temperatures lead to a high driving force, but result in a low thermal activation. On the right hand side is depicted a TTT-diagram of a generic isothermal transition with the characteristic nose-temperature T_N where the waiting time shows a minimum until a certain amount has transformed. 33

3.14. TTT-diagrams of an athermal (a) and an isothermal transition (b) in the Kakeshita model. The arrows indicate the holding temperatures [128]. 34

3.15. Comparison of the classical picture of athermal transition kinetics with the models proposed by Kakeshita *et al.* [67], Otsuka *et al.* [128], and Planes *et al.* [143]. The authors follow different approaches which are contradictory with respect to the role of diffusion, the statistical nature of M_s , and the coexistence of isothermal and athermal transitions [90, 112]. 35

3.16. Schema of the development of avalanche dynamics in athermal martensites. A continuous driving force is applied to a system, for example by changing the temperature at a fixed rate (a). The way through the complex energy landscape consisting of several metastable states (here represented by the football *Teamgeist*) (b) leads in spite of the continuous excitation to a discontinuous response (c). The sudden changes of the response function (d) indicate the avalanche behavior of the transition dynamics. 36

3.17. Simulation of a fluctuationless first-order phase transition of Cu-Al-Mn as a function of disorder. Hysteresis cycles at different degrees of disorder on the left. Little disorder leads to a few (large) avalanches and a sharp hysteresis (bottom), whereas large disorder results in many (tiny) avalanches with a smooth hysteresis (top). The corresponding avalanche distributions on the right are shown as a function of disorder, too. The dotted curves are fits of equations 3.2. The first four histograms show subcritical behavior ($\lambda > 0$). The fifth histogram almost displays critical behavior without exponential correction ($\lambda \approx 0$) and the last two histograms show supercritical behavior ($\lambda < 0$) (adapted from [190]). 38

3.18. Incomplete phonon softening of the $[\zeta\zeta 0]$ TA_2 mode in $Ni_{62.5}Al_{37.5}$, analyzed by neutron scattering. (a) Dispersion curves of the TA_2 mode at different temperatures with a minimum at $\zeta = 0.16$. (b) Temperature-dependence of elastic neutron scattering in the same direction leading to the central peak. (c) Temperature-dependence of the squared energy of the same mode at its minimum (adapted from [166]).	40
3.19. Incomplete phonon softening of the $[\zeta\zeta 0]$ TA_2 mode in Ni_2MnGa , analyzed by neutron scattering. (a) Dispersion curves at different temperatures with a minimum at $\zeta = 0.33$. (b) Temperature-dependence of the squared energy of the same mode at its minimum. T_p indicates the premartensitic transition, T_m the martensitic transition and T_C the Curie temperature [209].	42
3.20. Pretransitional tweed pattern experimentally observed (left) and simulated (right). Micrograph of the mesoscopic tweed structure of a Ni-Al sample observed via transmission electron microscopy [72] (left). Visualization of calculations based on a two dimensional model for tweed pattern [71] (right) (for more details about the simulation process and for some visualizations of the simulation results see [162]).	43
3.21. Magnetic-field-dependent shift of the martensitic equilibrium temperature T_0 for a Ni_2MnGa alloy. The solid curve represents the calculated result using the integrated Clausius-Clapeyron equation 3.4 (adapted from [74]).	44
3.22. Mechanism of the magnetic-field-induced twin boundary motion (left) and phase boundary motion (right) in case of the weak anisotropy limit with a relatively large Zeeman energy [118]. . . .	45
3.23. Mechanism of the magnetic-field-induced twin boundary motion (left) and phase boundary motion (right) in case of the strong anisotropy limit with a relatively low Zeeman energy [118].	46
3.24. Depiction of the optimal field orientation for achieving large strains regarding the twin boundary Θ as a function of the angle ϕ , describing the orientation relation between both twin variants [118].	47
3.25. Summary of the stress-strain behavior of a generic shape memory alloy at different temperatures. The first coordinate system in the front shows the usual stress-strain behavior of solids with the linear elastic strain and a plastic deformation at high stresses. The second coordinate system shows superelasticity at a constant temperature. In the back of the coordinate system the shape memory effect is shown (adapted from [11]).	48

3.26. Two applications of the shape memory effect: A stent used in medical engineering (left) and an adaptive winglet as part of an aircraft (right).	49
3.27. Schematic representation of the microscopic mechanism responsible for the shape memory effect. One cycle consists of three steps: 1) cooling into the martensitic phase, 2) deformation by an external force, and 3) heating into the high temperature phase.	50
3.28. Illustration of the shape memory effect. The temperatures of the paper clip example at the bottom have been chosen according to the transition temperatures of the $\text{Ni}_{63}\text{Al}_{37}$ sample analyzed in this work ($M_s = 298 \text{ K}$, $A_s = 264 \text{ K}$; see table 7.1 in section 3.5.1) (adapted from [129] and [56]).	51
3.29. Typical stress-strain diagram of a NiTi shape memory alloy exhibiting superelasticity [105]).	52
3.30. Magnetic-field-induced growth of twin-variants with a favorable orientation consuming the unfavorably oriented variants with respect to the externally applied field. At zero field (left) the martensitic structure consists of self-accommodated variants. At small fields H_1 (middle), when the pressure caused by the differences in anisotropy energy exceeds the effective elastic modulus, some variants rotate and align with the field. Fields H_2 larger than the critical field H_c give rise to a single-variant state (right). An important factor in this process is the mobility of the martensitic domain walls [184].	53
3.31. Magnetic-field-induced strains in a $\text{Ni}_{0.498}\text{Mn}_{0.285}\text{Ga}_{0.217}$ single crystal at selected stresses externally applied opposing the strain (with 795.77 kA/m being equivalent to 10 kOe being equivalent to 1 T) [113].	55
3.32. Acoustic activity of a stress-driven martensitic transition. The red dashed line shows the acoustic activity \dot{N} and the black continuous line represents the time derivative of the strain $\dot{\epsilon}$, both as a function of time. The correlation indicates a proportionality relation between the transformed fraction of martensite and the corresponding acoustic activity \dot{N} . The curves in (a) correspond to a constant stress and the curves in (b) to increasing stress at a fixed rate ($\dot{\sigma} = 0.28 \text{ Mpa/s}$). The inset shows the correlation function between the acoustic and the strain data [21].	58
3.33. Illustration of possible components of a strain tensor $\sigma_{ij}(t, \vec{x})$ in Cartesian coordinates [155].	59

3.34. Equilibrium phase diagram of Ni-Al [145] which has been extended to the martensitic transitions. Martensitic transitions are observed only in a narrow composition range of $0.60 \leq x \leq 0.68$ $\text{Ni}_x\text{Al}_{1-x}$. The represented martensitic transition temperatures have been extracted from [154]. The combined phase diagram can be found in [141].	64
3.35. Equilibrium phase diagram of Au-Cd with indicated martensitic phase [145]. Close to its stoichiometric composition Au-Cd shows a martensitic transition and the shape memory effect.	66
3.36. Equilibrium phase diagram of Fe-Pd (left). Martensitic phase diagram with a composition of approximately 30 % Palladium (right). The black arrow indicates a possible path through the martensitic transition. The shape memory effect occurs in the ferromagnetic phase which enables a magnetoelastic coupling (adapted from [146]).	67
3.37. Lattice parameters a and c of the cubic high temperature phase and the tetragonal low temperature phase of a $\text{Fe}_{0.312}\text{Pd}_{0.688}$ polycrystal on cooling (left) (adapted from [169]). Lattice parameter a and c of a $\text{Fe}_{0.312}\text{Pd}_{0.688}$ single crystal as function of temperature under cooling (right) (adapted from [64]). Both samples have the same nominal composition as the samples analyzed in this work.	68
3.38. Unit cell of the austenitic phase of Ni_2MnGa in the $L2_1$ structure. Ni atoms are represented in blue, Mn and Ga in red and green, respectively.	69
3.39. Functional phase diagram of the ternary alloy Ni-Mn-Ga. In the ferromagnetic region (yellow), the red area has the highest magnetization. The dotted line surrounds the region of reversible martensites. In the overlapping areas a magnetostructural interplay is possible (adapted from [174]).	70
3.40. Transition temperatures of $\text{Ni}_{2+x}\text{Mn}_{1-x}\text{Ga}$ as a function of the composition parameter x . The number 1 labels the ferromagnetic-paramagnetic coexistence line. Line 2 represents the temperature of the premartensitic transition. Line 3 represents the martensitic transition. Note that there is a composition where the premartensitic transition temperature meets the martensitic transition temperature and the martensitic transition temperature is equal to the Curie temperature (adapted from [174]).	71
3.41. The magnetic and martensitic transition temperatures (a) and the tetragonal distortion of the martensitic unit cell via the c/a -ratio (b) as a function of the electron concentration. The relation between the stoichiometry and the electron concentration can be found in table 3.3 (adapted from [186] and [174]).	72

4.1. Flow process chart of the acoustic emission measurement chain (adapted from [50]).	76
4.2. Photograph of the acoustic emission transducers used in this work. From left to right: R15-LT, NANO30, PICO, and as a reference a 1-cent coin (adapted from [172]).	76
4.3. A wave packet recorded during a martensitic transition. Two extracted acoustic emission features, amplitude, and duration of a hit are illustrated (adapted from [172]).	79
4.4. Interior view of the vacuum chamber. The compound of the heat reservoir, the thermopile, and the sample holder with an embedded temperature sensor are mounted on an isolated column (adapted from [172]).	83
4.5. Top view of the vacuum chamber and its lead-throughs. Starting at the bottom, the following lead-throughs can be seen in a clockwise order: power supply for the thermopile, tubes for the cooling liquid, measuring leads for the AE signals, vacuum tube, and measuring leads for the temperature sensor [172]).	83
4.6. Schematic representation of the acoustic emission setup consisting of a temperature-controlled sample holder and an electromagnet.	85
4.7. The figure shows a photograph of the disassembled custom-made differential scanning calorimeter. On the left thermopile the $\text{Ni}_{52}\text{Mn}_{23}\text{Ga}_{25}$ sample (analyzed in this work) is placed, and on the other thermopile is situated a copper reference sample. In the background can be seen the copper housing of the apparatus on the right and the disk for sample fixing on the left.	86
5.1. Photograph of an aluminium test block prepared for the transducer performance test (left). The concentrically arranged points mark the breaking points. Due to different transducer diameters, circles of three radii are drawn. On the right hand side is shown a customized mechanical pencil from the manufacturer <i>Physical Acoustics</i> , which enables a constant breaking angle of 45° (right) [172].	88
5.2. Three-dimensional <i>computer-aided design</i> (CAD) model of the $\text{Au}_{50.5}\text{Cd}_{49.5}$ dummy sample, consisting of two copper parts and a temperature sensor. The upper and the lower part, which perfectly match, have a gap for the Pt-100 sensor. With the temperature data from the embedded sensor the real sample temperature can be calculated (c.f. equation 5.2).	90

5.3. The plot shows temperature T_A , which is measured inside the sample holder, and temperature T_B , which is measured on top of the sample holder. Both temperatures are measured at equilibrium conditions with a homogenous temperature in order to estimate the constant offset between both sensors. 91

5.4. The temperature of the dummy sample T_B and the temperature of the sample holder T_A show a linear dependence. The represented data belong to the $\text{Ni}_{63}\text{Al}_{37}$ calibration, which spreads over a wide temperature range because of the relatively broad transition. For clarity reasons, only every sixth point is plotted (adapted from [172]). 92

5.5. Exemplary results of the temperature calibration with the AuCd dummy sample using the relation $T_B = A \cdot T_A + B$, where T_A is the temperature of the sample holder and T_B the temperature inside the dummy sample. Results are depicted as a function of the rate for both cooling and heating. 93

5.6. Three-dimensional model of the inner components of the vacuum chamber. 94

5.7. Exemplary part of the grid for the FEM simulation at the sample/sample holder interface. Note the different node densities with a maximum at the interface between the sample and the sample holder where the highest temperature gradients are expected. . . . 95

5.8. Results of an FEM temperature simulation of the sample environment. The figures show the temperature distribution at different sample holder temperatures T_A . At $T_A = 223\text{ K}$ a small temperature gradient between the sample holder and the reservoir can be seen (left). As the sample is the coolest point in the chamber, a positive heat flux into the sample occurs. At $T_A = 293\text{ K}$ the sample holder is the hottest point in the chamber, resulting in a large temperature difference to the thermal reservoir (right). A different microclimate develops, showing large gradients. The thermal bypass of the screws and the thermal mass of the sandwich brass plate can be identified by the deformed microclimate. 96

5.9. Temperature distribution calculated by an FEM simulation. The (almost) unicolored areas of the sample holder, the surrounding teflon disk, and the sample show that the temperature gradients appear at the interfaces. This behavior is reflected by the abrupt temperature changes between the components. 97

5.10. Thermal network representing the components of the AE setup, including thermal masses and resistivities of the components sample, sample holder, AE transducer, thermal reservoir, screws, brass-teflon disk, and the chamber. All components named with a leading C are thermal capacities. Their numerical values have the unit J/K . Thermal resistances are named with a leading R and are measured in K/W . The temperatures of the components are located at the intersection points, named with a leading T and are given in Kelvin. 98

5.11. Qualitative comparison between experimental and simulated data for $Au_{50.5}Cd_{49.5}$. The experimental data are measured with the dummy Au-Cd sample (see section 5.2) For clarity reasons, only every 5th point is plotted. Both curves show similar features. A quantitative comparison can be found in figure 5.13. 101

5.12. Simulated heat fluxes into the sample and the transducer and the temperature of the sample holder for $Au_{50.5}Cd_{49.5}$. The different thermal masses of the sample and the transducer result in largely varying time constants. To ensure the absence of transient effects the second cycle is depicted. For clarity reasons, only every 4th point is plotted. 101

5.13. Quantitative comparison between experimental data from the temperature calibration with the AuCd dummy sample and simulated data. All rates are represented using the linear relation $T_B = A \cdot T_A + B$. A qualitative comparison can be found in figure 5.11. Despite of the large error bars, the simulation results are robust, because the errors on A and B stabilize each other. A smaller factor A leads in agreement with the error bar to a small increment of B and vice versa. 103

7.1. Exemplary histograms of the amplitude (left) and energy (right) distribution with exponentially corrected power law fits (red line). The data originate from a martensitic transition in $Au_{50.5}Cd_{49.5}$ at a rate of 1 K/min. 111

7.2. Noise measurement with the vacuum setup using a steel dummy sample and the PICO AE transducer. The diagram shows the acoustic activity with a bin width of 200 mK. Several runs at selected rates are averaged for cooling (blue line) and heating (red line). The acoustic activity of the analyzed martensitic transitions is much higher than this noise level. Depending on the sample the signal to noise ratio lies between 100 and 2000. 112

- 7.3. Noise measurement with the magnetic field setup using a copper dummy sample and the R15-LT AE transducer. The diagram shows the acoustic activity histogram with a bin width of 100 mK in analogy to the real measurements with $\text{Ni}_{52}\text{Mn}_{23}\text{Ga}_{25}$. In the range of the martensitic transition below 210 K the noise can be neglected. At higher temperatures in the region of the premartensitic transition the noise level is comparable to the transition activity. 113
- 7.4. Noise measurement with the field setup using a copper dummy sample and the R15-LT AE transducer. The figure shows the color-coded acoustic activity in a log-log histogram of the amplitude-duration distribution. The comparison with figure 7.5 reveals that the noise displays a special pattern, which allows to distinguish between transition and noise signals. 114
- 7.5. On the left can be seen the color-coded acoustic activity in a log-log histogram showing the duration against the amplitude of useful AE events and noise, which can be separated by an amplitude-duration filter as indicated by the white dotted line (noise above and transition signal below). On the right hand side is depicted a histogram of the unfiltered amplitude data from the premartensitic forward transition of the Ni_2MnGa sample at selected applied magnetic fields. The distributions show marked deviations from power law behavior. 115
- 7.6. On the left hand side is shown the color-coded acoustic activity in a log-log histogram showing the filtered signal distribution of the duration against the amplitude (analog figures of the unfiltered data set can be seen in figure 7.5). The right hand side shows the corresponding histogram of the filtered amplitude distribution of the premartensitic forward transition of the Ni_2MnGa sample. In contrast to the unfiltered data the distributions now can be described by power laws over more than three orders of magnitude, providing evidence for a consistent filtering procedure. 115
- 7.7. Schematical depiction of the hit energy detection process where the vertical cutoff at the threshold leads to a smaller hit energy. The energy integral includes the green colored oscillations and excludes the red edge regions. In real waveforms, the fraction of rejected areas is usually very small (see figure 4.3). 116

7.8. Photograph showing the analyzed samples in their parent phase at room temperature and a 1-eurocent coin as a reference. From left to right: $\text{Au}_{50.5}\text{Cd}_{49.5}$, $\text{Ni}_{63}\text{Al}_{37}$, $\text{Cu}_{68}\text{Zn}_{16}\text{Al}_{16}$ (which will serve as a reference in section 8.5 and in the introduction of chapter 8), and $\text{Fe}_{68.8}\text{Pd}_{31.2}^{\text{single}}$ (both the single crystal and the polycrystal have identical shapes). In the upper right corner a photograph of the $\text{Ni}_{52}\text{Mn}_{23}\text{Ga}_{25}$ sample has been added according to scale.	117
7.9. Micrograph showing the $\text{Ni}_{63}\text{Al}_{37}$ sample surface in the martensitic phase. The surface relief, originating from the self-accommodation process, is highly oriented.	118
7.10. Micrographs showing a section of the $\text{Ni}_{63}\text{Al}_{37}$ sample surface in the high temperature phase (top) and in the low temperature phase (center and bottom). In the low temperature phase cracks can be identified. The dotted white line is a guide to the eye tracing a crack. In the micrograph at the bottom the same crack is highlighted by arrows [90].	119
7.11. Comparison between the mean acoustic activity and calorimetric data during the martensitic forward and reverse transition of the $\text{Ni}_{63}\text{Al}_{37}$ sample. For clarity reasons, the data of the reverse transition have been plotted with negative values. The temperature offset between the acoustic and calorimetric data can be explained by the absent temperature calibration of the calorimetric measurement.	120
7.12. Comparison of the mean energy distribution and the acoustic activity of the $\text{Ni}_{63}\text{Al}_{37}$ sample as a function of temperature, exemplarily shown at a rate of 1 K/min. With adequately chosen ordinates both curves show a high degree of scaling. The forward transition can be seen on the left and the reverse transition on the right.	120
7.13. Color-coded acoustic activity in an amplitude-duration histogram of all rate-dependent measurements of the $\text{Ni}_{63}\text{Al}_{37}$ sample. Amplitude and duration show a positive correlation centered at low amplitudes and small durations.	121
7.14. Mean acoustic activity of the forward (left) and reverse transitions (right) of the $\text{Ni}_{63}\text{Al}_{37}$ sample at three selected rates (0.1 K/min, 1 K/min, and 10 K/min).	121
7.15. Total acoustic activity of the forward (blue) and reverse transitions (red) of the $\text{Ni}_{63}\text{Al}_{37}$ sample during a multi-cycle measurement (152 cycles at a rate of 10 K/min). For clarity reasons, the acoustic activity of the forward transition has been divided by two.	122

- 7.16. Power laws, exponents, and exponential corrections for the forward and reverse transition of the $\text{Ni}_{63}\text{Al}_{37}$ sample at selected rates.
Top: Log-log histograms of the mean amplitude (left) and energy distribution (right).
Center: Amplitude and energy exponents α (left) and ϵ (right). The exponents have been determined by the maximum likelihood method using the equations $p(A) \propto A^{-\alpha} e^{-\lambda_A A}$ and $p(E) \propto E^{-\epsilon} e^{-\lambda_E E}$. The red dotted lines are guides to the eye indicating the trends or the mean values, respectively.
Bottom: λ -values of the exponential correction terms $e^{-\lambda_A A}$ (left) and $e^{-\lambda_E E}$ (right) of the amplitude and energy distributions. 124
- 7.17. Micrographs showing the sample surface in the high temperature phase (left) and the low temperature phase (right) of a Au-Cd sample with a stoichiometry of $\text{Au}_{52.5}\text{Cd}_{47.5}$, which is very similar to the analyzed sample. The polished sample surface of the high temperature phase solely shows some scratches whereas the low temperature surface is characterized by a highly oriented relief. Note the different length scales of the martensitic relief in the center and near the edges of the micrograph [111]. 125
- 7.18. Comparison between the mean acoustic activity and calorimetric data during the forward and reverse transition of the $\text{Au}_{50.5}\text{Cd}_{49.5}$ sample. For clarity reasons, the data of the reverse transition have been plotted with negative values. The temperature offset and the different peak widths between the acoustic and calorimetric data can be explained by the absent temperature calibration of the calorimetric measurement and a much larger thermal mass of the calorimetric setup. Note the different temperature scale compared to figure 7.11 for the $\text{Ni}_{63}\text{Al}_{37}$ sample. 126
- 7.19. Comparison of the mean energy distribution and the acoustic activity of the $\text{Au}_{50.5}\text{Cd}_{49.5}$ sample as a function of the temperature exemplarily shown at a rate of 1 K/min. With adequate ordinates both curves show an excellent scaling. The forward transition can be seen on the left and the reverse transition on the right. 127
- 7.20. Color-coded acoustic activity in an amplitude-duration histogram of all rate-dependent measurements of the $\text{Au}_{50.5}\text{Cd}_{49.5}$ sample. The characteristic color distribution indicates the positive correlation between the two features. 127
- 7.21. Mean acoustic activity of the forward transition of the $\text{Au}_{50.5}\text{Cd}_{49.5}$ sample at eight rates ranging from 0.1 K/min to 10 K/min. 128

- 7.22. Power laws, exponents, and exponential corrections for the forward and reverse transition of the $\text{Au}_{50.5}\text{Cd}_{49.5}$ sample at selected rates. **Top:** Log-log histograms of the mean amplitude (left) and energy distributions (right). **Center:** Rate-dependence of the amplitude and energy exponents α (left) and ϵ (right). The exponents have been determined by the maximum likelihood method using the equations $p(A) \propto A^{-\alpha} e^{-\lambda_A A}$ and $p(E) \propto E^{-\epsilon} e^{-\lambda_E E}$. The red dotted lines are guides to the eye indicating the trends or the mean values, respectively. **Bottom:** λ -values of the exponential correction terms $e^{-\lambda_A A}$ (left) and $e^{-\lambda_E E}$ (right) of the amplitude and energy distributions. . . . 129
- 7.23. Comparison between the mean acoustic activity and calorimetric data during the martensitic forward and reverse transition of the $\text{Fe}_{68.8}\text{Pd}_{31.2}^{\text{single}}$ sample. The arrows point at transition patterns which can be identified in both the AE and calorimetric data. For clarity reasons, the data of the reverse transition have been plotted with negative values. The temperature offset between the acoustic and calorimetric data can be explained by the absent temperature calibration of the calorimetric measurement. 130
- 7.24. Comparison between the mean acoustic activity and calorimetric data during the martensitic forward and reverse transition of the $\text{Fe}_{68.8}\text{Pd}_{31.2}^{\text{poly}}$ sample. For clarity reasons, the data of the reverse transition have been plotted with negative values. The temperature offset between the acoustic and calorimetric data can be explained by the absent temperature calibration of the calorimetric measurement. 131
- 7.25. Details of the mean acoustic activity of the $\text{Fe}_{68.8}\text{Pd}_{31.2}^{\text{single}}$ (top) and the $\text{Fe}_{68.8}\text{Pd}_{31.2}^{\text{poly}}$ samples (bottom) at three selected rates (0.1 K/min, 1 K/min, and 10 K/min). The forward transitions are plotted on the left and the reverse transitions on the right. 132
- 7.26. Mean acoustic activity of the forward (left) and reverse transitions (right) of the $\text{Fe}_{68.8}\text{Pd}_{31.2}^{\text{single}}$ sample at three selected rates (0.1 K/min, 1 K/min, and 10 K/min). 133
- 7.27. Mean acoustic activity of the forward (left) and reverse transitions (right) of the $\text{Fe}_{68.8}\text{Pd}_{31.2}^{\text{poly}}$ sample at three selected rates (0.1 K/min, 1 K/min, and 10 K/min). 133

- 7.28. Power laws, exponents, and exponential corrections for the forward and reverse transition of the $\text{Fe}_{68.8}\text{Pd}_{31.2}^{\text{single}}$ sample at selected rates.
Top: Log-log histograms of the mean amplitude (left) and energy distributions (right).
Center: Amplitude and energy exponents α (left) and ϵ (right). The exponents have been determined by the maximum likelihood method using the equations $p(A) \propto A^{-\alpha} e^{-\lambda_A A}$ and $p(E) \propto E^{-\epsilon} e^{-\lambda_E E}$. The red dotted lines are guides to the eye indicating the mean values.
Bottom: λ -values of the exponential correction terms $e^{-\lambda_A A}$ (left) and $e^{-\lambda_E E}$ (right) of the amplitude and energy distributions. . . . 134
- 7.29. Power laws, exponents, and exponential corrections for the forward and reverse transitions of the $\text{Fe}_{68.8}\text{Pd}_{31.2}^{\text{poly}}$ sample at selected rates.
Top: Log-log histograms of the mean amplitude (left) and energy distributions (right).
Center: Amplitude and energy exponents α (left) and ϵ (right). The exponents have been determined by the maximum likelihood method using the equations $p(A) \propto A^{-\alpha} e^{-\lambda_A A}$ and $p(E) \propto E^{-\epsilon} e^{-\lambda_E E}$. The red dotted lines are guides to the eye indicating the mean values.
Bottom: λ -values of the exponential correction terms $e^{-\lambda_A A}$ (left) and $e^{-\lambda_E E}$ (right) of the amplitude and energy distributions. . . . 135
- 7.30. Comparison between the acoustic activity and calorimetric data during the premartensitic and martensitic forward and reverse transition of the $\text{Ni}_{52}\text{Mn}_{23}\text{Ga}_{25}$ sample. The temperature cycles have a rate of 1 K/min. An enlargement of the region of the premartensitic transitions can be found in figure 7.31. For clarity reasons, the data of the reverse transition have been plotted with negative values. The excellent matching of the AE data and the DSC data in case of the forward transition must be regarded as accidental as the DSC data is not temperature calibrated. 137
- 7.31. Enlargement of the premartensitic region of the $\text{Ni}_{52}\text{Mn}_{23}\text{Ga}_{25}$ sample with the acoustic activity on the left and the calorimetric data on the right. The maximum, arising during cooling, appears to be more pronounced than the maximum during heating. The same holds for the calorimetric data after a proper baseline correction. The cycles have been performed without an applied magnetic field. 138
- 7.32. Color-coded acoustic activity in a log-log histogram showing the filtered signal distribution of the duration against the amplitude during the forward premartensitic transition of the $\text{Ni}_{52}\text{Mn}_{23}\text{Ga}_{25}$ sample. 139

- 7.33. Exemplary acoustic activity during the premartensitic forward transition of the $\text{Ni}_{52}\text{Mn}_{23}\text{Ga}_{25}$ sample at selected magnetic fields (a). Integrated acoustic activity during the forward transition at selected fields of the same sample (b). The dotted line is a guide to the eye. In both cases the field was applied along the [001] direction. 140
- 7.34. Smoothed acoustic activity of the premartensitic forward transition of the $\text{Ni}_{52}\text{Mn}_{23}\text{Ga}_{25}$ sample at selected magnetic fields applied along the [001] direction (normalized to a total acoustic activity of one). 141
- 7.35. Temperature shift of the premartensitic transition of the $\text{Ni}_{52}\text{Mn}_{23}\text{Ga}_{25}$ sample as a function of the applied magnetic field. The dotted line is a guide to the eye. 142
- 7.36. Duration (a), amplitude (b), and energy (c) distributions of the premartensitic forward transition of the $\text{Ni}_{52}\text{Mn}_{23}\text{Ga}_{25}$ sample at selected fields applied along the [001] direction. Because of an amplitude threshold, the amplitude distribution shows a sharp cutoff whereas the duration and energy distributions show a window effect. Data affected by the window effect cannot be used for statistical analysis (see introduction of chapter 8). 143
- 7.37. Exponents and exponential corrections for the premartensitic transition of the $\text{Ni}_{52}\text{Mn}_{23}\text{Ga}_{25}$ sample. Exponents with error bars for the duration (a), the amplitude (b), the energy (c), and the corresponding λ -values (d - f) as a function of the magnetic field applied in [001] direction. The values have been determined by the maximum likelihood method using the equation $p(X) \propto X^{-x} e^{-\lambda X}$. The dotted lines serve as guides to the eye. 144
- 7.38. Acoustic activity of the $\text{Ni}_{52}\text{Mn}_{23}\text{Ga}_{25}$ sample during the martensitic forward transition on cooling at selected values of the field applied along the [001] direction (a). Accumulated acoustic activity during forward transition at selected fields applied along the [001] direction (b). Inset: Martensitic start temperature M_s as a function of the applied magnetic field with a dotted line as a guide to the eye. 146
- 7.39. Power laws, exponents, and exponential corrections for the forward and reverse martensitic transition of the $\text{Ni}_{52}\text{Mn}_{23}\text{Ga}_{25}$ sample at selected magnetic fields applied along the [001] direction.
Top: Amplitude (left) and energy (right) distributions of the forward transition. Note that the energy distributions cover more than 6 decades.
Center: Amplitude α (left) and energy exponents ϵ (right). The dotted lines serve as a guide to the eye indicating the trends.
Bottom: λ -values of the exponential correction terms $e^{-\lambda_A A}$ (left) and $e^{-\lambda_E E}$ (right) of the amplitude and energy distributions. . . . 148

- 7.40. Acoustic emission by the magnetic-field-induced rearrangement of martensitic variants in the martensitic phase of the $\text{Ni}_{52}\text{Mn}_{23}\text{Ga}_{25}$ sample measured in acoustic activity and energy versus time. The maximal acoustic activity and energy detected during the first field cycle represent a lower bound due to hardware restrictions. The lower part of the figure displays the magnetic field applied along $[\bar{1}10]$ with a period of $\tau_{mf} = 130$ s. 149
- 7.41. Amplitude distributions (top) and corresponding exponents (bottom) detected during quick cycles of the magnetic field in the martensitic phase of the $\text{Ni}_{52}\text{Mn}_{23}\text{Ga}_{25}$ sample. The quick magnetic field cycles have an amplitude of 10 kOe, a period of $\tau_{mf} = 130$ s, and are applied along the $[001]$ direction.
Top: The amplitude distributions on the left belong to increasing fields, the distributions on the right to decreasing fields.
Bottom: Exponents of the amplitude distribution with increasing fields on the left and decreasing fields on the right. The exponents of the first cycle have been ignored due to a memory overflow arising from hardware limitations. The exponent values have been determined by the maximum likelihood method using the equation $p(A) \propto A^{-\alpha} e^{-\lambda_A A}$. The dotted lines are guides to the eye and represent a mean value. 150
- 7.42. Amplitude distributions (top) and corresponding exponents (bottom) detected during slow cycles of the magnetic field in the martensitic phase of the $\text{Ni}_{52}\text{Mn}_{23}\text{Ga}_{25}$ sample. The slow magnetic field cycles have an amplitude of 10 kOe, a period of $\tau_{mf} = 1300$ s, and are applied along the $[001]$ direction.
Top: The amplitude distributions on the left belong to increasing fields, the ones on the right to decreasing fields.
Bottom: Exponents of the amplitude distribution with increasing fields on the left and decreasing fields on the right. The values of the exponents have been determined by the maximum likelihood method using the equation $p(A) \propto A^{-\alpha} e^{-\lambda_A A}$. The dotted lines serve as guides to the eye. 151
- 8.1. Acoustic activity of the martensitic transition of the $\text{Au}_{50.5}\text{Cd}_{49.5}$ sample at a rate of 0.1 K/min. The bin width of 1 s is equivalent to a temperature bin width of 1.667 mK. The inset shows a section of the activity between 200 s and 300 s. Due to the fine binning the jerky transition character is evident. 154

8.2.	The four quadrants of all possible amplitude and duration values in a log-log histogram of the martensitic transition in the Ni ₆₃ Al ₃₇ sample. The first quadrant shows the color-coded amplitude-duration distribution including all accessible data. The other three quadrants are not accessible due to hardware limitations.	156
8.3.	Amplitude window effect and its influence on the power law distributions of the duration (a), the energy (b), and the amplitude (c).	157
8.4.	Color-coded acoustic activity in a log-log histogram showing the duration against the amplitude of all measurable AE events. The red hatched area indicates a region of strong acoustic activity with low amplitudes and short durations, which cannot be detected owing to hardware settings causing a window effect.	158
8.5.	Exemplary hit energy versus hit amplitude cloud map corresponding to cooling ramps of the Fe _{68.8} Pd _{31.2} ^{single} sample. Data have been averaged over 20 ramps at a cooling rate of 1 K/min. The amplitude is given in dB with 20 dB being equal to one decade ($\text{dB} = 20 \log(\frac{U_0}{1\mu\text{V}})$). The dashed line indicates the behavior $E \propto A^2$	161
8.6.	Mean total acoustic activity and mean total energy of the forward and reverse transitions of all analyzed samples on a linear scale (top) and a log scale (bottom). Cooling runs are colored in blue and heating runs in red. The acoustic activity is represented by the first two columns respectively symbols. The energy is represented by the last two columns respectively symbols. For a better comparison, the mean total activity has been normalized to a sample mass of 1 g.	163
8.7.	Analysis of the correlation of the total activity of the forward (blue) and the reverse transition (red) of the Ni ₆₃ Al ₃₇ sample during a multi-cycle measurement of approximately 150 temperature cycles at a rate of 10 K/min. Top: The acoustic activities of both transition directions show a strong correlation. For clarity reasons, the acoustic activity (left) of the forward transition has been divided by two. Note that the abrupt activity changes first occur in the martensitic transition and subsequently in the austenitic transition (cooling run i is followed by heating run i). Scatter plot of the total acoustic activity of each cooling and heating run i (right). The linear shape with a positive slope indicates a high positive correlation with a correlation coefficient of $\rho = 0.922$. Bottom: Numerical derivative of the activity (left). Enlargement of a selected interval of the activity derivative where the high positive correlation can be explicitly observed (right).	166

- 8.8. Amplitude exponents of cooling and heating runs during a multi-cycle measurement with the $\text{Ni}_{63}\text{Al}_{37}$ sample at a rate of 10 K/min . . 168
- 8.9. Correlations between AE transition characteristics of the $\text{Ni}_{63}\text{Al}_{37}$ sample during a multi-cycle measurement at a rate of 10 K/min . On the left can be seen a scatter plot of the total acoustic activity of the forward transition and the corresponding exponents of the amplitude distribution. The oval shape with a negative slope and the correlation coefficient of $\rho \approx -0.5$ for cooling and heating indicate a negative correlation. On the right is shown a scatter plot of the amplitude exponents of the forward and reverse transition. The oval shape with a positive slope and the correlation coefficient of $\rho \approx 0.644$ indicate a rather strong correlation. 169
- 8.10. Normalized acoustic activity of the $\text{Ni}_{63}\text{Al}_{37}$ forward transition at selected rates. 170
- 8.11. Rate-dependent behavior of the $\text{Ni}_{63}\text{Al}_{37}$ sample. Amplitude exponents of cooling and heating runs (top). Total acoustic activity of the forward transition under cooling sorted according to the rate (left). Mean total activity as a function of the driving time τ_{dr} (right). The dotted line is a guide to the eye. 171
- 8.12. Distribution of the hit duration of the forward (left) and reverse (right) transition of the $\text{Ni}_{63}\text{Al}_{37}$ sample at three selected rates. For a better comparison the cooling curves have been normalized to compensate the rate-dependent hit number. Both transition directions show each a high degree of scaling in spite of their different classification as partly isothermal (forward transition) and athermal (reverse transition). 173
- 8.13. (top) Rescaling of the acoustic activity of the forward transition of the $\text{Au}_{50.5}\text{Cd}_{49.5}$ sample at selected rates. An incomplete data collapse of the rescaled activity can be seen. The legend displays the randomized order of the rates. (bottom) Rate-dependent rescaling coefficients as defined in equation 8.5. The non-monotonic behavior indicates partly isothermal kinetics. 175

- 8.14. Illustration of the aging process as explained by the symmetry-conforming short-range order model. The black and grey areas symbolize the probability of finding an A atom (P_i^A grey) or a B atom (P_i^B black) at lattice site i .
- (a) High temperature phase of an alloy A-B with disorder.
 - (b) Low temperature phase immediately after the martensitic phase transition with an inherited local structure ("microstructure").
 - (c) Diffusion leads to new equilibrium configurations of the sublattices A and B.
 - (d) The stress-induced reorientation of the variants leads to new out-of-equilibrium sublattices. If the stress is only applied for a short time, the variant jumps back into the old orientation due to the constraints arising from the preserved local atomic configuration. This time-dependent out-of-equilibrium effect is called rubber-like behavior or twin stabilization.
 - (e) In case of a stress applied for a sufficiently long time, diffusion leads to a new equilibrium situation that stabilizes the new variant orientation.
 - (f) Under increasing temperatures the stabilized martensite is exposed to constraints from the equilibrated sublattices that hinder the sample from starting the reverse transition immediately. A larger driving force, i. e. a larger superheating, is required to start the reverse transition, leading to higher A_s and A_f temperatures. This effect is called martensite stabilization (adapted from [151] and [127]). 177
- 8.15. Acoustic activity (top) and start temperature (bottom) of the reverse transition of the $Au_{50.5}Cd_{49.5}$ sample at selected rates. The acoustic activity curves show absent scaling and a shift of A_s towards higher temperatures with lower rates, i. e. longer aging times. The austenitic start temperature shows a shift towards higher temperatures with longer aging times. 179
- 8.16. Amplitude exponents of $Au_{50.5}Cd_{49.5}$ during heating cycles after staying for different time periods in the low temperature phase owing to different driving rates. The black dotted line indicates the characteristic time for martensite stabilization in Au-Cd which is fully consistent with the fact that the two exponents belonging to larger times are considerably lower than the others. The red dotted line is a guide to the eye. 180

8.17. Results of the detrended fluctuation analysis applied to the acoustic activity of the $\text{Au}_{50.5}\text{Cd}_{49.5}$ sample at a cooling rate of 0.1 K/min (see figure 8.1). The log-log plot reveals a correlated behavior of the data over short time intervals of less than 117 s and a rather uncorrelated distribution over longer time scales. Red lines indicate the fits of the two regimes. 182

8.18. Hit amplitude as a function of the waiting time between subsequent hits of the forward transition of the $\text{Au}_{50.5}\text{Cd}_{49.5}$ sample at a rate of 0.1 K/min. The main plot shows the correlation of hit_i with the waiting time between hit_i and hit_{i+1} . The inset shows the amplitude of hit_{i+1} with the waiting time between hit_i and hit_{i+1} 183

8.19. Acoustic activity and amplitude distributions of the martensitic transition of the $\text{Au}_{50.5}\text{Cd}_{49.5}$ sample at a rate of 0.1 K/min. The acoustic activity is represented in a time-histogram with a bin width of 1 s, which corresponds to a temperature bin width of 1.667 mK. The amplitude is depicted in a scatter plot. The similar distribution of the features indicates that high amplitudes occur predominantly in regions of high activity. 184

8.20. Development of the exponent α of the amplitude distribution of $\text{Fe}_{68.8}\text{Pd}_{31.2}^{\text{single}}$ as a function of the cooling run number. The trend of the exponent is visualized by the red dotted line. The black dotted lines indicate the saturation range of the majority of the exponents. The exponent ϵ of the energy distribution shows a similar behavior. 188

8.21. Comparison of the temperature shift of the premartensitic transition as a function of the applied magnetic field, in the field range relevant here, reported by various authors. Note that directions of the applied field as well as results from single and polycrystals are displayed together (see legend and table 8.8). 189

8.22. Total acoustic activity during the forward and the reverse transition at selected fields applied along the [001] direction. The acoustic activity under heating shows, in contrast to the cooling runs, essentially no field-dependence. 193

8.23. Acoustic activity (left) and energy (right) versus temperature during the reverse transition on heating at selected values of the field applied along the [001] direction. Note that the acoustic activity is basically field independent, whereas the acoustic energy strongly increases with increasing fields and that both plots originate from the same heating runs. This observation is consistent with the rate-dependent signal strength, as depicted in figure 7.39. 194

- 8.24. Frequency spectrum detected with an AE transducer resonant at 150 kHz during the martensitic transition of the $\text{Ni}_{52}\text{Mn}_{23}\text{Ga}_{25}$ sample without applied magnetic field. Note that the discrete spectra result from a 10 kHz binning of the AE acquisition system. 195
- 8.25. Acoustic activity during magnetic-field-induced rearrangement of martensitic variants under increasing and decreasing fields. For a better comparison the subsequent cycles have been plotted within the same time frame. On the left, the acoustic emission is shown for slow cycles with $\tau_{mf} = 1300$ s and on the right for quick cycles with $\tau_{mf} = 130$ s. The bin width of 10 s in case of the slow cycle and 1 s in case of the quick cycle compensate the different rates and are both equivalent to a field change of approximately 0.15 kOe. The inset (left) enlarges the region of small activity during increasing fields of the cycle numbers 2, 3, 4, and 5. Note that the drop in AE during the first quick cycle between 25 s and 50 s is caused by hardware limitations of the AE acquisition system. 196
- 8.26. Total acoustic activity of increasing and decreasing magnetic fields at a slow rate with a period of 1300 s and at a high rate with a period of 130 s. The figure starts with run number two to exclude a problem arising from hardware restrictions. 197
- 8.27. Amplitude exponents α as a function of the run number obtained during magnetic-field-induced rearrangement of martensitic variants of $\text{Ni}_{52}\text{Mn}_{23}\text{Ga}_{25}$ under increasing fields (left) and decreasing fields (right). The field is applied in [001] direction. Results of the energy exponents ϵ are similar and follow the scaling relation $\epsilon = \alpha + 1/2$.
Top: Decreasing amplitude exponents during slow field increase (left) and slow field decrease (right) with a cycle period $\tau_{mf} = 1300$ s.
Bottom: Constant amplitude exponents during quick field increase (left) and quick field decrease (right) with a cycle period $\tau_{mf} = 130$ s. Experiments with an applied field in $[\bar{1}10]$ direction yield comparable results. 200
- 8.28. Comparison of the integrated acoustic activities as a function of the cycle number of both field orientations [001] and $[\bar{1}10]$. In contrast to O’Handley’s prediction that the strain should be maximized by a field applied along $[\bar{1}10]$ (see reference [118]), both directions show the same total amount of AE. 201

8.29. Overview of all experimentally determined amplitude (top) and energy exponents (bottom) of all analyzed samples. Exponents with an explicit time- ($\text{Ni}_{63}\text{Al}_{37}$ and $\text{Au}_{50.5}\text{Cd}_{49.5}$) or field-dependence ($\text{Ni}_{52}\text{Mn}_{23}\text{Ga}_{25}$) are included in a sufficiently large bar. 203

List of Tables

3.1. Characteristics of strongly and weakly discontinuous martensitic phase transitions. The given quantities are typical examples of each group [38, 75, 141, 198].	31
3.2. Lattice parameters of cubic and tetragonal crystal structures of the austenite respectively martensite phase in a stoichiometric Ni ₂ MnGa crystal [125]. Note the little volume difference between the martensitic and austenitic elementary cell $V_A/V_M = 0.992$ which gives rise to the stress-dependent transition temperature (see section 7.2.4) and the phenomenon of superelasticity (see section 3.3.2).	55
3.3. Electronic and magnetic characteristics of Ni ₂ MnGa.	69
4.1. Characteristics of the piezoelectric acoustic emission transducers used in this work [1], which are depicted in figure 4.2.	77
5.1. Overview of the specific heat capacities of the alloys, of the dummy samples, and for comparison, of the elements. The specific heat capacity of Au _{50.5} Cd _{49.5} is assessed by Dulong–Petit’s law. In order to facilitate an application to a sample of a given size the heat capacities are expressed in J/(cm ³ K). This allows an easy calculation of the heat capacities per sample J/K.	90
5.2. Analogous electrical and thermal quantities used in the dynamic simulation.	98
6.1. Overview of all experiments. The randomized order displays the chronology of the measurements as well as the order of the applied rates respectively fields. The randomized rate respectively field order is mirrored as well in the rate respectively field order in the legends of the subsequent figures in chapters 7 and 8. Cycle numbers and rates apply to either temperature or magnetic cycles.	106
7.1. Characteristic quantities of the analyzed Ni ₆₃ Al ₃₇ sample. 7 R structures are reported for Ni _x Al _{1-x} with $x \lesssim 63\%$. The martensite phase structure of the sample under investigation has not been determined.	122

7.2.	Characteristic quantities of the analyzed Au _{50.5} Cd _{49.5} sample. . . .	126
7.3.	Characteristic quantities of the analyzed single- (top) and polycrystalline (bottom) Fe _{68.8} Pd _{31.2} sample.	136
7.4.	Characteristic quantities of the analyzed Ni ₅₂ Mn ₂₃ Ga ₂₅ sample. The temperature values have been estimated from the AE measurements. All values have been taken without an applied field. . . .	137
7.5.	Zero field exponents for the AE distributions of the premartensitic transition obtained by a maximum likelihood fit. The inverse of λ indicates where the exponential correction becomes relevant. . . .	145
8.1.	Part I of the overview of the experimentally determined mean exponents of the rate-dependent measurements. In cases of detected significant rate-dependence (Au _{50.5} Cd _{49.5} , Ni ₆₃ Al ₃₇) the corresponding values are listed explicitly. The z value describes the scaling relation between amplitude and energy $\alpha^{-1/\epsilon-1} = z$. Abbreviations: r = rate, fwd = forward transition, and rev = reverse transition.	159
8.2.	Part II of the overview of the experimentally determined mean exponents of the magnetic-field-dependent measurements. The value z describes the scaling relation between amplitude and energy $\alpha^{-1/\epsilon-1} = z$. Abbreviations: r = rate, fwd pm = forward premartensitic transition, and rev pm = reverse premartensitic transition. . .	160
8.3.	Overview of the transition enthalpy of the analyzed samples. . . .	162
8.4.	Overview of the crystal structures in the high and low temperature phase. In the high temperature phase all shape memory samples exhibit a cubic symmetry. If all atoms of the B2, L2 ₁ , DO ₃ structures were the same they would form a bcc structure.	164
8.5.	Comparison of the acoustic activity ratio and the signal strength ratio of the forward and reverse transition. Samples that transform into an orthorhombic low temperature symmetry have in their forward transition more acoustic activity with stronger signals than in their reverse transition. For samples with a tetragonal or trigonal low temperature symmetry the situation is inverse. . . .	165
8.6.	Overview of experimentally observed characteristic times for martensite stabilization t_g of different materials at room temperature. Additionally, the martensitic transition temperature reduced by the melting temperature M_s/T_m is given, which correlates with the stabilization times [149].	176
8.7.	Overview of the exponents determined by the detrended fluctuation analysis and the corresponding statistics [59, 132, 133]. . . .	182
8.8.	Published values for the temperature shift from various authors. .	190

8.9. Overview of cooling amplitude exponents of materials that transform into the same low temperature symmetry. Two universality classes are proposed, which are compatible with literature [22]. The exponents of Ni₂MnGa have been determined at zero magnetic field, the exponents of the other materials in the adiabatic limit at a cooling rate of 10 K/min (see the tables 8.1 and 8.2). 202

Bibliography

- [1] PCI-2 based AE system user's manual rev 2 October 2004.
- [2] R. Ahluwalia and G. Ananthakrishna. Power-law statistics for avalanches in a martensitic transformation. *Physical Review Letters*, 86(18):4076–4079, 2001.
- [3] K. Aizu. Possible species of ferromagnetic, ferroelectric, and ferroelastic crystals. *Physical Review B*, 2(3):754, 1970.
- [4] S. Aksoy, T. Krenke, M. Acet, E. F. Wassermann, X. Moya, L. Manosa, and A. Planes. Magnetization easy axis in martensitic Heusler alloys estimated by strain measurements under magnetic field. *Applied Physics Letters*, 91(25):251915, 2007.
- [5] M. Aspelmeyer, U. Klemradt, H. Abe, S. C. Moss, and J. Peisl. Martensitic relief formation on an electropolished Ni-37 at.% al (001) surface by diffuse X-ray scattering under grazing angles. *Materials Science and Engineering A-Structural Materials Properties Microstructure and Processing*, 273:286–290, 1999.
- [6] M. Aspelmeyer, U. Klemradt, L. T. Wood, and S. C. Moss. Growth kinetics of an athermal martensitic transformation by time-resolved optical diffraction from a Ni₆₃Al₃₇ (001) surface. *Journal de Physique IV*, 112:151–157, 2003.
- [7] M. Aspelmeyer, U. Klemradt, L. T. Wood, S. C. Moss, and J. Peisl. Time-dependent aspects of the athermal martensitic transformation: First observation of incubation time in Ni-Al. *Physica Status Solidi A-Applied Research*, 174(1):R9–R10, 1999.
- [8] Y. K. Au and C. M. Wayman. Thermoelastic behavior of martensitic transformation in β' -NiAl alloys. *Scripta Metallurgica*, 6(12):1209–1214, 1972.
- [9] P. Bak, C. Tang, and K. Wiesenfeld. Self-organized criticality - an explanation of 1/f noise. *Physical Review Letters*, 59(4):381–384, 1987.
- [10] P. Bak, C. Tang, and K. Wiesenfeld. Self-organized criticality. *Physical Review A*, 38(1):364–374, 1988.

- [11] K. Bammel. Immer wieder gut in Form. *Physik Journal*, 7:56 – 57, 2008.
- [12] J. Baram, Y. Gefen, and M. Rosen. Acoustic-emission generated during a single-interface movement in the martensitic-transformation of Au-47.5at.% Cd alloy. *Scripta Metallurgica*, 15(8):835–838, 1981.
- [13] J. Baram, Y. Gefen, and M. Rosen. Effect of cooling rate on the microstructure and acoustic-emission energy during the thermoelastic transformation in Au-Cd single-crystals. *Scripta Metallurgica*, 15(1):105–107, 1981.
- [14] J. Baram and M. Rosen. Some observations on acoustic-emission generated during thermoelastic phase-transformation in Al-Ni and Ti-Ni alloys. *Scripta Metallurgica*, 13(7):565–568, 1979.
- [15] J. Baram and M. Rosen. The thermoelastic phase-transition in Au-Cd alloys studied by acoustic-emission. *Philosophical Magazine A*, 44(4):895–903, 1981.
- [16] J. M. Barandiaran, V. A. Chernenko, P. Lazpita, J. Gutiérrez, I. Orue, J. Feuchtwanger, and S. Besseghini. Magnetic field effect on premartensitic transition in Ni–Mn–Ga alloys. *Applied Physics Letters*, 94:051909, 2009.
- [17] J. Bevk, T. B. Massalski, and U. Mizutani. Specific-heat of Au-Cd α and ζ alloys in range between 1.5 and 4.2 k. *Physical Review B*, 16(8):3456–3463, 1977.
- [18] Bhattacharya. *Microstructure of martensite*. Oxford series on materials modelling. Oxford, 2003.
- [19] H. W. J. Blote, E. Luijten, and J. R. Heringa. Ising universality in 3 dimensions - a Monte-Carlo study. *Journal of Physics A-Mathematical and General*, 28(22):6289–6313, 1995.
- [20] E. Bonnot, L. Manosa, A. Planes, D. Soto-Parra, E. Vives, B. Ludwig, C. Strothkaemper, T. Fukuda, and T. Kakeshita. Acoustic emission in the fcc-fct martensitic transition of Fe_{68.8}Pd_{31.2}. *Physical Review B*, 78(18):184103, 2008.
- [21] E. Bonnot, E. Vives, L. Manosa, A. Planes, and R. Romero. Acoustic emission and energy dissipation during front propagation in a stress-driven martensitic transition. *Physical Review B*, 78(9):094104, 2008.
- [22] L. Carrillo, L. Manosa, J. Ortin, A. Planes, and E. Vives. Experimental evidence for universality of acoustic emission avalanche distributions during structural transitions. *Physical Review Letters*, 81(9):1889–1892, 1998.

-
- [23] T. Castan, A. Planes, and A. Saxena. Modulated phases in multi-stage structural transformations. *Physical Review B*, 67(13):134113, 2003.
- [24] E. Cesari, V. A. Chernenko, V. V. Kokorin, J. Pons, and C. Segui. Internal friction associated with the structural phase transformations in Ni-Mn-Ga alloys. *Acta Materialia*, 45(3):999–1004, 1997.
- [25] S. Chakravorty and C. M. Wayman. Thermoelastic martensitic-transformation in β' Ni-Al alloys. 1. Crystallography and morphology. *Metallurgical Transactions A-Physical Metallurgy and Materials Science*, 7(4):555–568, 1976.
- [26] L. C. Chang and T. A. Read. Plastic deformation and diffusionless phase changes in metals - the Gold-Cadmium β -phase. *Transactions of the American Institute of Mining and Metallurgical Engineers*, 191(1):47–52, 1951.
- [27] J. W. Christian. *The theory of transformations in metals and alloys*, chapter Mechanical twinning, pages 788–789. Pergamon Press, 2 edition, 1975.
- [28] J. W. Christian, G. B. Olson, and M. Cohen. Classification of displacive transformations: What is a martensitic transformation? *Journal de Physique IV*, 5(C8):3–10, 1995.
- [29] P. C. Clapp. How would we recognize a martensitic transformation if it bumped into us on a dark & austy night? *Journal de Physique IV*, 5(C8):11–19, 1995.
- [30] M. Cohen, G. B. Olson, and P. C. Clapp. On the classification of displacive phase transformations. In *Proc. of the International Conference on Martensitic Transformations ICOMAT-79*, 1979.
- [31] Susanne Conradt. Dynamik der martensitischen Umwandlung in Formgedächtnislegierungen mittels akustischer Emissionsspektroskopie. Diploma thesis in physics, II. Physikalisches Institut, RWTH Aachen University, 2009.
- [32] A. Corral, C. J. Perez, and A. DiazGuilera. Self-organized criticality induced by diversity. *Physical Review Letters*, 78(8):1492–1495, 1997.
- [33] J. Cui, T. W. Shield, and R. D. James. Phase transformation and magnetic anisotropy of an iron-palladium ferromagnetic shape-memory alloy. *Acta Materialia*, 52(1):35–47, 2004.

- [34] Y. T. Cui, J. L. Chen, G. D. Liu, G. H. Wu, and W. L. Wang. Characteristics of the premartensitic transition strain in ferromagnetic shape memory $\text{Ni}_{50.5}\text{Mn}_{24.5}\text{Ga}_{25}$ single crystals. *Journal of Physics-Condensed Matter*, 16(18):3061–3069, 2004.
- [35] K. A. Dahmen, J. P. Sethna, M. C. Kuntz, and O. Perkovic. Hysteresis and avalanches: phase transitions and critical phenomena in driven disordered systems. *Journal of Magnetism and Magnetic Materials*, 226:1287–1292, 2001.
- [36] L. Y. Dai, M. Wuttig, and E. Pagounis. Twin stabilization in a ferromagnetic shape memory alloy. *Scripta Materialia*, 55(9):807–810, 2006.
- [37] T. Davenport, C. Grehofsky, M. Gonzalez, J. Worgull, and J. Trivisonno. Temperature and uniaxial stress dependence of the martensitic transformation temperature in $\text{Ni}_{63}\text{Al}_{37}$. *Journal de Physique IV*, 5(C8):1023–1028, 1995.
- [38] L. Delaey. *Materials Science and Technology: A Comprehensive Treatment: Phase Transformations in Materials v. 5*. Wiley VCH, 1990.
- [39] V. Dohm. *Encyclopedia of Physics, 3rd edition*, chapter Phase Transitions, page 1. Wiley-VCH, 2005.
- [40] P. Entel, V. D. Bucheinikov, V. V. Khovailo, A. T. Zayak, W. A. Adeagbo, M. E. Gruner, H. C. Herper, and E. F. Wassermann. Modelling the phase diagram of magnetic shape memory Heusler alloys. *Journal of Physics D-Applied Physics*, 39(5):865–889, 2006.
- [41] E. Esmail and I. Grabec. Quantitative-analysis of acoustic-emission during martensitic-transformation of the β -CuZnAl alloy. *Journal of Physics D-Applied Physics*, 19(4):605–614, 1986.
- [42] P. P. Ewald and C. Hermann, editors. *Strukturbericht*, volume 1. Akademische Verlagsgesellschaft m. b. H., Leipzig, 1931.
- [43] T. R. Finlayson, G. L. Kelly, and T. F. Smith. The effects of stress on the martensitic transformation in Ni–Al. *Materials Science and Engineering A-Structural Materials Properties Microstructure and Processing*, A273-275:366–369, 1999.
- [44] Deutsche Gesellschaft für Zerstörungsfreie Prüfung e.V. Richtlinie zur Charakterisierung der Aufnehmer und ihrer Ankopplung im Labor. Technical report, DGZfP, 1992.

-
- [45] V. Frette, K. Christensen, A. Malthesorensen, J. Feder, T. Jossang, and P. Meakin. Avalanche dynamics in a pile of rice. *Nature*, 379(6560):49–52, 1996.
- [46] G. Fritsch, V. V. Kokorin, and A. Kempf. Soft modes in Ni₂MnGa single-crystals. *Journal of Physics-Condensed Matter*, 6(8):L107–L110, 1994.
- [47] M. Fromm, U. Klemradt, G. Landmesser, and J. Peisl. Grazing incidence X-ray reflectivity: A new experimental approach to the martensitic surface relief. *Materials Science and Engineering A-Structural Materials Properties Microstructure and Processing*, 273:291–295, 1999.
- [48] C. Frontera and E. Vives. Studying avalanches in the ground state of the two-dimensional random-field ising model driven by an external field. *Physical Review E*, 62(5):7470–7473, 2000.
- [49] G. Ghosh and V. Raghavan. The kinetics of isothermal martensitic-transformation in an Fe-23.2wt-% Ni-2.8wt-% Mn alloy. *Materials Science and Engineering*, 80(1):65–74, 1986.
- [50] Vallen Systeme GmbH. Schallemissionsprüfung: Grundlagen - Gerätetechnik - Anwendungen. Technical report.
- [51] C. Gottfried and F. Schossberger, editors. *Strukturbericht*, volume 3. Akademische Verlagsgesellschaft m. b. H., Leipzig, 1937.
- [52] R. B. Griffiths. Dependence of critical indices on a parameter. *Physical Review Letters*, 24(26):1479, 1970.
- [53] E. A. Guggenheim. The principle of corresponding states. *Journal of Chemical Physics*, 13(7):253–261, 1945.
- [54] G. Guénin. The γ - ϵ martensitic transformation: A model for stress induced variant and its interaction with grain boundary. *Journal de Physique IV*, 5:433–438, 1995.
- [55] D. Halliday, R. Resnick, and J. Walker. *Physik*. Wiley-VCH, 2003.
- [56] B. Hanebach. Formgedächtnislegierungen für adaptive Tragwerke. Diploma thesis, Bauhaus-Universität Weimar, 2003.
- [57] C. Hermann, O. Lohrmann, and H. Philipp, editors. *Strukturbericht*, volume 2. Akademische Verlagsgesellschaft m. b. H., Leipzig, 1937.
- [58] T. L. Ho. Universal thermodynamics of degenerate quantum gases in the unitarity limit. *Physical Review Letters*, 92:090402, 2004.

- [59] K. Hu, P. Ch. Ivanov, Z. Chen, P. Carpena, and H. E. Stanley. Effect of trends on detrended fluctuation analysis. *Physical Review E*, 64:011114, 2001.
- [60] J. Humbeeck and R. Stalmans. *Shape Memory Materials*, page 169. Cambridge University Press, 1998.
- [61] T. Ichitsubo, K. Tanaka, M. Koiwa, and Y. Yamazaki. Kinetics of cubic to tetragonal transformation under external field by the time-dependent Ginzburg-Landau approach. *Physical Review B*, 62(9):5435–5441, 2000.
- [62] H. M. Jaeger, C. H. Liu, and S. R. Nagel. Relaxation at the angle of repose. *Physical Review Letters*, 62(1):40–43, 1989.
- [63] J. Jayender, R. V. Patel, S. Nikumb, and A. Ostojic. A robust controller for shape memory alloy actuators. *Proceedings of the 45th IEEE Conference on Decision and Control, Vols 1-14*, pages 2412–2417, 2006.
- [64] T. Kakeshita, T. Fukuda, and T. Takeuchi. Magneto-mechanical evaluation for twinning plane movement driven by magnetic field in ferromagnetic shape memory alloys. *Materials Science and Engineering A-Structural Materials Properties Microstructure and Processing*, 438:12–17, 2006.
- [65] T. Kakeshita, J. Katsuyama, T. Fukuda, and T. Saburi. Time-dependent nature of displacive transformations in Fe–Ni and Fe–Ni–Mn alloys under magnetic field and hydrostatic pressure. *Materials Science and Engineering*, A312:219–226, 2001.
- [66] T. Kakeshita, K. Kuroiwa, K. Shimizu, T. Ikeda, A. Yamagishi, and M. Date. Effect of magnetic fields on athermal and isothermal martensitic transformations in Fe-Ni-Mn alloys. *Materials Transactions JIM*, 34:415–422, 1993.
- [67] T. Kakeshita, K. Kuroiwa, K. Shimizu, T. Ikeda, A. Yamagishi, and M. Date. A new model explainable for both the athermal and isothermal natures of martensitic transformations in Fe-Ni-Mn alloys. *Materials Transactions JIM*, 34:423–428, 1993.
- [68] T. Kakeshita, T. Saburi, K. Kino, and S. Endo. Effect of magnetic field and hydrostatic pressure on martensitic transformation and its kinetics. *Japanese Journal of Applied Physics*, 36:7083–7094, 1997.
- [69] T. Kakeshita, T. Saburi, and K. Shimizu. Effects of hydrostatic pressure and magnetic field on martensitic transformations. *Materials Science and Engineering A-Structural Materials Properties Microstructure and Processing*, A273-275:21–39, 1999.

-
- [70] T. Kakeshita, T. Takeguchi, T. Fukuda, and T. Saburi. Time dependent nature of the athermal martensitic transformation in a Cu-Al-Ni shape memory alloy. *Materials Transactions JIM*, 37:299–303, 1996.
- [71] S. Kartha, T. Castan, J. A. Krumhansl, and J. P. Sethna. Spin-glass nature of tweed precursors in martensitic transformations. *Physical Review Letters*, 67(25):3630–3633, 1991.
- [72] S. Kartha, J. A. Krumhansl, J. P. Sethna, and L. K. Wickham. Disorder-driven pretransitional tweed pattern in martensitic transformations. *Physical Review B*, 52(2):803–822, 1995.
- [73] A. G. Khachaturyan, S. M. Shapiro, and S. Semenovskaya. Adaptive phase formation in martensitic-transformation. *Physical Review B*, 43(13):10832–10843, 1991.
- [74] J. H. Kim, F. Inaba, T. Fukuda, and T. Kakeshita. Effect of magnetic field on martensitic transformation temperature in Ni-Mn-Ga ferromagnetic shape memory alloys. *Acta Materialia*, 54(2):493–499, 2006.
- [75] U. Klemradt. *Zur Rolle der Oberfläche bei diffusionslosen Phasenumwandlungen*. Habilitationsschrift, Ludwig-Maximilians-Universität München, 2001.
- [76] U. Klemradt. *Effekte der Physik*, chapter 15. Phasenübergänge, page 1082. Harri Deutsch, 2005.
- [77] U. Klemradt, M. Aspelmeyer, L. T. Wood, and S. C. Moss. An experimental method to investigate the structure and kinetics of patterned surfaces using laser light diffraction. *Review of Scientific Instruments*, 73(1):108–113, 2002.
- [78] G. Krey. *Phasenübergänge und kritische Phänomene*. Vieweg, 1980.
- [79] J. A. Krumhansl. Multiscale science: Materials in the 21st century. *Shape Memory Materials*, 327-3:1–7, 2000.
- [80] J. A. Krumhansl and R. J. Gooding. Structural phase transitions with little phonon softening and first-order character. *Physical Review B*, 39:3047–3053, 1989.
- [81] P. K. Kumar and Dimitris C. Lagoudas. *Shape Memory Alloys*, page 30. Springer, 2008.
- [82] M. C. Kuntz and J. P. Sethna. Noise in disordered systems: The power spectrum and dynamic exponents in avalanche models. *Physical Review B*, 62(17):11699–11708, 2000.

- [83] L. D. Landau and M. Lifshitz. *Theory of elasticity*. Pergamon Press, 1959.
- [84] A. Ölander. An electrochemical investigation of solid Cadmium-Gold alloys. *Journal of the American Chemical Society*, 54:3819–3833, 1932.
- [85] G. Landmesser, U. Klemradt, R. L. Johnson, and T. R. Finlayson. Surface enhancement of soft-mode transformation in Ni₂MnGa. *Applied Physics Letters*, 90(2):021907, 2007.
- [86] J. Langejürgen. Modellierung von wärmeflussproblemen an oberflächen unter besonderer berücksichtigung der messung der körperkerntemperatur am menschen. Diploma thesis in physics, II. Physikalisches Institut, RWTH Aachen University, 2008.
- [87] Y. C. Liang, H. Kato, and M. Taya. Model calculation of 3D-phase transformation diagram of ferromagnetic shape memory alloys. *Mechanics of Materials*, 38(5-6):564–570, 2006.
- [88] A. A. Likhachev, A. Sozinov, and K. Ullakko. Different modeling concepts of magnetic shape memory and their comparison with some experimental results obtained in Ni-Mn-Ga. *Materials Science and Engineering A-Structural Materials Properties Microstructure and Processing*, 378(1-2):513–518, 2004.
- [89] G. D. Liu, J. L. Chen, Y. T. Cui, Z. H. Liu, M. Zhang, G. H. Wu, E. Bruck, F. R. de Boer, F. B. Meng, and Y. X. Li. Characterization of preferential orientation of martensitic variants in a single crystal of NiMnGa. *Solid State Communications*, 130(10):687–690, 2004.
- [90] B. Ludwig. Experimentelle Bestimmung von Inkubationszeiten bei athermischen martensitischen Phasenumwandlungen. Diploma thesis in physics, II. Physikalisches Institut, RWTH Aachen University, 2005.
- [91] B. Ludwig, C. Strothkaemper, U. Klemradt, X. Moya, Ll. Mañosa, E. Vives, and A. Planes. An acoustic emission study of the effect of a magnetic field on the martensitic transition in Ni₂MnGa. *Applied Physics Letters*, 94:121901, 2009.
- [92] B. Ludwig, C. Strothkaemper, U. Klemradt, X. Moya, Ll. Mañosa, E. Vives, and A. Planes. The premartensitic transition in Ni₂MnGa Heusler alloys: An acoustic emission study. *Physical Review B*, 80:144102, 2009.
- [93] R. Maddin. *Martensite: A tribute to Morris Cohen*, chapter 2, pages 11 –20. ASM International, 1992.

-
- [94] L. Manosa, L. Carrillo, E. Vives, E. Obrado, A. Gonzalez-Comas, and A. Planes. Acoustic emission at the premartensitic and martensitic transitions of Ni₂MnGa shape memory alloy. *Shape Memory Materials*, 327-3:481–484, 2000.
- [95] L. Manosa, A. Gonzalez-Comas, E. Obrado, and A. Planes. Premartensitic phase transformation in the Ni₂MnGa shape memory alloy. *Materials Science and Engineering A-Structural Materials Properties Microstructure and Processing*, 273:329–332, 1999.
- [96] L. Manosa, A. GonzalezComas, E. Obrado, A. Planes, V. A. Chernenko, V. V. Kokorin, and E. Cesari. Anomalies related to the TA(2)-phonon-mode condensation in the Heusler Ni₂MnGa alloy. *Physical Review B*, 55(17):11068–11071, 1997.
- [97] L. Manosa, A. Planes, D. Rouby, and J. L. Macqueron. Dynamics of the acoustic-emission source during a martensitic-transformation. *Journal of Physics F-Metal Physics*, 18(8):1725–1731, 1988.
- [98] L. Manosa, A. Planes, J. Zarestky, T. Lograsso, D. L. Schlagel, and C. Stassis. Phonon softening in Ni-Mn-Ga alloys. *Physical Review B*, 64(2):024305, 2001.
- [99] L. I. Manosa, A. Planes, and E. Cesari. Acoustic-emission amplitude distribution during the martensitic-transformation of Cu-Zn-Al alloys. *Journal of Physics D-Applied Physics*, 22(7):977–982, 1989.
- [100] J. Marcos, A. Planes, L. Manosa, F. Casanova, X. Batlle, A. Labarta, and B. Martinez. Magnetic field induced entropy change and magnetoelasticity in Ni-Mn-Ga alloys. *Physical Review B*, 66(22):224413, 2002.
- [101] M. A. Marioni, R. C. O’Handley, and S. M. Allen. Pulsed magnetic field-induced actuation of Ni-Mn-Ga single crystals. *Applied Physics Letters*, 83(19):3966–3968, 2003.
- [102] A. Martens. Zur Mikrostruktur des Spiegeleisens. *Zeitschrift Verein deutscher Ingenieure*, 22:481–488, 1878.
- [103] A. Martens. Zur Mikrostruktur des Spiegeleisens. *Zeitschrift Verein deutscher Ingenieure*, 22:205–214, 1878.
- [104] A. Martens. Über das mikroskopische Gefüge und die Krystallisationen des Roheisens, speciell des grauen Eisens. *Zeitschrift Verein deutscher Ingenieure*, 24:397, 1880.

- [105] Johnson Matthey Medical. How does Nitinol work? All about nitinol shape memory and superelasticity. Technical report, Johnson Matthey Medical, 2009.
- [106] A. P. Mehta, A. C. Mills, K. A. Dahmen, and J. P. Sethna. Universal pulse shape scaling function and exponents: Critical test for avalanche models applied to Barkhausen noise. *Physical Review E*, 65(4):046139, 2002.
- [107] K.N. Melton. *Shape Memory Materials*, page 220. Cambridge University Press, 1998.
- [108] R. Meyer and P. Entel. Martensite-austenite transition and phonon dispersion curves of $\text{Fe}_{1-x}\text{Ni}_x$ studied by molecular-dynamics simulations. *Physical Review B*, 57(9):5140–5147, 1998.
- [109] D. B. Miracle. Overview no-104 - the physical and mechanical-properties of NiAl. *Acta Metallurgica et Materialia*, 41(3):649–684, 1993.
- [110] M. Mitsuka, T. Ohba, T. Fukuda, T. Kakeshita, and M. Tanaka. Martensitic transformation in FePd alloy revealed by synchrotron radiation. *Materials Science and Engineering A-Structural Materials Properties Microstructure and Processing*, 438:332–335, 2006.
- [111] L. Mueller. *Zeitabhängige Phänomene in athermischen Formgedächtnislegierungen*. Doctoral dissertation, Faculty of math and natural sciences, RWTH Aachen University, 2009.
- [112] L. Mueller, U. Klemradt, and T. R. Finlayson. Time-dependent phenomena in athermal martensitic transformations. *Materials Science and Engineering A-Structural Materials Properties Microstructure and Processing*, 438:122–125, 2006.
- [113] S. J. Murray, M. Marioni, S. M. Allen, R. C. O’Handley, and T. A. Lograsso. 6% magnetic-field-induced strain by twin-boundary motion in ferromagnetic Ni-Mn-Ga. *Applied Physics Letters*, 77(6):886–888, 2000.
- [114] Y. Nakajima, S. Aoki, K. Otsuka, and T. Ohba. The rubber-like behaviour of ζ' (trigonal) martensite in Au-49.5 to 50.0at% Cd alloy. *Material Letters*, 21:271–274, 1994.
- [115] Zenji Nishiyama. *Martensitic Transformations*. Academic Press, New York, 1978.
- [116] W. Nolting. *Grundkurs Theoretische Physik 6: Statistische Physik*. Springer, 2007.

-
- [117] E. Obrado, A. Gonzalez-Comas, L. Manosa, and A. Planes. Magnetoelastic behavior of the Heusler Ni₂MnGa alloy. *Journal of Applied Physics*, 83(11):7300–7302, 1998.
- [118] R. C. O’Handley. Model for strain and magnetization in magnetic shape-memory alloys. *Journal of Applied Physics*, 83(6):3263–3270, 1998.
- [119] T. Ohba, Y. Emura, S. Miyazaki, and K. Otsuka. Crystal structure of γ'_2 martensite in Au-47.5at%Cd alloy. *Materials Transactions JIM*, 31:12–17, 1990.
- [120] T. Ohba, Y. Emura, and K. Otsuka. Structure determination of the ζ'_2 martensite and the mechanism of $\beta_2 \rightarrow \zeta'_2$ transformation in a Au-49.5at%Cd alloy. *Materials Transactions JIM*, 33:29–37, 1992.
- [121] T. Ohba, K. Otsuka, and S. Sasaki. Study of rubber-like behaviour in a Au-47.5at%Cd alloy by synchrotron-orbital radiation. *Material Science Forum*, 56-58:317–322, 1990.
- [122] T. Ohba, M. Sato, and K. Otsuka. Asymmetric behaviour of elastic scattering appearing prior to the transformation in Au-47.5at%Cd. *Material Science Forum*, 327-328:377–380, 2000.
- [123] T. Ohba, S. M. Shapiro, S. Aoki, and K. Otsuka. Phonon softening in Au-49.5 at%Cd alloy. *Japanese Journal of Applied Physics*, 33:L1631–L1633, 1994.
- [124] T. Ohba, L. Shi, T. Hara, H. Funaki, and M. Sato. Precursor behavior in structure factors of AuCd alloy observed by different wavelength X-ray. *Materials Science and Engineering A-Structural Materials Properties Microstructure and Processing*, 312(1-2):244–247, 2001.
- [125] N. Okamoto, T. Fukuda, T. Kakeshita, T. Takeuchi, and K. Kishio. Rearrangement of variants in Ni₂MnGa under magnetic field. *Science and Technology of Advanced Materials*, 5(1-2):29–34, 2004.
- [126] R. Oshima. Successive martensitic transformations in Fe-Pd alloys. *Scripta Metallurgica*, 15(8):829–833, 1981.
- [127] K. Otsuka and X. Ren. Mechanism of martensite aging effect. *Scripta Materialia*, 50(2):207–212, 2004.
- [128] K. Otsuka, X. Ren, and T. Takeda. Experimental test for a possible isothermal martensitic transformation in a Ti-Ni alloy. *Scripta Materialia*, 45:154–152, 2001.

- [129] K. Otsuka and C. M. Wayman. *Shape memory materials*. Cambridge, 1998.
- [130] Q. Pan and R. D. James. Micromagnetic study of Ni₂MnGa under applied field. *Journal of Applied Physics*, 87(9):4702–4706, 2000.
- [131] H. S. Park, Y. Murakami, D. Shindo, V. A. Chernenko, and T. Kanomata. Behavior of magnetic domains during structural transformations in Ni₂MnGa ferromagnetic shape memory alloy. *Applied Physics Letters*, 83(18):3752–3754, 2003.
- [132] C.-K. Peng, S. V. Buldyrev, S. Halvin, M. Simons, H. E. Stanley, and A. L. Goldberger. Mosaic organization of DNA nucleotides. *Physical Review E*, 49:1685–1689, 1994.
- [133] C.-K. Peng, S. Halvin, H. E. Stanley, and A. L. Goldberger. Quantification of scaling exponents and crossover phenomena in nonstationary heartbeat series. *Chaos*, 5:82–87, 1995.
- [134] F. J. Perez-Reche, M. Stipcich, E. Vives, L. Manosa, A. Planes, and M. Morin. Kinetics of martensitic transitions in Cu-Al-Mn under thermal cycling: Analysis at multiple length scales. *Physical Review B*, 69(6):064101, 2004.
- [135] F. J. Perez-Reche, B. Tadic, L. Manosa, A. Planes, and E. Vives. Driving rate effects in avalanche-mediated first-order phase transitions. *Physical Review Letters*, 93(19):195701, 2004.
- [136] F. J. Perez-Reche, L. Truskinovsky, and G. Zanzotto. Training-induced criticality in martensites. *Physical Review Letters*, 99(7):075501, 2007.
- [137] F. J. Perez-Reche, E. Vives, L. Manosa, and A. Planes. Athermal character of structural phase transitions. *Physical Review Letters*, 87(19):195701, 2001.
- [138] F. J. Perez-Reche, E. Vives, L. Manosa, and A. Planes. Acoustic emission study of martensitic transition kinetics in Cu-based shape-memory alloys. *Journal de Physique IV*, 112:597–600, 2003.
- [139] F. J. Perez-Reche, E. Vives, L. Manosa, and A. Planes. Calorimetric and acoustic emission study of the premartensitic and martensitic transitions in Ni-Mn-Ga. *Materials Science and Engineering A-Structural Materials Properties Microstructure and Processing*, 378(1-2):353–356, 2004.
- [140] A. Planes, J. L. Macqueron, M. Morin, and G. Guenin. Study of martensitic-transformation of Cu-Zn-Al alloy by coupled enthalpy and acoustic-emission measurements. *Physica Status Solidi A-Applied Research*, 66(2):717–724, 1981.

-
- [141] A. Planes and L. Manosa. Vibrational properties of shape-memory alloys. *Solid State Physics: Advances in Research and Applications, Vol 55*, 55:159–267, 2001.
- [142] A. Planes, E. Obrado, A. Gonzalez-Comas, and L. Manosa. Premartensitic transition driven by magnetoelastic interaction in bcc ferromagnetic Ni_2MnGa . *Physical Review Letters*, 79(20):3926–3929, 1997.
- [143] A. Planes, F. J. Perez-Reche, E. Vives, and L. Manosa. Kinetics of martensitic transitions in shape-memory alloys. *Scripta Materialia*, 50(2):181–186, 2004.
- [144] A. Planes, M. Porta, T. Castan, and A. Saxena. Magnetostructural tweed in ferromagnetic Heusler shape-memory alloys. *Materials Science and Engineering A-Structural Materials Properties Microstructure and Processing*, 438:916, 2006.
- [145] B. Predel. *Al-Ni (Aluminum-Nickel)*, chapter Phase Equilibria, Crystallographic and Thermodynamic Data of Binary Alloys: Ac-Au - Au-Zr, pages 1–7. Landolt-Börnstein. Springer, 1991.
- [146] B. Predel. *Fe-Pd (Iron-Palladium)*, chapter Phase equilibria, crystallographic and thermodynamic data of binary alloys - Dy-Er ... Fr-Mo, pages 1–7. Springer, 1995.
- [147] I. Rafols and E. Vives. Statistics of avalanches in martensitic transformations. 2. Modeling. *Physical Review B*, 52(17):12651–12656, 1995.
- [148] V. Raghavan and A.R. Entwisle. The physical properties of martensite and bainite. Technical report, Iron and Steel Institute (London), 1965.
- [149] X. Ren and K. Otsuka. Recent advances in understanding the origin of martensite aging phenomena in shape memory alloys. *Phase Transitions*, 69:329–350, 1999.
- [150] X. Ren and K. Otsuka. Universal symmetry property of point defects in crystals. *Physical Review Letters*, 85:1016–1019, 2000.
- [151] X. B. Ren and K. Otsuka. Origin of rubber-like behaviour in metal alloys. *Nature*, 389(6651):579–582, 1997.
- [152] D. Rouby, P. Fleischmann, and C. Duvergier. An acoustic-emission source model for both continuous and burst-type emission analysis. 2. Experiments. *Philosophical Magazine A*, 47(5):689–705, 1983.

- [153] A. L. Roytburd. Kurdjumov and his school in martensite of the 20th century. *Materials Science and Engineering*, A273-275:1–10, 1999.
- [154] S. Rubini, C. Dimitropoulos, S. Aldrovandi, F. Borsa, D. R. Torgenson, and J. Ziolo. Electronic-structure and the martensitic-transformation in β -phase Ni-Al alloys - Al-27 NMR and specific-heat measurements. *Physical Review B*, 46(17):10563–10572, 1992.
- [155] Sanpaz. This figure is licensed under the creative commons attribution sharealike 3.0 license. Wikipedia, 2009.
- [156] M. Sato, B. H. Grier, S. M. Shapiro, and M. Miyajima. Effect of magnetic ordering on the lattice dynamics of fcc $\text{Fe}_{1-x}\text{Pd}_x$. *Journal of Physics F-Metal Physics*, 12:2117–2129, 1982.
- [157] A. Saxena, T. Castan, A. Planes, M. Porta, Y. Kishi, T. A. Lograsso, D. Viehland, M. Wuttig, and M. De Graef. Origin of magnetic and magnetoelastic tweedlike precursor modulations in ferroic materials. *Physical Review Letters*, 92(19):197203, 2004.
- [158] S. M. Schmitz. Kinetische Aspekte diffusionsloser Phasenumwandlungen von Formgedächtnislegierungen. Diploma thesis in physics, II. Physikalisches Institut, RWTH Aachen University, 2007.
- [159] D. Schryvers. *An approach to the martensitic transformation in Ni-Al*. PhD thesis, Vrije Universiteit Brussel und Rijksuniversitair Centrum Antwerpen, 1991.
- [160] C. Segui and E. Cesari. Effect of Mn on aging of Cu-Al-Ni-Mn-B alloys, February 1995.
- [161] C. Segui, E. Cesari, J. Font, J. Muntasell, and V. A. Chernenko. Martensite stabilization in a high temperature Ni-Mn-Ga alloy. *Scripta Materialia*, 53(3):315–318, 2005.
- [162] J. P. Sethna. Website: <http://www.lassp.cornell.edu/sethna>. Internet, accessed at 06-15-2009.
- [163] J. P. Sethna, K. Dahmen, S. Kartha, J. A. Krumhansl, B. W. Roberts, and J. D. Shore. Hysteresis and hierarchies - dynamics of disorder-driven 1st-order phase-transformations. *Physical Review Letters*, 70(21):3347–3350, 1993.
- [164] J. P. Sethna, K. A. Dahmen, and C. R. Myers. Crackling noise. *Nature*, 410(6825):242–250, 2001.

-
- [165] S. M. Shapiro, J. Z. Larese, Y. Noda, S. C. Moss, and L. E. Tanner. Neutron-scattering study of premartensitic behavior in Ni-Al alloys. *Physical Review Letters*, 57(25):3199–3202, 1986.
- [166] S. M. Shapiro, B. X. Yang, Y. Noda, L. E. Tanner, and D. Schryvers. Neutron-scattering and electron-microscopy studies of the premartensitic phenomena in $\text{Ni}_x\text{Al}_{100-x}$ alloys. *Physical Review B*, 44(17):9301–9313, 1991.
- [167] S. M. Shapiro, B. X. Yang, and G. Shirane. Neutron scattering study of the martensitic transformation on a Ni-Al β -phase alloy. *Physical Review Letters*, 62:1298–1301, 1989.
- [168] J. L. Smialek and R. F. Hehemann. Transformation temperatures of martensite in β -phase nickel aluminide. *Metallurgical Transactions*, 4(6):1571–1575, 1973.
- [169] T. Sohmura, R. Oshima, and F. E. Fujita. Thermoelastic fcc-fct martensitic-transformation in Fe-Pd alloy. *Scripta Metallurgica*, 14(8):855–856, 1980.
- [170] A. Sozinov, A. A. Likhachev, N. Lanska, and K. Ullakko. Giant magnetic-field-induced strain in NiMnGa seven-layered martensitic phase. *Applied Physics Letters*, 80(10):1746–1748, 2002.
- [171] S. Sreekala and G. Ananthakrishna. Two-dimensional model for ferromagnetic martensites. *Physical Review B*, 72(13):134403, 2005.
- [172] C. Strothkaemper. Akustische Emissionsspektroskopie an diffusionslosen strukturellen Phasenumwandlungen mit symmetriebrechendem Charakter. Diploma thesis in physics, II. Physikalisches Institut, RWTH Aachen University, 2008.
- [173] V. A. Sutilov. *Physik des Ultraschalls*. Springer, 1984.
- [174] I. Takeuchi, O. O. Famodu, J. C. Read, M. A. Aronova, K. S. Chang, C. Craciunescu, S. E. Lofland, M. Wuttig, F. C. Wellstood, L. Knauss, and A. Orozco. Identification of novel compositions of ferromagnetic shape-memory alloys using composition spreads. *Nature Materials*, 2(3):180–184, 2003.
- [175] J. W. Tester and M. Modell. *Thermodynamics and its applications*. Robert C. Reid, 1997.
- [176] N. N. Thadhani and M. A. Meyers. Kinetics of isothermal martensitic-transformation. *Progress In Materials Science*, 30(1):1–37, 1986.

- [177] Paul A. Tipler, editor. *Physik*. Spektrum Akademischer Verlag, 2006.
- [178] J.-C. Tolédano and P. Tolédano. *The Landau theory of phase transitions*. World Scientific, 1987.
- [179] H. C. Tong and C. M. Wayman. Stress-temperature-energy relationships for thermoelastic martensitic transformations. *Scripta Metallurgica*, 8(2):93–100, 1974.
- [180] K. Tsuchiya, H. Nakamura, D. Ohtoyo, H. Ohtsuka, and M. Umemoto. Structures and phase transformations in the Heusler-type ferromagnetic shape memory alloys. *Prism 4: Forth Pacific Rim International Conference on Advanced Materials and Processing, Vols I and II*, pages 1665–1668, 2001.
- [181] M. A. Uijttewaal, T. Hickel, J. Neugebauer, Gruner M. E., and P. Entel. Understanding the phase transitions of the Ni₂MnGa magnetic shape memory system from first principles. *Physical Review Letters*, 102:035702, 2009.
- [182] K. Ullakko. Magnetically controlled shape memory alloys: A new class of actuator materials. *Journal of Materials Engineering and Performance*, 5(3):405–409, 1996.
- [183] K. Ullakko, J. K. Huang, C. Kantner, R. C. OHandley, and V. V. Kokorin. Large magnetic-field-induced strains in Ni₂MnGa single crystals. *Applied Physics Letters*, 69(13):1966–1968, 1996.
- [184] K. Ullakko, J. K. Huang, V. V. Kokorin, and R. C. OHandley. Magnetically controlled shape memory effect in Ni₂MnGa intermetallics. *Scripta Materialia*, 36(10):1133–1138, 1997.
- [185] B. B. Van Aken, J. P. Rivera, H. Schmid, and M. Fiebig. Observation of ferrotoroidic domains. *Nature*, 449(7163):702–705, 2007.
- [186] A. N. Vasil'ev, V. D. Buchel'nikov, T. Takagi, V. V. Khovailo, and E. I. Estrin. Shape memory ferromagnets. *Physics*, 46(6):559–588, 2003.
- [187] S. Vatanayon and R. F. Hehemann. *Shape memory effects in alloys*, chapter 5. Martensitic transformations in β -phase alloys, pages 115–146. Plenum Press, 1975.
- [188] E. Vives. Personal communication, 02 2009.
- [189] E. Vives, J. Goicoechea, J. Ortin, and A. Planes. Universality in models for disorder-induced phase-transitions. *Physical Review E*, 52(1):R5–R8, 1995.

-
- [190] E. Vives, E. Obrado, and A. Planes. Hysteresis and avalanches in the site-diluted Ising model: comparison with experimental results in Cu-Al-Mn alloys. *Physica B*, 275(1-3):45–49, 2000.
- [191] E. Vives, J. Ortin, L. Manosa, I. Rafols, R. Perezmagrane, and A. Planes. Distributions of avalanches in martensitic transformations. *Physical Review Letters*, 72(11):1694–1697, 1994.
- [192] E. Vives, I. Rafols, L. Manosa, J. Ortin, and A. Planes. Statistics of avalanches in martensitic transformations. 1. Acoustic-emission experiments. *Physical Review B*, 52(17):12644–12650, 1995.
- [193] W. Wagner. *Wärmeübertragung*. Vogel Verlag, 2004.
- [194] T. Waitz, H.P. Karnthaler, and C. Rentenberger. Atomic scale self accommodation observed at hcp/dhcp martensitic transformation interfaces. *Journal de Physique IV*, 7:185, 1997.
- [195] F. X. Wang, editor. *Design and control of linear actuators made by magnetically controlled shape memory alloys*, 2005.
- [196] F. X. Wang, Q. X. Zhang, W. J. Li, C. X. Li, and X. J. Wu. Actuation principle and property of magnetically controlled shape memory alloy actuators. *2005 IEEE International Conference on Mechatronics*, pages 579–582, 2005.
- [197] W. H. Wang, J. L. Chen, S. X. Gao, G. H. Wu, Z. Wang, Y. F. Zheng, L. C. Zhao, and W. S. Zhan. Effect of low dc magnetic field on the premartensitic phase transition temperature of ferromagnetic Ni₂MnGa single crystals. *Journal of Physics-Condensed Matter*, 13(11):2607–2613, 2001.
- [198] C.M Wayman. *Physical Metallurgy II*. Elsevier, 1983.
- [199] P. J. Webster, K. R. A. Ziebeck, S. L. Town, and M. S. Peak. Magnetic order and phase-transformation in Ni₂MnGa. *Philosophical Magazine B*, 49(3):295–310, 1984.
- [200] P. E. Weiss. L’hypothèse du champ moléculaire et la propriété ferromagnétique. *Journal de Physique et Le Radium*, 6:661–90, 1907.
- [201] R. A. White and K. A. Dahmen. Driving rate effects on crackling noise. *Physical Review Letters*, 91(8):085702, 2003.
- [202] K. G. Wilson. Renormalization group and critical phenomena. 1. Renormalization group and Kadanoff scaling picture. *Physical Review B*, 4(9):3174, 1971.

- [203] K. G. Wilson. Renormalization group and critical phenomena. 2. Phase-space cell analysis of critical behavior. *Physical Review B*, 4(9):3184, 1971.
- [204] K. G. Wilson. Renormalization group - critical phenomena and Kondo problem. *Reviews of Modern Physics*, 47(4):773–840, 1975.
- [205] Y. Xin, L. Yan, L. Chai, and H. B. Xu. The effect of aging on the Ni-Mn-Ga high-temperature shape memory alloys. *Scripta Materialia*, 54(6):1139–1143, 2006.
- [206] C. Zener. Contributions to the theory of β -phase alloys. *Physical Review*, 71(12):846–851, 1947.
- [207] C. Zener. Theory of strain interaction of solute atoms. *Physical Review*, 74(6):639–647, 1948.
- [208] J. M. Zhang. The non-equilibrium phase-transition theory of martensitic-transformation. *Journal of Physics F-Metal Physics*, 14(3):769–783, 1984.
- [209] A. Zheludev, S. M. Shapiro, P. Wochner, A. Schwartz, M. Wall, and L. E. Tanner. Phonon anomaly, central peak, and microstructures in Ni₂MnGa. *Physical Review B*, 51(17):11310–11314, 1995.
- [210] A. Zheludev, S. M. Shapiro, P. Wochner, and L. E. Tanner. Precursor effects and premartensitic transformation in Ni₂MnGa. *Physical Review B*, 54(21):15045–15050, 1996.
- [211] F. Zuo, X. Su, and K. H. Wu. Magnetic properties of the premartensitic transition in Ni₂MnGa alloys. *Physical Review B*, 58(17):11127–11130, 1998.

Danksagung

Mein Dank gilt allen Menschen, die mich während meiner Doktorarbeit begleitet und unterstützt haben!

Professor Uwe Klemradt danke ich für die exzellente Betreuung und die inspirierenden Gespräche, nicht nur über Themen der Arbeit. Die ausgewogene Mischung aus eigenverantwortlichem Forschen, wissenschaftlichen Anregungen und der Einbindung in die Institutsarbeit haben mich über die gesamte Zeit besonders motiviert. Zu der angenehmen Arbeitsatmosphäre und zu den spannenden Diskussionen haben in großem Maße meine Doktorandenkollegen Dagmar Carmele, Leonard Müller und Axel Solbach und die ehemaligen Diplomanden aus meinem Bereich - Susanne Conradt, Jens Langejürgen und Steffen Schmitz - beigetragen. Ein besonderer Dank gilt dem ehemaligen Diplomanden Christian Strothkämper, der gemeinsam mit mir nächtelang an der Messapparatur, an Analysemethoden und möglichen Interpretationsansätzen gearbeitet hat. Des Weiteren haben mir die tatkräftige Unterstützung von Sekretariat und Werkstatt ein erfolgreiches Arbeiten ermöglicht.

Voldria donar el meu més profund agraïment al professor Antoni Planes així com al seu grup de treball de la Universitat de Barcelona amb qui vaig tenir la sort de treballar en diverses jornades de recerca. La seva càlida acollida i el seu suport actiu en totes les preguntes han estat la base d'una excel·lent formació acadèmia a l'estranger. Pel gran suport al laboratori i les intenses discussions sobre resultats experimentals, possibles interpretacions i la situació del Barça vull donar les gràcies als professors Lluís Mañosa i Eduard Vives i als meus col·legues Erell Bonnot i Xavier Moya.

Mein ganz besonderer Dank gilt denen, die mich nicht in inhaltlicher Hinsicht, sondern auf allen weiteren Ebenen unterstützt haben: Dieser Dank gilt den Freunden und treuen Weggefährten im Studium. Meinen Eltern danke ich für den vollkommenen Rückhalt und die fortwährende Unterstützung bei allen Fragen des (universitären) Lebens. Meinem Bruder danke ich für spannende interdisziplinäre Diskussionen und eine übergreifende Inspiration. Mein größter Dank gilt meiner Freundin, die mich auf diesem Weg mit Herz, Verstand und Lebenslust begleitete.

CURRICULUM VITAE BENNO LUDWIG

Personal Details

Name: Benno Ludwig
D.O.B: 14th June 1978
Place of birth: Bremen
Citizenship: German



Education

- 02/2006 – 09/2009 **PhD in applied solid state physics** at RWTH Aachen University
- Title: “Avalanche dynamics of structural phase transitions in shape memory alloys by acoustic emission spectroscopy”
 - Talks as invited speaker
 - Publications in the international journals “Physical Review B” and “Applied Physics Letters”
- 03/2008 – 05/2008 &
12/2006 – 01/2007 **International research stays** at University of Barcelona, UB
- Design of experimental devices and execution of test series
 - Publications of results in international journals
- 10/2001 – 12/2005 **Advanced study period in physics** at RWTH Aachen University
- Diploma thesis in solid state physics on phase transition phenomena of shape memory alloys by optical methods
 - Philosophy as subsidiary subject
- 09/2002 – 07/2003 **Studies abroad** at Technical University of Catalonia, UPC Barcelona
- Classes in innovation, management, and economics
- 10/1999 – 09/2001 **Basic courses in physics** at RWTH Aachen University
- 09/1998 – 09/1999 **Community service** at cultural centre “Haus im Park”, Bremen
- Cultural and event management
- 05/1998 **A-levels** at “Altes Gymnasium zu Bremen”

Additional Skills

Languages

German:	Mother tongue
English:	Fluent in writing and speaking
Spanish:	Fluent in writing and speaking

Aachen, 15th October 2009